Modeling and simulations of light emission and propagation in open nanophotonic systems

de Lasson, Jakob Rosenkrantz

Publication date:
2015

Document Version
Publisher's PDF, also known as Version of record

Modeling and simulations of light emission and propagation in open nanophotonic systems

A dissertation submitted in partial fulfillment of the requirements
for the degree of philosophiae doctor

Jakob Rosenkrantz de Lasson
Ph.D. Thesis
October 2015

DTU Fotonik
Department of Photonics Engineering
Technical University of Denmark

Project period:	October 2012 – October 2015
Supervisors:	Assoc. Prof. Niels Gregersen Prof. Jesper Mørk Dr. Philip Trøst Kristensen
Ph.D. defense date:	December 16, 2015
Ph.D. defense committee:	Assoc. Prof. Andrei Lavrinenko, Technical University of Denmark Prof. Stephen Hughes, Queen's University Assoc. Prof. Thomas Søndergaard, Aalborg University
Comments and feedback:	jakob@jakobrdl.dk

Abstract

Light emission and propagation in photonic crystal membranes are studied theoretically, with an emphasis on waveguides, slow light effects, and coupled cavity-waveguide systems.

A Bloch mode expansion formalism for optical modeling of photonic crystal membranes is presented, and perfectly matched layer boundary conditions are introduced to emulate the inherent openness of the photonic crystal membrane. The impact of the computational domain size and perfectly matched layer parameters on dipole emission in a photonic crystal membrane waveguide is investigated, and we find the associated computational uncertainty to be of larger magnitude than typical estimates found in literature.

A photonic crystal waveguide with one or two side-coupled cavities is considered, and the local density of states is described using a semi-analytical quasi-normal mode theory. We propose original techniques for computing and normalizing quasi-normal modes in extended systems, and comparing to numerically exact calculations, the theory correctly predicts a slight asymmetry (one cavity) and a peak and a dip (two cavities) in the local density of states spectra.

Next, the photonic crystal waveguide is interfaced with a side-coupled cavity and a scattering site in the waveguide, and we demonstrate that the shape of the transmission spectrum can be controlled by the cavity-scattering site distance, for example to exhibit asymmetric Fano shapes.

Subsequently, we investigate an active photonic crystal waveguide in the slow light region and present an original coupled Bloch mode model, with material gain treated as a perturbation, that includes back-coupling between the counter propagating passive Bloch modes. We show that this gives rise to distributed feedback, which puts fundamental limitations on the maximum achievable gain of the slow light amplifier.

Finally, dipole emission in photonic crystal membrane waveguides is analyzed, where we design slow and fast light waveguides for enhanced single-photon emission into a guided mode. We investigate spectra and spatial maps of dipole emission and find that the relative coupling into the guided mode, β, remains in excess of 50%, even in non-optimum situations, and quickly approaches unity towards the band edge. Preliminary experimental results that build on the theoretical designs demonstrate emission from position-controlled quantum dots into the waveguide mode.

In a disjoint chapter, we study the localized surface plasmon modes of plasmonic nano dimers, and both theoretically and experimentally, we find an almost-inverse scaling of the relative shift of the plasmon wavelength with particle distance in the sub-radius range.

Resumé

Lysudsendelse og -udbredelse i fotoniske krystal membraner studeres teoretisk, med fokus på bølgeledere, langsomt lys og koblede kavitet-bølgeleder systemer.

En formalisme baseret på udvikling på Bloch modes til optisk modellering af fotoniske krystal membraner præsenteres, og perfectly matched layer grænsebetingelser introduceres for at efterligne åbenheden af den fotoniske krystal membran. Indflydelsen på dipolemission i en fotonisk krystal membran bølgeleder af størrelsen af beregningsdomænet samt perfectly matched layer parametre undersøges, og vi finder, at de tilhørende beregningsusikkerheder er større end typiske estimater fra litteraturen.

En fotonisk krystal bølgeleder med en eller to sidekoblede kaviteter behandles, og den lokale tilstandstæthed beskrives med en semi-analytisk quasi-normal mode teori. Vi præsenterer originale metoder til at beregne og normalisere quasi-normal modes i udstrakte systemer, og ved sammenligning med numerisk eksakte beregninger forudsiger teorien korrekt en svag asymmetri (en kavitet) samt en top og et dyk (to kaviteter) i spektre for den lokale tilstandstæthed.

Som det næste forbinder vi den fotoniske krystal bølgeleder med en sidekoblet kavitet og et spredningspunkt i bølgelederen, og vi demonstrerer, at formen af transmissionsspektret kan kontrolleres af kavitet-spredningspunkt-afstanden og f.eks. udvise asymmetriske Fano-former.

Derpå undersøger vi en aktiv fotonisk krystal bølgeleder i langsomt lys området og præsenterer en original koblet Bloch mode model, hvor materialeforstærkning behandles perturbativt, og som inkluderer tilbagekobling mellem de kontrapropagerende Bloch modes. Vi viser, at dette giver anledning til distribueret tilbagekobling, der sætter fundamentale begrænsninger på den maksimale forstærkning, som langsomt lys komponenten kan yde.

Endelig analyseres dipolemission i fotoniske krystal membran bølgeledere, hvor vi designer langsomt og hurtigt lys bølgeledere for øget udsendelse af enkelte fotoner til en guidet mode. Vi undersøger spektre og rumlige kort af dipolemission og finder, at den relative kobling til den guidede mode, β, forbliver større end 50%, også i ikke-optimale situationer, og hurtigt nærmer sig 100% imod båndkanten. Foreløbige eksperimentelle resultater, der bygger på de teoretiske designs, demonstrerer udsendelse fra positions-kontrollerede kvantepunkter til bølgeledermoden.

I et uafhængigt kapitel studerer vi lokaliserede overfladeplasmoner af plasmoniske nano dimere, og både teoretisk og eksperimentelt finder vi en næsten-invers skalering af det relative skift af plasmonbølgelængden med partikelafstanden i sub-radius området.

Preface

This thesis is submitted in candidacy for the Ph.D. degree from the Technical University of Denmark (DTU). The project has been carried out at DTU Fotonik, the Department of Photonics Engineering, in the Nanophotonics Theory & Signal Processing group from October 2012 to October 2015 and has been supervised by Niels Gregersen, Jesper Mørk, and Philip Trøst Kristensen. From January to March 2015, a research stay at École Polytechnique Fédérale de Lausanne (EPFL), Switzerland, in the Laboratory of Physics of Nanostructures (LPN) was undertaken, with the aim of designing and demonstrating single-photon emission in photonic crystal waveguides.

The project has partly been independent and partly been affiliated with the NAnophotonics for TErabit Communications (NATEC) Centre of Excellence, that is based at DTU Fotonik. The topics covered in the thesis focus on photonic crystals and the use of these for controlling light emission and propagation. This ties in closely with NATEC activities, for example on exploiting slow light effects for developing compact lasers and amplifiers as well as optical switches, while the work on spontaneous emission control of quantum dots for development of single-photon sources is an independent activity at DTU Fotonik, led by the main supervisor of this thesis. The combination of photonic crystals and single quantum dots for single-photon generation is a new activity at DTU Fotonik that has been initiated in the present project in collaboration with EPFL-LPN.

Acknowledgments First and foremost, I am indebted to my supervisors and grateful for their guidance and input in the course of the project; I could not have wished for a more competent team of researchers to assist me during my Ph.D. journey. This team has brought diverse scientific interests and viewpoints to the table, which has given me the chance to explore interesting problems of both fundamental and practical nature. I thank Niels for introducing me to the Bloch mode formalism, that most of the work in the thesis builds on, and for *always* having the time to discuss the little details and the big picture. I thank Jesper for being the best group leader that one could ask for, for being impressively engaged in my project in spite of many other obligations, and for occasional reminders to remember to stay curious. I thank Philip for introducing me to the concept of quasi-normal modes as a practical and powerful tool for open systems and for being enthusiastic and persistent about my work and project.

I thank all members of the Theory & Signal Processing group as well as of the Nanophotonics research section at DTU Fotonik for creating an inspiring scientific atmosphere. A special thanks goes to Andrei Andryieuski, that I shared an office with, and with whom I had many stimulating and fun discussions, about nanophotonics, computer simulations, researcher life, and much more.

I also thank the entire staff at EPFL-LPN for welcoming me during my research stay with them in early 2015. This visit expanded my understanding of the experimental aspects and challenges when interfacing single quantum dots with photonic crystals, which

I believe my theoretical thesis has benefited from. I was happy to share an office with Bruno Rigal and Clément Jarlov that I thank for social and scientific hospitality.

I express my gratitude towards colleagues and collaborators that have contributed to my understanding and with ideas during discussions. Among many people, I especially thank Shima Kadkhodazadeh from DTU Cen and Bruno Rigal from EPFL-LPN for being the leading contributors to the experimental results reported in this thesis.

On the social side of things, I thank the "usual suspects" (Per, Philip, Jesper, Per, Dara, Nika) from my daily lunch team, that also occasionally transformed into a "Copenhagen beer bar crawl" team, for healthy distraction. Likewise, the DTU Fotonik Tuesday morning football team is recognized for energizing and fun matches.

Finally, I wish to acknowledge Oticon Fonden, Otto Mønsteds Fond, Torben og Alice Frimodts Fond, Ingeniør Alexandre Haynmann og hustru Nina Haynmann's Fond, Augustinusfonden, and Thomas B. Thriges Fond for economical support towards conference participation, my external research stay, and summer school attendance.

Jakob Rosenkrantz de Lasson
Technical University of Denmark, Kgs. Lyngby
October 2015

Publications

Below we list the journal publications and conference contributions that have resulted from the Ph.D. project reported in this thesis. An overview of the contributions by the author to the journal publications is also given.

Journal publications

J6 J. R. de Lasson, P. T. Kristensen, J. Mørk and N. Gregersen, "Semianalytical quasi-normal mode theory for the local density of states in coupled photonic crystal cavity-waveguide structures", Opt. Lett. **40**, 5790-5793 (2015)

J5 Y. Chen, J. R. de Lasson, N. Gregersen, and J. Mørk, "Impact of slow-light enhancement on optical propagation in active semiconductor photonic-crystal waveguides", Phys. Rev. A, **92**, 053839 (2015)

J4 P. T. Kristensen, J. R. de Lasson, and N. Gregersen, "Calculation, normalization, and perturbation of quasinormal modes in coupled cavity-waveguide systems", Opt. Lett. **39**, 6359-6362 (2014)

J3 J. R. de Lasson, P. T. Kristensen, J. Mørk, and N. Gregersen, "Roundtrip matrix method for calculating the leaky resonant modes of open nanophotonic structures", J. Opt. Soc. Am. A **31**, 2142-2151 (2014)

J2 S. Kadkhodazadeh, J. R. de Lasson, M. Beleggia, H. Kneipp, J. B. Wagner, and K. Kneipp, "Scaling of the Surface Plasmon Resonance in Gold and Silver Dimers Probed by EELS", J. Phys. Chem. C **118**, 5478-5485 (2014)

J1 J. R. de Lasson, J. Mørk, and P. T. Kristensen, "Three-dimensional integral equation approach to light scattering, extinction cross sections, local density of states, and quasi-normal modes", J. Opt. Soc. Am. B **30**, 1996-2007 (2013)

Submitted manuscripts

J7 A. D. Osterkryger, J. R. de Lasson, M. Heuck, Y. Yu, J. Mørk, and N. Gregersen, "Spectral symmetry of Fano resonances in a waveguide coupled to a microcavity" (arXiv:1512.05869 [physics.optics])

Conference contributions

C9 J. R. de Lasson, B. Rigal, E. Kapon, J. Mørk, and N. Gregersen, "Design of Slow and Fast Light Photonic Crystal Waveguides for Single-photon Emission Using a Bloch

Mode Expansion Technique", Progress In Electromagnetics Research Symposium (PIERS) (2015)

C8 N. Gregersen, J. R. de Lasson, and J. Mørk, "Design and simulations of highly efficient single-photon sources", Progress In Electromagnetics Research Symposium (PIERS) (2015)

C7 A. D. Osterkryger, J. R. de Lasson, Y. Yu, J. Mørk, and N. Gregersen, "Investigations on the parity of Fano resonances in photonic crystals", CLEO Europe (2015)

C6 J. R. de Lasson, P. T. Kristensen, J. Mørk, and N. Gregersen, "A Bloch mode expansion approach for analyzing quasi-normal modes in open nanophotonic structures", META'14 (2014)

C5 J. R. de Lasson, P. T. Kristensen, J. Mørk, and N. Gregersen, "A Bloch modal approach for engineering waveguide and cavity modes in two-dimensional photonic crystals", SPIE Photonics Europe 2014 [Proc. SPIE 9127, 91270F (2014)]

C4 S. Kadkhodazadeh, J. R. de Lasson, H. Kneipp, J. B. Wagner, and K. Kneipp "Calibrating Au and Ag plasmonic rulers with EELS", Electron Microscopy and Analysis Group Conference (2013)

C3 S. Kadkhodazadeh, J. R. de Lasson, S. Raza, P. T. Kristensen, J. Mørk, J. B. Wagner, and K. Kneipp, "Probing plasmon resonance's dependence on gap size in silver dimers by EELS", Scandem 2013 - Annual Meeting of the Nordic Microscopy Society (2013)

C2 S. Kadkhodazadeh, J. R. de Lasson, S. Raza, P. T. Kristensen, J. Mørk, J. B. Wagner, and K. Kneipp, "Probing plasmon resonance's dependence on gap size in silver dimers by EELS", International Electron Energy Loss Spectroscopy Meeting on Enhanced Data Generated by Electrons (2013)

C1 J. R. de Lasson, P. T. Kristensen, and J. Mørk, "Multiple-scattering formalism beyond the quasistatic approximation: Analyzing resonances in plasmonic chains", TaCoNa Photonics 2012 [AIP Conf. Proc. 1475, 158-160 (2012)]

Contributions to journal publications by the author

For journal publications J1, J3, and J6, all research, development and implementation of numerical code, and writing of the manuscripts were carried out by the author.

For journal publication J2, the author contributed computational data, participated in discussions on interpretations of both experimental and computational data, and wrote a smaller part of the manuscript.

For journal publications J4 and J7, the author contributed via discussions on and interpretations of theory and computational data as well as via feedback for the manuscript.

For journal publication J5, the author contributed part of the computational data, participated in discussions on interpretations of computational data, and finalized the manuscript before submission.

Contents

Acronyms

1D One-dimensional, one dimension.
2D Two-dimensional, two dimensions.
3D Three-dimensional, three dimensions.
BC Boundary condition.
DA Dipole approximation.
DBR Distributed Bragg reflector.
DDA Discrete dipole approximation.
DFB Distributed feedback.
EEL Electron energy loss.
EELS Electron energy-loss spectroscopy.
FDTD Finite-difference time-domain.
FEM Finite element method.
FMM Fourier modal method.
FP Fabry-Pérot.
LDOS Projected local density of states.
LHS Left hand side.
LSP Localized surface plasmon.
PhC Photonic crystal.
PML Perfectly matched layer.
PTE Partially transmitting element.
QD Quantum dot.
QNM Quasi-normal mode.
RHS Right hand side.
SE Spontaneous emission.
STEM Scanning transmission electron microscopy.
TE Transverse electric.
TM Transverse magnetic.

Chapter 1

Introduction

> *If you just focus on the smallest details, you never get the big picture right.*
>
> Leroy Hood

In this introductory chapter, we briefly describe the perspectives, potential applications, structures, and methods covered in this thesis. Literature surveys on specific topics are presented in later chapters.

Integrated optical circuits and quantum information technology

Electronics is increasingly becoming a bottleneck in terms of bandwidth in communication systems and data centers, and for transmission of information over long distances, optical fibers have already replaced electronic signals and copper cables [1]. The success of optical communication on long distances and the challenges with high-speed electronics on short distances (chip-to-chip and ultimately on-chip) [1] have motivated research in integrated optical circuits, including substantial efforts by both Intel [2] and IBM [3]. In addition to low energy consumption and high speed, integrated optical circuits should be compact, and to this end photonic crystals [4] have been proposed as a practical platform for photonic miniaturization with wavelength-scale components [5]. Photonic crystals can confine light both temporally and spatially, which are key functionalities for developing integrated optical circuits [6], and may additionally guide light at dramatically lowered speeds, an effect known as slow light [7, 8].

The quantum nature of light and matter was discovered approximately a century ago, and besides being fundamentally interesting, quantum phenomena are now also being

explored for applications in, for example, quantum cryptography and quantum information technology [9]. One scheme for realizing quantum communication networks is by interfacing single quanta of light (photons) with single quantum emitters (atoms, molecules, or quantum dots, for example) [9], where development of systems for generating [10] and routing [11] single photons becomes central. As well as being potentially useful for integrated optical circuits, photonic crystals could provide a versatile platform for on-chip generation and manipulation of single photons [12].

In this thesis, we focus on photonic crystals, more specifically photonic crystal membranes to be introduced in more detail in Chapter 2, in the context of both integrated optical circuits and quantum information technology. These structures are inherently open; they are coupled to the surrounding world, either intentionally (in- and out-coupling) or parasitically (radiative losses), and this open and leaky nature of photonic crystal membrane systems will be emphasized. The work to be reported is focused on modeling and simulations of light emission and propagation in such systems, which is part of the research field of *nanophotonics*. In the following section, we provide an overview of popular computational methods in nanophotonics.

Computational nanophotonics

Most structures in nanophotonics of practical interest are sufficiently complex in shape and composition that Maxwell's equations cannot be solved in closed form. Hence, much analysis and design is based on numerical solutions, and below we briefly review the most important computational techniques and motivate the choice of method for this thesis. We also refer to a recent textbook on this topic [13].

The finite-difference time-domain (FDTD) method [14] is the de facto standard for numerical calculations in nanophotonics and is by many considered the reference for other approaches and methods.[1] FDTD uses the differential form of Maxwell's equations and a discrete spatio-temporal grid, originally proposed by Yee [15], for approximating the electromagnetic fields numerically. The simplicity of the FDTD formulation and algorithms makes it robust to structure shapes and deformations, but also causes large speed and memory requirements for simulations of full 3D structures. Today, both self-developed and commercial FDTD software is widely used, and Lumerical Solutions provides a commercial FDTD implementation that is both versatile and efficient.

The finite element method (FEM) [16] is used in many branches of the sciences for solving partial differential equations, and it can be used for solving Maxwell's equations in both the time and frequency domains. In FEM, the structure is divided into a number of mesh elements, and a set of basis functions is used for representing the solutions, for example the electromagnetic fields, on the discrete mesh grid. A standard feature of FEM is the ability to impose a non-homogeneous mesh, for example with finer meshing where solutions are expected to vary more rapidly. Also, FEM can efficiently handle multiphysics problems, for example both the electrical, optical, and thermal problems of photonic crystals, and the commercial COMSOL Multiphysics is widely used for this purpose. As with FDTD, FEM computations are fairly memory demanding for 3D problems; Javadi [17], for example, reports the use of 256 GB of memory per computation for modeling of dipole emission in photonic crystal membrane waveguides.

An alternative to Maxwell's equations formulated in differential form is integral equation formulations, where equivalent currents replace the structure of interest [18]. Such

[1] A common question in the computational nanophotonics community is: "*Why* don't you use FDTD?".

integral formulations involve Green's functions that by construction satisfy a radiation condition at infinity and, as opposed to FDTD and FEM, formally only involve discretization of bounded parts of space [19]. The radiation condition is crucial for modeling of radiating structures, which has made this approach, together with the Method of Moments [20], popular for the design of radio antennas [18]. A drawback of the method is the complexity in expressing the Green's function for non-homogeneous backgrounds [19, 21], as required for modeling of, for example, the photonic crystal membrane.

A less known class of techniques is the modal methods [22, 23], that are frequency domain methods for solving Maxwell's equations in differential form. The starting point is the division of the structure of interest into layers that are uniform along a chosen propagation direction. The electromagnetic fields are expanded on the local solutions in each layer and coupled together using a scattering matrix algorithm. Along the propagation direction, the solutions are described semi-analytically, and the computational complexity locally in each layer thus only depends on the transverse topography. This makes the modal methods efficient and viable for analyzing (long) waveguide-based structures. Also, the natural solutions in periodic systems, the Bloch modes, can naturally be computed and used as an expansion basis with the modal methods.

Most of the work in this thesis builds on a modal method formulation, where Bloch modes are computed numerically and used as an expansion basis for the analysis of light emission and propagation in photonic crystal membranes. This choice is partly motivated by in-house expertise in the use of modal method techniques [10, 24]; partly by existing literature on the use of these methods for modeling of photonic crystal membranes [25–28]. In Chapters 3 and 4, we present the method in detail and also discuss its strengths and weaknesses. In two situations, Bloch mode expansion calculations are compared with FEM results (Chapters 5 and 7), and in Chapter 9, a volume integral equation method is presented and used for analyzing a plasmonic nanostructure. Approximate analytical or semi-analytical models can sometimes constitute a useful compromise between transparency and accuracy, and in Chapters 5 and 7 we present such models. We refer to [29, 30] for recent studies that compare the performance of several of the above-mentioned numerical methods.

Scope of thesis

Two overall goals of the project reported in this thesis are: (1) To assess the quality and feasibility of the Bloch mode expansion framework for modeling and analysis of full 3D photonic crystal membrane structures, and (2) to use the framework for gaining new insights into photonic crystal structures, with an emphasis on waveguides, slow light effects, and coupled cavity-waveguide structures.

Overview of thesis

The thesis is divided into ten chapters, and below we provide short summaries of structures and methods in Chapters 2 to 9.

> **Chapter 2** The preliminaries of theory and structures that we use and build on in the following chapters are presented. Maxwell's equations and related electrodynamic relations are presented, the theory of spontaneous emission and local density of states is outlined, and photonic crystal membrane waveguides and cavities are introduced.

Chapter 3 The Bloch mode expansion formalism for modeling of light emission and propagation in photonic crystal membrane structures is presented. Likewise, the computational flow is outlined, and strengths and weaknesses of the formalism are discussed.

Chapter 4 The importance of formulating proper boundary conditions when modeling open systems is discussed, and perfectly matched layers are introduced as a remedy for emulating the openness and added to the formalism of Chapter 3. The impact of perfectly matched layer parameters and computational domain size on dipole emission in a photonic crystal membrane waveguide is investigated systematically.

Chapter 5 A quasi-normal mode theory for describing light emission and propagation in coupled photonic crystal cavity-waveguide structures is presented. A semi-analytical quasi-normal mode theory for the local density of states is proposed and validated against numerically exact calculations. Original techniques for computing and normalizing quasi-normal modes in extended systems are developed, and a quasi-normal mode perturbation theory is presented and validated.

Chapter 6 The transmission through a photonic crystal waveguide with a side-coupled cavity and a scattering site is investigated. The impact of the cavity-scattering site distance on the shape of the transmission spectrum is analyzed.

Chapter 7 An optical amplifier consisting of a finite-length active slow light photonic crystal waveguide is analyzed. A coupled Bloch mode model is presented, with material gain treated as a perturbation and including back-coupling that is typically neglected. The model is validated against numerically exact calculations, and the impact of both slow light and material gain on optical amplification is analyzed.

Chapter 8 Dipole emission in photonic crystal membrane waveguides is analyzed, and dispersion engineering is used to design slow and fast light waveguides for efficient single-photon emission. Spectra and spatial maps of guided and radiation mode couplings as well as of the β factor are demonstrated, and preliminary experimental results of light emission from position-controlled quantum dots in photonic crystal membrane waveguides are presented.

Chapter 9 Localized surface plasmon modes of gold and silver nano dimers are analyzed, and the scaling of the bright dipolar plasmon mode energy with particle spacing is investigated experimentally and theoretically.

Finally, Chapter 10 summarizes highlights from the thesis and provides an outlook.

CHAPTER 2

Photonics engineering in nanostructures

> *Everything should be made as simple as possible, but no simpler.*
>
> Albert Einstein

In this chapter, we introduce the basic equations, concepts, and structures that we use and build on in the rest of this thesis. In Section 2.1, we introduce Maxwell's equations and other electrodynamic relations; in Section 2.2, we discuss spontaneous emission engineering, local density of states, and the Purcell factor; in Section 2.3, we introduce photonic crystal membranes, with an emphasis on waveguides and cavities, and finally, in Section 2.4, we briefly introduce the notion of optical antennas and the β factor.

2.1 Electrodynamics

Much of the work in the present thesis is related to solving Maxwell's equations in different structures and with different types of sources. In the following sections, we present these equations, give the constitutive relations that we use throughout the work, and state two relations, Poynting's theorem and the Lorentz reciprocity theorem, that are direct consequences of Maxwell's equations. We also introduce the dyadic Green's function that in the following Section 2.2 is shown to play an important role in the description of light-matter interactions. All material is taken from [31].

2.1.1 Maxwell's equations

In the time domain, Maxwell's equations read as follows

$$\nabla \times \mathbf{E} = -\partial_t \mathbf{B}, \tag{2.1a}$$
$$\nabla \times \mathbf{H} = \mathbf{j} + \partial_t \mathbf{D}, \tag{2.1b}$$
$$\nabla \cdot \mathbf{D} = \rho_\mathrm{e}, \tag{2.1c}$$
$$\nabla \cdot \mathbf{B} = 0, \tag{2.1d}$$

where $\mathbf{E}$, $\mathbf{D}$, $\mathbf{H}$, and $\mathbf{B}$ are the electric field, the electric displacement field, the magnetic field, and the magnetic induction field, respectively, while $\mathbf{j}$ and ρ_e are the free current density and free charge density, respectively. Throughout the thesis, ∂_α is shorthand notation for partial derivative with respect to the variable α, e.g. $\partial_t \equiv \partial/\partial t$. All fields are functions of space and time, and by invoking the harmonic time dependence

$$\mathbf{E}(\mathbf{r}; t) = \mathbf{E}(\mathbf{r}; \omega) \exp(-\mathrm{i}\omega t), \tag{2.2}$$

and similarly for all other fields, we obtain Maxwell's equations in the frequency domain

$$\nabla \times \mathbf{E} = \mathrm{i}\omega \mathbf{B}, \tag{2.3a}$$
$$\nabla \times \mathbf{H} = \mathbf{j} - \mathrm{i}\omega \mathbf{D}, \tag{2.3b}$$
$$\nabla \cdot \mathbf{D} = \rho_\mathrm{e}, \tag{2.3c}$$
$$\nabla \cdot \mathbf{B} = 0, \tag{2.3d}$$

where all fields are functions of space and frequency. Finally, we assume non-magnetic, linear, isotropic, and local materials, which allows us to use the following constitutive relations

$$\mathbf{D} = \epsilon_0 \epsilon \mathbf{E}, \tag{2.4a}$$
$$\mathbf{B} = \mu_0 \mathbf{H}, \tag{2.4b}$$

where ϵ_0 and μ_0 are the vacuum permittivity and permeability, while ϵ is the relative permittivity that could be a function of space and frequency. Inserting Eqs. (2.4) into Eqs. (2.3) puts Maxwell's equations in the final form to be used here

$$\nabla \times \mathbf{E} = \mathrm{i}\omega \mu_0 \mathbf{H}, \tag{2.5a}$$
$$\nabla \times \mathbf{H} = \mathbf{j} - \mathrm{i}\omega \epsilon_0 \epsilon \mathbf{E}, \tag{2.5b}$$
$$\epsilon_0 \nabla \cdot (\epsilon \mathbf{E}) = \rho_\mathrm{e}, \tag{2.5c}$$
$$\nabla \cdot \mathbf{H} = 0. \tag{2.5d}$$

Throughout this thesis, the free charge density is $\rho_\mathrm{e} = 0$, while we both consider situations without ($\mathbf{j} = \mathbf{0}$) and with ($\mathbf{j} \neq \mathbf{0}$) free current densities.

2.1.2 Poynting's theorem and Lorentz reciprocity

A consequence of Maxwell's equations in the frequency domain is the following relation that is known as Poynting's theorem

$$\int_S \mathbf{S} \cdot \mathbf{n} \, \mathrm{d}A = -\frac{1}{2} \int_V \mathrm{Re}\left(\mathbf{j}^* \cdot \mathbf{E}\right) \, \mathrm{d}V, \tag{2.6a}$$
$$\mathbf{S} \equiv \frac{1}{2} \mathrm{Re}\left(\mathbf{E} \times \mathbf{H}^*\right), \tag{2.6b}$$

where $\mathbf{S}$ is the time-averaged Poynting vector, and $\mathbf{n}$ is an outward pointing normal vector on the closed boundary of V, S. Eq. (2.6a) states that the power out through S (LHS) equals the power dissipation inside V due to the current $\mathbf{j}$ (RHS), and in practice we later use this relation to quantify the power radiated by dipoles in different environments by evaluation of either side of this equation.

Another consequence of Maxwell's equations is the Lorentz reciprocity theorem that reads as follows

$$\int_S [\mathbf{E}_1 \times \mathbf{H}_2 - \mathbf{E}_2 \times \mathbf{H}_1] \cdot \mathbf{n} \, \mathrm{d}A = \int_V [\mathbf{j}_1 \cdot \mathbf{E}_2 - \mathbf{j}_2 \cdot \mathbf{E}_1] \, \mathrm{d}V \tag{2.7}$$

where fields $[\mathbf{E}_1, \mathbf{H}_1]$ ($[\mathbf{E}_2, \mathbf{H}_2]$) are produced by the source $\mathbf{j}_1$ ($\mathbf{j}_2$), all at the same frequency ω. In Chapter 3, the Lorentz reciprocity theorem is the starting point for determining the dipole excitation of Bloch modes.

2.1.3 Dyadic Green's function

If we take the curl of either side of Eq. (2.5a) and replace $\nabla \times \mathbf{H}$ using Eq. (2.5b), we obtain the driven wave equation for the electric field

$$\nabla \times \nabla \times \mathbf{E} - k_0^2 \epsilon \mathbf{E} = \mathrm{i}\omega\mu_0 \mathbf{j}, \tag{2.8}$$

where we have defined the free-space wave number $k_0 \equiv \omega/\mathrm{c}$. A type of source that we are particularly interested in is a point source, or a dipole, with current density

$$\mathbf{j}(\mathbf{r}) = \mathbf{j}_\mathrm{D} \delta(\mathbf{r} - \mathbf{r}_\mathrm{D}), \tag{2.9}$$

that is located at position $\mathbf{r}_\mathrm{D}$. In the view of this and Eq. (2.8), we define the dyadic Green's function, $\mathbf{G}(\mathbf{r}, \mathbf{r}_\mathrm{D})$, as the solution of the following equation

$$\nabla \times \nabla \times \mathbf{G}(\mathbf{r}, \mathbf{r}_\mathrm{D}) - k_0^2 \epsilon \mathbf{G}(\mathbf{r}, \mathbf{r}_\mathrm{D}) = \mathbf{I} \delta(\mathbf{r} - \mathbf{r}_\mathrm{D}), \tag{2.10}$$

where $\mathbf{I}$ is a unit dyad (that can be represented as a 3×3 unity matrix), and where we stress the two-position dependence of the dyadic Green's function.[1] By combining Eqs. (2.8) and (2.10), the electric field at $\mathbf{r}$ due to a dipole at $\mathbf{r}_\mathrm{D}$ is

$$\mathbf{E}(\mathbf{r}) = \mathrm{i}\omega\mu_0 \mathbf{G}(\mathbf{r}, \mathbf{r}_\mathrm{D}) \mathbf{j}_\mathrm{D}, \tag{2.11}$$

and each column of the dyadic Green's function is thus proportional to the electric field produced by a dipole. In the following section, we discuss the role of the Green's function as a link between classical dipole emission and spontaneous emission from quantum emitters.

2.2 Spontaneous emission and local density of states

The spontaneous emission (SE) rate of a quantum emitter was, until Purcell's seminal work in 1946 [32], thought to be an intrinsic property of the emitter, but Purcell proposed that this rate can be enhanced inside a resonant cavity by a factor that is now known as the Purcell factor. This effect was verified experimentally by Drexhage in the 1960s and 1970s, where the radiative lifetime of molecules in front of planar interfaces was shown to

[1] In addition to satisfying Eq. (2.10), we require that the dyadic Green's function be an outgoing wave, i.e., that it satisfies a *radiation condition*.

depend on the distance to the interface as well as the dipole orientation [33], and later by Goy *et al.* for atoms in cavities [34]. SE is a quantum mechanical phenomenon, caused by vacuum field fluctuations, but as we quantify below, the *modification* of the SE rate can be described classically; in this picture, the radiation initially emitted scatters in the photonic environment and arrives back at the emitter position, which may suppress or enhanced the SE rate [35].

The following, and all work in this thesis, builds on the dipole approximation of light-matter interactions. In this approximation, the quantum emitter is treated as a dipole, and the dependence of the light-matter coupling on the light field is given solely by the electric field strength at the dipole position. For microscopic quantum emitters like atoms and molecules, this is a very good description, while quantum dots (QDs) are mesoscopic, which renders the validity of the dipole approximation questionable. It is, however, an accurate approximation when QDs are embedded in the center of photonic crystal (PhC) membranes [11], while close to material interfaces (especially metallic ones [36]) electric field gradients might give rise to non-negligible corrections to the total light-matter coupling.

The SE rate of a quantum emitter, γ, is proportional to the (projected) local density of states (LDOS), ρ, that, in turn, can be expressed from the dyadic Green's function [35]

$$\gamma^{\alpha}(\mathbf{r}_{\mathrm{D}};\omega) = \frac{\pi\omega}{\hbar\epsilon_0}|\mathbf{p}|^2\rho^{\alpha}(\mathbf{r}_{\mathrm{D}};\omega), \tag{2.12}$$

$$\rho^{\alpha}(\mathbf{r}_{\mathrm{D}};\omega) = \frac{2\omega}{\pi c^2}\mathrm{Im}\left[\mathbf{n}_{\alpha}\cdot\mathbf{G}(\mathbf{r}_{\mathrm{D}},\mathbf{r}_{\mathrm{D}};\omega)\cdot\mathbf{n}_{\alpha}\right], \tag{2.13}$$

where $\mathbf{p}$ is the transition dipole moment of the quantum emitter at $\mathbf{r}_{\mathrm{D}}$, while $\mathbf{n}_{\alpha}$ is a unit normal vector in the direction of $\mathbf{p}$.[2] The LDOS, $\rho^{\alpha}(\mathbf{r}_{\mathrm{D}};\omega)$, is a measure for the local density of electromagnetic modes per unit frequency and volume that the emitter can decay spontaneously into, and by engineering this quantity via design of the photonic environment, the SE rate of embedded quantum emitters can be suppressed or enhanced. Furthermore, the relation in Eq. (2.13) provides a practical recipe for obtaining the LDOS; we need the dyadic Green's function at the position of the quantum emitter. Finally, we note that the modification of the SE rate of a quantum emitter due to a given photonic environment is the same as the modification of the power emission from a classical dipole in the same photonic environment [35][3]

$$\frac{\gamma^{\alpha}(\mathbf{r}_{\mathrm{D}};\omega)}{\gamma_0(\omega)} = \frac{P^{\alpha}(\mathbf{r}_{\mathrm{D}};\omega)}{P_0(\omega)}, \tag{2.14}$$

where the reference values, γ_0 and P_0, for example in bulk can be expressed analytically; see Appendix A.1. By normalization to a reference value, the dependencies on the transition dipole moment, $|\mathbf{p}|$ (LHS), and the classical dipole moment (RHS) vanish, and the modification of the SE rate can thus be computed by evaluation of the power emitted by a classical dipole.

The ratio in Eq. (2.14) is the Purcell factor *if* evaluated *on resonance* of a *single dominating mode* [40]. In this case, the SE (or LDOS) modification can be expressed in

[2] Here, and throughout the thesis, we assume a linear dipole. For treatment of a more general situation of, for example, a circular dipole, see [37, 38].

[3] The intrinsic quantum yield, or quantum efficiency, of the emitter is assumed to be unity here, $q_{\mathrm{i}} = 1$, i.e., all decays are assumed to be radiative. In solid-state systems of, for example, QDs in PhCs, non-radiative decay might be non-negligible, yielding $q_{\mathrm{i}} < 1$, but examples of InAs QDs with $q_{\mathrm{i}} \simeq 95\%$ have been reported [39].

the form originally proposed by Purcell [32]

$$F_{\mathrm{P}} = \frac{3}{4\pi^2}\left(\frac{\lambda_0}{n}\right)\frac{Q}{V_{\mathrm{eff}}}, \tag{2.15}$$

where λ_0 is the resonance wavelength, n is the refractive index at the position of the emitter, and Q (V_{eff}) is the quality factor (mode volume) of the dominating optical mode. This expression makes reference to two properties of an underlying optical mode, and engineering the SE rate thus amounts to modifying the temporal (Q) and/or spatial (V_{eff}) confinement of light in this one mode. Later, we demonstrate rigorously that the partial LDOS enhancement into single modes can be expressed in the form in Eq. (2.15), both for PhC cavities (Chapter 5) and PhC waveguides (Chapter 8). At the same time, we stress that the Purcell factor is an approximation to the rigorous LDOS enhancement, and that the validity of the underlying single-resonant-mode assumption must be assessed in each individual case.[4]

2.3 Photonic crystal membranes

PhCs are periodic structures, often made of silicon or III-V semiconductors, that may be used to control the emission, confinement, and propagation of light. Due to Bragg scattering, PhCs may form photonic bandgaps that are frequency ranges where light cannot propagate through the PhC crystal. PhCs thus inherently rely on wave interference, and for experiments and applications in the near-infrared part of the spectrum their characteristic dimensions are thus on the order of $\sim 300\,\mathrm{nm}$. The simplest type of PhC is a 1D periodic structure with alternating layers of two materials, a so-called Bragg stack or distributed Bragg reflector (DBR) [41]. For certain choices of materials and thicknesses of these layers, the counter propagating plane waves in each periodic element interfere destructively, and repeating the periodic element thus produces a stronger and stronger attenuation; a PhC bandgap forms. This makes DBRs practical candidates for realizing mirrors in micro- and nanostructured systems, and by introducing a defect somewhere in the DBR, for example by changing the thickness of one layer, a resonator may be created. Photonic bandgaps are spectral regions where the LDOS vanishes, and defect resonators may create LDOS peaks inside the bandgap. Thus, the DBR with a defect resonator may be used as a frequency selective filter, that transmits frequencies close to the defect frequency and reflects all other frequencies [41], or for SE enhancement of embedded quantum emitters [42–45].

The concept of Bragg scattering can be adopted for structures with periodicity in higher dimensions (2D or 3D), and as first discussed by Yablonovitch [46] and John [47], this may have important implications for localization of light in 3D as well as for the SE in such systems. SE control of QDs in inverse opal 3D PhCs has been demonstrated experimentally [48], and the advantage of full 3D PhCs is that they may exhibit a *complete* bandgap, i.e., a bandgap for *all* optical modes [49]. However, in the words of Busch *et al.* [50], fabrication of full 3D PhCs is not straightforward; "To date, the 'holy grail' of flexible and inexpensive fabrication of large-scale, high-quality, three-dimensional photonic-band-gap materials, and complex photonic architectures based on this platform, remains elusive. Thus, the field of three-dimensional PhCs is dominated by fabrication and characterization issues rather than physics or device applications". As an alternative,

[4] We note that some authors make no distinction between "LDOS enhancement" and "Purcell factor". Here, we adhere to Purcell's original idea of a single resonant mode (Purcell factor) as a special case of the more general coupling to many radiative channels (LDOS enhancement).

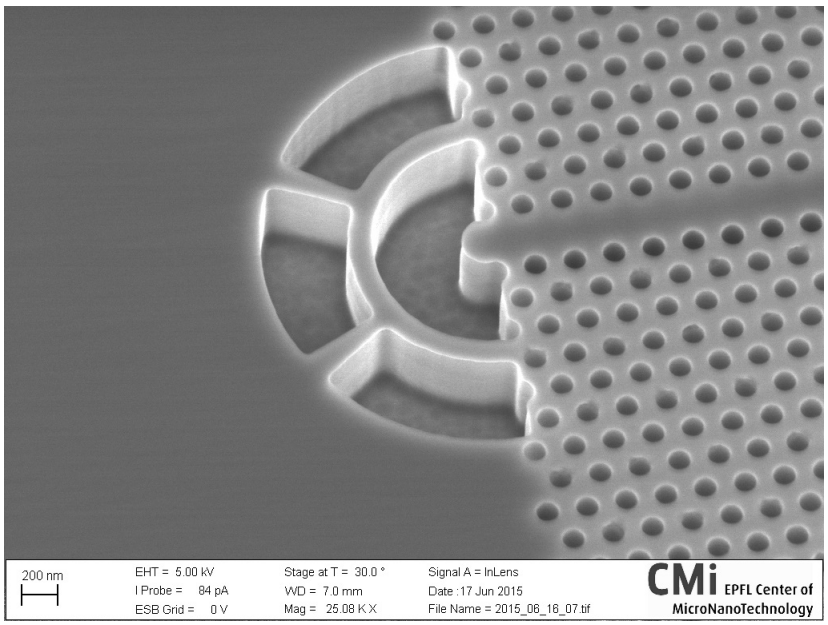

Figure 2.1 Image of PhC membrane waveguide with circular air holes in a GaAs membrane and with the waveguide terminated in a second-order Bragg grating. The scale bar (bottom left) indicates 200 nm. Image by courtesy of Bruno Rigal, Laboratory of Physics of Nanostructures, EPFL, Switzerland.

PhC #	Lattice	h_{Mem}	r/a	ϵ_{B}	$\epsilon_{\mathrm{Holes}}$	Bandgap	Chapter(s)
1	Rectangular	∞	0.2	1	8.9	$\mathbf{E}_{\perp}$	4, 5
2	Triangular	∞	0.3	9.61	1	$\mathbf{E}_{\parallel}$	6
3	Triangular	∞	0.25	12.1	1	$\mathbf{E}_{\parallel}$	7
4	Triangular	250 nm[a]	$0.22 - 0.38$	~ 12[b]	1	$\mathbf{E}_{\parallel}$	4, 8

[a] Unless otherwise stated, we use this value.
[b] We use $\epsilon_{\mathrm{B}} = (3.4648)^2$ or the frequency dependent refractive index of GaAs from [53].

Table 2.1 Parameters of PhC membrane structures investigated in this thesis.

therefore, PhC membranes or slabs have been proposed; 2D PhCs in the plane of the membrane that may exhibit a *partial* bandgap for *certain* optical modes and that confine light in the out-of-plane direction by total internal reflection [51]. These are easier to fabricate than full 3D PhCs, "can conveniently be probed by laser excitation from the top of the membrane" [11] and thus allow focus on "physics and device applications", as we explore in later chapters. All work on PhCs in the present thesis will focus on PhC membrane structures, and while many shapes of periodic elements in such PhC membranes can be envisioned, in particular when designed from inverse topology optimization methods [52], we also focus on PhC membranes with circular holes or rods. As an example, Fig. 2.1 displays a microscopy image of a PhC membrane waveguide with circular air holes in a GaAs membrane and with the waveguide terminated in a second-order Bragg grating. We return to this structure in Chapter 8.

In Table 2.1, we collect parameters for the PhC lattices we use in this work. The table

gives information on the type of PhC lattice, the membrane thickness, the hole/rod radius, the background and hole/rod permittivity, the type of bandgap, and the chapters where the PhCs are used. When the membrane thickness is taken to be infinite, the PhC is truly 2D, with a decoupling of the transverse electric (TE) and transverse magnetic (TM) modes, and PhCs 1, 2, and 3 exhibit a bandgap for one of these polarizations only. Such perfect 2D PhCs exist approximately if $h_{\mathrm{Mem}}/\lambda_0 \gg 1$, but often $h_{\mathrm{Mem}}/\lambda_0 \sim 1$ in practice. Nevertheless, as we explore in Chapters 5, 6, and 7, 2D approximations can provide qualitative and semi-quantitative insights on certain properties of PhC membranes. Of particular interest are PhC membrane structures including waveguides and/or cavities that we discuss more in the following sections.

2.3.1 Waveguides

If we remove a single row of holes or rods in the otherwise perfect PhC lattice, we create a line defect, called a W1 waveguide, in which light may be guided. In Fig. 2.2, we display a single supercell of such a line defect for the rectangular [triangular] lattice in panel (a) [(b)] with gray (red) color indicating the high-index (low-index) material. The length of the supercell is called the lattice constant and is denoted a, and an ideal and infinitely extended PhC membrane waveguide is made up of an infinite number of repetitions of this supercell along z. As we discuss in more detail in Chapter 3, the natural modes in such periodic structures are the Bloch modes [54]. For the PhC membrane waveguides, certain of these Bloch modes are confined along x due to the photonic bandgap and along y (if the membrane thickness is finite) due to total internal reflection, while their propagation along z is of the Bloch form and essentially determined by the associated Bloch wave number, k_z. These guided modes exist in a continuous band of frequencies, and the dependence of k_z on ω is the waveguide dispersion.[5] The dispersion of PhC 1 in Table 2.1 can be found in [55], while for PhC 3 we present the dispersion in Chapter 7.

In Fig. 2.3, we show the dispersion for the finite-thickness membrane, PhC 4 in Table 2.1, where the solid blue (dashed red) curve is the dispersion for the E_x x-y even-even (E_x x-y odd-even) Bloch mode. The black line at $k_z = \omega/\mathrm{c}$ is the light line, and modes existing below (above) it are bound to (unbound from) the PhC membrane. The gray area above the light line is the light cone where a continuum of modes in k_z exist at each frequency; these are the radiation modes. Under the light line, the bound and guided modes exist, and in the specific situation both an E_x x even and odd mode exist in the frequency range of interest. The membrane thickness is $h_{\mathrm{Mem}} = 250\,\mathrm{nm}$, and as we analyze in more detail in Chapter 8, the odd mode can be pushed into the light cone by reducing the thickness of the membrane.

The relevant speed of the guided modes is the group velocity, whose component along the waveguide is given by

$$v_{\mathrm{G}} \equiv \frac{\mathrm{c}}{n_{\mathrm{G}}} = \frac{\partial \omega}{\partial k_z}, \tag{2.16}$$

where n_{G} is the associated group index. The even mode exhibits a region of linear and a region of flattening dispersion, and from the definition in Eq. (2.16) these correspond to relatively large and small group velocities, respectively. Hence, we refer to the linear region as the fast light regime (small n_{G}) and the flattening region as the slow light regime (large

[5] More generally, the dependence on frequency of the Bloch mode wave vector along the symmetry directions of the PhC crystal is called the band diagram. For the PhC membrane with a defect waveguide, the only symmetry direction is the k_z axis, and the band diagram then simply reduces to a (k_z, ω) map.

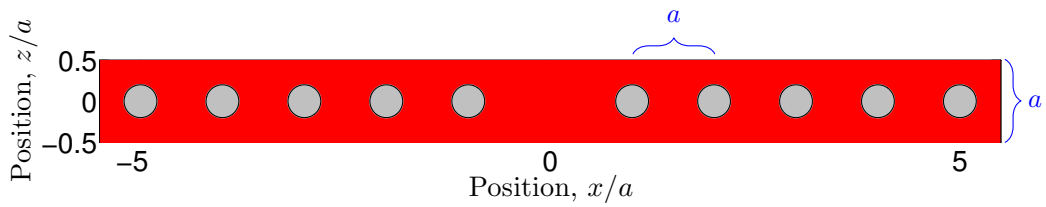

(a) Rectangular lattice. PhC 1 in Table 2.1.

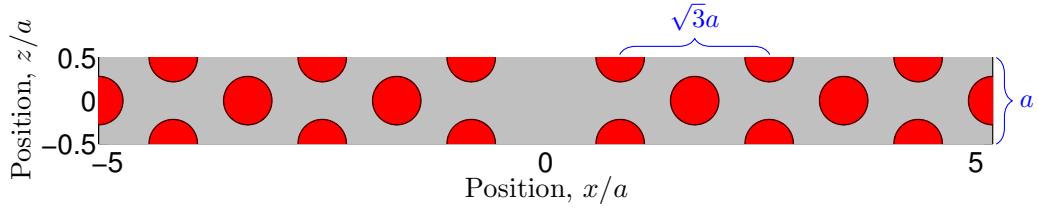

(b) Triangular lattice. PhCs 2, 3, and 4 in Table 2.1.

Figure 2.2 Supercells of PhC waveguides in xz-plane at $y = 0$. Gray (red) color indicates high-index (low-index) material, and PhC dimensions are indicated in blue.

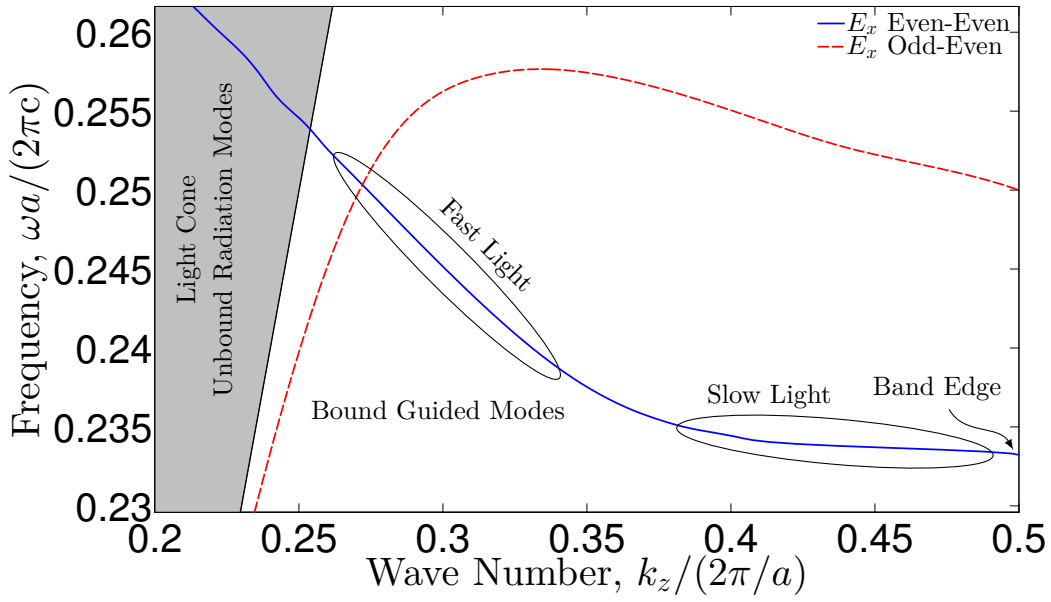

Figure 2.3 Dispersion curves for E_x x-y even-even (E_x x-y odd-even) Bloch modes in solid blue (dashed red) for PhC 4 in Table 2.1. The shaded gray area indicates the light cone, where the continuum of unbound radiation modes exist, and the fast and slow light regions as well as the band edge of the even-even mode are indicated.

n_{G}). Slow light in PhC waveguides might be used for enhancing light-matter interactions,

for optical signal processing, and for miniaturization of devices [7, 8], but the properties of PhCs in the slow light region also become a lot more sensitive to imperfections and irregularities upon fabrication, both for waveguides [56–61] and cavities [59, 62]. Finally, the point $k_z/(2\pi/a) = 0.5$ is the band edge that defines the crossover from the bound mode being propagating and lossless (k_z purely real, in theory, at frequencies above band edge) to the bound mode being evanescent ($\mathrm{Re}(k_z)/(2\pi/a) = 0.5$ and $\mathrm{Im}(k_z) > 0$ at frequencies below the band edge). In the 2D PhC structures, PhC 2 and 3 in Table 2.1, the dispersion of the guided modes looks qualitatively as in Fig. 2.3, however without a light line and light cone; all modes exist in the plane of the PhC due to the infinite thickness. For later reference, we define the power flow of a guided mode as the component of the Poynting vector along the waveguide of that mode integrated over the transverse plane, S

$$P_z = \frac{1}{2}\int_S \mathrm{Re}\left[\mathbf{E}_\mathrm{G} \times \mathbf{H}_\mathrm{G}^*\right] \cdot \mathbf{z}\,\mathrm{d}S. \tag{2.17}$$

We note that P_z is independent of the z-coordinate in the PhC supercell [28], which we have verified numerically with the computational formalism from Chapter 3.

In Chapter 7, we investigate the potential for optical amplification in active PhC waveguides in the slow light region, while in Chapters 4 and 8 we analyze light emission from QDs in PhC waveguides and derive a closed-form expression for the partial LDOS into the guided mode. In Chapter 8, we also demonstrate how the dispersion of the PhC membrane waveguide can be engineered via the PhC design.

2.3.2 Cavities

As described in the previous section, a waveguide is a *line* defect where an entire row of holes or rods are left out of the otherwise perfect PhC lattice. If, instead, we remove only a finite number of holes, we get a *point* defect that we refer to as a cavity or a resonator. While the waveguide supports a *continuum* of modes, as illustrated by the continuous dispersion curves in Fig. 2.3, the cavity supports *discrete* modes that are localized inside the cavity, but that may leak into the environment as quantified by the Q factor of the mode [63]. As an example, Fig. 2.4 displays the fundamental cavity mode ($|E_x|^2$) of an L3 cavity, consisting of three unit cells of the W1 waveguide, in the xz-plane (at $y = 0$). This mode exists at a discrete frequency, ω_Cav, but due to leakage, for example via contributions inside the light cone, the mode is broadened with a linewidth $\Delta\omega_\mathrm{Cav}$. In Chapter 5, we define more rigorously what is meant by a "cavity mode" and present techniques for computing such modes. We also derive closed-form expressions for the LDOS related to structures with one or more PhC cavities, and for a single cavity such a spectrum is almost a Lorentzian with a width given by $\Delta\omega_\mathrm{Cav}$.

We stress that in PhC waveguides the LDOS originates from a spectral continuum of modes, while in a cavity a single discrete mode, that is broadened, is responsible for the shape of the LDOS. In Chapters 5 and 8, we analyze these systems in more detail and in particular show that the LDOS may be highly position dependent. But to illustrate the qualitative difference between a PhC cavity and a PhC waveguide, we show their LDOS spectra in schematic form in Fig. 2.5, where the solid red (dashed blue) curve is the cavity (waveguide) LDOS spectrum. An L3 cavity exists at a higher frequency than the band edge, $\omega_\mathrm{Cav} > \omega_\mathrm{BE}$, which can be explained with arguments as those in Section 8.3.1, and gives rise to an LDOS spectrum that is peaked at ω_Cav with a peak value that is proportional to $1/\Delta\omega_\mathrm{Cav}$. In contrast, the waveguide LDOS increases monotonously

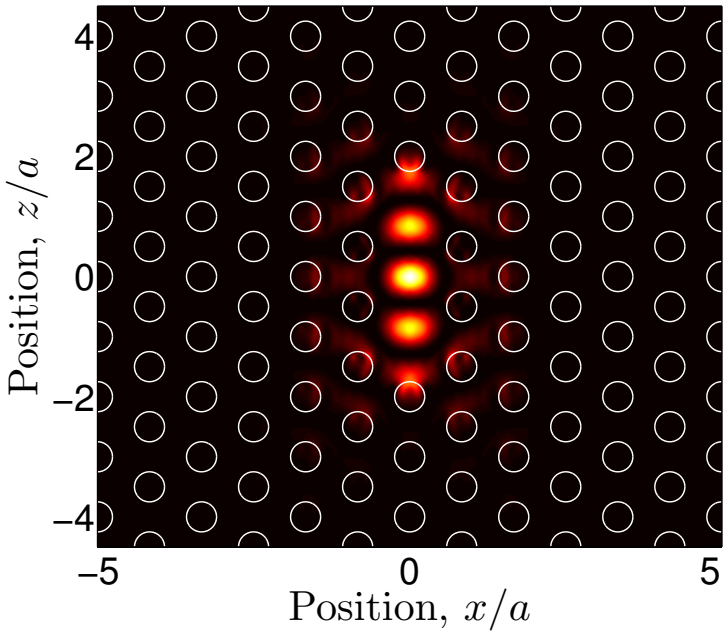

Figure 2.4 Field profile ($|E_x|^2$) of fundamental cavity mode in PhC L3 cavity, shown in the xz-plane and at $y = 0$.

towards the band edge and is dominated by the partial LDOS of the guided mode that is proportional to the group index, n_{G}.

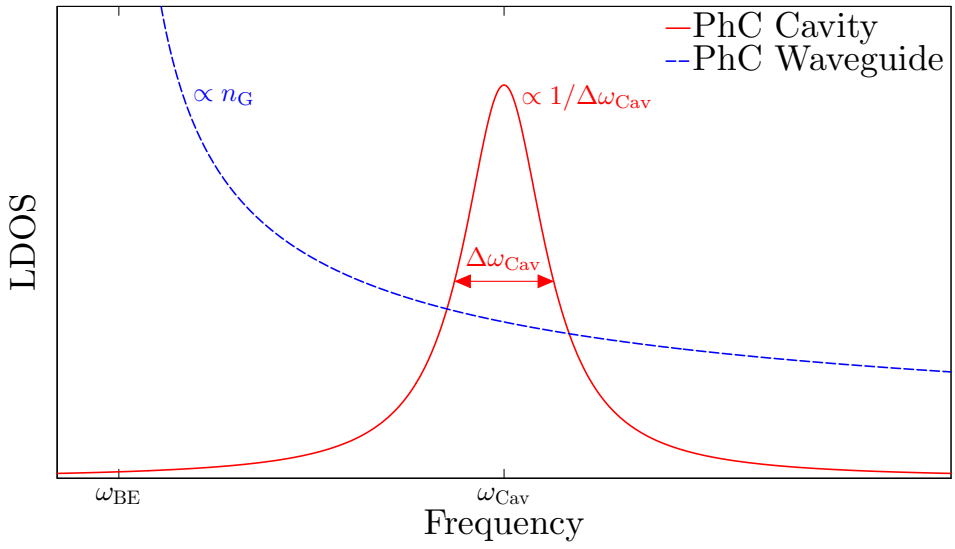

Figure 2.5 Schematic of LDOS for a PhC cavity mode (solid red), at frequency ω_{Cav} and with linewidth $\Delta\omega_{\mathrm{Cav}}$, and for a PhC waveguide (dashed blue), with band edge at ω_{BE}.

2.4 Optical antennas and the β factor

As discussed in Section 2.2, we can modify the emission from quantum emitters by designing the photonic environment that the emitter is embedded in, as quantified via the LDOS. In this way, the photonic environment may mediate the conversion of energy from a localized source (quantum emitter) into (quasi-)freely propagating radiation, which is similar to how radio antennas work, but here in the near-infrared or optical part of the spectrum. Thus, we may think of the photonic environment as an *optical antenna* that "enhances the LDOS, thereby making it possible for the emitter to dissipate its energy more easily" [64].

As specific examples of such antennas, we in Chapter 9 investigate a plasmonic dimer, consisting of a pair of metallic nano spheres, and its impact on the LDOS for different positions and orientations of the dipole moment. In Chapter 8, we analyze and design PhC membrane waveguides for efficient emission of single photons. In addition to an enhancement of the *total* LDOS, we are in this situation particularly interested in the *partial* LDOS enhancement into a single well-controlled optical mode, a guided mode of the waveguide. In analogy with the SE β factor for lasers, also simply referred to as the SE factor [65], we therefore introduce the β factor as the relative coupling into this waveguide mode [27, 66, 67]

$$\beta \equiv \frac{\rho_{\mathrm{G}}}{\sum_i \rho_i} = \frac{\rho_{\mathrm{G}}}{\rho_{\mathrm{G}} + \rho_{\mathrm{Rad}} + \rho_{\mathrm{NR}}}, \tag{2.18}$$

where ρ_{Rad} (ρ_{NR}) is the partial LDOS associated with other radiative modes (non-radiative decay).[6] The β factor takes a value between zero and unity, and for an ideal single-photon antenna it approaches unity; all of the photons are coupled into the waveguide mode. We analyze the relative magnitudes of ρ_{G} and ρ_{Rad} in PhC membrane waveguides in Chapters 4 and 8.

2.5 Summary

We have introduced the central equations, concepts, and structures that we use and build on in the rest of the thesis. Specifically, we have introduced Maxwell's equations in the frequency domain as well as Poynting's theorem and the Lorentz reciprocity theorem, and we have introduced the dyadic Green's function as the electric field resulting from a delta function source (dipole). Next, we have discussed the concept of Purcell modified spontaneous emission from quantum emitters, and we have stated that the spontaneous emission rate is proportional to the local density of states that, in turn, is proportional to the imaginary part of the dyadic Green's function, all within the dipole approximation of light-matter interactions. Thus, the Green's function contains all the information we need to understand and analyze spontaneous emission in nanophotonic and plasmonic systems, and we have emphasized that the Purcell factor is the local density of states enhancement on resonance if a single optical mode dominates this local density of states enhancement. We have introduced photonic crystals as periodic and wavelength-scale semiconductor structures that can confine and guide light due to photonic bandgaps. We focus, in this chapter and in the rest of the thesis, on photonic crystal membranes that feature partial bandgaps in the plane and that confine light in the vertical direction due to total internal reflection. We have introduced waveguides as line defects in photonic crystal membranes

[6] In experiments, ρ_{NR} should be included for accurate estimates of β [68]. In the computational results to be presented in later chapters, however, we set $\rho_{\mathrm{NR}} = 0$

and discussed the dispersion of such structures that in particular exhibits bound and guided modes below the light line and a continuum of unbound radiation modes above the light line (inside the light cone). For the guided modes, we have discussed the fast (slow) light regions of the associated dispersion that correspond to small (large) group indices. We have also introduced point defects that give rise to photonic crystal cavities, and we have schematically compared the local density of states spectrum for a photonic crystal waveguide and cavity. Finally, we have briefly talked about optical antennas and in particular introduced the spontaneous emission β factor that gives the relative local density of states for a single optical mode, for example a guided mode in a photonic crystal waveguide.

CHAPTER 3

Bloch mode expansion technique for periodic photonic structures

> *To make my life easy, I began by considering wave functions in a one-dimensional periodic potential. By straight Fourier analysis I found to my delight that the wave differed from a plane wave of the free electron only by a periodic modulation. This was so simple that I didn't think it could be much of a discovery, but when I showed it to Heisenberg he said right away, 'That's it'.*
>
> Felix Bloch

The natural solutions of the wave equation in periodic systems are what we now know as Bloch states or *Bloch modes*, after Felix Bloch who introduced this concept in the context of electrons in crystal lattices in 1929 [54].[1] Specifically, Bloch proved that in a periodic system, with primitive lattice vector $\mathbf{T}$, these natural solutions are of the following form

$$\psi(\mathbf{r}) = u(\mathbf{r}) \exp\left(\mathrm{i}\mathbf{k} \cdot \mathbf{r}\right), \tag{3.1}$$

where $\mathbf{k}$ is the Bloch wave vector, and where $u(\mathbf{r} + \mathbf{T}) = u(\mathbf{r})$. In periodic photonic structures, for example in PhCs, the natural solutions for the *electromagnetic* fields are of the Bloch mode form, analogously to the *quantum mechanical* fields originally discussed by Bloch [69]. In this chapter, we develop a computational framework for determining

[1] Edwin M. Purcell, after whom the Purcell effect is named, and Felix Bloch shared the 1952 Nobel Prize in physics for their work on nuclear magnetic resonances.

the Bloch modes in periodic nanophotonic structures, with a focus on PhC membrane waveguide and cavity-based structures, that we introduce in Section 3.1. In Section 3.2, we present a practical technique for computing the Bloch modes in a single periodic structure, giving for example information on waveguide dispersion. Then, in Section 3.3, we proceed to coupled periodic structures, where coupling (reflection and transmission) between Bloch modes comes into play, as well as dipole emission and excitation of Bloch modes in Section 3.4. We conclude the chapter with an overview of the computational flow (Section 3.5) as well as strengths and weaknesses of the methodology (Section 3.6). The overall ideas of the Bloch mode framework to be presented here were first presented in [70, 71] and later more specifically for PhC membrane structures in [28]; all these references generalize a technique originally proposed by Yeh *et al.* [72].

3.1 Photonic crystal membranes and Bloch modes

We are interested in analyzing and designing PhC membrane structures, and in Fig. 3.1 we show an example of a PhC membrane waveguide, created by omitting a single hole centered at $x = 0$. In Fig. 3.1(a), part of the structure is shown in the xz-plane at $y = 0$, and in Fig. 3.1(b) the structure is shown in the xy-plane at $z/a = -0.25$.

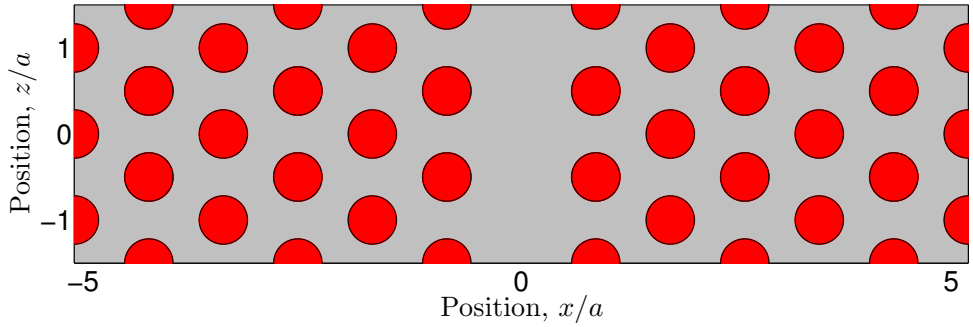

(a) PhC membrane waveguide in xz-plane at $y = 0$.

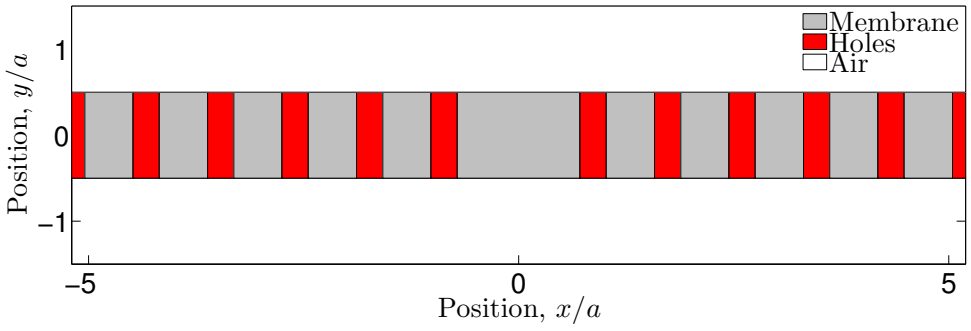

(b) PhC membrane waveguide in xy-plane at $z/a = -0.25$.

Figure 3.1 Sketch of open PhC membrane waveguide. Colors indicate membrane material (gray), PhC holes (red) and air (white).

In general, the structure is not periodic along y, and the periodicity along x is broken due to the introduction of waveguides, as in Fig. 3.1, and cavities as well as termination

of the PhC, either to air or by extension of the bulk membrane (termination of the PhC along x is not displayed in Fig. 3.1). In contrast, the structure will in general be periodic along z, with discrete, translational symmetry, due to a finite or infinite number of repetitions of an underlying *supercell*. The natural solutions in such periodic structures are the Bloch modes that via Eq. (3.1) obey the following relation[2]

$$\begin{bmatrix}\mathbf{E}(\mathbf{r}_\perp, z+a)\\ \mathbf{H}(\mathbf{r}_\perp, z+a)\end{bmatrix} = \exp\left(\mathrm{i}k_z a\right)\begin{bmatrix}\mathbf{E}(\mathbf{r}_\perp, z)\\ \mathbf{H}(\mathbf{r}_\perp, z)\end{bmatrix} \tag{3.2}$$

where k_z is the Bloch mode wave number along z, to be determined. As the fundamental relation in Eq. (3.2) only makes reference to a length of $\Delta z = a$, we simply need to solve *any* section of this length of the full structure in Fig. 3.1(a) to determine the Bloch mode field distributions, $[\mathbf{E}(\mathbf{r}), \mathbf{H}(\mathbf{r})]$, and wave numbers, k_z. One possible choice of the supercell is shown in the xz-plane in Fig. 3.2. No closed-form expressions for the Bloch modes of the structure introduced in Figs. 3.1 and 3.2 exist, and we therefore in the following section present a numerical technique for solving Eq. (3.2) in this type of system.

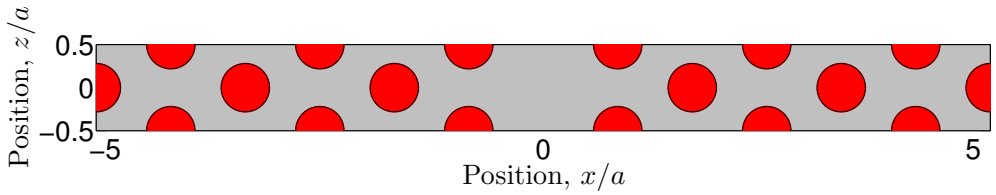

Figure 3.2 Supercell of PhC membrane waveguide in Fig. 3.1 in xz-plane at $y = 0$. Colors indicate membrane material (gray) and PhC holes (red).

3.2 Transverse modal expansion of Bloch modes

We pursue, as motivated in Chapter 1, a *transverse modal expansion* of the Bloch modes. The starting point is the definition of a *propagation axis*, taken here as the z axis, along which any structure is partitioned into *layers*, whose material distribution (ϵ and $\mu = \mu_0$) is uniform along this propagation axis. We label layers with the letter q, and by construction then $\epsilon^q(\mathbf{r}) \equiv \epsilon^q(\mathbf{r}_\perp)$, i.e., the relative permittivity only depends on the lateral coordinates, $\mathbf{r}_\perp$, inside a given layer. Returning to the PhC supercell in Fig. 3.2, we note that this structure, due to the round holes, cannot readily be partitioned into layers. Therefore, as in the spatial discretization techniques, we impose an approximation to the exact structure in the form of a staircase approximation. Fig. 3.3 shows two examples for the supercell introduced in Fig. 3.2; the thin blue lines outline the staircase approximated PhC membrane waveguide supercell. The number of layers in this approximation, N_l, becomes a computational parameter, and in later chapters we check its impact on computed quantities. For more details and investigations on the use of the staircase approximation, see [30, 73–75].

The strategy is to expand each Bloch mode on the natural solutions in each layer, that we term *eigenmodes*. Using a scattering matrix (S-matrix) technique, these eigenmode expansions in different layers are then coupled together, which eventually permits us

[2]From Eq. (3.1), we have that $\psi(\mathbf{r} + a\mathbf{z}) = \exp(\mathrm{i}k_z a)\psi(\mathbf{r})$. So the fields introduced in Eq. (3.2), $\mathbf{E}$ and $\mathbf{H}$, play the role of ψ, and not u, in Eq. (3.1).

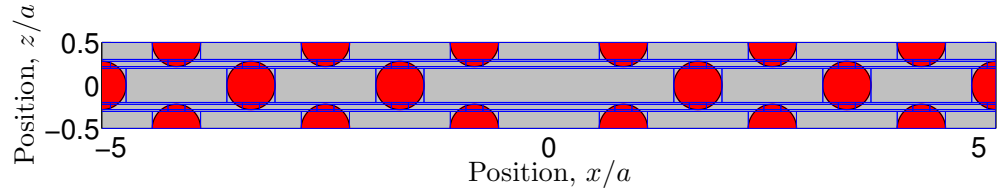

(a) Coarser staircasing: $N_\mathrm{l} = 9$ layers per supercell.

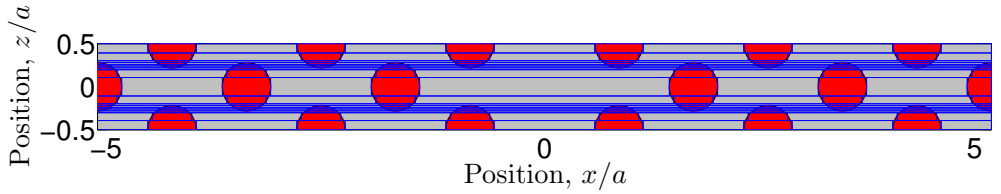

(b) Finer staircasing: $N_\mathrm{l} = 17$ layers per supercell.

Figure 3.3 Staircase approximation (thin blue lines) to PhC membrane waveguide in Fig. 3.2.

to express the Bloch mode condition in Eq. (3.2) as an eigenvalue equation in the eigenmode basis. Most of the underlying formalism and machinery is described in other references [23, 28, 70, 71, 76–81], and we only review central expressions, with more details given in appendices.

3.2.1 Eigenmodes in layers

For structures exhibiting a symmetry, for example rotational or continuous translational symmetry along one axis, the problem in each layer is effectively 2D, and the eigenmodes can be expressed semi-analytically [22, 24]. In turn, if the structure exhibits no or a lower degree of symmetry (e.g. mirror symmetries), as in the case of the PhC membrane with a cross section as in Fig. 3.1(b), semi-analytical solutions do not exist,[3] and we instead resort to a plane wave, or Fourier series, expansion in the *lateral* coordinates inside *each layer*. This is the basis of the *Fourier modal method* (FMM) that is also known as the rigorous coupled wave-analysis (or RCWA). Historically this approach dates (at least) back to Tamir and Wang's analysis of electromagnetic scattering on periodically stratified media [83, 84], for which the lateral periodicity invites for a Fourier representation. In general, the PhC structures to be analyzed here are not periodic functions of the lateral coordinates, which calls for appropriate handling of the lateral boundary conditions (BCs); this is the topic of Chapter 4. As a word of caution, the FMM is not to be confused with the plane wave expansion method where a plane wave expansion in *all* coordinates of the *full structure* is employed.

The starting point in the FMM is expansions in each layer (with index q that we suppress when this is unambiguous) of the relative permittivity and the lateral electric and magnetic field components in plane waves, or Fourier series, in the lateral coordinates

[3] The basis in the semi-analytical technique is analytic solutions in restricted parts of space, for example in each rectangular region of constant permittivity in the PhC membrane in Fig. 3.1(b). However, analytical solutions do not exist for rectangular waveguides [82] and consequently the semi-analytical technique is inapplicable here.

$$\epsilon(\mathbf{r}_\perp) = \sum_{j,n} \hat{\epsilon}_{j;n} \exp\left[\mathrm{i}\left(k_j^x x + k_n^y y\right)\right], \tag{3.3a}$$

$$E_x(\mathbf{r}_\perp) = \sum_{j,n} \hat{e}_{j;n}^x \exp\left[\mathrm{i}\left(k_j^x x + k_n^y y\right)\right], \tag{3.3b}$$

$$E_y(\mathbf{r}_\perp) = \sum_{j,n} \hat{e}_{j;n}^y \exp\left[\mathrm{i}\left(k_j^x x + k_n^y y\right)\right], \tag{3.3c}$$

$$H_x(\mathbf{r}_\perp) = \sum_{j,n} \hat{h}_{j;n}^x \exp\left[\mathrm{i}\left(k_j^x x + k_n^y y\right)\right], \tag{3.3d}$$

$$H_y(\mathbf{r}_\perp) = \sum_{j,n} \hat{h}_{j;n}^y \exp\left[\mathrm{i}\left(k_j^x x + k_n^y y\right)\right], \tag{3.3e}$$

where $\sum_{j,n} \equiv \sum_{j=-\infty}^{\infty} \sum_{n=-\infty}^{\infty}$ and $k_j^\alpha = j2\pi/d_\alpha$, with d_α being the size of the computational domain along the direction α. In computations, we truncate these sums at $|j| = j_{\max}$ and $|n| = n_{\max}$ and later investigate the impact from these truncations on computed quantities. Maxwell's equations can then be expressed (see Appendix B.1) as the following eigenvalue problem

$$\frac{1}{k_0^2}\mathbf{F}\mathbf{G}\begin{bmatrix}\mathbf{e}^x\\ \mathbf{e}^y\end{bmatrix} = \beta^2 \begin{bmatrix}\mathbf{e}^x\\ \mathbf{e}^y\end{bmatrix}, \tag{3.4}$$

where matrices $\mathbf{F}$ and $\mathbf{G}$ are Fourier representations of the operators that couple the lateral electric and magnetic field components (see Eqs. (B.5)). Each eigenvector of the matrix on the LHS in Eq. (3.4) contains the Fourier coefficients of E_x and E_y for an eigenmode, while the associated magnetic Fourier coefficients are obtained by explicit evaluation of Eq. (B.7b). The z-dependence of each field component is $\sim \exp(\pm\mathrm{i}\beta z)$, with β^2 being the eigenvalue of the associated eigenvector in Eq. (3.4). We choose to always have $\mathrm{Re}(\beta) + \mathrm{Im}(\beta) > 0$ [80, 85], and interpret the $+\beta$ ($-\beta$) solutions as propagating or decaying in the $+z$ ($-z$) direction. In the next section, we expand the fields in two adjacent layers on eigenmodes and couple these together by satisfying the electromagnetic BCs; this yields the layer interface reflection and transmission.

3.2.2 Layer interfaces: Reflection and transmission matrices

To derive the equations for the reflection and transmission matrices at layer interfaces, we expand the lateral electric and magnetic fields in layer q on eigenmodes

$$\mathbf{E}_\perp^q = \sum_\zeta \mathbf{E}_{\perp,\zeta}^q(\mathbf{r}_\perp)\left[u_\zeta^q \exp\left(\mathrm{i}\beta_\zeta^q(z - z_{q-1,q})\right) + d_\zeta^q \exp\left(-\mathrm{i}\beta_\zeta^q(z - z_{q,q+1})\right)\right], \tag{3.5a}$$

$$\mathbf{H}_\perp^q = \sum_\zeta \mathbf{H}_{\perp,\zeta}^q(\mathbf{r}_\perp)\left[u_\zeta^q \exp\left(\mathrm{i}\beta_\zeta^q(z - z_{q-1,q})\right) - d_\zeta^q \exp\left(-\mathrm{i}\beta_\zeta^q(z - z_{q,q+1})\right)\right], \tag{3.5b}$$

where ζ enumerates the eigenmodes, i.e., the eigensolutions of Eq. (3.4), and where $z_{q-1,q}$ and $z_{q,q+1}$ bound layer q. The coefficients u_ζ^q [d_ζ^q] are the amplitudes of the upward ($+z$) [downward ($-z$)] propagating and decaying eigenmodes. For the interface between layers q and $q+1$, we *define* the reflection and transmission matrices for illumination from layer

q by the following relations

$$d_\zeta^q = \sum_{\zeta'} R_{\zeta,\zeta'}^{q,q+1} \tilde{u}_{\zeta'}^q, \tag{3.6a}$$

$$u_\zeta^{q+1} = \sum_{\zeta'} T_{\zeta,\zeta'}^{q,q+1} \tilde{u}_{\zeta'}^q, \tag{3.6b}$$

where $\tilde{u}_\zeta^q \equiv \exp(\mathrm{i}\beta_\zeta^q(z_{q,q+1} - z_{q-1,q}))u_\zeta^q$. Using this, the following expression for the R- and T-matrices can be derived (see Appendix B.2) by satisfying the electromagnetic BCs

$$\mathbf{T}^{q,q+1} = 2\left[(\mathbf{e}^q)^{-1}\,\mathbf{e}^{q+1} + (\mathbf{h}^q)^{-1}\,\mathbf{h}^{q+1}\right]^{-1}, \tag{3.7a}$$

$$\mathbf{R}^{q,q+1} = (\mathbf{e}^q)^{-1}\,\mathbf{e}^{q+1}\mathbf{T}^{q,q+1} - \mathbf{I}. \tag{3.7b}$$

where $\mathbf{e}^q$ is the matrix of eigenvectors from Eq. (3.4) for layer q. The reflection and transmission matrices for illumination from layer $q+1$, $\mathbf{R}^{q+1,q}$ and $\mathbf{T}^{q+1,q}$, can be derived similarly and are obtained by interchanging q and $q+1$ in Eqs. (3.7). Returning to the structure of interest, Fig. 3.3, the R- and T-matrices couple fields together at the horizontal blue lines, the layer interfaces. The final step to formulate the Bloch mode eigenvalue problem in the eigenmode basis is to couple fields between layers that are not neighbors; this is handled with S-matrices as discussed in the next section.

3.2.3 Multiple interfaces: Scattering matrices

For structures with a total of $Q \geq 3$ layers, multiple scattering of the eigenmodes in the internal layers ($2 \leq q \leq Q-1$) needs to be accounted for, which is achieved with an iterative S-matrix approach. This scheme was initially proposed in [78], and the detailed expressions are derived in [23] and stated in Appendix B.4.

In analogy with the definition of the single-interface R- and T-matrices (see Eqs. (3.6)), the S-matrices relate eigenmode amplitudes as follows

$$d_\zeta^1 = \sum_{\zeta'} SR_{\zeta,\zeta'}^{1,Q} \tilde{u}_{\zeta'}^1, \tag{3.8a}$$

$$u_\zeta^Q = \sum_{\zeta'} ST_{\zeta,\zeta'}^{1,Q} \tilde{u}_{\zeta'}^1 \tag{3.8b}$$

for illumination from layer 1 onto layer Q, and

$$d_\zeta^1 = \sum_{\zeta'} ST_{\zeta,\zeta'}^{Q,1} \tilde{d}_{\zeta'}^Q, \tag{3.8c}$$

$$u_\zeta^Q = \sum_{\zeta'} SR_{\zeta,\zeta'}^{Q,1} \tilde{d}_{\zeta'}^Q, \tag{3.8d}$$

for illumination from layer Q onto layer 1. Returning again to the structure of interest, Fig. 3.3, it is apparent that the eigenmode S-matrices describe how to couple fields in the bottom and top most layers of the supercell, as prescribed by Eqs. (3.8). We thus proceed to formulate the Bloch mode condition in the eigenmode basis in the following section.

3.2.4 Supercell: Bloch modes in eigenmode basis

We focus on determining the Bloch modes in an arbitrary periodic *section*, with index w, where we expand each Bloch mode on eigenmodes as in Eqs. (3.5)

$$\mathbf{E}^w(\mathbf{r}_\perp, z) = \sum_\zeta \mathbf{E}^q_\zeta(\mathbf{r}_\perp) \left[u^q_\zeta \exp\left(\mathrm{i}\beta^q_\zeta (z - z_{q-1,q})\right) + d^q_\zeta \exp\left(-\mathrm{i}\beta^q_\zeta (z - z_{q-1,q})\right)\right], \tag{3.9a}$$

$$\mathbf{H}^w(\mathbf{r}_\perp, z) = \sum_\zeta \mathbf{H}^q_\zeta(\mathbf{r}_\perp) \left[u^q_\zeta \exp\left(\mathrm{i}\beta^q_\zeta (z - z_{q-1,q})\right) - d^q_\zeta \exp\left(-\mathrm{i}\beta^q_\zeta (z - z_{q-1,q})\right)\right], \tag{3.9b}$$

where it is understood that layer q is inside section w.[4] N_l^w denotes the number of layers in the supercell, and by virtue of periodicity layers q and $q + N_\mathrm{l}^w$ are then identical. This implies that the eigenmodes in layers q and $q + N_\mathrm{l}^w$ are the same, and evaluation of $\mathbf{E}^w(\mathbf{r}_\perp, z + a)$ and $\mathbf{H}^w(\mathbf{r}_\perp, z + a)$ in terms of the fields in Eqs. (3.9) can thus be expressed solely in terms of the eigenmode amplitudes

$$u^{q+N_\mathrm{l}^w}_\zeta = \exp(\mathrm{i}k_z a)\, u^q_\zeta, \tag{3.10a}$$

$$d^{q+N_\mathrm{l}^w}_\zeta = \exp(\mathrm{i}k_z a)\, d^q_\zeta, \tag{3.10b}$$

which is the eigenmode representation of Bloch's theorem, Eq. (3.2). By using the eigenmode S-matrix formalism, we can also relate the four eigenmode amplitudes in Eqs. (3.10) as follows

$$\begin{bmatrix} \mathbf{u}^{q+N_\mathrm{l}^w} \\ \mathbf{d}^q \end{bmatrix} = \begin{bmatrix} \mathbf{S}^w_{11} & \mathbf{S}^w_{12} \\ \mathbf{S}^w_{21} & \mathbf{S}^w_{22} \end{bmatrix} \begin{bmatrix} \mathbf{u}^q \\ \mathbf{d}^{q+N_\mathrm{l}^w} \end{bmatrix}, \tag{3.11}$$

where the supercell S-matrices, $\mathbf{S}^w_{ij}$, are stated in Appendix B.5. Replacing via Eqs. (3.10) and rearranging, Eq. (3.11) becomes the generalized Bloch mode eigenvalue equation

$$\begin{bmatrix} \mathbf{S}^w_{11} & \mathbf{0} \\ \mathbf{S}^w_{21} & -\mathbf{I} \end{bmatrix} \begin{bmatrix} \mathbf{u}^q \\ \mathbf{d}^q \end{bmatrix} = \exp(\mathrm{i}k_z a) \begin{bmatrix} \mathbf{I} & -\mathbf{S}^w_{12} \\ \mathbf{0} & -\mathbf{S}^w_{22} \end{bmatrix} \begin{bmatrix} \mathbf{u}^q \\ \mathbf{d}^q \end{bmatrix}. \tag{3.12}$$

Solving this generalized eigenvalue problem yields the Bloch mode expansion coefficients and the Bloch mode wave numbers.

Half of the eigensolutions from Eq. (3.12) are upward ($+z$) propagating or decaying, the other half is downward ($-z$) propagating or decaying. In passive structures and at real frequencies, sorting into the up- and downward sets is straightforwardly based on the magnitude of the Bloch eigenvalue and the power flux [86]; Bloch modes with $|\exp(\mathrm{i}k_z a)| < 1$ (> 1) belong to the $+z$ ($-z$) set and are decaying, while modes with $|\exp(\mathrm{i}k_z a)| = 1$ (within a numerical tolerance) are propagating and classified based on the sign of the power flux along $+z$ (P_z in Eq. (2.17)). In active structures or at complex frequencies (that will be used in Chapter 5), the situation may be more involved as discussed in Appendix A in [87]. In all cases, superscript + (−) denotes an upward (downward) propagating or decaying Bloch mode, and in Table 3.1 we collect short descriptions of all sub-/superscripts used in Bloch mode expansions.

[4] For convenience of the following derivations, we have defined the downward eigenmodes (second terms in the brackets in Eqs. (3.9)) relative to the bottom of layer q. Previously, in Eqs. (3.5), we defined these relative to the top of layer q.

Sub-/superscript	Description
q	Layer index
w	Periodic section index
W	Total number of periodic sections
ζ	Eigenmode index
γ	Bloch mode index
$\pm$	Up- or downward ($\pm z$) Bloch mode
N_{l}^{w}	Number of layers in supercell of periodic section w
N_{s}^{w}	Number of supercells in periodic section w

Table 3.1 Overview of sub- and superscripts used in Bloch mode expansion of electric and magnetic fields.

3.3 Bloch mode S-matrices

The procedure from Section 3.2 gives the Bloch modes in a PhC described by a single supercell, e.g. an infinitely extended waveguide. In some cases, we will be interested in coupling several periodic sections, each described by a distinct supercell, together, and we here need the Bloch modes in each periodic section and the associated Bloch mode S-matrices. As an example, Fig. 3.4 shows three coupled PhC waveguides in the xz-plane, with hole radii $r/a = 0.28$ (red, $w = 1$), $r/a = 0.24$ (blue, $w = 2$) and $r/a = 0.2$ (green, $w = W = 3$). The reflection and transmission in this coupled waveguide structure are described by the Bloch mode S-matrices $\mathbf{SR}^{1,W}$ and $\mathbf{ST}^{1,W}$, as indicated in the figure.

In analogy with the eigenmode R-, T- and S-matrices of Sections 3.2.2 and 3.2.3, a similar formalism can be established for periodic structures with expansions on Bloch modes; this is covered in detail in [23], and we briefly review parts of this and provide alternative formulations in Appendix B.6. In analogy with the eigenmode S-matrices, the Bloch mode S-matrices relate Bloch modes amplitudes in different periodic sections

$$b_{\zeta}^{1} = \sum_{\zeta'} SR_{\zeta,\zeta'}^{1,W} \tilde{a}_{\zeta'}^{1}, \tag{3.13a}$$

$$a_{\zeta}^{W} = \sum_{\zeta'} ST_{\zeta,\zeta'}^{1,W} \tilde{a}_{\zeta'}^{1} \tag{3.13b}$$

for illumination from section 1 onto section W, and

$$b_{\zeta}^{1} = \sum_{\zeta'} ST_{\zeta,\zeta'}^{W,1} \tilde{b}_{\zeta'}^{W}, \tag{3.13c}$$

$$a_{\zeta}^{W} = \sum_{\zeta'} SR_{\zeta,\zeta'}^{W,1} \tilde{b}_{\zeta'}^{W}, \tag{3.13d}$$

for illumination from section W onto section 1. In these equations, a_{γ}^{w} (b_{γ}^{w}) is an upward (downward) Bloch mode amplitude, introduced in Eqs. (B.17), while $\tilde{a}_{\gamma}^{w} = P_{\gamma,\gamma}^{w,+} a_{\gamma}^{w}$ and $\tilde{b}_{\gamma}^{w} = P_{\gamma,\gamma}^{w,-} b_{\gamma}^{w}$, with $\mathbf{P}_{\gamma,\gamma}^{w,\pm}$ defined in Eq. (B.22). The Bloch mode S-matrices give directly the coupling strength in multiple-section structures and also play an important in dipole emission in periodic structures; this is the topic of the following section.

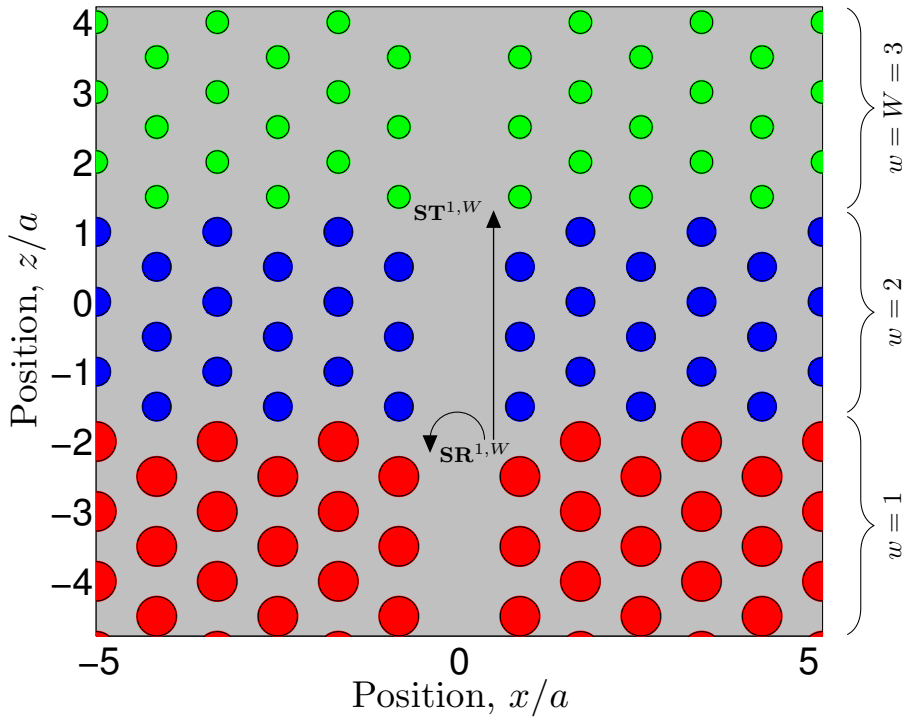

Figure 3.4 Sketch in xz-plane of coupled PhC waveguides, with hole radii $r/a = 0.28$ (red, $w = 1$), $r/a = 0.24$ (blue, $w = 2$) and $r/a = 0.2$ (green, $w = W = 3$). The Bloch mode S-matrices, $\mathbf{SR}^{1,W}$ and $\mathbf{ST}^{1,W}$, are indicated.

3.4 Dipole excitation of Bloch modes

One type of excitation that we have already discussed is *external* sources where the amplitudes of the incoming Bloch modes in the outermost sections are specified. Using the associated S-matrices, all other amplitudes can be expressed as function of these external excitation amplitudes, e.g. as in Eqs. (3.13). Another important type of excitation is *internal* sources where in an arbitrary periodic section a current distribution excites the Bloch modes of the structure. To lowest order in its size, any current distribution is an electric dipole [35], and we shall only be concerned with such point sources

$$\mathbf{j}(\mathbf{r};\omega) = \mathbf{j}_{\mathrm{D}}(\omega)\delta\left(\mathbf{r} - \mathbf{r}_{\mathrm{D}}\right), \tag{3.14}$$

where $\mathbf{j}_{\mathrm{D}}(\omega) = -\mathrm{i}\omega\mathbf{p}$, with $\mathbf{p}$ being the dipole moment, and where $\mathbf{r}_{\mathrm{D}}$ is the center of the current distribution; we simply refer to this as the dipole position.

3.4.1 Single periodic section

We first consider a dipole in a single periodic section, $w = \tilde{w}$, and essentially follow the procedure from [28]. As a specific example, this could correspond to placing a dipole in an infinitely extended, or *open*, PhC membrane waveguide, as the one illustrated in Fig. 3.1.

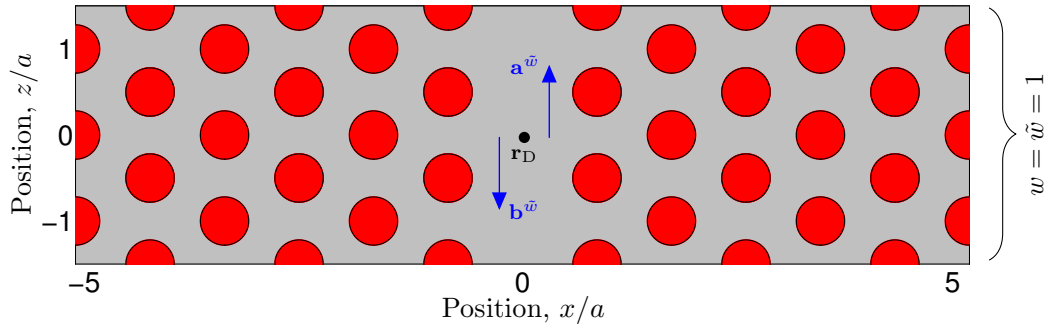

Figure 3.5 Sketch in xz-plane of dipole at $\mathbf{r}_\mathrm{D}$ in *open* PhC waveguide. The dipole excited Bloch mode amplitudes, the solutions of Eq. (3.16a), are indicated.

Since the source is embedded in a single periodic section, we can, as a manifestation of the radiation condition mentioned in footnote 1, p. 7, expand the fields above ($z \geq z_\mathrm{D}$) [below ($z \leq z_\mathrm{D}$)] the dipole on upward [downward] propagating and decaying Bloch modes of that periodic section

$$\mathbf{E}(\mathbf{r}) = \begin{cases} \sum_\gamma a_\gamma^{\tilde{w}} \mathbf{E}_\gamma^{\tilde{w},+}(\mathbf{r}_\perp, z), & z \geq z_\mathrm{D} \\ \sum_\gamma b_\gamma^{\tilde{w}} \mathbf{E}_\gamma^{\tilde{w},-}(\mathbf{r}_\perp, z), & z \leq z_\mathrm{D} \end{cases} \tag{3.15a}$$

$$\mathbf{H}(\mathbf{r}) = \begin{cases} \sum_\gamma a_\gamma^{\tilde{w}} \mathbf{H}_\gamma^{\tilde{w},+}(\mathbf{r}_\perp, z), & z \geq z_\mathrm{D} \\ \sum_\gamma b_\gamma^{\tilde{w}} \mathbf{H}_\gamma^{\tilde{w},-}(\mathbf{r}_\perp, z), & z \leq z_\mathrm{D} \end{cases} \tag{3.15b}$$

where $\left[\mathbf{E}_\gamma^{\tilde{w},+}, \mathbf{H}_\gamma^{\tilde{w},+}\right]$ $\left(\left[\mathbf{E}_\gamma^{\tilde{w},-}, \mathbf{H}_\gamma^{\tilde{w},-}\right]\right)$ is an upward (downward) propagating or decaying Bloch mode. Starting from the Lorentz reciprocity theorem, the dipole Bloch mode amplitudes can be shown (see Appendix B.7) to satisfy the following equation

$$\begin{bmatrix} \mathbf{M}^{++} & \mathbf{M}^{+-} \\ \mathbf{M}^{-+} & \mathbf{M}^{--} \end{bmatrix} \begin{bmatrix} \mathbf{a}^{\tilde{w}} \\ \mathbf{b}^{\tilde{w}} \end{bmatrix} = \begin{bmatrix} \mathbf{j}_\mathrm{D} \cdot \mathbf{E}^{\tilde{w},+}(\mathbf{r}_{\perp,\mathrm{D}}, z_\mathrm{D}) \\ \mathbf{j}_\mathrm{D} \cdot \mathbf{E}^{\tilde{w},-}(\mathbf{r}_{\perp,\mathrm{D}}, z_\mathrm{D}) \end{bmatrix}, \tag{3.16a}$$

$$M_{\gamma',\gamma}^{+-} \equiv \int_S \left[\mathbf{E}_\gamma^{\tilde{w},-}(\mathbf{r}_\perp, z_\mathrm{D}) \times \mathbf{H}_{\gamma'}^{\tilde{w},+}(\mathbf{r}_\perp, z_\mathrm{D}) - \mathbf{E}_{\gamma'}^{\tilde{w},+}(\mathbf{r}_\perp, z_\mathrm{D}) \times \mathbf{H}_\gamma^{\tilde{w},-}(\mathbf{r}_\perp, z_\mathrm{D})\right] \cdot \mathbf{z}\, \mathrm{d}S, \tag{3.16b}$$

where the vector on the RHS in Eq. (3.16a) contains all Bloch modes in section $\tilde{w}$ evaluated at $\mathbf{r}_\mathrm{D}$. The matrix elements $M_{\gamma',\gamma}^{+-}$ are surface integrals over the lateral extent of the computational domain at $z = z_\mathrm{D}$. According to [28], Bloch modes satisfy an orthogonality relation such that matrices $\mathbf{M}^{+-}$ and $\mathbf{M}^{-+}$ ($\mathbf{M}^{++}$ and $\mathbf{M}^{--}$) are diagonal (zero), which simplifies Eq. (3.16a) into a closed-form expression for each $a_\gamma^{\tilde{w}}$ and $b_\gamma^{\tilde{w}}$. In numerical computations, we find this orthogonality relation to hold approximately, with residual, non-vanishing elements possibly stemming from numerical rounding errors [88, 89]. In practice, therefore, we solve Eq. (3.16a) as a matrix equation and obtain the dipole excited Bloch mode amplitudes. The solutions of Eqs. (3.16a) give the coupling to both guided and radiation modes in a single periodic section, for example the *open* PhC membrane waveguide shown schematically in Fig. 3.5. If we close or terminate the waveguide, the Bloch mode amplitudes are modified due to scattering, which we treat in the following section.

3.4.2 Multiple periodic sections

Dipole excitation in structures consisting of multiple periodic sections is not covered in detail in the literature on Bloch mode expansions, and we here present the central equations in this case. When the dipole is embedded in a structure of $W \geq 2$ periodic sections, the dipole excited Bloch mode amplitudes in the uniform section (i.e. the solutions of Eqs. (3.16)) scatter at section interfaces and must be replaced by effective amplitudes that account for this scattering. As a consequence of the scattering, the fields above and below the dipole now, in general, comprise both up- and downward propagating and decaying Bloch modes

$$\mathbf{E}^{\tilde{w}}(\mathbf{r}) = \begin{cases} \sum_\gamma \left[a_\gamma^{\tilde{w},\mathrm{ab}} \mathbf{E}_\gamma^{\tilde{w},+}(\mathbf{r}_\perp, z) + b_\gamma^{\tilde{w},\mathrm{ab}} \mathbf{E}_\gamma^{\tilde{w},-}(\mathbf{r}_\perp, z) \right], & z \geq z_\mathrm{D} \\ \sum_\gamma \left[a_\gamma^{\tilde{w},\mathrm{be}} \mathbf{E}_\gamma^{\tilde{w},+}(\mathbf{r}_\perp, z) + b_\gamma^{\tilde{w},\mathrm{be}} \mathbf{E}_\gamma^{\tilde{w},-}(\mathbf{r}_\perp, z) \right], & z \leq z_\mathrm{D} \end{cases} \tag{3.17}$$

and similarly for the magnetic field. The effective Bloch mode amplitudes can be derived using the Bloch mode S-matrix formalism in analogy with the procedure for eigenmodes in [23]

$$\mathbf{a}^{\tilde{w},\mathrm{ab}} = \left[\mathbf{I} - \mathbf{S}\mathbf{R}^{\tilde{w},1} \mathbf{P}^{\tilde{w},-} \mathbf{S}\mathbf{R}^{\tilde{w},W} \mathbf{P}^{\tilde{w},+} \right]^{-1} \left[\mathbf{a}^{\tilde{w}} + \mathbf{S}\mathbf{R}^{\tilde{w},1} \mathbf{P}^{\tilde{w},-} \mathbf{b}^{\tilde{w}} \right], \tag{3.18a}$$

$$\mathbf{b}^{\tilde{w},\mathrm{ab}} = \mathbf{S}\mathbf{R}^{\tilde{w},W} \mathbf{P}^{\tilde{w},+} \mathbf{a}^{\tilde{w},\mathrm{ab}}, \tag{3.18b}$$

$$\mathbf{b}^{\tilde{w},\mathrm{be}} = \left[\mathbf{I} - \mathbf{S}\mathbf{R}^{w,W} \mathbf{P}^{w,+} \mathbf{S}\mathbf{R}^{\tilde{w},1} \mathbf{P}^{\tilde{w},-} \right]^{-1} \left[\mathbf{b}^{\tilde{w}} + \mathbf{S}\mathbf{R}^{\tilde{w},W} \mathbf{P}^{\tilde{w},+} \mathbf{a}^{\tilde{w}} \right], \tag{3.18c}$$

$$\mathbf{a}^{\tilde{w},\mathrm{be}} = \mathbf{S}\mathbf{R}^{\tilde{w},1} \mathbf{P}^{\tilde{w},-} \mathbf{b}^{\tilde{w},\mathrm{be}}. \tag{3.18d}$$

We note that when the matrix $\mathbf{S}\mathbf{R}^{\tilde{w},1} \mathbf{P}^{\tilde{w},-} \mathbf{S}\mathbf{R}^{\tilde{w},W} \mathbf{P}^{\tilde{w},+}$ in Eq. (3.18a), that we define as the roundtrip matrix in Chapter 5, has a unity eigenvalue, the matrix to be inverted becomes singular; the elements in $\mathbf{a}^{\tilde{w},\mathrm{ab}}$ diverge. So as this situation is approached, the dipole fields, i.e., the dyadic Green's function and thus the LDOS, will exhibit resonances. We return to this in Chapter 5. In Appendix B.8, we discuss the practical evaluation of the dipole power emission in the specific situations we consider in later chapters.

As an example, we terminate the PhC membrane waveguide in Fig. 3.5 in both ends with the bulk PhC lattice, as shown in Fig. 3.6. This then creates a *closed* PhC membrane waveguide that is also referred to as an L3 cavity. This structure consists of $W = 3$ sections, and due to the Bloch mode form of the expansion basis we describe infinitely extended PhC mirrors along $+z$ and $-z$. If we place the dipole anywhere in the cavity section, $\tilde{w} = 2$, the Bloch mode scattering and propagation matrices that enter into Eqs. (3.18) are as indicated in Fig. 3.6.

3.5 Computational flow, optimization, and symmetries

The Bloch mode expansion techniques that we have developed in this chapter have been implemented into a MATLAB software package, and in Fig. 3.7 we summarize the computational flow. Blue boxes indicate separate tasks in the flow, with the numbers indicating the order in which these must be performed. Physically relevant quantities are, or can be, obtained at different steps of the flow as indicated by the red boxes. Green boxes on the right side indicate sections where the computational tasks are described.

At different steps of the computational flow, we can minimize computation time and data stored in the memory and exploit parallel computing, as we discuss in the following section.

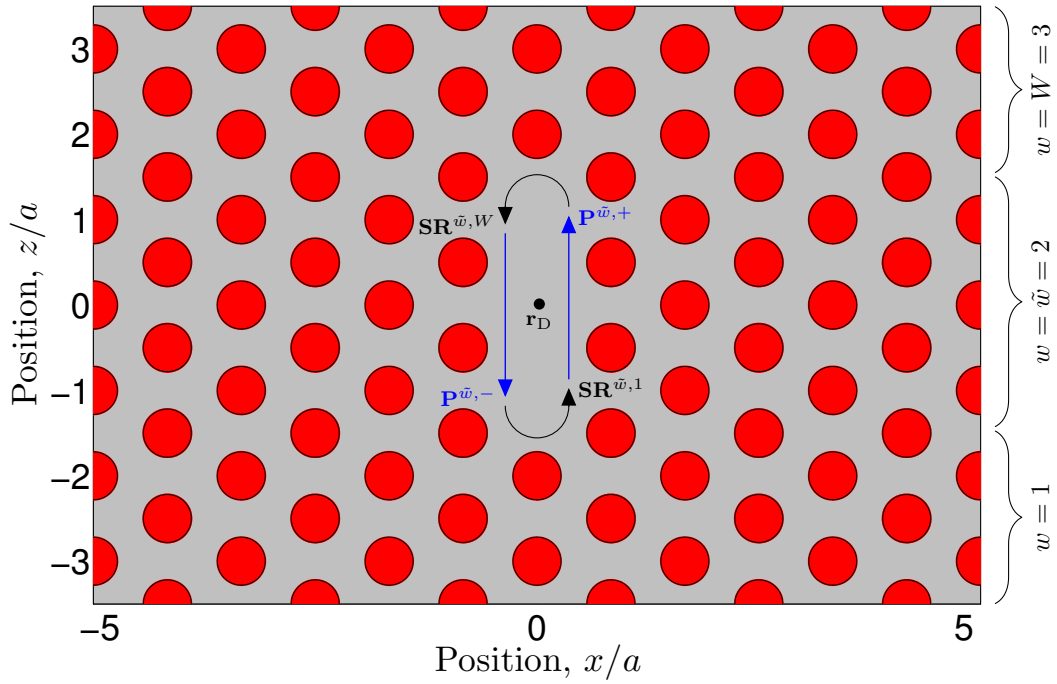

Figure 3.6 Sketch in xz-plane of dipole at $\mathbf{r}_\mathrm{D}$ in *closed* PhC waveguide of $W = 3$ periodic sections, creating an L3 cavity. For a dipole positioned in the cavity, $\tilde{w} = 2$, the Bloch mode scattering and propagation matrices that enter into Eqs. (3.18) are indicated

3.5.1 Minimum computations and parallelization

In the computational flow outlined in Fig. 3.7, we adopt a *minimum computations* strategy where we strive to perform as few computations and to store as little data in the memory as possible to obtain the physical quantities of interest. Referring to the computational task numbers in Fig. 3.7, this is done as follows.

(2) **Eigenmodes in layers**. Before starting to solve for eigenmodes in layers, we index all layers, giving identical layers the same index. Subsequently we only solve eigenmodes in unique layers, thus avoiding to solve the eigenmodes in identical layers several times. Eigenmode data is only stored for unique layers and in later steps parsed according to the layer index list.

(3) **Eigenmode R- and T-matrices**. Layer interfaces are indexed as described in the previous item, and eigenmode R- and T-matrices are only solved and stored for unique interfaces.

(3) **Eigenmode supercell S-matrices**. When we are only interested in obtaining the Bloch mode dispersion in a single periodic section or the Bloch mode S-matrices between several periodic sections, we only need the "forward" iteration eigenmode S-matrices of the relevant supercells, cf. Eqs. (B.15a). That is, we can in these cases avoid the "backward" iteration eigenmode S-matrices, cf. Eqs. (B.15b). If we want

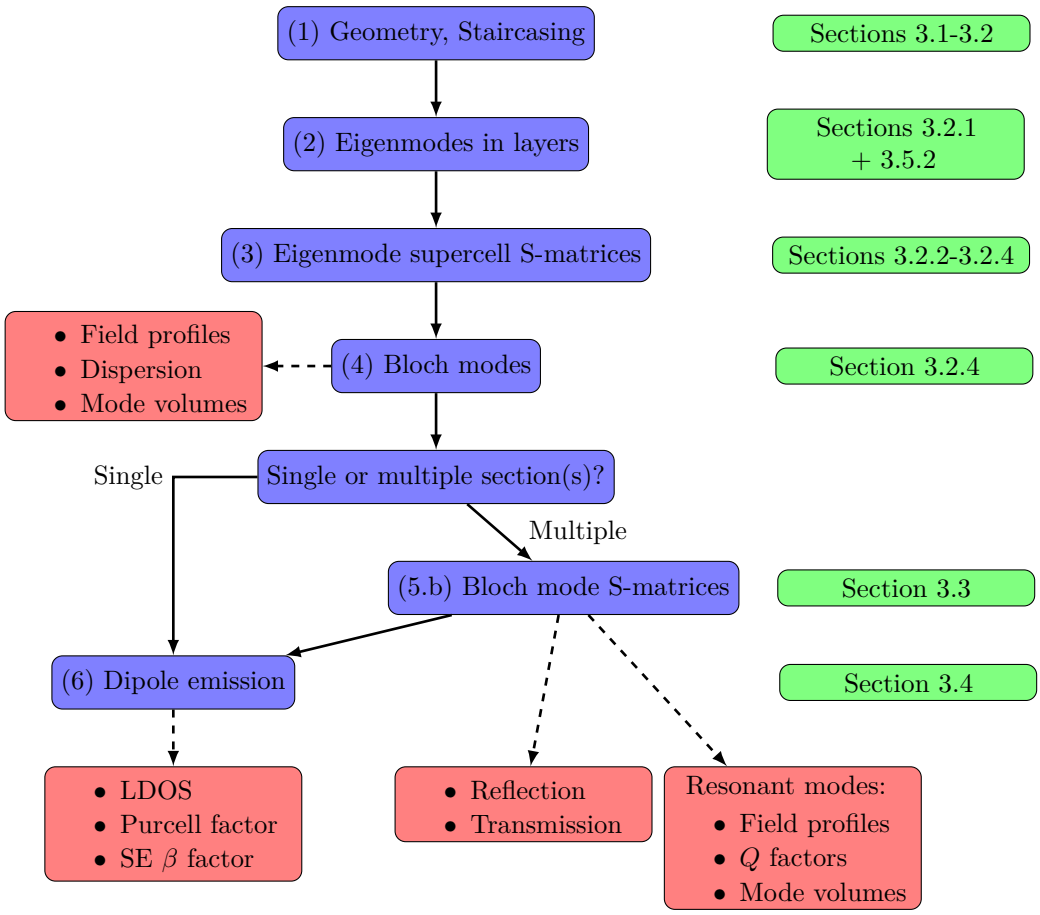

Figure 3.7 Flow diagram of Bloch mode expansion computations. Blue boxes indicate separate tasks in the flow, with the numbers indicating the order in which these must be performed. Red boxes indicate physically relevant quantities that are, or can be, obtained at different steps in the flow. Green boxes refer to sections where computational tasks are described.

anything more, for example field profiles or dipole coupling to Bloch modes, we also need the "backward" iteration eigenmode S-matrices.

(4) **Bloch modes**. In analogy with step (2), we index periodic sections and only solve for the Bloch modes (and thus for eigenmode S-matrices in supercells, cf. the previous item) in unique sections. Bloch mode data is only stored for unique sections and parsed according to the section index list.

Another important aspect of optimizing the computational flow is to exploit the potential for parallelization. With access to multiple-core computers, either on desktops that typically have two or four cores or on computing clusters with even more cores, we can, at the price of a communication overhead, solve independent parts of the computational flow in parallel. The eigenmode layer problems (step (2) above) as well as the eigenmode interface R- and T-matrices (step (3) above) are independent and are solved in parallel for faster computations. The Bloch mode sections (step (4) above) are also independent

and can likewise be solved in parallel. In practice, however, we have in some specific situations found the Bloch mode section parallelization to be slower than a serial solution procedure, and we have therefore generally not used parallelization for this step. This last point is caused by a large communication overhead, since a large number of data structures (eigenmode data and layer interface R- and T-matrices for all layers in each supercell) need to be parsed in step (4), while in steps (2) and (3) the amount of data, and thus the communication overhead, is a lot smaller.

3.5.2 Exploiting symmetries

When the structure of interest exhibits a symmetry, the computational complexity can be decreased. In later chapters, two symmetries have been exploited in certain situations: Mirror and continuous translational, the latter giving an effective 2D problem.

Mirror symmetries

When a structure exhibits mirror symmetries, the solutions are either even or odd functions of the symmetry coordinates. The structure in Fig. 3.1, for example, is mirror symmetric in both x and y, and the solutions, i.e., the field components are even and/or odd functions of x and y. Such symmetries in a field component translate into symmetries in its Fourier coefficients (Eqs. (3.3)), which can be used to convert the eigenmode eigenvalue problem, Eq. (3.4), into a smaller eigenvalue problem for the smaller set of independent Fourier coefficients for the x-y even-even, even-odd, odd-even or odd-odd solutions [90–92]. A given symmetric PhC structure often only exhibits a bandgap for some of these solutions (which we referred to as a partial bandgap in Chapter 2), and the analysis can typically be focused on these, effectively decreasing the computational complexity. The rest of the formalism for obtaining the Bloch modes proceeds exactly as described in Sections 3.2.2 to 3.4, but in a reduced basis of the independent Fourier coefficients.

Continuous translational: 2D limit

If the structure exhibits continuous translational symmetry along one axis, for example by letting the PhC membrane thickness go to infinity along the y axis, the structure is effectively 2D and only needs to be solved in the xz-plane. Formally, this implies that only the y k-vector that equals zero, $k^y_{n=0}$, contributes in the plane waves expansions in Eqs. (3.3), and the matrices $\mathbf{F}$ and $\mathbf{G}$, that enter into the layer eigenmode eigenvalue problem in Eq. (3.4), become block diagonal. This, therefore, yields two independent problems; the TE ($\mathbf{E} = E_y\mathbf{y}$, $\mathbf{H} = H_x\mathbf{x} + H_z\mathbf{z}$) and TM ($\mathbf{H} = H_y\mathbf{y}$, $\mathbf{E} = E_x\mathbf{x} + E_z\mathbf{z}$) problems, as shown in Appendix B.9.[5] In this case as well, the rest of the formalism for obtaining the Bloch modes proceeds exactly as described in Sections 3.2.2 to 3.4.

While the 3D simulations reported in Chapters 4 and 8 have been performed on a computing cluster (typically on 8 processors, with a memory consumption of ~ 60 GB, and solution times of ~ 30 minutes per frequency), 2D simulations have been performed on a desktop computer, with typical memory usage of a few GB or less and solution times of a few minutes or less per frequency.

[5] Our convention of TE and TM is consistent with the literature on waveguides and the FMM, but opposite of that in the PhC literature.

3.6 Strengths and weaknesses of modal expansion techniques

Different numerical techniques have advantages and disadvantages, and for efficient analysis of different classes of problems it is useful to be aware of these to be able to choose the most efficient approach. In this section, we cover both strengths and weaknesses of the transverse modal and Bloch mode expansion techniques that we have developed in this chapter.

In [93], Pissoort *et al.* cover three numerical techniques for modeling of 2D PhC structures, and for each method advantages and disadvantages are stated. For the modal expansion techniques, the following is mentioned:

Advantages

(1) Linear computation time in total number of layers, not in total length of structure.

(2) Logarithmic, and not linear, computation time in number of repetitions of supercell in periodic structures.

(3) PML BCs can easily be implemented.

(4) In the propagation direction (z), infinite structures can be treated without artificial parasitic reflections from computational domain termination.

Disadvantages

(a) Without a repetition of layers, the method behaves less advantageously.

(b) For non-rectangular structures, many layers are needed.

(c) The method relies on absorbing BCs.

(d) For structures with different propagation directions, for example with nonparallel waveguides, performance is lost.

Especially items (2) and (4) for advantages and (a) and (b) for disadvantages are important and relevant for the PhC structures we here focus on. Concerning (2), we describe each periodic section by a supercell and the associated Bloch modes, and in many situations it suffices to only analyze the supercell, no matter how many repetitions of the supercell the full periodic section consists of. If we return to the coupled PhC waveguide structure in Fig. 3.4, the computational complexity is the same for any number of repetitions of the supercell in the intermediate (blue) section, while in spatial discretization techniques (FEM and FDTD, for example) this complexity goes up with the length of this section. For item (4), we model infinitely extended PhC waveguides, described as $z \to -\infty$ $(+\infty)$ by the supercell in periodic section $w = 1$ $(w = W)$. In each of the outermost sections ($w = 1$ and $w = W$), we can choose to retain only the outgoing Bloch modes whose propagation along $\pm z$ is described analytically via Bloch's theorem in Eq. (3.2). In spatial discretization techniques, this infiniteness in the propagation direction of the simulated domain can only be emulated approximately, for example using absorbing or active BCs. These approximate approaches rely on a priori knowledge of the system, for example that a PhC waveguide only supports a single guided mode, and typically require larger domain sizes to make the approximations more accurate. In [17, 94], a FEM simulation approach of light emission in PhC membrane waveguides was used, with waveguides terminated by active BCs, and with substantial and problem

specific optimization of these active BCs and the length of the computational domain [17]. In Chapter 5, we use a FEM solver and an approximate outgoing Bloch mode BC to model an extended PhC waveguide structure. Here, we compare results to those obtained with the exact Bloch mode BC in the modal expansion techniques developed in this chapter.

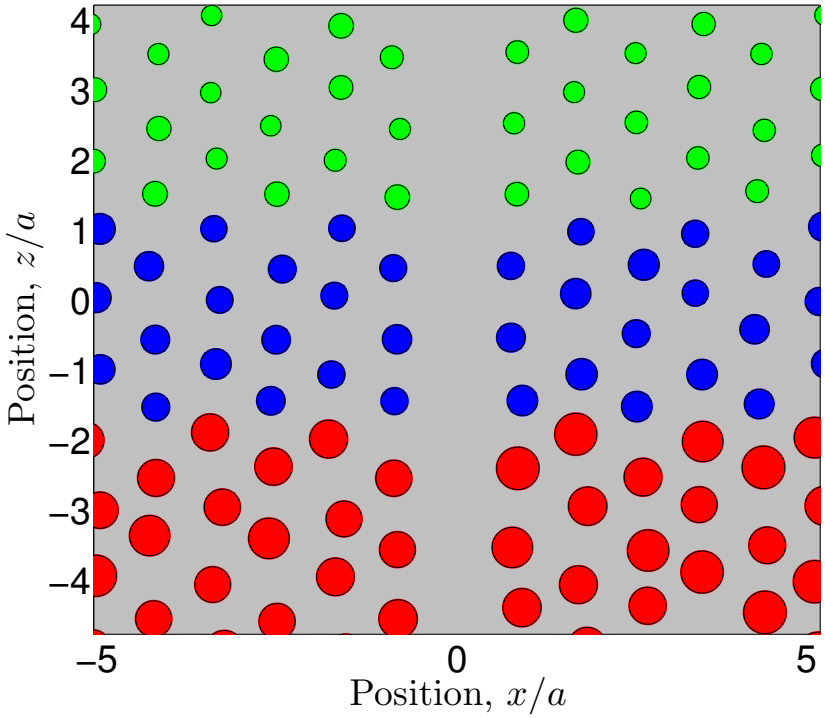

Figure 3.8 Disordered PhC waveguide structure: Same coupled PhC waveguide structure as in Fig. 3.4, but with random perturbations of hole radii and positions.

For the disadvantages, item (b) relates to the circular PhC holes that we approximate with a staircase as shown in Fig. 3.3. In later chapters, we check the impact on computed quantities from the number of layers in the staircase approximation, and for quantitative convergence, with at least a couple of correct digits, we find that we need substantially more layers than in the examples shown in Fig. 3.3. Item (a), by construction, only applies to non-periodic structures, and this is therefore not relevant for the *perfect* PhC lattices we have considered so far. In practice, however, PhC lattices are *imperfect* upon fabrication, with small fluctuations in hole sizes and positions as typical examples [61]. In Fig. 3.8, we show the coupled PhC waveguide structure in Fig. 3.4, but now with random perturbations of hole radii and positions. The advantages of the supercell approach and infiniteness along the waveguide axis do not apply for such disordered structures that are more efficiently treated with other numerical approaches [56, 95]. However, we do note that modal expansion methods have been applied for investigating disordered PhC structures [58, 96].

An aspect of the modal expansion techniques that is not covered in [93] is the specific technique we here use for computing the lateral eigenmodes: The plane wave, or Fourier series, expansions introduced in Eqs. (3.3). In the PhC structures we here

consider, the permittivity profile, $\epsilon(x, y)$, is piecewise constant and discontinuous, as shown in Fig. 3.1(b), and the lateral electric field components E_x and E_y thus also become discontinuous functions of x and y, respectively. The expansions are consequently sums of *continuous* functions for resolving *discontinuous* functions, which is well-known to be challenging. This is the Gibbs phenomenon, and "because of it the Fourier series representation may be highly unreliable for precise numerical work, especially in the vicinity of a discontinuity" [97]. Or put more bluntly; "Fluctuation of the truncated series from the actual case is large and the convergence is very slow" [98]. As we explore in later chapters, we can analyze relatively complicated PhC structures qualitatively and semi-quantitatively with modest numbers of plane waves included, but for quantitative investigations, the convergence with the Fourier truncation is slow and for certain 3D structures unfeasible. For effective 2D systems, the semi-analytical technique for describing the lateral eigenmodes is an alternative, and as analyzed in [24] it resolves the electric field discontinuities substantially better than the FMM. However, for full 3D structures, as the PhC membrane we target here, the semi-analytical technique cannot be applied and is therefore not an alternative. One possible path for improving the Fourier convergence is to introduce adaptive spatial meshing, where a higher spatial resolution is imposed close to material interfaces, a well-known strategy in FEM. This has been developed and applied for different structures [99–101], however not for the PhC membrane. It therefore remains an open question to what extent such adaptive spatial resolution improves the FMM and Bloch mode expansions for modeling of the PhC membrane.

Finally, we mention that no commercial software implementing the Bloch mode expansion techniques is available, but that some open source packages are [10].

3.7 Summary

We have introduced Bloch modes, that are quasi-periodic functions, as the natural solutions of Maxwell's equations in periodic photonic structures, and by focusing on photonic crystal membrane structures, we have developed a computational method for computing the Bloch modes. The method relies on a rectangular staircase approximation of the circular photonic crystal holes, and afterwards the local solutions in these staircase layers, the transverse eigenmodes, are computed via plane wave, or Fourier series, expansions. The staircase layers and the associated transverse eigenmodes are coupled together using a scattering matrix technique, which puts the Bloch mode condition (Bloch's theorem) in the form of a generalized eigenvalue problem in the transverse eigenmode basis. Next, we have introduced a Bloch mode scattering matrix formalism that gives the coupling between Bloch modes when several photonic crystal elements are interfaced, and we have derived the dipole excited Bloch mode amplitudes in both single- and multiple-element photonic crystals. This essentially allows us to construct the dyadic Green's function in photonic crystals in the Bloch mode basis, and in later chapters we use this for investigating both the local density of states and spontaneous emission β factor. Finally, we have sketched the computational flow, briefly discussed how to exploit two types of symmetries (mirror and continuous translational) in the computations, and discussed strengths and weaknesses of the computational methodology developed in this chapter.

Chapter 4

Boundary conditions for open photonic structures

> *Science is a differential equation. Religion is a boundary condition.*
>
> Alan Turing

All computational electrodynamic techniques rely on a discretization of the governing equations, and generally two starting points can be adopted: Maxwell's equations formulated in differential form or in integral form. In the latter case, discretization of bounded parts of space is required, while in the former discretization of unbounded spatial regions is, in principle, needed [18]. In either case, computations are performed on computers with finite memory, and in the differential form approach we thus need to truncate the physically unbounded space to a computationally bounded space to fit the data in the computer memory. This truncation is *artificial* and in many situations does not reflect the physics of the problem, but is invoked on computational grounds. Hence, it must be made with care and with an eye on the physical problem, which is the topic of this chapter. In the present thesis, both integral and differential formulations of Maxwell's equations are explored. The Bloch mode expansion technique, that we developed in Chapter 3 and use extensively in the following chapters, is a differential formulation, and in this chapter we discuss how to handle the domain truncation with this method. Later, in Chapter 9, we present a volume integral formulation where an unbounded space and a radiation condition at infinity are included by construction and where artificial truncation is thus avoided.

4.1 Periodic boundary conditions

If we return to the PhC membrane waveguide that was introduced in Chapter 3, then Fig. 3.1 outlines one way of defining the bounded computational domain that we need for the Bloch mode expansion technique. In Fig. 3.1(b), the PhC membrane is given a finite width along x, and along y the air regions above and below the PhC membrane are given finite heights, with domain dimensions d_x and d_y. On the boundaries of the computational domain, i.e., at $x = \pm d_x/2$ and $y = \pm d_y/2$, we need to impose conditions on the electromagnetic fields, and the use of Fourier series expansions in Eqs. (3.3) implicitly defines these BCs; the domain is periodic in x and y and so are the solutions. Thus, what we model is in fact not the structure in Fig. 3.1(b), but an infinite repetition of this computational domain, translated along x and y by d_x and d_y, respectively. Fig. 4.1 illustrates this with nine repetitions and dashed blue lines separating the computational domains.

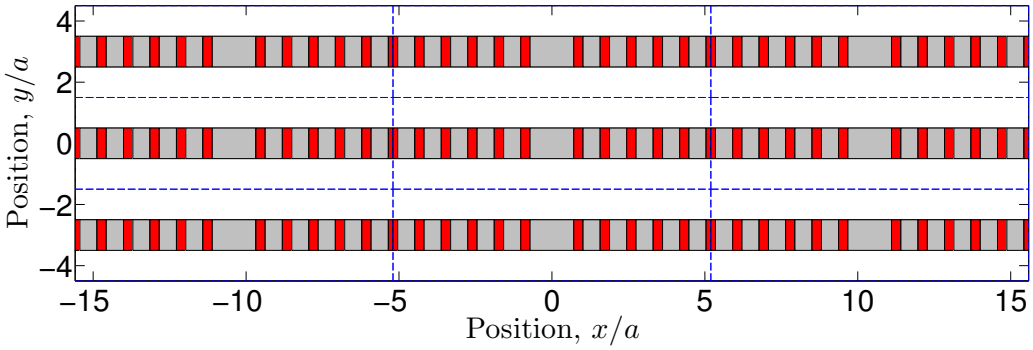

Figure 4.1 Nine repetitions of the PhC membrane waveguide computational domain that was introduced in Fig. 3.1(b). Dashed blue lines outline the domain boundaries.

Waves that arrive at these domain boundaries will interfere among the different computational domains. In some situations, as we discuss more in Section 4.2.1, this lateral periodicity may correspond to the physical structure at hand, and this interference then accurately reflects the physics. However, here we target the PhC membrane outlined in Fig. 3.1, and the lateral domain wave interference in this case becomes an *artifact of the method* that does not reflect the physics we seek to describe.[1] From this consideration, we can establish a rule of thumb:

- For optical modes that are well confined in the center of the computational domain, for example a bound PhC membrane waveguide mode, we can use the formalism as developed in Chapter 3, since by construction such bound modes will decay exponentially towards the domain boundaries. The dependence of their properties on d_x and d_y, in general, *decreases* with d_x and d_y.
- Unbound optical modes, like the radiation modes of the PhC membrane waveguide, will propagate to the boundaries and interfere artificially across different domains.

[1] We note that by making suitable linear combinations of the complex exponentials in the Fourier expansions in Eqs. (3.3), the Fourier basis can be changed into sine and cosine functions. These functions satisfy homogeneous Dirichlet and Neumann BCs, respectively, and choosing periodic BCs or Dirichlet and Neumann BCs is thus equivalent; both choices give rise to the parasitic interference [88, 102].

This interference will depend sensitively on the domain sizes; the properties of such unbound modes will, in general, depend in an *oscillatory* manner on d_x and d_y. Thus, making d_x and d_y large will not eliminate the parasitic interference, and any problem involving radiative losses, with coupling to unbound optical modes, cannot immediately be solved with the formalism of Chapter 3.

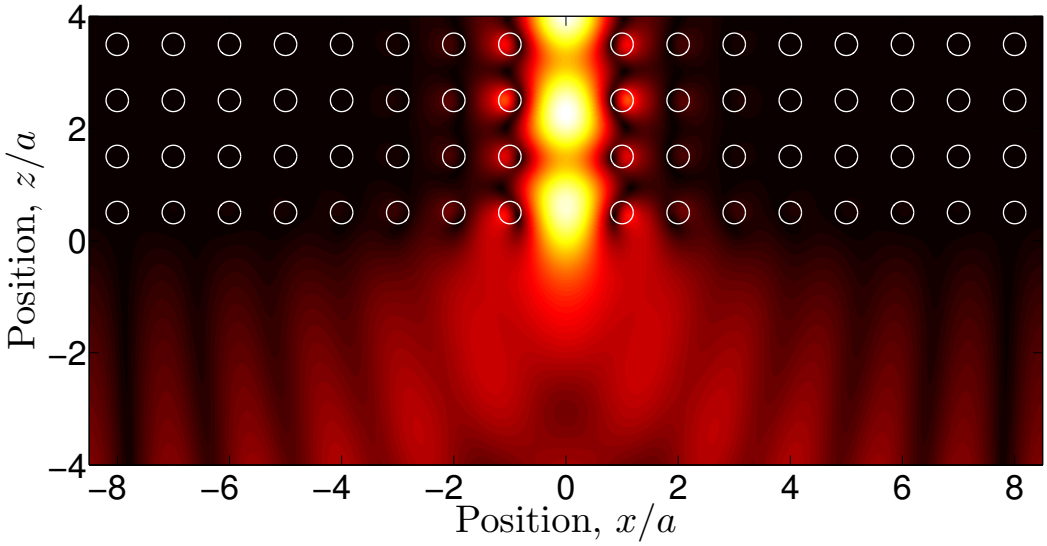

Figure 4.2 Rectangular 2D PhC lattice of high-index rods in air (PhC 1 in Table 2.1) with a semi-infinite W1 waveguide coupled to air. The structure is excited with the propagating waveguide mode at $\omega a/(2\pi c) = 0.395$, and the resulting field magnitude ($|E_y|$) is shown. The field has been computed without PMLs, and a parasitic standing wave-like pattern along x is visible in the air region ($z < 0$).

To illustrate this qualitatively, we consider a 2D PhC with a rectangular lattice of high-index rods in air that has a bandgap for the out-of-plane polarization ($\mathbf{E} = E_y\mathbf{y}$). We leave out one row of rods, which creates a single-mode W1 waveguide, and couple the semi-infinite PhC waveguide to air. The structure is then excited with the waveguide mode, and Fig. 4.2 illustrates the resulting field magnitude ($|E_y|$). If we take the PhC waveguide end facet to be a point source, the field in the air region ($z < 0$) should spread as a cylindrical (spherical in 3D) wave, which is clearly not the case. In the PhC waveguide, the bound mode is well separated from the domain boundary, but as it scatters at the PhC-air interface, it excites freely propagating plane waves that eventually arrive at the domain boundary and interfere with the neighboring computational domain, cf. Fig. 4.1. This gives rise to the standing wave-like pattern along x, which is a visual signature of the parasitic interference.

The problem outlined in this section is not specific to the FMM-Bloch mode expansion method developed in Chapter 3, but applies to any numerical method based on the differential form of Maxwell's equations. In spatial discretization techniques, like FDTD and FEM, the problem is formulated on a discrete spatial grid, and at the outermost grid elements BCs need to be imposed, e.g. as periodic or Dirichlet BCs. The net effect of this is the same as discussed above, namely unwanted parasitic interference in the computational domain. In the following section, we discuss how to address this problem.

4.2 Absorbing boundary conditions: Perfectly matched layers

The basic problem is that we do not know the form of the electromagnetic fields on the computational domain boundary, which is at a *finite* distance from the structure we seek to analyze. Thus, we cannot, in an exact manner, specify them on this boundary. This problem of defining appropriate BCs for radiating structures has been known and analyzed for decades, especially in the context of the FDTD technique. Already in 1969, it was discussed by Taylor *et al.* [103], who noted that homogeneous Dirichlet or Neumann BCs on the domain boundary is "an unnecessary restriction". From 1971 to 1980, approaches on imposing the radiation condition at infinity at the domain boundary [104, 105], a "soft lattice truncation" and a field averaging procedure [106] as well as introduction of an artificial, lossy material for absorption of the outgoing radiation [107] were proposed. In 1981, Mur proposed the first stable and efficient FDTD scheme [108] that is now known as "Mur's absorbing BCs", and the biggest breakthrough to date in defining absorbing BCs came in 1994 with Bérenger's proposal of *perfectly matched layers* (PMLs) [109]. PMLs are absorbing boundary regions of the computational domain, in which electromagnetic energy is dissipated, and that are perfectly matched to the computational domain to suppress reflection at the physical domain-PML domain interfaces. Today, PMLs are the de facto standard for implementing absorbing BCs with all computational methods, and the PML technique has been refined and optimized for the past 20 years, in particular for use with FDTD and FEM techniques.

As noted in Section 3.2.1, the FMM was originally developed for laterally periodic structures, for example 1D [110] and 2D [76] planar diffraction gratings, for which the lateral Fourier expansion accurately reflects the physical structures. More recent FMM developments also adhere to this lateral periodicity, e.g. with applications to plasmonic grating surfaces [100, 111]. At the same time, developments of the FMM for non-laterally-periodic structures, coined aperiodic FMM (or aFMM), were explored, with early applications to 2D [71, 112] and 3D [113] PhCs and with various proposals for absorbing BCs. In 2005, Hugonin and Lalanne proposed to formulate the FMM PMLs as complex coordinate transformations [114], which is the PML technique we adopt here and describe further in the following section.[2]

4.2.1 Implementation with Fourier modal method

The FMM PMLs proposed in [114] build on Chew and Weedon's idea of implementing PMLs as complex and stretched coordinates in the PML regions [119]. Specifically, we pad each computational domain with spatial regions of the same refractive index as the surrounding medium (typically air), but in which the spatial coordinates are mapped onto new complex ones. The (desirable) effect of this coordinate transformation is to provide a reflectionless interface to the physical domain and to suppress the radiation entering into these PML regions, which, in turn, will suppress the interference between different computational domains.

For the structure in Fig. 4.1, the PML regions can, for example, be implemented as in Fig. 4.3 with PML regions shown in green. With α denoting either x or y, the PMLs are

[2] As noted in Section 3.2.1, semi-analytical eigenmodes are not applicable for the 3D PhC membranes we here aim to describe. However, absorbing BCs in connection with semi-analytical eigenmodes were developed in parallel, and we refer to [22, 115–118] for details.

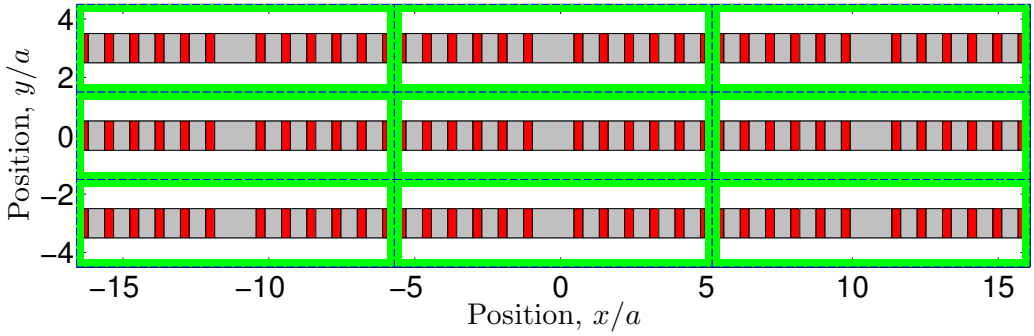

Figure 4.3 Nine repetitions of the PhC membrane waveguide computational domain, as in Fig. 4.1, but here with PML regions included in green.

introduced formally via coordinate transformations

$$\alpha = A(\alpha') = \begin{cases} \alpha' & |\alpha'| \leq d_\alpha/2 \\ f_\alpha(\alpha') & d_\alpha/2 \leq |\alpha'| \leq \tilde{d}_\alpha/2 \end{cases}, \tag{4.1}$$

where α' is a real parameter, and where $f_\alpha(\alpha')$ is a coordinate transformation to be specified. The physical domain still has extent d_α, while the PMLs exist where $d_\alpha/2 \leq |\alpha'| \leq \tilde{d}_\alpha/2$;[3] both d_α and $\tilde{d}_\alpha$ are computational parameters to be specified, too. The coordinate transformation changes the differential operators in Maxwell's equations as follows

$$\frac{\partial}{\partial \alpha} = \frac{\partial}{\partial A} = \left(\frac{\partial A}{\partial \alpha'}\right)^{-1} \frac{\partial}{\partial \alpha'}, \tag{4.2}$$

where, from Eq. (4.1), we have

$$\left(\frac{\partial A}{\partial \alpha'}\right)^{-1} = \begin{cases} 1 & |\alpha'| \leq d_\alpha/2 \\ (\partial f_\alpha/\partial \alpha')^{-1} & d_\alpha/2 \leq |\alpha'| \leq \tilde{d}_\alpha/2 \end{cases}. \tag{4.3}$$

So the PMLs appear as renormalizations of the partial derivatives in the lateral coordinates by a factor of 1 $[(\partial f_\alpha/\partial \alpha')^{-1}]$ in the physical [PML] domain. The transformation of the partial derivative in Eq. (4.2) can be used directly in Maxwell's equations, and the functions $(\partial A/\partial \alpha')^{-1}$ merely appear as additional factors herein. Upon converting these coordinate transformed Maxwell's equations into the Fourier space, these functions become additional matrices in the definition of matrices $\mathbf{F}$ and $\mathbf{G}$ in the eigenmode layer eigenvalue problem in Eq. (3.4); details on this extension are given in Appendix C.1. Once these matrices have been generalized to take into account the PMLs, the rest of the formalism proceeds as described in Chapter 3.[4]

[3] We here assume symmetric PMLs with the same thickness and transformation in both PML regions $\alpha' \leq -d_\alpha/2$ and $\alpha' \geq d_\alpha/2$. The extension to asymmetric PMLs is straightforward [102].

[4] We still solve matrix eigenvalue problems for eigenmodes (Eq. (3.4)) and Bloch modes (Eq. (3.12)) and thus avoid tedious root finding in the complex plane, as required with PMLs and semi-analytical eigenmodes [117, 118]. Also, as discussed in detail in [88], spatial integrals, like those in Eq. (3.16b), must take the coordinate transformation in Eq. (4.1) into account.

Different types of coordinate transformations and PML thicknesses can be chosen, and in the original work [114] a single class of transformations, depending on a number of parameters, was investigated, inspired by earlier work on a similar problem [120]. The behavior of this class of transformations was tested with different values of the parameters, and in particular the convergence of one physical quantity, a modal reflection coefficient, with the Fourier resolution was tested on a single size of the computational domain; this led to conclusions about optimum choices of the PML parameters. But, as we argue in Section 4.3.4, conclusions about the quality of PMLs and the accuracy in computations cannot be made without varying the size of the computational domain. So while the proposals for transformations in [114] are a good starting point, that much subsequent work has built on [28, 88, 102, 121–123], some basic tests appear to be missing to fully assess the quality of the PMLs. We address this in the following sections, where we use some of the transformations proposed in [114] and vary the size of the computational domain systematically; this allows us to draw quantitative conclusions about *these* PML transformations. We note that investigations with variations of the domain size have been reported for some specific structures, both with FDTD [124, 125] and FMM [126] simulations.

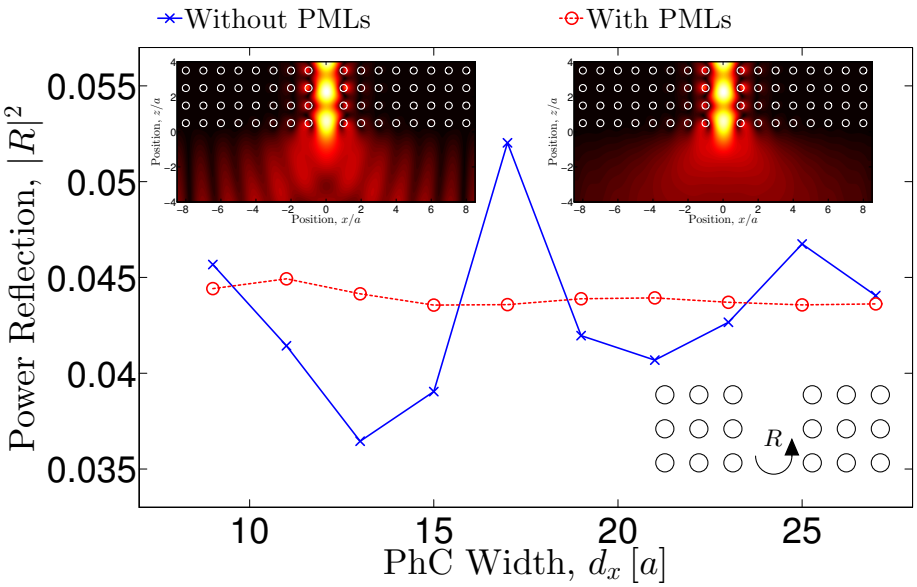

Figure 4.4 Power reflection for the bound waveguide mode, $|R|^2$, in the 2D PhC structure introduced in Fig. 4.2 as function of the width of the PhC, d_x. Data without (with) PMLs are included as blue crosses (red circles), with PML parameters stated in the main text. The top left (right) inset shows the field magnitudes without (with) PMLs included.

We now revisit the 2D semi-infinite PhC waveguide coupled to air from Fig. 4.2, but this time with PMLs on the x boundaries. Specifically, we include PMLs with a thickness of $\tilde{d}_x/2 - d_x/2 = 250\,\text{nm}$ on each domain boundary and, inspired by [114], let $\partial f_x/\partial x' = 1 + \text{i}$. At the same frequency as previously we then excite the structure from above with the bound waveguide mode, and the associated field magnitude is shown in the top right inset in Fig. 4.4 (for comparison, the field magnitude without PMLs is reproduced in the top left inset). Clearly, the transverse standing-wave pattern observed

without PMLs is gone, and the light spreads into the air region as quasi-cylindrical waves, as expected on physical grounds. To be more quantitative, the power reflection of the bound waveguide mode, $|R|^2$, is computed as function of the PhC width, d_x; data without (with) PMLs are shown as blue crosses (red circles).[5] When averaged over all values of d_x, the two approaches give approximately the same value ($|R|^2 \simeq 0.044$), but the oscillations for the situation without PMLs are substantially larger than with PMLs included. The field plots and the reflection coefficients thus demonstrate that the PMLs work qualitatively and semi-quantitatively; the interference between computational domains is largely suppressed. In the following sections, we test the effect and quality of the PMLs more systematically.

4.3 Dipole emission in photonic crystal waveguide: Convergence with perfectly matched layer parameters and domain size

As a specific example, we consider a GaAs PhC membrane W1 waveguide surrounded by air, with structural parameters as given in the caption of Fig. 4.6. The waveguide is infinitely extended along z, and we embed an x-oriented dipole in the PhC membrane waveguide and analyze the emission from this dipole as function of computational parameters, especially the size of the computational domain and the PML parameters. Inspired by work employing the FMM-Bloch mode expansion techniques for modeling of PhC cavities [26] and waveguides [28] with PMLs only on the y boundaries, and periodic BCs on the x boundaries, we test this configuration. In view of the qualitative observations in Figs. 4.2 and 4.4, the omission of PMLs on the x boundaries may appear questionable, but as this approach has been employed in the literature (apparently successfully), and as we always attempt to make the computational domain as small as possible, we test this setup. Fig. 4.5 illustrates a cross-sectional view of the structure, with computational parameters to be investigated indicated in blue. The dipole, at position $\mathbf{r}_\mathrm{D}$, is located in the center of the membrane and in the center of the supercell (at $z_\mathrm{D} = 0$ in Fig. 3.2) where the guided mode has its field maximum. Inspired by [28, 114], we choose a linear PML transformation, for which

$$\partial f_y / \partial y' = f_\mathrm{PML}, \tag{4.4}$$

is a constant, and test different values of f_PML in Section 4.3.1. In the language of Chapter 3, this structures consists of a single periodic section, for which we compute the associated Bloch modes, and we then obtain the coupling from the dipole to each of these Bloch modes as described in Section 3.4. In the following, we focus on the total emitted power, the power into the guided mode and the power into radiation modes as functions of the computational parameters to estimate their accuracy.

As we discuss in more detail in Chapter 8, the dipole emission in a PhC membrane waveguide is highly dispersive, largely due to the dispersive nature of the bound waveguide mode, and in Fig. 4.6 we therefore present computations of the waveguide dispersion of this (E_x even-even) Bloch mode, where the x Fourier truncation, j_max, is a parameter.[6]

[5] We use x Fourier truncations, j_max, and a number of staircase approximation layers, N_l, that we in a similar problem in Chapter 5 find to be sufficiently accurate for the purposes here, see details in Appendix D.3. We also observe that the convergence of R with j_max is slower with than without PMLs, however the variations in Fig. 4.4 are not dominated by these Fourier truncations.

[6] The waveguide dispersion is a continuous curve, but is computed at discrete frequencies. In later situations, we interpolate these, but in this case we simply display the computed, discrete dispersion data.

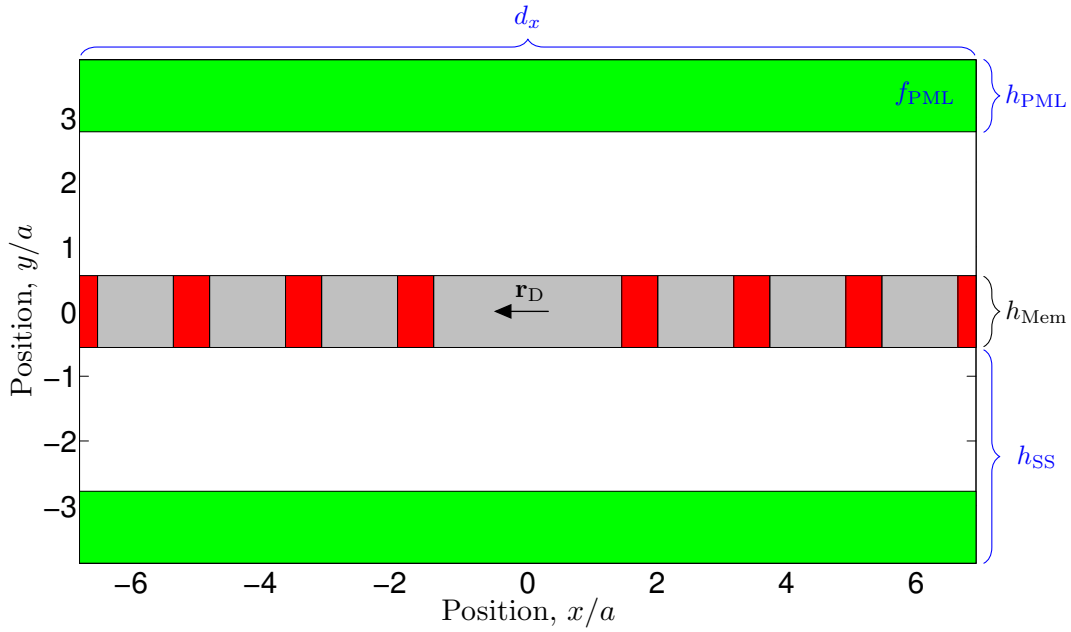

Figure 4.5 Computational domain (xy-plane) of PhC membrane W1 waveguide with an x-oriented dipole (black arrow) embedded in the center of the waveguide. The PML regions are shown in green, and computational parameters are indicated in blue.

As described in Section 2.3.1, the waveguide dispersion displays a region of almost-linear dispersion ($\omega a/(2\pi \mathrm{c}) \gtrsim 0.244$), the fast light regime, and a region of flattening dispersion ($\omega a/(2\pi \mathrm{c}) \lesssim 0.244$), the slow light regime, corresponding to small and large group indices, respectively. We have chosen a frequency in either regime, as indicated by the dashed green lines, and in the following sections investigate the convergence of the dipole emitted powers at these two frequencies.

4.3.1 Total dipole power vs. domain height and perfectly matched layer transformation

In this section, we vary the height of the air sub- and superstrates, h_{SS}, and take the specific PML transformation as a parameter via f_{PML}. We fix the width of the PhC ($d_x = 8\sqrt{3}a$), the x Fourier truncation ($j_{\max} = 30$) and the thickness of the PMLs ($h_{\mathrm{PML}}/h_{\mathrm{Mem}} = 3/2$). With $h_{\mathrm{SS}}/h_{\mathrm{Mem}} = 3$, we take the y Fourier truncation to be $n_{\max} = 10$, and we increase this truncation with h_{SS} such that the density of y plane waves remains roughly constant.

In Fig. 4.7, we show the total dipole emitted power as function of h_{SS} and with different colors and data markers corresponding to different values of f_{PML}; the top (bottom) panel shows data for the fast (slow) light frequency, as indicated in Fig. 4.6. The power is normalized to the best estimate, $P_{\mathrm{Tot}}^{\mathrm{Best}}$, taken at the largest value of h_{SS}. In the fast [slow] light regime, the total emitted power at the largest values of the domain height stabilizes around a value of $P_{\mathrm{Tot}}^{\mathrm{Best}}/P_{\mathrm{Bulk}} \sim 1.1$ [4.5] (not shown), i.e., as expected the emitted power increases from the fast to the slow light regime. Furthermore, the

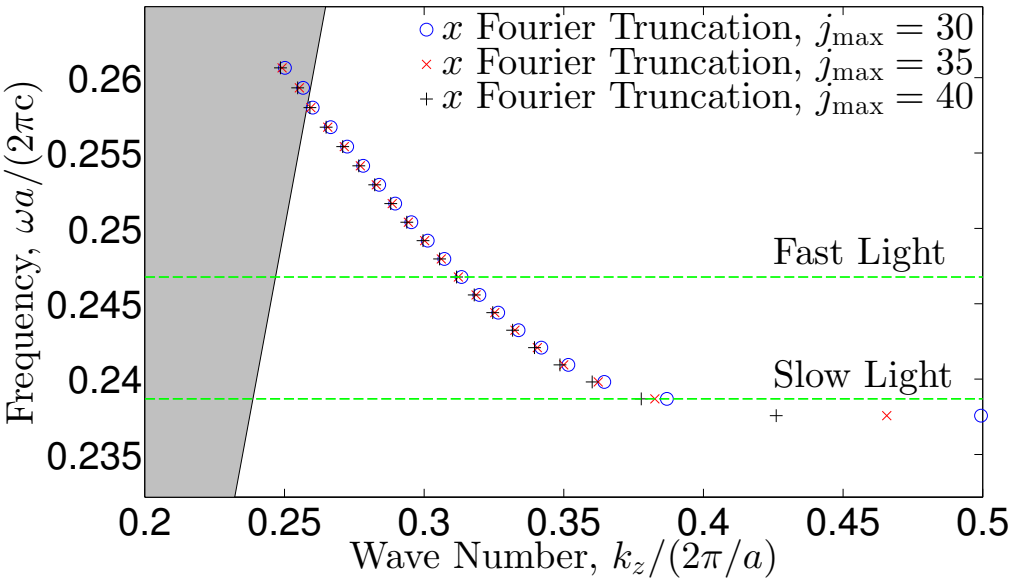

Figure 4.6 Dispersion of guided (E_x even-even) Bloch mode in GaAs PhC membrane W1 waveguide surrounded by air (PhC 4 in Table 2.1, with $n_B = 3.4638$ and hole radii $r/a = 0.3$). Gray shading indicates the light cone, and green dashed lines show the fast light frequency $\omega a/(2\pi c) = 0.247$ and the slow light frequency $\omega a/(2\pi c) = 0.239$. Computational parameters: PhC width $d_x = 8\sqrt{3}a$, air sub- and superstrate heights $h_{SS}/h_{Mem} = 3$, number of staircase layers per supercell $N_l = 33$. The y Fourier truncation is $n_{max} = 10$, the x Fourier truncation, j_{max}, is a parameter.

curves exhibit fluctuations that slowly decrease as h_{SS} is increased, and it is apparent that different choices of the PML transformation yield different magnitudes of these fluctuations, especially for the smallest values of h_{SS}. Based on these investigations we in the following choose $f_{PML} = 1 + i$ that overall gives the smallest fluctuations and thus appears to be the most efficient choice for the PML transformation considered here.

4.3.2 Guided and radiation mode power and β factor vs. domain height and perfectly matched layer thickness

In this section, we split the total dipole power into the contribution to the guided mode and to the radiation modes and investigate these as well as the β factor (Eq. (2.18)) as function of the thickness of the air sub- and superstrates, h_{SS}, and with the PML thickness, h_{PML}, as a parameter. Fig. 4.8 displays these data, with results for the fast [slow] light frequency in panel (a) [(b)], and with all quantities normalized to the best estimates obtained at the largest values of h_{SS}. In the fast [slow] light regime, the computed quantities approximately stabilize at $P_G/P_{Bulk} \sim 0.93$, $P_{Rad}/P_{Bulk} \sim 0.15$ and $\beta \sim 0.86$ [$P_G/P_{Bulk} \sim 4.4$, $P_{Rad}/P_{Bulk} \sim 0.12$ and $\beta \sim 0.97$] at the largest values of h_{SS} (not shown).

If we first consider the guided mode power, P_G, then in both regimes we observe oscillations that gradually become smaller as h_{SS} increases, and there are no pronounced differences among the different choices the PML thickness. The latter point stems from the localization of the guided mode in the center of the computational domain, making

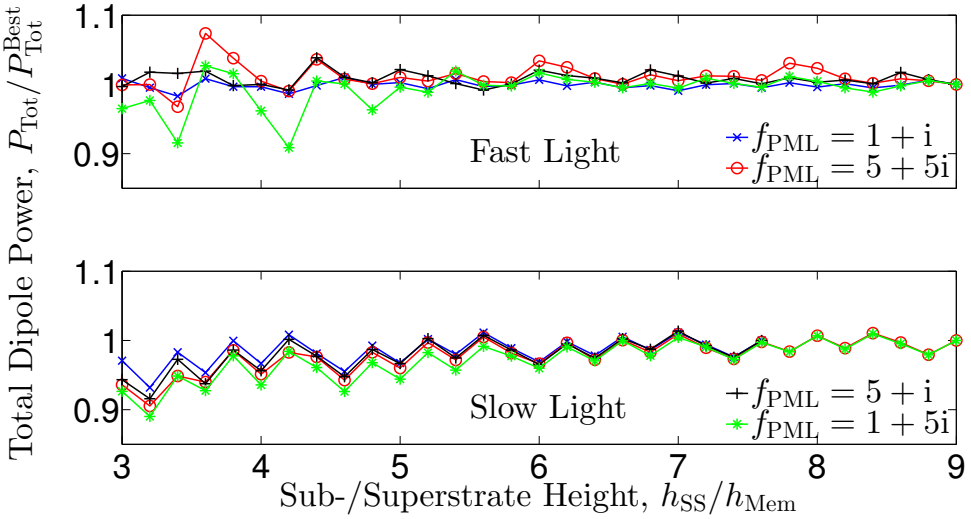

Figure 4.7 Total dipole power, P_{Tot}, as function air sub-/superstrate height, h_{SS}, and with the PML transformation, f_{PML}, as a parameter. The power is normalized to the best estimate, $P_{\mathrm{Tot}}^{\mathrm{Best}}$, taken at the largest value of h_{SS}. The width of the PhC ($d_x = 8\sqrt{3}a$), the x Fourier truncation ($j_{\max} = 30$), the thickness of the PMLs ($h_{\mathrm{PML}}/h_{\mathrm{Mem}} = 3/2$) and the number of staircase layers ($N_{\mathrm{l}} = 33$) are fixed, while the y Fourier truncation is $n_{\max} = 10$ at $h_{\mathrm{SS}}/h_{\mathrm{Mem}} = 3$ and increased to keep the density of y plane waves constant. The top (bottom) panel shows data for the fast (slow) light frequency, as indicated in Fig. 4.6.

it relatively insensitive to the exact PML implementation. In turn, as we compare the magnitude of the oscillations in the two regimes, we observe an increase from $\sim 1\%$ in the fast to $\sim 8\%$ in the slow light regime. Closer to the band edge, the guided mode becomes exceedingly delocalized by penetration into the PhC (along x), which makes the computation of its properties more sensitive to the exact x resolution (as we saw in the dispersion diagram in Fig. 4.6) and the size of the domain as the present results demonstrate.

Proceeding to the radiation mode power, P_{Rad}, this quantity oscillates more strongly with h_{SS} than P_{G}, as expected; the radiation modes are not localized in the PhC membrane and are consequently more sensitive to the form of the BCs and the size of the computational domain. The magnitude of these oscillations slowly decreases with h_{SS}, and as opposed to the guided mode, the radiation modes indeed depend on the form of the PMLs; the thinnest PMLs (blue, $h_{\mathrm{PML}}/h_{\mathrm{PML}} = 1/3$) give rise to the largest oscillations. The thickest PMLs (green, $h_{\mathrm{PML}}/h_{\mathrm{PML}} = 3.8$), at the smallest values of h_{SS}, give rise to very large variations, which is caused by (too) small air regions in this situation; if the PMLs come (too) close to the PhC membrane, the physical quantities are artificially distorted. If we disregard this and the thinnest PMLs, the oscillations are still $\sim 15 - 25\%$ in both regimes, which demonstrates the difficulty in computing accurately the emission into the radiation modes. Finally, for the β factor the oscillations with h_{SS} decrease from $\sim 3\%$ to $\sim 1\%$ from the fast to the slow light regime. This stems from the increase in the relative importance of P_{G} over P_{Rad}; the former quantity increases by more than a factor of four, while the latter decreases slightly. So even though the uncertainty in computing P_{G} increases from the fast to the slow light regime, the uncertainty in computing β at the same time decreases.

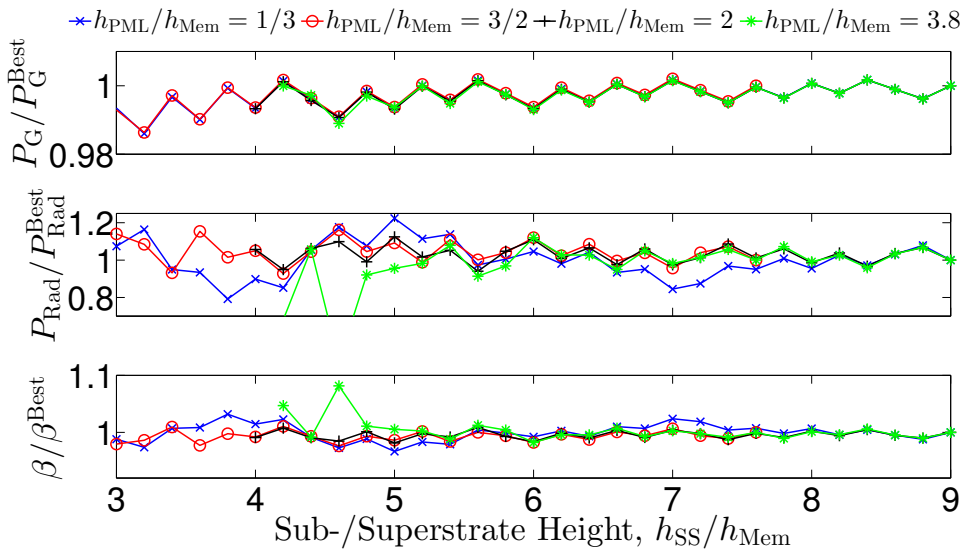

(a) Fast Light.

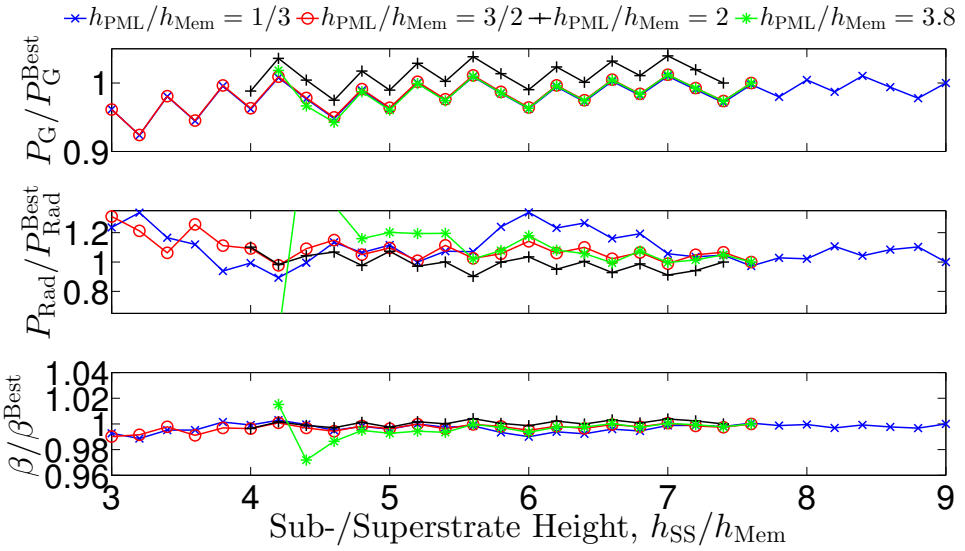

(b) Slow Light.

Figure 4.8 Guided mode dipole power, P_{G}, radiation mode dipole power, P_{Rad}, and β factor as function air sub-/superstrate height, h_{SS}, and with the PML thickness, h_{PML}, as a parameter. The powers are normalized to the best estimate, taken at the largest value of h_{SS}. The width of the PhC ($d_x = 8\sqrt{3}a$), the x Fourier truncation ($j_{\max} = 30$), the PML transformation ($f_{\mathrm{PML}} = 1 + \mathrm{i}$) and the number of staircase layers ($N_{\mathrm{l}} = 33$) are fixed, while the y Fourier truncation is $n_{\max} = 10$ at $h_{\mathrm{SS}}/h_{\mathrm{Mem}} = 3$ and increased to keep the density of y plane waves constant. Data for the fast and slow light frequencies, as indicated in Fig. 4.6, are included.

A general observation from Fig. 4.8 is that except for the thinnest PMLs (blue data), there are no important differences among the different thicknesses, and as we are interested

in making the computational domain and the PMLs as small as possible, we therefore proceed with $h_{\mathrm{PML}}/h_{\mathrm{PML}} = 3/2$ (red data in the figure). We also in the following choose $h_{\mathrm{SS}}/h_{\mathrm{Mem}} = 5$ and the associated y Fourier truncation $n_{\max} = 16$. With these parameters, and the PML transformation from the previous section ($f_{\mathrm{PML}} = 1 + \mathrm{i}$) fixed, we proceed to the final convergence tests.

4.3.3 Guided and radiation mode power and β factor vs. domain width and staircasing

In this final section, we fix parameters as described in the last paragraph of the previous section and vary the width of the PhC membrane, d_x, and the number of staircase layers per supercell, N_{l}. To appreciate the difference that different values of N_{l} give rise to, we here normalize the powers to the bulk value, and in panel (a) [(b)] of Fig. 4.9 show data for the fast [slow] light regime.

For the guided mode power, all curves find a plateau as d_x is increased, however with some residual oscillations, especially in the slow light regime. The number of staircase layers give rise to vertical offsets that become smaller as N_{l} is increased; the variation from $N_{\mathrm{l}} = 33$ to $N_{\mathrm{l}} = 129$ is $\sim 0.2\%$ ($\sim 5\%$) in the fast (slow) light regime. This demonstrates once again the increased sensitivity to computational parameters of the computation of guided mode properties in the slow light regime. For the radiation mode power, the picture is markedly different; the curves do not find plateaus as d_x is increased, and while the curves with different values of N_{l} follow the same trend, the distance between data points with increasing values of N_{l} does not decrease. These observations, and especially the peak in P_{Rad} at $d_x = 12\sqrt{3}a$ in the slow light regime, demonstrate the complexity in computing the coupling to the radiation modes accurately. Finally, the β factor does not saturate with d_x in the fast light regime, but rather continues to decrease with d_x, while in the slow light regime it varies within a few percent with the width of the PhC, exhibiting in particular a dip where P_{Rad} has a peak.

4.3.4 Summary of convergence analysis

Among the PML configurations we have investigated, the transformation $\partial f_y/\partial y' = f_{\mathrm{PML}} = 1 + \mathrm{i}$ with a thickness of $h_{\mathrm{PML}}/h_{\mathrm{PML}} = 3/2$ has turned out to give the smallest oscillations of computed data when varying the computational domain height via h_{SS} (Figs. 4.7 and 4.8). We varied the PML thickness from sub-wavelength to wavelength ($\sim 1/10 \lesssim h_{\mathrm{PML}}/\lambda_0 \lesssim 1$), and while we could have made the PMLs even thicker, there was no indication that thicker PMLs produce smaller oscillations. For the PML transformation, we chose a linear coordinate transformation, giving a constant PML derivative (f_{PML}, Eq. (4.4)), and tested four complex values of this quantity. This investigation is consequently not exhaustive, and other linear transformations as well as other classes of coordinate transformations could be tested.

We find that the dipole coupling to the guided mode, P_{G}, oscillates by approximately 1% (8%) in the fast (slow) light regime when we vary the height of the computational domain (Fig. 4.7). The similar oscillations for the coupling to the radiation modes, P_{Rad}, is $\sim 15 - 25\%$, in both the fast and slow light regimes, while the oscillations of the β factor are approximately 3% (1%) in the fast (slow) light regime. Overall β therefore appears to vary the least with the height of the computational domain, which is caused by β being dominated by P_{G} in the problem at hand; the smaller that the $P_{\mathrm{G}}/P_{\mathrm{Rad}}$ ratio becomes, the more the large variations in P_{Rad} will spill over into variations in β.

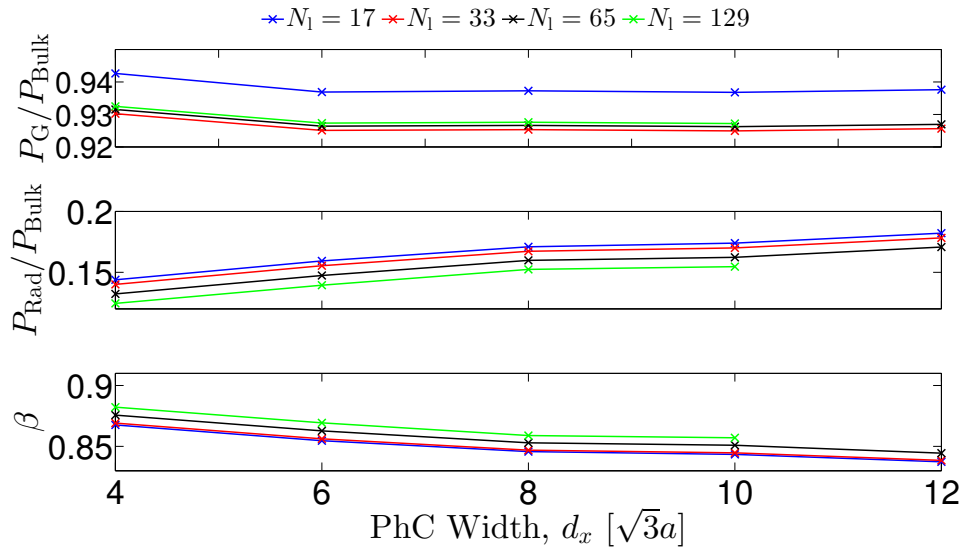

(a) Fast Light.

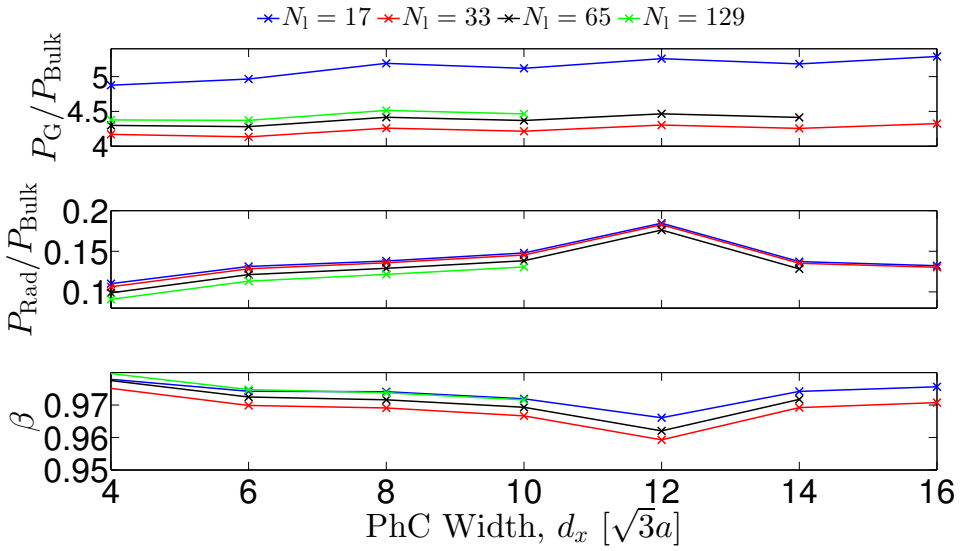

(b) Slow Light.

Figure 4.9 Guided mode dipole power, P_G, radiation mode dipole power, P_{Rad}, and β factor as function PhC width, d_x, and with the number of staircase layers per supercell, N_l, as a parameter. The powers are normalized to the GaAs bulk value. The height of the computational domain ($h_{SS}/h_{Mem} = 5$), the y Fourier truncation ($n_{max} = 16$) and the PML parameters ($f_{PML} = 1 + i$, $h_{PML}/h_{PML} = 3/2$) are fixed, while the x Fourier truncation is $j_{max} = 30$ at $d_x = 8\sqrt{3}a$ and varied to keep the density of x plane waves constant. Data for the fast and slow light frequencies, as indicated in Fig. 4.6, are included.

The variation of P_G with the PhC width, d_x, is $< 0.1\%$ ($< 5\%$) when $d_x \geq 6\sqrt{3}a$ in the fast (slow) light regime (Fig. 4.9). The same quantity varies by $\simeq 0.3\%$ ($\simeq 6\%$) when

varying the number of staircase layers per supercell from $N_\mathrm{l} = 33$ to $N_\mathrm{l} = 129$ in the fast (slow) light regime. For the radiation mode coupling, P_Rad, the picture is different; this quantity does not appear to converge with the width of the PhC, with data that continues to increase or exhibits resonant-like peaks. Recalling the setup without PMLs on the x boundaries (Fig. 4.5), this is not surprising; the radiation modes in different computational windows interfere via the x boundaries, an interference that depends on the width of the domain, d_x. Finally, as the β factor is dominated by P_G, it only varies by a few percent with d_x, but, as P_Rad, it also continues to decrease or exhibits resonant-like features when d_x is increased. These observations demonstrate that PMLs must be imposed on the x boundaries as well, to suppress the parasitic interference that causes the large variations of computational data for increasing values of d_x.

In addition to the convergence checks we have presented in the previous sections and summarized above, the x and y Fourier truncations should be varied to estimate the associated computational errors at a given truncation. This is, for example, done for the β factor in a PhC membrane waveguide in [28] and small fluctuations $\sim 0.1\%$ are found. Above we found the errors on β from the size of the computational domain to be larger than these Fourier truncation errors, which suggests that this quantity is more sensitive to variations in the computational domain size than Fourier truncation. It also accentuates that it is insufficient to only check the Fourier truncation (or spatial resolution in FDTD or FEM); the domain size must be varied to estimate computational errors when modeling structures with radiative losses.

Finally, as a perspective, we mention that an alternative to PMLs is to formulate the modal expansion techniques in infinite domains. Here, the discrete, equidistant lateral k-vector *series* are replaced by continuous lateral k-vector *integrals* over all space [127, 128]. Eventually, these integrals are discretized in k-space, but as opposed to the present approach where the size in k-space of each point is constant ($\Delta\mathbf{k}_\perp = (2\pi/d_x)(2\pi/d_y)$) a non-equidistant sampling ($\Delta\mathbf{k}_\perp = \Delta\mathbf{k}_\perp(\mathbf{k}_\perp)$) can be chosen, which effectively emulates an open and infinitely extended structure. We have previously, with semi-analytical eigenmodes, demonstrated a proof-of-principle of this approach [129], but the extension to full 3D structures requires a Fourier based approach.

4.4 Summary

We have explained that the computational technique developed in Chapter 3 uses periodic boundary conditions on the lateral domain boundaries, and that this leads to parasitic interference across these domain boundaries for the photonic crystal membrane structures that we target in this thesis. We have illustrated this problem for a 2D photonic crystal waveguide coupled to air, and we have discussed the concept of absorbing boundary conditions as a practical remedy to suppress this undesirable interference. In particular, we have introduced perfectly matched layers as the de facto standard for absorbing boundary conditions, and we have explained how these can straightforwardly be implemented as complex coordinate transformations in the computational framework from Chapter 3. We have, for the 2D photonic crystal waveguide coupled to air, shown how the implementation of perfectly matched layers suppresses the parasitic interference, which is visible in the associated electric field profile. We have then turned to the challenging problem of dipole emission in a 3D photonic crystal membrane waveguide and investigated the impact from both perfectly matched layer parameters and computational domain size on the dipole emission powers. This has been done in both the fast and slow light regions of the waveguide and have allowed us to estimate the best choices for the perfectly matched

layer parameters that give rise to the smallest uncertainty in the computed quantities. We have also, even when perfectly matched layers are included, shown that computed powers, both to a guided mode and to radiation modes, and the β factor are relatively sensitive to the size of the computational domain, and relative errors on these quantities due to variations of the domain size have been found to be larger than those previously reported in the literature. These results accentuate the need to check the size of the computational domain when structures with radiative losses are modeled, not just with the technique from Chapter 3, but with any finite-size domain technique.

Chapter 5

Coupled photonic crystal cavity-waveguide structures: A quasi-normal mode approach

> *Should you find yourself in a chronically leaking boat, energy devoted to changing vessels is likely to be more productive than energy devoted to patching leaks.*
>
> Warren Buffett

Photonic and plasmonic resonators are important building blocks that may pave the way for enhanced light-matter interactions with potential applications in energy efficient photovoltaics, integrated photonic circuits, and quantum information technology. Such resonators are typically discussed in terms of their *modes*, and in nanophotonics jargon these are often referred to as "cavity modes", "resonant modes" or simply "resonances". Examples of the modes of resonators include the well-known Mie resonances of spherical objects [130, 131], localized surface plasmons of plasmonic nanostructures [132–134], and the optical modes of microcavities in micropillars or PhCs [44, 135–139]. Inherent to the modes of realistic resonators is their *leaky* nature; they dissipate energy into heat or by radiation into the environment, and the leakiness is typically quantified via the quality factor, Q, which measures the stored energy relative to the energy lost per cycle [140].

In this chapter, we focus on coupled PhC cavity-waveguide structures and establish theoretical and computational tools for describing these systems in terms of their leaky modes. In Section 5.1, we review approaches for treating leaky resonators and introduce the concept of quasi-normal modes, while in Section 5.2 we introduce the coupled PhC

cavity-waveguide structures that we focus on. In Section 5.3, we introduce quasi-normal modes formally, discuss their properties, and propose a semi-analytical quasi-normal mode theory for the LDOS in PhC cavity-waveguide structures. In Sections 5.4 and 5.5, we present techniques for computing and normalizing quasi-normal modes in extended systems, before in Section 5.6 (5.7) we consider specific structures with one cavity (two cavities) side-coupled to a PhC waveguide, and in particular demonstrate the accuracy of the quasi-normal mode theory for the LDOS. Finally, perturbation theory with quasi-normal modes in coupled PhC cavity-waveguide structures is considered in Section 5.8.

5.1 Theoretical approaches to open systems

An immediate consequence of energy leakage from the resonator is that it is non-conservative, and mathematically its modes must therefore be solutions of non-hermitian problems. One way of dealing with such systems is the "system plus bath" or "modes of the universe" approach due to Lang *et al.* [141], where the resonator ("system") is embedded into a large surrounding environment ("bath"). The "system plus bath" is conservative, and the modes are taken as the quantized solutions of the full structure. Eventually the size of the "bath" is allowed to go to infinity, and in this way the modes become continuous in frequency, but with certain modes, the "cavity modes", localized inside the resonator [142]. Drawbacks of this approach include the arbitrary partitioning of the full structure into a "system" and a "bath" [143], the challenges related to dealing with a continuum of modes and the necessity for high-Q resonators for application of the "modes of the universe" in quantum optics [144].

An alternative is to consider the modes of the resonator ("system") only, which leads to the aforementioned non-hermitian problem. This gives rise to leaky modes with *discrete* and *complex* frequencies, as first discussed by Vaĭnshteĭn [145] and Ujihara [146] and, later, by Ching and co-workers [147] (see also references therein). These are the *quasi-normal modes* (QNMs). The QNMs are solutions of Maxwell's equations without sources that satisfy an outgoing wave BC at infinity, and this choice of BC directly renders the problem non-hermitian. Since the QNMs are discrete in frequency, an appealing hypothesis is that important physical characteristics of resonators, for example the LDOS, can be decomposed onto a small set of QNMs, allowing for transparent analysis of the resonators. Such QNM theories have been demonstrated for highly symmetric resonators [131, 148] and have in recent years been extended to more complex dielectric [125, 149] and plasmonic [150–152] systems. A common feature of all these successful applications of QNMs is the treatment of resonators embedded in a homogeneous background. In this chapter, we focus on integrated optical circuits, where PhC cavities are coupled to an extended PhC waveguide, and demonstrate that the QNM descriptions are useful and highly accurate in these systems as well.

We note that both the "system plus bath" and QNM approaches are developed and explained for simple resonators in [142], while extensive discussions and reference lists on the topic of modes in open resonators are presented in [144, 153]. In quantum mechanics, the similar solutions are known as Siegert states, metastable states, or auto-ionizing states [154] of, for example, atoms and molecules, and due to their non-hermitian nature they are known to be inherently difficult to compute [155].

5.2 Photonic crystal waveguide with side-coupled cavities

As an example that we use and build on throughout the chapter, we consider a rectangular 2D PhC lattice of high-index rods surrounded by air (PhC 1 in Table 2.1). This structure is known to possess a TE bandgap [55], with the electric field having only a y component, $\mathbf{E} = E_y\mathbf{y}$.[1] By removing a single row of rods in the crystal a W1 waveguide, supporting a single guided Bloch mode, is created, and by furthermore removing one or more rods in the bulk of the PhC, side-coupled cavities are created. An example with a single cavity is shown in Fig. 5.1, where the cavity-waveguide distance is $d_{\text{cav}} = 2a$. Coloring shows the associated QNM field distribution ($|E_y|$), and it is apparent that this mode is localized inside the cavity ("system") and leaks into the waveguide ("bath"), a manifestation of the leaky nature of QNMs.

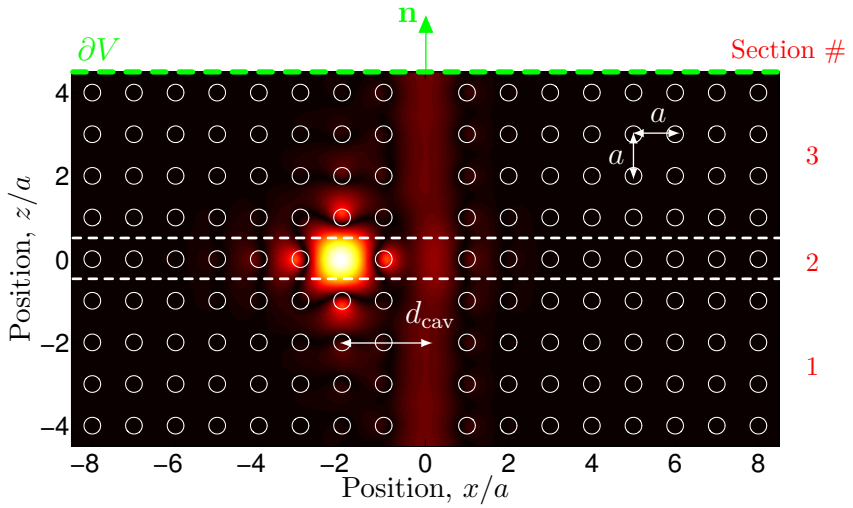

Figure 5.1 QNM field distribution ($|E_y|$) in a cavity side-coupled to a W1 waveguide in a 2D rectangular PhC lattice with lattice constant a. Dashed lines separate periodic sections with distinct sets of Bloch modes, and Section 2 is the cavity section for constructing the roundtrip matrix, see Fig. 5.3. The center-to-center distances between the cavity and the W1 waveguide is $d_{\text{cav}} = 2a$, and the QNM frequencies and Q factors for different values of d_{cav} are given in Table 5.1. The green dashed line and arrow indicate the computational domain boundary and outward pointing unit normal vector that enter into the FEM nonlocal BC in Eq. (5.6).

5.2.1 Indirect characterization via scattering

In the literature, resonators and their underlying modes are often characterized indirectly via scattering experiments or calculations: The resonator is excited externally, and some characteristic quantity, for example the fields at one or several positions in the resonator, is recorded as function of, for example, the frequency. Computationally, this strategy dates (at least) back to Fox and Li's proposal in [156], where they note that "The method is a computer simulation of the physical experiment of exciting a resonator externally". However, they also note that external excitation might excite not just the resonator mode

[1] As noted in Chapter 3: Our convention of TE and TM is consistent with the literature on waveguides and the FMM, but opposite of the convention used in the literature on PhCs.

of interest, but several of these, leading to a contaminated spectrum. As a solution to this problem, it was proposed to pass the output through successive repetitions of the same resonator to suppress the non-resonant contributions from other modes and thus refine the resonant signal corresponding to the resonator mode of interest. Another drawback of the scattering approach is the need for an ad hoc choice of polarization and/or spatial shape of the excitation field; choosing these properly requires an a priori knowledge of the resonator that might not always be available. In Chapter 9, we explore one such example for a plasmonic resonator, where scattering calculations are "blind" to certain modes.

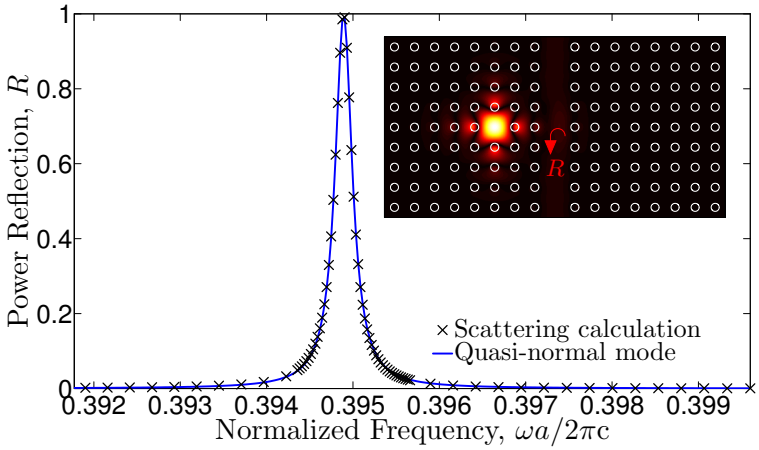

Figure 5.2 Spectrum of power reflection R of propagating Bloch mode in W1 defect waveguide in 2D rectangular PhC lattice with a side-coupled cavity. The inset shows the structure and the field distribution ($|E_y|$) at the reflection maximum. The black crosses are obtained from scattering calculations, whereas the blue solid curve is obtained from Eq. (5.13) and the complex frequency of the associated QNM. Reprinted with permission from [87]. Copyright (2014) Optical Society of America.

As an example of the indirect scattering characterization of a resonator, the black crosses in Fig. 5.2 show the spectrum of the power reflection, R, of the propagation Bloch mode in the coupled 2D PhC cavity-waveguide structure that we introduced in Fig. 5.1, here with $d_{\text{cav}} = 3a$. The power reflection is, at most frequencies, small; the waveguide Bloch mode simply propagates through the system with only a small reflection occurring due to the cavity. However, as the frequency of the cavity mode is approached, R starts to increase, stemming from the resonant coupling of part of the propagating waveguide mode into the cavity. As a consequence, two paths for the light exist, and the waves going via the cavity interfere destructively with those going directly through the waveguide; the field is extinct in the transmission part of the waveguide, giving rise to the strong reflection. The coloring in the inset shows the field magnitude at the reflection maximum, which is highly reminiscent of the associated cavity mode field distribution, and in Section 5.6.1 we quantify the relation between the scattering spectrum and the underlying QNM.

5.3 Semi-analytical theory for the local density of states

QNMs are solutions of Maxwell's equations without sources, $\mathbf{f}_\mu = [\mathbf{E}_\mu, \mathbf{H}_\mu]$, where μ indexes the QNMs, that satisfy an outgoing wave BC [157]. As stated in Section 5.1, this BC leads to discrete and complex QNM frequencies, $\tilde{\omega}_\mu = \omega_\mu - \mathrm{i}\gamma_\mu$, and where $\gamma_\mu > 0$ to reflect the dissipation of energy.[2] The QNM quality factor is given by [63, 158]

$$Q = \frac{\omega_\mu}{2\gamma_\mu}, \tag{5.1}$$

from which non-leaky resonators ($\gamma_\mu = 0$) directly acquire their expected infinite Q. For resonators embedded in a homogeneous background, the outgoing wave BC for scalar fields is the Sommerfeld radiation condition, and the generalization for vector fields is the Silver-Müller radiation condition [157, 159]. These conditions are *not* the correct QNM BC at infinity when the resonator is coupled to an extended structured system (e.g. a waveguide), for which we introduce a new QNM BC in Section 5.4. Irrespective of the specific form of the outgoing wave BC, the complex QNM frequency translates into an (exponential) spatial divergence of the QNM fields far from the resonator. We explain this and the associated complications in defining a QNM normalization and mode volume in Section 5.5.

As an alternative to brute force computations of the Green's function, $\mathbf{G}(\mathbf{r}, \mathbf{r}'; \omega)$, as a path to obtain the LDOS, we assume that for frequencies close to the cavity resonance frequencies, and at positions in or close to the cavities, $\mathbf{G}(\mathbf{r}, \mathbf{r}'; \omega)$ may be approximated by an expansion on one or a few QNMs. The QNMs are computed (Section 5.4) and normalized (Section 5.5) at their discrete frequencies once and for all, and following an approach similar to that of [150], for example, the (transverse component of the) Green's function can then be expanded as

$$\mathbf{G}(\mathbf{r}, \mathbf{r}'; \omega) = \frac{\mathrm{c}^2}{2} \sum_\mu \frac{\mathbf{E}_\mu(\mathbf{r}) \otimes \mathbf{E}_\mu(\mathbf{r}')}{\tilde{\omega}_\mu(\tilde{\omega}_\mu - \omega)}, \tag{5.2}$$

where $\mathbf{E}_\mu(\mathbf{r})$ is the *normalized* electric field of the μth QNM. Inserting the expression in Eq. (5.2) into Eq. (2.13) provides a semi-analytical QNM representation for the LDOS

$$\rho^\alpha(\mathbf{r}; \omega) = \frac{\omega}{\pi} \sum_\mu \mathrm{Im}\left[\mathbf{n}_\alpha \cdot \frac{\mathbf{E}_\mu(\mathbf{r}) \otimes \mathbf{E}_\mu(\mathbf{r})}{\tilde{\omega}_\mu(\tilde{\omega}_\mu - \omega)} \cdot \mathbf{n}_\alpha\right]. \tag{5.3}$$

In many coupled cavity-waveguide systems of interest, a single or a few QNMs dominate, and retaining only these in the expansion in Eq. (5.3) provides a compact and accurate approximation of the LDOS that is more transparent and easier to obtain than a fully numerical computation of the Green's function. Importantly, we do not seek a representation of the Green's function or the LDOS at all positions or frequencies. Therefore, we do not formally rely on a completeness relation for the QNMs, but rather consider the finite sum in Eq. (5.3) to be an approximation, which we show to be extraordinarily good. The work that remains to obtain the LDOS is thus to compute and normalize the QNMs, which we detail in the following sections.

[2] With the time convention $\exp(-\mathrm{i}\omega t)$, $\gamma_\mu > 0$ reflects dissipation, while $\gamma_\mu < 0$ would represent accumulation and an *incoming* wave BC at infinity.

5.4 Computing quasi-normal modes in extended systems

An intricate part of QNM calculations is to satisfy the outgoing wave BC. For spatial discretization techniques, like FDTD the FEM, this BC is notoriously difficult to implement and is typically approximated using PMLs [160, 161]. In contrast, Green's function techniques can lead to solutions satisfying the outgoing wave BC exactly, and the QNMs can be determined as nontrivial solutions of "excitation-free" volume [125, 162] or surface [163] integral equations. Later, in Chapter 9, we use the technique of [162] for characterizing the localized surface plasmon modes of plasmonic dimers as QNMs. While in principle possible, extension of the Green's function based techniques to the extended PhC structure we focus on here is not straightforward.

As an alternative, therefore, Bloch mode expansion and scattering matrix techniques provide a powerful framework for satisfying the outgoing wave BC, since the propagation along one axis, the PhC waveguide axis, is handled analytically. This implies that satisfying the outgoing wave BC amounts to setting the amplitude of the incoming waves equal to zero, which, complemented with a condition on the so-called cavity roundtrip matrix, forms the basis of the FMM roundtrip matrix method [87]. We note that alternative approaches based on the poles of the total scattering matrix exist [111, 164–166], but in our experience these techniques are difficult to handle numerically for the structures we consider here.

5.4.1 Fourier modal method: Roundtrip matrix method

To introduce the cavity roundtrip matrix method, we consider a general periodic structure where each periodic section is described by a set of Bloch modes, as introduced in Chapter 3. We select, as indicated in the left part of Fig. 5.3, an internal section w, $2 \leq w \leq W-1$, that we refer to as the cavity section, and an example of a cavity is section $w = 2$ in Fig. 5.1. In structures of a total of $W = 3$ periodic sections, only $w = 2$ can act as the cavity section, but when $W > 3$, several sections could act as the cavity section. In Appendix D.4, we consider a case with $W = 9$ and show that different choices of the cavity section, w, lead to the same QNM.

In the cavity section, we search for the QNMs as superpositions of Bloch modes $\mathbf{c}_\mathrm{c}$ that replicate themselves upon a roundtrip

$$\mathbf{M}\mathbf{c}_\mathrm{c} = \alpha_\mathrm{c}\mathbf{c}_\mathrm{c}, \quad \alpha_\mathrm{c} = 1, \tag{5.4}$$

where α_c is an eigenvalue of the cavity roundtrip matrix $\mathbf{M}$ [167]. $\mathbf{M}$ is obtained by multiplying the reflection and propagation matrices in the order indicated by the arrows in the right part of Fig. 5.3

$$\mathbf{M}(\tilde{\omega}) \equiv \mathbf{R}^\mathrm{bot}\mathbf{P}^-\mathbf{R}^\mathrm{top}\mathbf{P}^+, \tag{5.5}$$

where $\mathbf{R}^\mathrm{top}$ ($\mathbf{R}^\mathrm{bot}$) is the scattering reflection matrix for the top (bottom) part of the structure, while $\mathbf{P}^+$ ($\mathbf{P}^-$) is the diagonal matrix accounting for the propagation of the Bloch modes from the bottom (top) to the top (bottom) of the cavity section [23]. The roundtrip matrix also enters into the expression for the dipole excited Bloch mode amplitudes (inside the first bracket in Eq. (3.18a)), and by inspection of Eq. (3.18a) it is clear that these amplitudes diverge when the roundtrip matrix has a unity eigenvalue.

In practice, we solve Eq. (5.4) by iterating the complex frequency until a unity eigenvalue of $\mathbf{M}$ is found. As indicated by the black crosses in the left part of Fig. 5.3, there are no incoming Bloch modes in the outermost sections (1 and W), but only outgoing

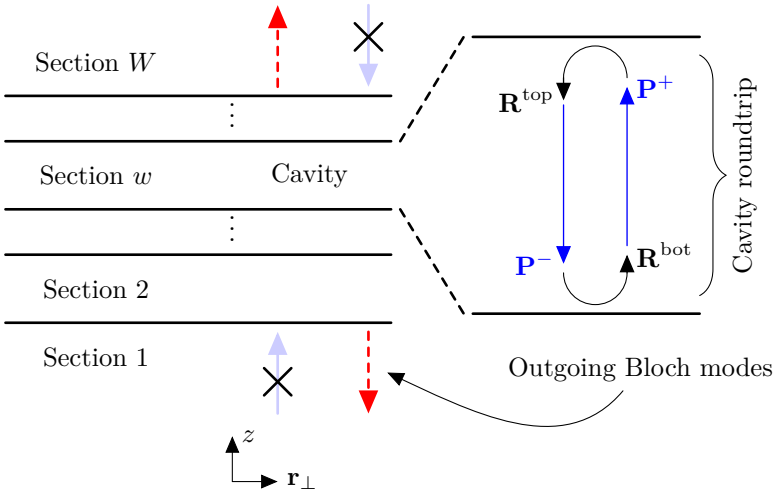

Figure 5.3 Schematic of the FMM roundtrip matrix method for determining QNMs. *Left panel:* An internal section w is chosen as the cavity. In the outermost regions, the amplitudes of the incoming (solid arrows) and outgoing (dashed arrows) Bloch modes vanish and have finite values, respectively. *Right panel:* Zoom in on cavity section with indication of the elements of the roundtrip matrix comprising the top and bottom scattering reflection matrices, $\mathbf{R}^{\mathrm{top}}$ and $\mathbf{R}^{\mathrm{bot}}$, and up- and downward propagation matrices, $\mathbf{P}^{+}$ and $\mathbf{P}^{-}$. Reprinted (adapted) with permission from [87]. Copyright (2014) Optical Society of America.

Bloch modes (dashed red arrows)[3], whose amplitudes can be determined directly from the QNM eigenvector, $\mathbf{c}_{\mathrm{c}}$, by using the scattering matrices of the structure. This, in effect, is the outgoing wave BC that the QNMs must satisfy in resonators coupled to waveguides. In the following section, we use an approximate, but more explicit form of this outgoing wave BC for QNM computations using a FEM technique.

5.4.2 Finite element method: Nonlocal boundary condition method

In this section, we outline a procedure for computing QNMs in the extended PhC structures we focus on here using a commercially available FEM solver (COMSOL Multiphysics). An intricate part in using a FEM solver is to satisfy the outgoing wave BC at the computational domain boundaries. With the FMM, this condition is imposed by only retaining the outgoing Bloch modes, but in a FEM calculation we do not have direct access to all the Bloch modes and thus cannot impose this condition explicitly. Therefore, we assume that the waveguide supports a single guided Bloch mode in the spectral range of interest, which is often the case in practical situations. Then, as we look farther and farther away from the resonator, the QNM will be dominated by this single guided mode, as all other contributions decay exponentially along the length of the waveguide or radiate out of the structure.[4] Thus, if we take the FEM computational boundary, ∂V, to be a

[3]The classification and sorting of Bloch modes into incoming and outgoing waves is non-trivial; see Appendix A in [87] for details.

[4]In the 2D structures considered in this chapter, the radiation modes do not exist and thus will not play a role for this argument. However, for extension to 3D structures, in finite-thickness membranes, the radiation modes will be present, but their contribution will become less and less important along the length of the waveguide [17, 94].

plane perpendicular to the waveguide (line in 2D), we may express the outgoing wave BC for the QNM as the following approximate nonlocal BC [168]

$$[\mathbf{E}(\mathbf{r}),\, \mathbf{H}(\mathbf{r})]_{\mathbf{r}\in\partial V} = \exp\left(\mathrm{i}\mathbf{k}\cdot\mathbf{n}a\right)[\mathbf{E}(\mathbf{r}-\mathbf{n}a),\, \mathbf{H}(\mathbf{r}-\mathbf{n}a)]\,, \tag{5.6}$$

where $[\mathbf{E}(\mathbf{r}),\, \mathbf{H}(\mathbf{r})]$ is the guided mode, with Bloch wave vector $\mathbf{k}$, $\mathbf{n}$ is an outward pointing normal unit vector on ∂V, and where the Bloch wave form of the modes in a PhC has been exploited. For the specific structures we consider here, ∂V and $\mathbf{n}$ are shown in green in Fig. 5.1. The guided mode dispersion, $\mathbf{k} \equiv \mathbf{k}(\tilde{\omega})$, is not known analytically and is therefore approximated using a Taylor expansion around a frequency close to the QNM frequency of interest. Similarly, as with the FMM method, the governing equation, Eq. (5.6), is solved iteratively by iterating over the complex frequency $\tilde{\omega}$, and the FEM resolution is kept sufficiently high so as not to influence the results to the quoted number of digits; more details on these technical aspects can be found in [169]. To validate the single guided mode QNM BC in Eq. (5.6), we vary the size of the simulation domain in Appendix D.1 to check convergence.

5.5 Normalizing quasi-normal modes in extended systems

For use of QNMs in semi-analytical descriptions of the LDOS and perturbation theory, a rigorous normalization of the modes is required to give them a correct weighting in these theories. In the frequency domain, QNMs diverge spatially, which we give a heuristic explanation of in Appendix D.2, and this divergence is also observed in the coupled PhC cavity-waveguide structures we consider here. In Fig. 5.4, we show the field magnitudes of the QNMs in the center of the waveguide ($x = 0$) and as functions of z for the single-cavity structure in Fig. 5.1. The figure (inset) shows the fields in the near (far) field of the cavity, and the divergence in the far field is clearly visible, especially for the structure with $d_{\mathrm{cav}} = 2a$ (solid green). This spatial divergence makes the "usual" normalization based on an integration of the electromagnetic energy density in a QNM meaningless; this quantity is infinite when integrated over all space [125].

To address this, an alternative mode normalization that compensates the spatial divergence was first proposed in simple, effective 1D resonators [131, 142, 148, 170], which was later generalized to more complicated resonators [125]. Using a different approach, an alternative formulation, that also accounted for material dispersion, was derived [150], and these results have been shown to be equivalent [152, 171]. The formulations in [125, 131, 142, 148, 170] rely explicitly on the Silver-Müller addition, while the procedure in [150] does not, but does rely on the use of PMLs to suppress the diverging QNM fields. The use of PMLs effectively regularizes the QNM normalization integral, and it has recently been pointed out [171] that a regularization is also needed for the integral in [125]. A third alternative [172] exists where regularization is not needed, but that is difficult to implement with numerical solvers [171]. In the coupled PhC cavity-waveguide structures, the outgoing wave BC, as discussed in Section 5.4, is not simply the Silver-Müller addition, and due to the extended waveguide, the structure cannot be terminated with PMLs. Therefore, none of the existing QNM mode volume formulations can be directly applied to the problem at hand, and in the following we describe and validate an alternative procedure.

The starting point is the normalization integral in [150]

$$\langle \mathbf{f}_\mu \,|\, \mathbf{f}_\mu \rangle = \frac{1}{2}\int_V \left\{ \epsilon(\mathbf{r})\mathbf{E}_\mu(\mathbf{r})\cdot\mathbf{E}_\mu(\mathbf{r}) - \frac{\mu_0}{\epsilon_0}\mathbf{H}_\mu(\mathbf{r})\cdot\mathbf{H}_\mu(\mathbf{r}) \right\} \mathrm{d}\mathbf{r}, \tag{5.7}$$

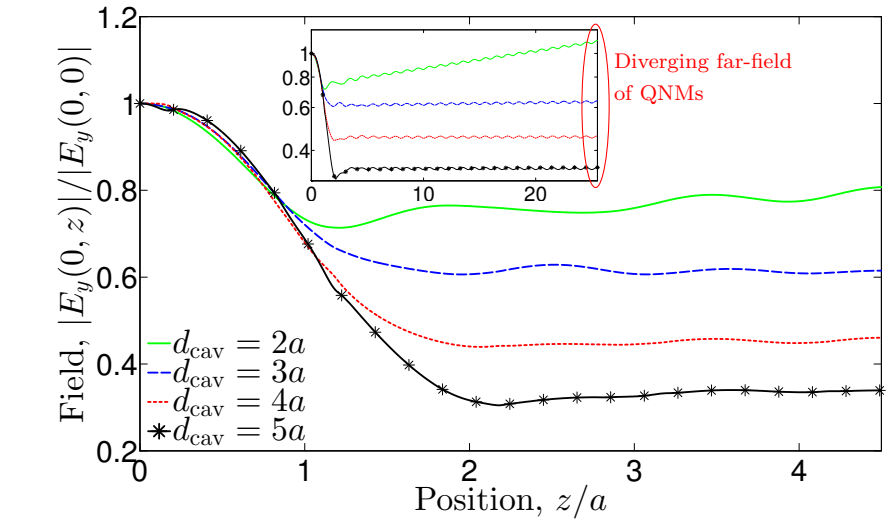

Figure 5.4 QNM field distribution in a cavity side-coupled to a W1 waveguide in a 2D rectangular PhC lattice in the middle of the W1 waveguide ($x = 0$) as function of z. Different curves correspond to different cavity-W1 distances d_{cav} (see Fig. 5.1). The figure shows the QNMs in the near field, corresponding to the z coordinates used in Fig. 5.1, while the inset includes the far-field behavior of the QNMs in a semilogarithmic plot. Reprinted (adapted) with permission from [87]. Copyright (2014) Optical Society of America.

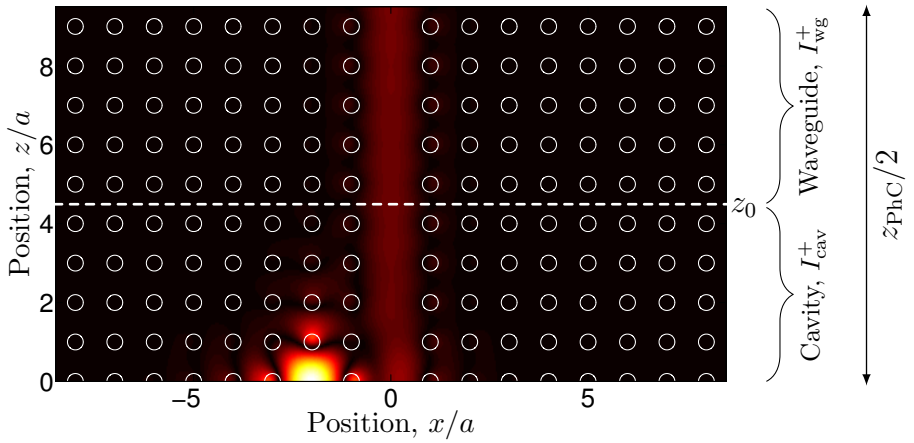

Figure 5.5 Illustration of splitting of QNM mode volume into a cavity and a waveguide part at $z = z_0$, cf. Eq. (5.8). Half of the total PhC z length, $z_{\mathrm{PhC}}/2$, as used in Fig. 5.6, is indicated.

where the integral is over all space. We have assumed non-magnetic and non-dispersive materials, but following [150] the extension to these situations is straightforward. Referring to the structure of interest, the side-coupled PhC cavity-waveguide, we split the integration into two parts: One for the cavity and one for the waveguide, as indicated in Fig. 5.5. Specifically, we split the integration along the waveguide axis at z_0, where the cavity

(waveguide) contribution comes from $|z| \leq z_0$ ($|z| \geq z_0$)

$$\langle \mathbf{f}_\mu \,|\, \mathbf{f}_\mu \rangle = \underbrace{\frac{1}{2}\int_\perp \int_{|z|\leq z_0} I(\mathbf{r})\,\mathrm{d}z\,\mathrm{d}\mathbf{r}_\perp}_{\equiv I_{\mathrm{cav}}} + \underbrace{\frac{1}{2}\int_\perp \int_{|z|\geq z_0} I(\mathbf{r})\,\mathrm{d}z\,\mathrm{d}\mathbf{r}_\perp}_{\equiv I_{\mathrm{wg}}}, \tag{5.8}$$

with $I(\mathbf{r})$ being the integrand introduced in Eq. (5.7). The cavity contribution, I_{cav}, thus stems from integration in a finite volume (area in 2D) and is straightforwardly evaluated numerically. For the waveguide contribution, the procedure is identical for each semi-infinite waveguide, and we here focus on the $z > z_0$ part. Alluding to the single guided Bloch mode form of the QNM far from the resonator, that was the basis for the FEM nonlocal BC method (see Eq. (5.6)), we may express the semi-infinite waveguide integral as follows

$$I^+_{\mathrm{wg}} = I_a(z_0) \sum_{m=0}^{\infty} \exp(2\mathrm{i}\tilde{k}_\mu a), \tag{5.9a}$$

$$I_a(z_0) \equiv \frac{1}{2}\int_\perp \int_{z_0}^{z_0+a} \left\{ \epsilon(\mathbf{r})\mathbf{E}_\mu(\mathbf{r})\cdot\mathbf{E}_\mu(\mathbf{r}) - \frac{\mu_0}{\epsilon_0}\mathbf{H}_\mu(\mathbf{r})\cdot\mathbf{H}_\mu(\mathbf{r}) \right\} \mathrm{d}z\,\mathrm{d}\mathbf{r}_\perp, \tag{5.9b}$$

where $\tilde{k}_\mu$ is the z-component of the guided Bloch mode wave vector evaluated at the QNM frequency $\tilde{\omega}_\mu$. Since this frequency is complex, $\tilde{k}_\mu$ will also be complex, with $\mathrm{Im}\left(\tilde{k}_\mu\right) < 0$, which renders the geometric series in Eq. (5.9a) divergent. However, using the theory of divergent series and the Lindelöf's or Mittag-Leffler's methods [173] (with $\exp(2\mathrm{i}\tilde{k}_\mu a) \in \mathbb{C}\backslash[1,\infty[$), the series can still be assigned a finite value

$$I^+_{\mathrm{wg}} = \frac{I_a(z_0)}{1-\exp(2\mathrm{i}\tilde{k}_\mu a)}. \tag{5.10}$$

This last step, the summation of the divergent geometric series, constitutes the regularization of the otherwise divergent QNM normalization integral.

For the single side-coupled cavity with $d_{\mathrm{cav}} = 2a$ that we analyze more in Section 5.6, we collect the contributions from Eqs. (5.8)-(5.10), and evaluating them numerically in COMSOL with $z_0 = 8a$, we find

$$a_\mu \equiv \frac{\langle \mathbf{f}_\mu \,|\, \mathbf{f}_\mu \rangle}{\epsilon(\mathbf{r}_{\mathrm{D}})\left[\mathbf{E}_\mu(\mathbf{r}_{\mathrm{D}})\cdot\mathbf{y}\right]^2} = (1.441 - 0.055\mathrm{i})\,a^2, \tag{5.11}$$

where $\mathbf{r}_{\mathrm{D}}$ is the center of the cavity. The *complex* area (volume in 3D), a_μ, was defined in [125], and as we shall see later, it plays an important role in the QNM LDOS approximation. The effective mode area (volume in 3D), A_μ, that plays the role of the "size of the mode" in the Purcell factor formula, was also defined in [125] and takes the value

$$A_\mu \equiv \frac{1}{\mathrm{Re}\,(1/a_\mu)} = 1.443a^2. \tag{5.12}$$

Since the integral in Eq. (5.7) is formally divergent, a brute force numerical evaluation of the integral in still larger domains will not converge, but will in fact eventually diverge. However, evaluation of the integral in this fashion will oscillate around the "true" value, with oscillations that increase in magnitude for larger integration domains [171]. To illustrate this, the integral has been computed with 2D FMM and Riemann sums on a discrete (x,z)-lattice and for varying lengths, z_{PhC}, of the integration domain. In Fig. 5.6,

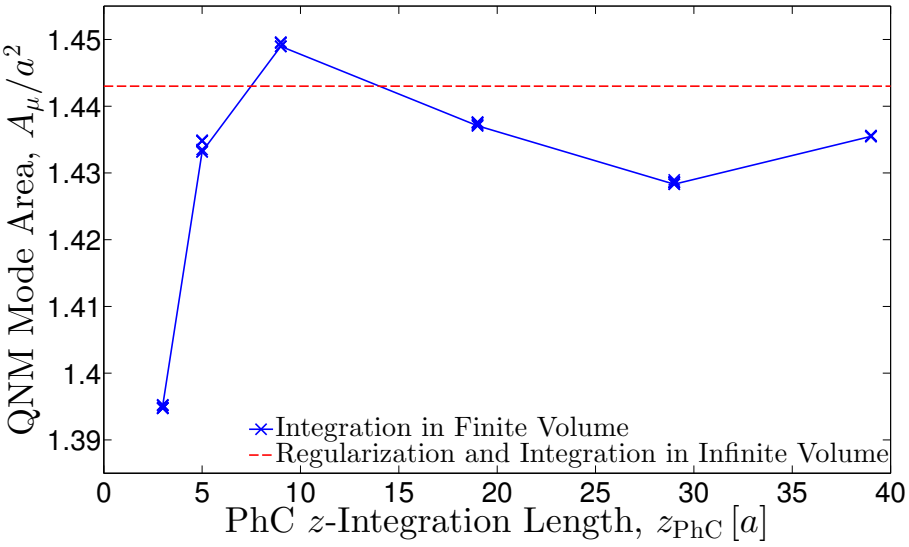

Figure 5.6 Effective QNM mode area, A_μ, as function of z size of the integration domain, z_{PhC}. Blue crosses are the FMM Riemann sum evaluation of Eq. (5.7), while the dashed red line is the "true" regularized FEM estimate from Eq. (5.12). At each value of z_{PhC}, Riemann sums have been evaluated with integration steps $\Delta x/a \in \{0.034, 0.017, 0.0113, 0.0085\}$ and $\Delta z/a \in \{0.0225, 0.01125, 0.0075\}$, and all data points are included.

these FMM data are shown as the blue crosses, while the value in Eq. (5.12) is included as the dashed red line. The oscillation around the "true" regularized value of the QNM mode area is observed. If a regularization procedure cannot be readily established, a running average of such numerically computed values of the integral for still larger domain sizes may provide a fairly accurate estimate of the QNM norm [171], which thus constitutes a pseudo-regularization procedure.

5.6 Example: Single side-coupled cavity

In this section, we go into more details about the QNMs of the single side-coupled cavity that we introduced in Fig. 5.1. Specifically, we outline how we compute the QNMs in this structure using the FMM roundtrip matrix method, with the cavity-waveguide distance, d_{cav}, as a parameter and demonstrate that we can reconstruct the reflection spectrum from Fig. 5.2 only based on the complex QNM frequency. Finally, we show that a single QNM is sufficient in the QNM LDOS expansion, Eq. (5.3), which leads to a slightly asymmetric spectrum.

To compute the QNMs, we first crudely estimate the QNM frequency by computing reflection spectra as in Fig. 5.2 and use the frequency at the reflection maximum as the starting point for an iteration towards a unity eigenvalue of the roundtrip matrix. For the FMM roundtrip matrix method, we use section $w = 2$ as the cavity section and compute all eigenvalues of its roundtrip matrix. We use the eigenvalue closest to unity and a Newton-Raphson algorithm to iterate the complex frequency $\tilde{\omega}$ until this eigenvalue deviates from unity by less than a chosen tolerance, taken here as $\sim 10^{-12}$. For four different values of d_{cav}, we give the complex QNM frequencies and Q factors in Table 5.1. These data have been obtained with a total of $N_{\mathrm{Fourier}} = 2j_{\max} + 1 = 101$ Fourier terms

d_{cav} $[a]$	ω_μ $[2\pi\mathrm{c}/a]$	γ_μ $[2\pi\mathrm{c}/a]$	Q
2	0.397	0.00136	$1.46 \cdot 10^2$
3	0.395	0.000119	$1.66 \cdot 10^3$
4	0.395	0.00000971	$2.03 \cdot 10^4$
5	0.395	0.000000775	$2.55 \cdot 10^5$

Table 5.1 QNM frequencies, $\tilde{\omega}_\mu = \omega_\mu - \mathrm{i}\gamma_\mu$, and Q factors for single cavities side-coupled to W1 waveguide structure at different cavity distances d_{cav} computed with the FMM roundtrip matrix method. The associated QNM field distribution with $d_{\mathrm{cav}} = 2a$ is shown in Fig. 5.1.

per layer and with each rod discretized by $N_{\mathrm{Staircase}} = 128$ staircase layers. Increasing these computational parameters further does not change the QNM frequencies and Q factors to the quoted number of digits; see Appendix D.3.

The real part of the QNM frequency, ω_μ, remains essentially constant as d_{cav} is increased, however with a small decrease from $d_{\mathrm{cav}} = 2a$ to $d_{\mathrm{cav}} = 3a$. In contrast, the (negative) imaginary part of the QNM frequency, γ_μ, decreases by more than an order of magnitude when d_{cav} is increased by a lattice constant, giving rise to Q factors that increase similarly as the cavity is moved away from the waveguide. This increase of the Q factor reflects a smaller rate of leakage from the cavity into the waveguide as d_{cav} becomes larger. The 2D calculations presented here lack the out-of-plane (y) contribution to the corresponding 3D Q factor, but the approach for determining QNMs and their Q factors is readily extendable to 3D.

Using the FEM nonlocal BC method introduced in Section 5.4.2 and a domain size deduced from convergence tests in Appendix D.1, we determine the QNM for $d_{\mathrm{cav}} = 2a$ at $\tilde{\omega}a/(2\pi\mathrm{c}) = 0.39687 - 0.00136\mathrm{i}$ with quality factor $Q = 146$. Comparing to the first row in Table 5.1, we thus observe a quantitative agreement between the FMM and FEM based approaches.

5.6.1 Reconstruction of reflection spectrum

As discussed by Ching *et al.* [142], there is a close relationship between a scattering resonance and the associated QNM, and for lossless systems the scattering amplitude, here in the form of the waveguide mode power reflection, R, is well approximated by a Lorentzian parametrized with the QNM frequency

$$R(\omega) = \frac{\gamma_\mu^2}{(\omega - \omega_\mu)^2 + \gamma_\mu^2}. \tag{5.13}$$

In Fig. 5.2, the black crosses are data from scattering calculations at each individual frequency, while the solid blue curve is obtained from Eq. (5.13) and the data in Table 5.1. For frequencies within a linewidth of the peak ($R > 0.5$), the deviation between the scattering calculation and the QNM-approximated spectrum is less than 1%, whereas the error increases further away from the cavity resonance frequency. Since the complex QNM frequencies can typically be obtained with fewer computations than the full scattering spectrum, QNMs thus constitute a simple and practical way of obtaining the spectrum and the Q factor of the resonator.

5.6.2 Local density of states

We focus on the situation with $d_{\text{cav}} = 2a$, and for this single-cavity structure a single QNM dominates for positions inside the cavity. Thus, it suffices to retain just one term in the LDOS QNM expansion in Eq. (5.3), and for a y-oriented dipole in the center of the side-coupled cavity we have

$$\rho^y(\mathbf{r}_{\text{D}};\omega) = \frac{\omega}{\pi}\frac{1}{\epsilon(\mathbf{r}_{\text{D}})}\text{Im}\left[\frac{1}{\tilde{\omega}_\mu(\tilde{\omega}_\mu-\omega)}\frac{1}{a_\mu}\right], \tag{5.14}$$

which can be expressed more explicitly as

$$\rho^y_{\text{PhC}}(\mathbf{r}_{\text{D}};\omega) = \frac{\omega}{\pi}\frac{1}{\epsilon(\mathbf{r}_{\text{D}})}\frac{1}{|\tilde{\omega}_\mu|^2}\frac{1}{|a_\mu|^2}\frac{1}{(\omega-\omega_\mu)^2+\gamma_\mu^2} \times\Big\{\text{Re}\,(a_\mu)\,[2\omega_\mu-\omega]\,\gamma_\mu+\text{Im}\,(a_\mu)\,\left[\omega_\mu\,(\omega-\omega_\mu)+\gamma_\mu^2\right]\Big\}. \tag{5.15}$$

This expression is the product of a linear function in ω, a Lorentzian and the term in the curled brackets that depends on the signs and relative magnitudes of $\text{Re}\,(a_\mu)$ and $\text{Im}\,(a_\mu)$. The expression in Eq. (5.15) constitutes a semi-analytical single-QNM approximation to the LDOS at $\mathbf{r}_{\text{D}}$ for the PhC structure considered here. Normalizing to the associated bulk LDOS (2D TE, see Appendix A.1) and evaluating the LDOS approximation in Eq. (5.15) on resonance ($\omega = \omega_\mu$), we find the Purcell factor

$$F^y_{\text{P}} \equiv \frac{\rho^y_{\text{PhC}}(\mathbf{r}_{\text{D}};\omega_\mu)}{\rho^y_{\text{Bulk}}(\omega_\mu)} = \frac{1}{\pi^2}\left(\frac{\lambda_0}{n(\mathbf{r}_{\text{D}})}\right)^2\frac{Q_\mu}{A_\mu}, \tag{5.16}$$

where $\omega_\mu/\text{c} = 2\pi/\lambda_0$, and where we discarded a small term $\gamma_\mu^2 \ll \omega_\mu^2$. The expression in Eq. (5.16) shows that the Purcell formula can be rigorously derived within the framework of QNMs when a single of these dominates the Green's function expansion [125]. Heuristically, it may be appealing to approximate the single-QNM LDOS enhancement with a Lorentzian curve parametrized with the QNM frequency and the Purcell factor

$$\frac{\rho^y_{\text{PhC}}(\mathbf{r}_{\text{D}};\omega)}{\rho^y_{\text{Bulk}}(\omega)} = F^y_{\text{P}}\frac{\gamma_\mu^2}{(\omega-\omega_\mu)^2+\gamma_\mu^2}. \tag{5.17}$$

In Fig. 5.7, the solid black curve shows the LDOS approximation in Eq. (5.15), while the dashed red curve is the Lorentzian approximation in Eq. (5.17). Numerically exact 2D simulations, obtained using the Bloch mode expansion and S-matrix technique from Chapter 3, are shown as the blue circles. It is apparent that both the single-QNM and the Lorentzian curves approximate the exact spectrum fairly well, but by closer inspection it is also seen that *only* the rigorous single-QNM approxmation (black curve, Eq. (5.15)) picks up the slight asymmetry of the spectrum, which, by construction, the symmetric Lorentzian does not. Since in this case the real part of a_μ is much larger than the magnitude of the imaginary part (see Eq. (5.11)), we can to a good approximation neglect the second term in the curled brackets in Eq. (5.15). The slight deviation from the Lorentzian shape of the spectrum thus stems from the first term in the curled brackets, leading to a super (sub) Lorentzian dependence on the red (blue) side of the peak. This deviation will be less and less important as the Q factor increases, and high-Q QNMs thus to a very good approximation exhibit Lorentzian LDOS spectra, as we showed schematically in Fig. 2.4. To be quantitative on the agreement, the right inset in Fig. 5.7

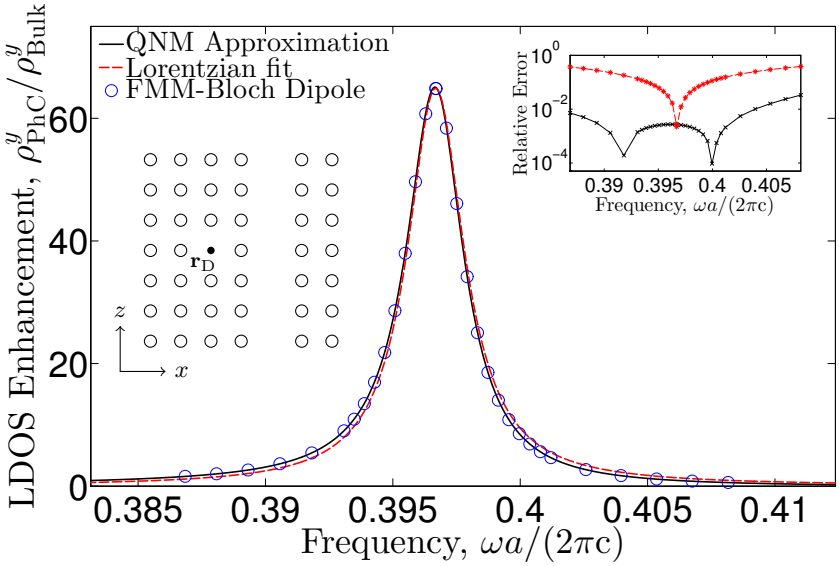

Figure 5.7 Spectrum of LDOS enhancement for a y-oriented dipole, $\rho^y_{\mathrm{PhC}}/\rho^y_{\mathrm{Bulk}}$, positioned in the center of a PhC cavity side-coupled at distance $d_{\mathrm{cav}} = 2a$ to a W1 waveguide. The spectrum has been obtained with the single-QNM approximation in Eq. (5.15) (solid black), with the Lorentzian fit in Eq. (5.17) (dashed red) and with numerically exact 2D FMM-Bloch mode-dipole computations (blue circles). The right inset shows the relative error for the QNM approximation (black) and the Lorentzian fit (red). Reprinted with permission from [174]. Copyright (2015) Optical Society of America.

shows the relative errors as function of frequency. Close to the QNM frequency, both approximations provide small errors below 1%, and while the error from the Lorentzian curve quickly increases away from the resonance, the error from the rigorous expression in Eq. (5.7) remains below 1% in most of the considered spectral range. This demonstrates the power of the QNM approach for obtaining accurate LDOS approximations, as also seen in resonators coupled to homogeneous media [125, 149, 150, 152].

5.7 Example: Two side-coupled cavities

As a second and more advanced example, we consider the same structure as above, but now add in an additional side-coupled cavity at a distance $d_{\mathrm{cav}} = 3a$ from the waveguide and a distance $d_{\mathrm{W1}} = 4a$ along the waveguide from the initial cavity. This structure supports two QNMs in the spectral range of interest, called M1 and M2, whose electric field magnitudes ($|E_y|$) are shown in Fig. 5.8 where the leakage into the W1 waveguide is clearly visible. The complex QNM frequencies are given in Table 5.2, and the two QNMs are offset by approximately 5 nm, while the Q factor for M2 is approximately an order of magnitude larger than that for M1. Since the two QNMs lie relatively close spectrally, and since each QNM has a non-negligible field strength in the adjacent cavity, it is natural to expect that they will both play a role in the QNM-approximated LDOS spectrum.

Using the normalization procedure from Section 5.5 for both QNMs,[5] we find the

[5]But with different contributions from the two semi-infinite waveguide, $I^+_{\mathrm{wg}} \neq I^-_{\mathrm{wg}}$, for each QNM.

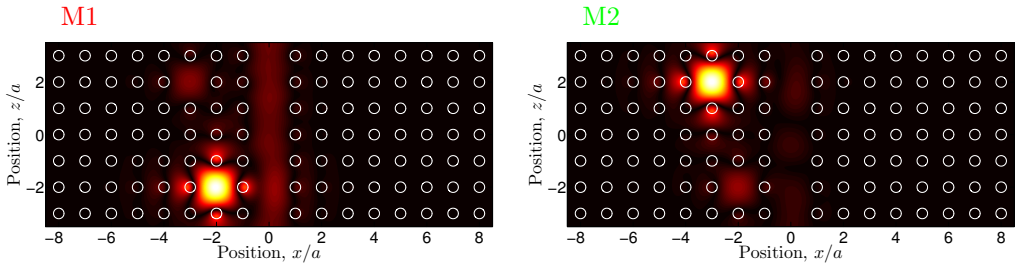

Figure 5.8 Electric field magnitudes ($|E_y|$) of two QNMs, M1 and M2, for a 2D PhC with two cavities side-coupled to an extended W1 waveguide. Reprinted with permission from [174]. Copyright (2015) Optical Society of America.

QNM	ω_μ $[2\pi c/a]$	γ_μ $[2\pi c/a]$	Q
M1	0.397	0.0013	$1.5 \cdot 10^2$
M2	0.395	0.00020	$9.9 \cdot 10^2$

Table 5.2 QNM frequencies, $\tilde{\omega}_\mu = \omega_\mu - \mathrm{i}\gamma_\mu$, and Q factors for two cavities side-coupled to a W1 waveguide structure, with cavity-W1 distances $d_{\mathrm{cav}} = 2a$ and $3a$ and separated a distance of $d_{\mathrm{W1}} = 4a$ along the length of the waveguide. The associated QNM field distributions are shown in Fig. 5.8.

following complex QNM mode areas

$$a_{\mathrm{M1}} = \frac{\langle \mathbf{f}_{\mathrm{M1}} \,|\, \mathbf{f}_{\mathrm{M1}} \rangle}{\epsilon(\mathbf{r}_{\mathrm{D}}) \left[\mathbf{E}_{\mathrm{M1}}(\mathbf{r}_{\mathrm{D}}) \cdot \mathbf{y}\right]^2} = (1.388 - 0.026\mathrm{i})\, a^2, \tag{5.18a}$$

$$a_{\mathrm{M2}} = \frac{\langle \mathbf{f}_{\mathrm{M2}} \,|\, \mathbf{f}_{\mathrm{M2}} \rangle}{\epsilon(\mathbf{r}_{\mathrm{D}}) \left[\mathbf{E}_{\mathrm{M2}}(\mathbf{r}_{\mathrm{D}}) \cdot \mathbf{y}\right]^2} = -(28.7 + 12.5\mathrm{i})\, a^2, \tag{5.18b}$$

where $\mathbf{r}_{\mathrm{D}}$ is at the field maximum of QNM M1, in the center of the associated cavity (indicated in the left inset in Fig. 5.9). For both mode areas, the fields are evaluated at the same position, and the emitter is thus spatially offset from the M2 field maximum. We note that for M1 the real part of the complex mode area again dominates and is positive, while for M2 the real and imaginary parts are of the same order of magnitude and both negative. Also, we find that $|\langle \mathbf{f}_{\mathrm{M1}} \,|\, \mathbf{f}_{\mathrm{M2}} \rangle| / |\langle \mathbf{f}_{\mathrm{M1}} \,|\, \mathbf{f}_{\mathrm{M1}} \rangle| \simeq 10^{-6}$, i.e., QNMs M1 and M2 are orthogonal under the inner product from [169].

Using the complex mode areas, we may approximate the LDOS by retaining QNM M1 (dashed red), QNM M2 (dotted green) or QNMs M1+M2 (solid black) in a sum over the single-QNM contribution (Eq. (5.15)) as shown in Fig. 5.9. Blue circles again show the numerically exact LDOS enhancement that features a Lorentzian-like peak close to the M1 QNM frequency and a dip close to the M2 QNM frequency. The approximation with only M2 included (dotted green) is negative in a large part of the spectrum, which arises from the negative real and imaginary parts of a_{M2}. Furthermore, while the first term in the curled brackets in Eq. (5.15) remains negative in the entire spectrum, the second term changes sign at ω_{M2}, causing the asymmetric lineshape. The approximation with only QNM M1 (dashed red), for which $a_{\mathrm{M1}}$is dominated by its real part, approximates the peak fairly well, but does not capture the dip close to the M2 frequency. In turn, by including

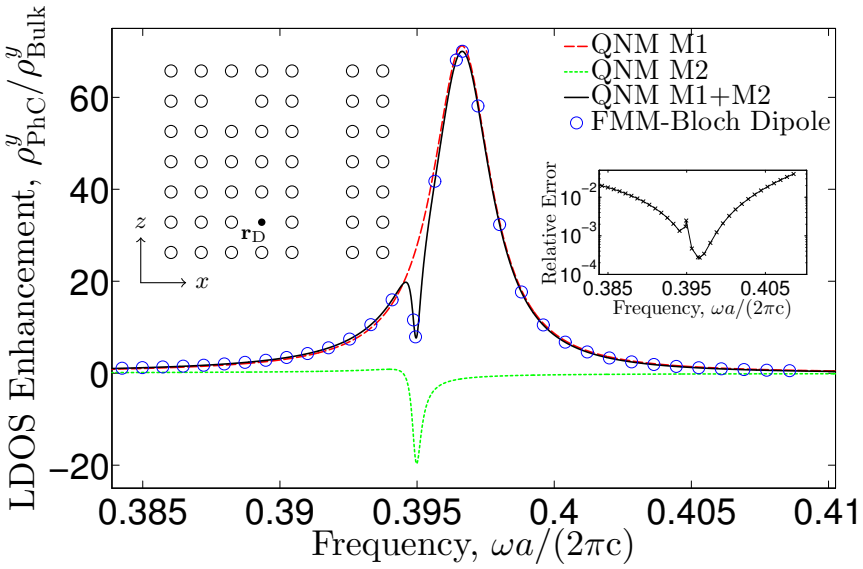

Figure 5.9 Spectrum of LDOS enhancement for a y-oriented dipole, $\rho^y_{\mathrm{PhC}}/\rho^y_{\mathrm{Bulk}}$, for the two-cavity configuration in Fig. 5.8 that also shows field profiles of the two QNMs, M1 and M2. The dipole is positioned in the center of the bottom PhC cavity, $\mathbf{r}_{\mathrm{D}} = (-2, 0, -2)a$. The spectrum is approximated with a sum over single-QNM terms (Eq. (5.15)) with the dashed red (dotted green) [solid black] curve obtained with QNM M1 (M2) [M1+M2] included, while numerically exact 2D FMM-Bloch mode-dipole computations are shown as blue circles. The inset shows the relative error for the QNM M1+M2 approximation. Reprinted with permission from [174]. Copyright (2015) Optical Society of America.

both M1 and M2 (solid black) both features are approximated very well. Close to the M2 frequency the emitter is spectrally (spatially) resonant, but spatially (spectrally) non-resonant with M2 (M1), and we here observe destructive interference between the M1 and M2 terms in the LDOS expansion, which, compared to the single-cavity situation (Fig. 5.7), lowers the LDOS enhancement. The inset shows that the M1+M2 relative error remains smaller than 1% in almost all of the considered spectral range, which demonstrates that also when more than one QNM is relevant, the semi-analytical QNM theory proposed here for coupled PhC cavity-waveguide structures is accurate and efficient.

5.8 Perturbation of cavity: Predicting the shift and broadening

As a final application of QNMs, we consider a permittivity change, $\Delta\epsilon(\mathbf{r})$, of the resonator and want to know the change of both the frequency and linewidth of the associated QNM. This can be obtained by recalculating the QNM of the perturbed system, but can also be predicted via perturbation theory according to which the first-order correction to the QNM frequency is given as [169]

$$\Delta\tilde{\omega}_\mu^{(1)} = -\frac{\tilde{\omega}_\mu}{2\,\langle \mathbf{f}_\mu \,|\, \mathbf{f}_\mu \rangle} \int_V \Delta\epsilon(\mathbf{r}) \mathbf{E}_\mu(\mathbf{r}) \cdot \mathbf{E}_\mu(\mathbf{r})\, \mathrm{d}\mathbf{r}. \tag{5.19}$$

Interestingly, this quantity is, in general, *complex* and therefore accounts for both the change of the QNM frequency ($\mathrm{Re}(\Delta\tilde{\omega}_\mu^{(1)})$) and the QNM linewidth ($\mathrm{Im}(\Delta\tilde{\omega}_\mu^{(1)})$).

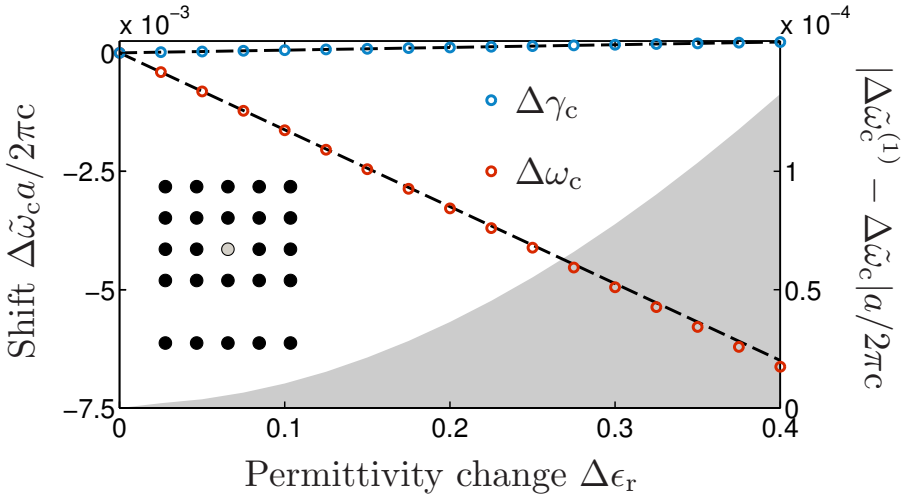

Figure 5.10 *Left axis:* Change of QNM frequency, $\Delta\tilde{\omega}_\mu = \Delta\omega_\mu - \mathrm{i}\Delta\gamma_\mu$, as function of permittivity change, $\Delta\epsilon$, of an additional rod inside the 2D PhC side-coupled cavity (gray in the inset). Data points have been obtained by numerical evaluation of QNMs of the perturbed system, while the dashed lines stem from first-order perturbation theory via Eq. (5.19). *Right axis:* Gray shading indicates the error of the first-order perturbation result of the QNM frequency change. Reprinted with permission from [169]. Copyright (2014) Optical Society of America.

As a specific example, we return to the single-cavity structure (with $d_{\mathrm{cav}} = 2a$) and consider a perturbation with an additional low-index rod inserted in the center of the cavity, shown in gray in the inset in Fig. 5.10. The data points in red (blue) are explicit calculations of the change in the real (negative imaginary) part of the QNM frequency under this perturbation, while the dashed lines are the corresponding data from Eq. (5.19), all related to the left axis. Gray shading shows the error in the perturbation theory estimate (right axis), and a good agreement even for relatively large index perturbations is observed. Finally, we note that for large-Q QNMs, the second-order correction to the linewidth, $\Delta\gamma_\mu$, is typically more important than the first-order correction [142].

5.9 Summary

We have given an overview of approaches for treating leaky resonators and have introduced the concept of quasi-normal modes, that are localized inside the resonator, but whose complex (and discrete) frequencies explicitly account for the leakage to the environment. We have focused on coupled photonic crystal cavity-waveguide structures, where, in the 2D examples considered here, the cavities are leaky due to coupling to the waveguide. We have outlined a semi-analytical quasi-normal mode theory for the local density of states in these structures, a theory that relies on access to the quasi-normal mode field profiles and complex frequencies. To address this, we have developed two computational techniques for obtaining quasi-normal modes in extended photonic crystal structures; one based on the Bloch mode expansion technique (Chapter 3) and one based on commercially available finite element method software (COMSOL Multiphysics). In both cases, a critical issue is to satisfy an outgoing wave boundary condition in the far field of the resonator, which we have proposed solutions for, and we have in a specific situation

validated that the two approaches give the same quasi-normal mode. We have shown that the quasi-normal mode field amplitudes diverge far away from the resonator, and we have devised a regularization technique for normalizing the quasi-normal modes, which relies on the Bloch mode form and the theory of divergent series. With a single side-coupled cavity, we have demonstrated that the scattering spectrum of the resonator can be reconstructed on the basis of only the quasi-normal complex frequency, and we have shown that the semi-analytical quasi-normal mode theory leads to a slightly asymmetric spectrum of the local density of states enhancement, consistent with numerically exact results. We have also shown that the Purcell factor, in this case where a single quasi-normal mode dominates, appears rigorously as the on-resonance local density of states enhancement. Next, we have considered a situation with two side-coupled cavities, and shown that the two associated quasi-normal modes, that exist spectrally within 5 nm, are orthogonal under the inner product that defines the quasi-normal normalization. We have then approximated the local density of states enhancement for an emitter inside one of the cavities with a summation over either or both of the quasi-normal modes, and the numerically exact spectrum with a dip and a peak is only well approximated when both quasi-normal mode contributions are included. We have, both with one and two side-coupled cavities, discussed the role of the complex quasi-normal mode areas on the local density of states spectra, and observed relative errors from the semi-analytical quasi-normal mode theory below 1% in the bandwidth of interest. Finally, we have presented a quasi-normal mode perturbation theory, that can be used for describing shape perturbations of the resonator. We have shown, for the single-cavity photonic crystal, that the theory predicts the correct first-order correction of both the quasi-normal mode frequency and linewidth.

Chapter 6

Fano resonances in photonic crystal cavity-waveguide structures

> *The universe is asymmetric and I am persuaded that life, as it is known to us, is a direct result of the asymmetry of the universe or of its indirect consequences. The universe is asymmetric.*
>
> Louis Pasteur

The implementation of on-chip optical communication systems relies, among other things, on the development of energy-efficient solutions, with < 10 fj/bit operation [6]. One important functionality is an optical switch that, loosely speaking, is a component, which in its on-state transmits an optical signal and in the off-state does not. One way to realize this is with a PhC cavity, whose transmission frequency can be controlled by tuning of the refractive index [175]. However, the required energy to shift the cavity resonance to obtain a large on-off switching contrast may be relatively large, and tailoring the transmission spectrum to exhibit sharp and asymmetric features could lower this energy requirement [176]. This idea was further developed by Heuck *et al.* [177], who proposed a PhC system with a single cavity side-coupled to a waveguide and with an additional scattering site to partially block the waveguide. This configuration may give rise to Fano resonances [178], with asymmetric transmission spectra, as also demonstrated experimentally [179]. Furthermore, by breaking the mirror symmetry of the structure around the cavity, which can be achieved by displacing the scattering site along the waveguide, the performance can be improved [180].

In this chapter, we investigate the impact of the position of the scattering site in the waveguide on the transmission through the system. In Section 6.1, we introduce

the structure we analyze, and in Section 6.2 we present simulations of the transmission spectrum, with the scattering site position being a parameter. In the general case, this numerical approach does not produce a simple explanation for the shape of the transmission spectrum, but in Section 6.3 we consider a limiting-case, where the full structure can be analyzed with a single-mode Fabry-Pérot (FP) model, and where the shape of the transmission spectrum is shown to be determined by the single-mode FP roundtrip phase at a single frequency.

All results and figures in this chapter are an "in progress" version of work that was later submitted for publication [181].

6.1 Structure

The structure we consider is similar to the coupled PhC cavity-waveguide structure from Chapter 5, where a single cavity is side-coupled to a single-mode waveguide. In Fig. 5.2, we observed that the reflection through this system is mostly very small, except when the cavity (or more precisely the QNM) resonance is approached; here, the side-coupled cavity turns into an efficient mirror in a narrow bandwidth, and the reflection (transmission) peaks (dips). The use of such a side-coupled PhC cavity as a highly dispersive mirror was recently proposed for realizing a high modulation speed laser [182]. In this chapter, to modify and control the transmission beyond the Lorentzian-like spectrum that the cavity gives rise, we add a partially transmitting element (PTE) in the waveguide at a variable distance, d, from the cavity. The left panel in Fig. 6.1 illustrates the full structure with air holes organized in triangular 2D PhC lattice in a high-index background (PhC 2 in Table 2.1). The line defect creates a W1 waveguide, and the cavity-waveguide distance is $d_{\text{cav}} = \sqrt{3}a$. The PTE is implemented as an additional air hole (of radius $r_{\text{PTE}}/r = 0.8$) in the middle of the waveguide and shifted the distance d along the waveguide from the cavity position ($d/a = 5$ in the left panel in Fig. 6.1).

As implied by its name, the PTE partially transmits (and partially reflects) incident light, and it thus acts as a second mirror. However, as opposed to the cavity it is to a very good approximation non-dispersive; the transmission and reflection over the PTE can be taken as a constant in the frequency range of interest [183]. The right panel in Fig. 6.1 illustrates the structure schematically, and in the language of Chapter 3 the structure consists of $W = 5$ periodic sections. As the cavity and the PTE may act as reflectors, the middle section ($w = 3$) may be thought of as a FP cavity, i.e., as an *additional* cavity. In the following section, we present transmission spectra for the full structure, which illustrates the crucial role played by the PTE distance, d.

6.2 Asymmetric transmission spectra

In Fig. 6.2, we show the power transmission of the guided Bloch mode through the full structure (i.e., from section $w = 1$ to section $w = W = 5$) for two values of the PTE distance; solid blue (dash-dotted red) is for $d/a = 0.32$ ($d/a = 0$). In both cases, the transmission exhibits a minimum at the frequency of the side-coupled cavity, ω_{cav}, which, as we return to in the next section, depends on the PTE distance, d. The coloring in Fig. 6.1 shows the field ($|H_y|$) at this transmission minimum, and as discussed in Section 5.2.1 this scattering field profile is highly reminiscent of the associated QNM field profile.

Away from the transmission minimum, where the single-cavity structure exhibits a symmetric Lorentzian spectrum (Fig. 5.2), we here observe asymmetric lineshapes; these

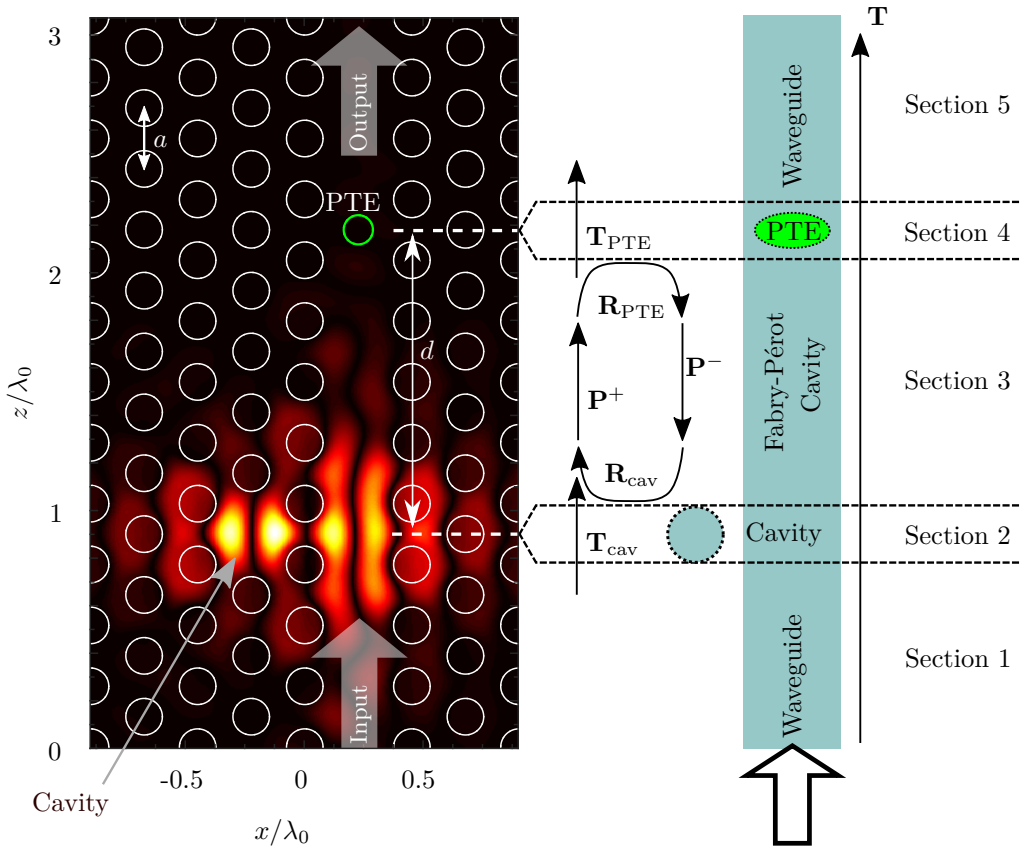

Figure 6.1 *Left panel:* Sketch of 2D PhC structure with a W1 waveguide, a side-coupled cavity, and a scattering site (PTE) in the middle of the waveguide, displaced a distance d from the cavity. Coloring shows the magnetic field ($|H_y|$) at the transmission minimum. *Right panel:* Schematic of the PhC structure in the left panel, with the periodic sections $w = 1, 2, 3, 4$ and 5 indicated in the right part. The transmission and roundtrip matrices appearing in Eqs. (6.1) are indicated schematically.

are the characteristic Fano lineshapes. We define the parity of such Fano spectra as the position of the minimum relative to the maximum, and $d = 0$ ($d/a = 0.32$) thus corresponds to red (blue) parity. More generally, the spectra will change from exhibiting red parity, to being symmetric (Lorentzian) to exhibiting blue parity, as d is varied, and the cause of this behavior has so far not been explained. In the general case, the transmission is one coefficient in the total transmission matrix that takes the form

$$\mathbf{T} = \mathbf{T}_{\mathrm{PTE}}\mathbf{P}^+ \left(\mathbf{I} - \mathbf{M}\right)^{-1} \mathbf{T}_{\mathrm{cav}}, \tag{6.1a}$$

$$\mathbf{M} \equiv \mathbf{R}_{\mathrm{cav}}\mathbf{P}^-\mathbf{R}_{\mathrm{PTE}}\mathbf{P}^+, \tag{6.1b}$$

where $\mathbf{T}_{\mathrm{cav}}$ ($\mathbf{T}_{\mathrm{PTE}}$) is the Bloch mode S-matrix from the input waveguide to the FP section (from the FP section to the output waveguide), i.e., $\mathbf{ST}^{1,3}$ ($\mathbf{ST}^{3,5}$) in the language of Section 3.3. The matrix $\mathbf{M}$ is the roundtrip matrix, indicated schematically in the right panel of Fig. 6.1, that we also encountered in Chapters 3 and 5. In the general case, where many Bloch modes contribute, the matrices in Eqs. (6.1) are computed numerically, which

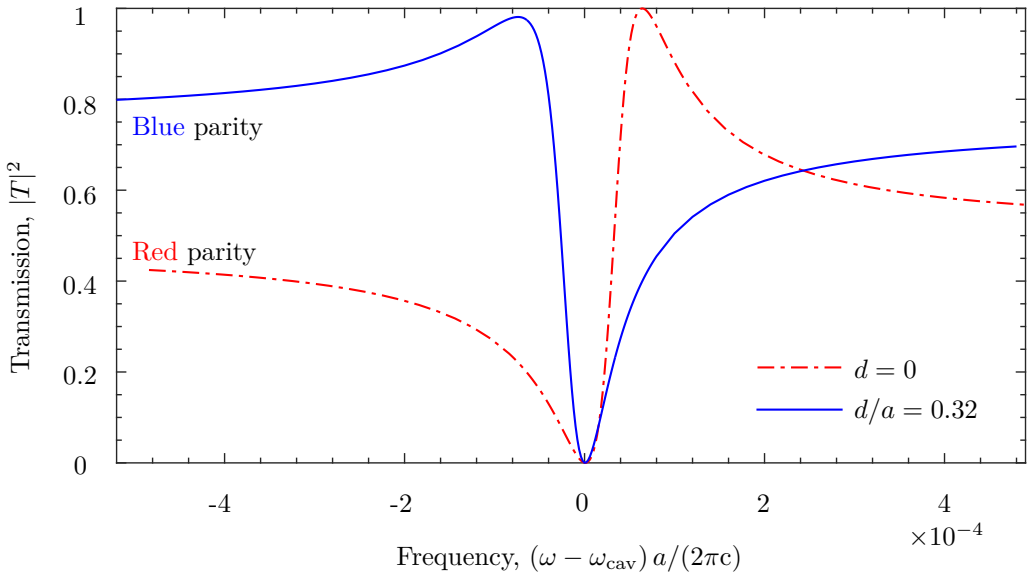

Figure 6.2 Power transmission spectra of the waveguide mode through the structure introduced in Fig. 6.1 with the PTE distance, d, as a parameter.

produces transmission spectra as those in Fig. 6.2. However, this numerical procedure does not lead to a simple explanation for the shape of the transmission spectra as function of d. In the following section, we consider a limiting case where the shape of the spectra can be correlated with a single quantity, the FP roundtrip phase of a single Bloch mode.

6.3 Single-mode Fabry-Pérot model

As the PhC waveguide is single-moded in the spectral range of interest, the full set of Bloch modes in these sections ($w = 1, 3$ and 5 in Fig. 6.1) consists of a single propagating Bloch mode and a large number of evanescent Bloch modes. The elements in the Bloch mode propagation matrices in Eqs. (6.1), $\mathbf{P}^+$ and $\mathbf{P}^+$, are functions of the length of the FP section, and in particular the elements corresponding to the evanescent modes decrease exponentially with d. Thus, for sufficiently large values of d, the *multi-mode matrices* in Eqs. (6.1) can, to a good approximation, be replaced by a *single-mode scalar* equation

$$T = T_{\mathrm{PTE}} P^+ \left(1 - M\right)^{-1} T_{\mathrm{cav}}, \tag{6.2a}$$

$$M \equiv R_{\mathrm{cav}} P^- R_{\mathrm{PTE}} P^+, \tag{6.2b}$$

where all scalar coefficients are for the propagating waveguide mode and taken as single coefficients from the multi-mode matrices introduced in Eqs. (6.1).

In Fig. 6.3, we show the transmission spectra at four PTE distances. Solid curves stem from the numerically exact approach [Eqs. (6.1)], while dash-dotted curves are results from the approximate single-mode model [Eqs. (6.2)]. At the smallest distances (top panel), the single-mode model predicts the correct parity, but otherwise deviates visibly from the numerically exact spectra, e.g. with a clear offset on the spectral position of

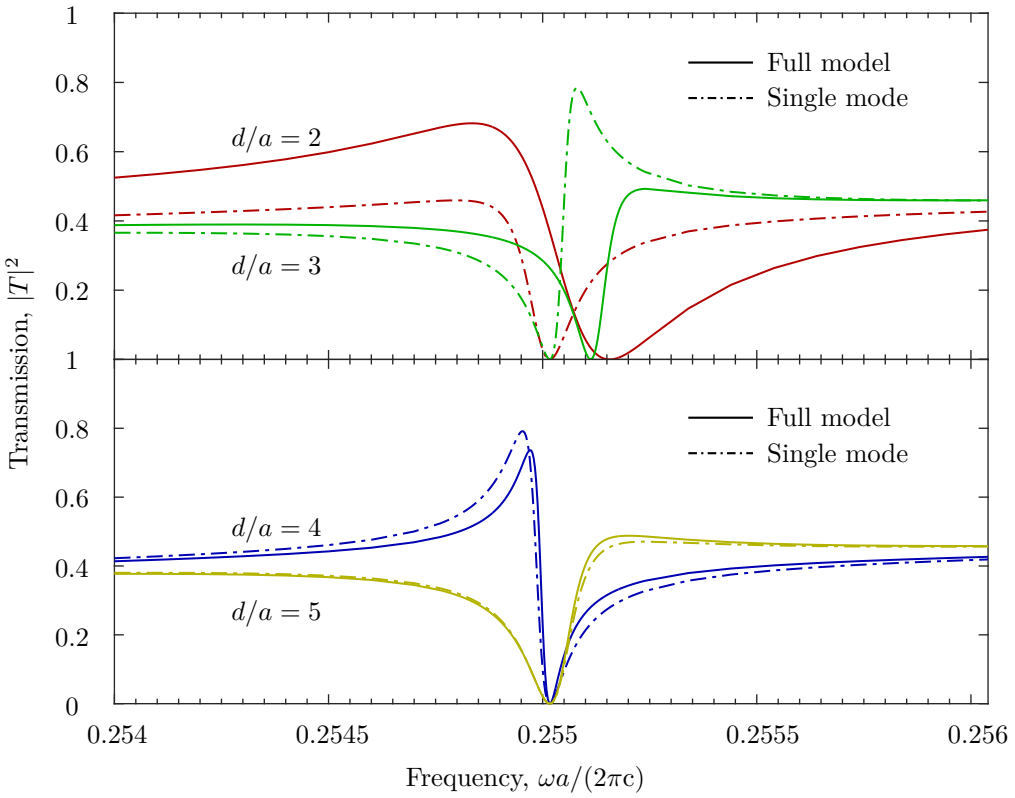

Figure 6.3 Power transmission spectra as in Fig. 6.2, with the PTE distance as a parameter. Solid (dash-dotted) curves are obtained from the numerically exact Eqs. (6.1) (the approximate single-mode model in Eqs. (6.2)).

the transmission minimum. As the distance is increased to $d/a = 4$ (bottom panel, blue curves), the agreement between the numerically exact and the single-mode model becomes substantially better, and at the largest distance considered here, $d/a = 5$, (bottom panel, yellow curves) the agreement is almost perfect. Thus, as also found with similar single-waveguide mode FP descriptions of PhC cavities [26, 63], the single-mode description of the structure appears valid when $d/a \gtrsim 4$.

To shed more light on the transmission in this FP limit, we express the power transmission as the magnitude squared of the field transmission in Eq. (6.2a) as follows

$$|T|^2 = \frac{|T_{\rm PTE}|^2|T_{\rm cav}|^2}{1+|R_{\rm PTE}|^2|R_{\rm cav}|^2-2|R_{\rm PTE}||R_{\rm cav}|\cos\left(\Phi_{\rm RT}\right)}, \tag{6.3a}$$

$$\Phi_{\rm RT} \equiv 2k_z d + \phi_{\rm PTE} + \phi_{\rm cav} \tag{6.3b}$$

where $R_{\rm cav} = |R_{\rm cav}|\exp(\mathrm{i}\phi_{\rm cav})$ and $R_{\rm PTE} = |R_{\rm PTE}|\exp(\mathrm{i}\phi_{\rm PTE})$, and where k_z is the waveguide mode wave number. The transmission function in Eqs. (6.3) is of the well-known FP-form [184], however with all elements, both amplitudes and phases, depending on frequency. For instance, the cavity reflection (transmission) amplitude, $|R_{\rm cav}|$ ($|T_{\rm cav}|$) increases (decreases) dramatically as the cavity frequency is approached, and the total transmission minimum occurs when $|T_{\rm cav}|$ is at a minimum. Similarly, the total trans-

mission maximum occurs when the FP-cavity is on resonance, which happens when $\cos(\Phi_{\mathrm{RT}}) = 1$, i.e., when

$$2k_z d + \phi_{\mathrm{PTE}} + \phi_{\mathrm{cav}} = 2\pi n, \qquad n = 0, 1, 2, \ldots. \tag{6.4}$$

For small values of the PTE distance, the spectral position of the cavity resonance will be disturbed by the PTE (as can, for example, be predicted with the QNM perturbation theory in Section 5.8), but at larger distances that we focus on here, the cavity resonance, i.e., the spectral position of the total transmission minimum, will be approximately constant with d. Thus, the parity of the total transmission spectrum is determined by the spectral position of the transmission maximum that occurs when Eq. (6.4) is satisfied. At a given value of d, this relation is satisfied at a given frequency that can be blue- or redshifted from the cavity resonance, which produces asymmetric transmission spectra, or that can fall on top of the cavity resonance, which gives a symmetric (Lorentzian) spectrum. In addition to the dispersive wave number, $k_z \equiv k_z(\omega)$, the reflection phases, especially ϕ_{cav}, also depend on frequency in Eq. (6.4), which complicates a further analytical treatment.

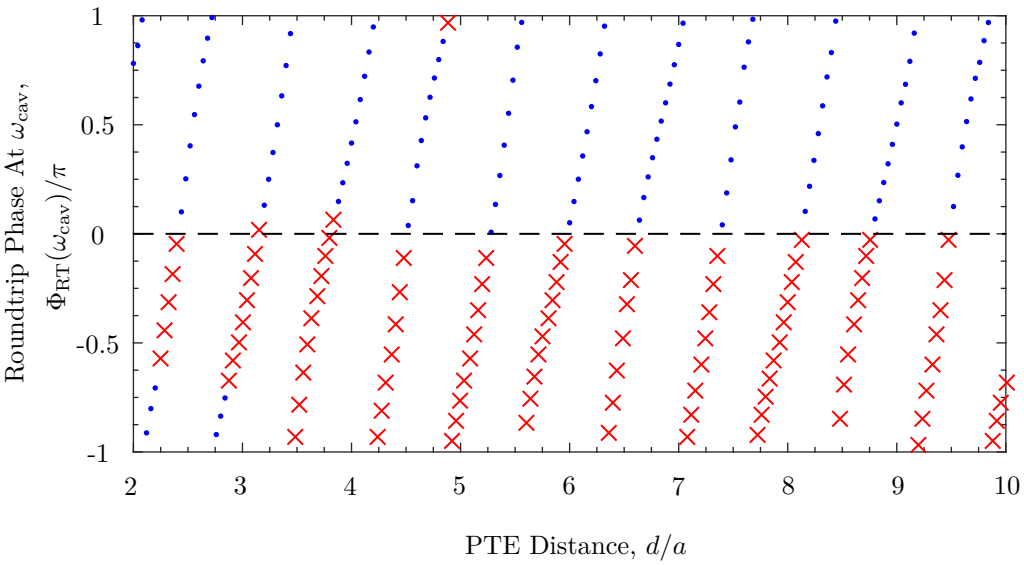

Figure 6.4 Single-mode roundtrip phase [Eq. (6.3b)] at the minimum transmission frequency, $\Phi_{\mathrm{RT}}(\omega_{\mathrm{cav}})$, as function PTE distance, d, for the structure introduced in Fig. 6.1. Each marker has in addition been colored as a red cross (blue dot) when the numerically exact spectrum, obtained from Eqs. (6.1), exhibits red (blue) parity.

In Fig. 6.4, we show the roundtrip phase at the cavity frequency, $\Phi_{\mathrm{RT}}(\omega_{\mathrm{cav}})$, as function of the PTE distance, d; these are indicated by markers. In addition, at each distance the parity from the numerically exact spectrum has been retrieved, and red cross (blue circle) markers correspond to red (blue) parity in these numerically exact spectra. As soon as we get into the regime where the single-mode description is valid, $d/a \gtrsim 4$, the parity of the exact spectrum and the roundtrip phase at ω_{cav} correlate; when the phase is > 0 (< 0) the parity is blue (red), and the transition from one parity to the other, i.e., a Lorentzian spectrum, occurs exactly when $\Phi_{\mathrm{RT}}(\omega_{\mathrm{cav}}) = 0, \pm\pi$. Thus, when

the single-mode description is valid, the parity of the transmission spectrum appears to be fully determined by the roundtrip phase evaluated at the single frequency ω_{cav}.

6.4 Summary

We have investigated the transmission through a 2D photonic crystal consisting of a single-mode W1 waveguide with a side-coupled cavity and an additional scattering site in the middle of the waveguide. We have, by means of numerical simulations, illustrated that the shape of the transmission spectrum can be controlled by varying the distance between the side-coupled cavity and the scattering site, d. In particular, the spectrum may be symmetric (Lorentzian) or asymmetric (Fano), and the spectra in general vary continuously with d from being Fano shaped with red parity, to being Lorentzian to being Fano shaped with blue parity, where red (blue) parity corresponds to red (blue) detuning of the transmission minimum relative to the corresponding maximum. In the limit of a distance of $d/a \gtrsim 4$, where a is the photonic crystal lattice constant, we have shown that a single-mode description, where the region between the cavity and the scattering site becomes a Fabry-Pérot-like cavity, reproduces the numerically exact transmission spectrum remarkably well. Finally, we have shown that the single-mode Fabry-Pérot roundtrip phase, evaluated at the frequency of the transmission minimum, directly correlates with the parity of the spectrum; when this phase is > 0 (< 0) the parity is blue (red), and when the phase is zero or $\pm\pi$ the spectrum is Lorentzian.

CHAPTER 7

Optical amplification in slow light photonic crystal waveguides

> *If you take a bale of hay and tie it to the tail of a mule and then strike a match and set the bale of hay on fire, and if you then compare the energy expended shortly thereafter by the mule with the energy expended by yourself in the striking of the match, you will understand the concept of amplification.*
>
> William Shockley

In the scope of realizing integrated optical circuits, PhCs have been proposed as a practical platform [5], with important functionality including all-optical switches, optical memories, electro-optic modulators, photo-detectors and lasers [6]. When interfacing several such devices, propagation and coupling losses inevitably arise, and to compensate these losses optical amplifiers become indispensable. As discussed by Dowling *et al.* in the context of lasers [185], high group indices in PhC waveguides enhance the light-matter coupling in these systems, which makes slow light PhC waveguides a promising candidate for compact optical amplifiers. Recently, slow light enhanced optical gain in PhC waveguides was demonstrated experimentally [186].

In this chapter, we investigate optical amplification in slow light PhC waveguides theoretically. We consider a finite-length active PhC W1 waveguide embedded in an otherwise passive PhC W1 structure and analyze the effect of both the length of the active section and the material gain. Fig. 7.1(a) displays a sketch of the structure, where red (gray) color indicates the active (passive) semiconductor, and where the ratio of the transmitted signal to the input signal gives the effective amplification of the structure. In

Section 7.1, we present a coupled Bloch mode model, where guided Bloch modes of the passive PhC waveguide are used as an expansion basis, and where material gain/loss is represented as an imaginary refractive index perturbation that gives rise to distributed feedback between the counter propagating passive Bloch modes. Such feedback has so far been neglected in the description of slow light enhanced gain [186, 187], and we show here that for sufficiently large material gain, this feedback in fact dominates the properties of the amplifier. In Section 7.2.1 (Section 7.2.2), we investigate the behavior of a slow light 2D PhC waveguide amplifier with a relatively long (short) active section and at relatively low (high) material gain/loss. Results from the semi-analytical coupled Bloch model are compared with numerically exact FMM (FEM) simulations, where the exact Bloch modes of both passive and active PhC waveguide sections are employed, and where the amplifier properties stem largely from reflection at active-passive section interfaces, with a FP-like behavior.

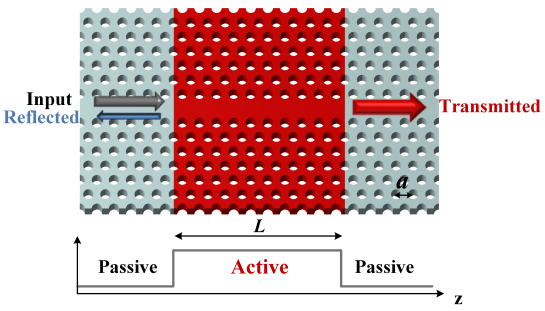

(a) Sketch of W1 PhC waveguide consisting of a passive (gray), an active (red) and a passive (gray) section. The active section has a finite length, L, and the input, reflected and transmitted signals are indicated.

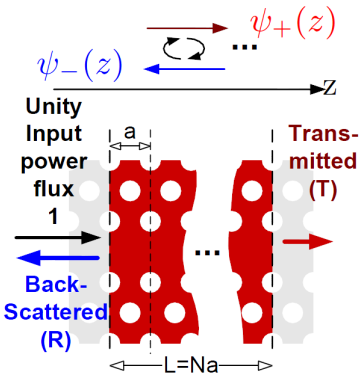

(b) Schematic of PhC structure in panel (a), where the DFB in the active region (red) between the counter propagating passive section Bloch modes is indicated in the top part.

Figure 7.1 Illustrations of PhC waveguide optical amplifier. Reprinted with permission from [188]. Copyright (2015) American Physical Society.

7.1 Coupled Bloch mode model

In the passive PhC waveguide, with permittivity profile $\epsilon_{\mathrm{B}}(\mathbf{r})$, we express the electric and magnetic field of the guided Bloch modes as follows

$$\mathbf{E}_{\mathrm{B},\pm} = \frac{1}{2}\mathbf{e}_{\pm}(\mathbf{r}_{\perp}, z)\exp(\pm \mathrm{i}k_z z), \tag{7.1a}$$

$$\mathbf{H}_{\mathrm{B},\pm} = \frac{1}{2}\mathbf{h}_{\pm}(\mathbf{r}_{\perp}, z)\exp(\pm \mathrm{i}k_z z), \tag{7.1b}$$

where $[\mathbf{e}_{\pm}, \mathbf{h}_{\pm}]$ are the complex amplitude Bloch functions, and where subscript $+$ $(-)$ refers to propagation along $+z$ $(-z)$. The above fields are individually solutions of Maxwell's equations in the passive waveguides, and in the following we use them as an expansion basis in the active PhC waveguide. To that end, we write the fields in the

active PhC waveguide as

$$\mathbf{E} = \psi_+(z)\mathbf{E}_{\mathrm{B},+} + \psi_-(z)\mathbf{E}_{\mathrm{B},-}, \tag{7.2a}$$

$$\mathbf{H} = \psi_+(z)\mathbf{H}_{\mathrm{B},+} + \psi_-(z)\mathbf{H}_{\mathrm{B},-} \tag{7.2b}$$

where $\psi_\pm(z)$ are slowly varying amplitudes to be determined. By use of the Lorentz reciprocity theorem, it is possible to derive a set of coupled differential equations for these amplitudes (see details in [188]) that read as follows

$$\partial_z\psi_+ = \frac{\mathrm{i}\omega}{\mathrm{c}} n_{\mathrm{G}}\chi_{\mathrm{pert}}(n_{\mathrm{i}}) \left[\delta(z)\psi_+ + \kappa^*(z)\exp(-2\mathrm{i}k_z z)\psi_-\right], \tag{7.3a}$$

$$\partial_z\psi_- = -\frac{\mathrm{i}\omega}{\mathrm{c}} n_{\mathrm{G}}\chi_{\mathrm{pert}}(n_{\mathrm{i}}) \left[\delta(z)\psi_- + \kappa(z)\exp(2\mathrm{i}k_z z)\psi_+\right], \tag{7.3b}$$

where n_{G} is the group index of the passive PhC waveguide Bloch mode at frequency ω. The susceptibility perturbation due to material gain or loss in the active PhC waveguide section is $\chi_{\mathrm{pert}}(n_{\mathrm{i}}) = -n_{\mathrm{i}}^2 + \mathrm{i}2n_{\mathrm{s}}n_{\mathrm{i}}$, with n_{s} being the passive semiconductor refractive index, and n_{i} the imaginary perturbation. The coefficients $\delta(z)$ and $\kappa(z)$ are given by

$$\delta(z) = \frac{a\int_S \epsilon_0 F(\mathbf{r})|\mathbf{e}|^2\,\mathrm{d}S}{\int_{\mathrm{uc}}\left[\epsilon_0\epsilon_{\mathrm{B}}(\mathbf{r})|\mathbf{e}|^2 + \mu_0|\mathbf{h}|^2\right]\,\mathrm{d}V}, \tag{7.3c}$$

$$\kappa(z) = \frac{a\int_S \epsilon_0 F(\mathbf{r})\mathbf{e}\cdot\mathbf{e}\,\mathrm{d}S}{\int_{\mathrm{uc}}\left[\epsilon_0\epsilon_{\mathrm{B}}(\mathbf{r})|\mathbf{e}|^2 + \mu_0|\mathbf{h}|^2\right]\,\mathrm{d}V}, \tag{7.3d}$$

where volume integrals are taken over one unit cell, and where S is the transverse (xy) plane at position z, and where $F(\mathbf{r}) = 1$ ($= 0$) in the active (passive) region. Importantly, the coefficient $\kappa(z)$ couples the forward and backward propagating passive Bloch modes that consequently experience *distributed feedback* (DFB) upon propagation through the active PhC waveguide section. This distributed back-coupling is illustrated in the top part of Fig. 7.1(b). In the passive PhC waveguide, $\delta(z) = \kappa(z) = 0$, and the z derivatives of ψ_+ and ψ_- [Eqs. (7.3a)-(7.3b)] vanish, making these amplitudes constant with z; $\mathbf{E}_{\mathrm{B},\pm}$ are unidirectional solutions in the passive waveguide, as expected. If we neglect back-coupling, as done, for example, in the analysis in [186, 187], we obtain the ideal slow light gain of the amplifier (see derivation in Appendix E.1)

$$T_{\mathrm{Ideal}} = \exp\left(\Gamma\frac{n_{\mathrm{G}}}{n_{\mathrm{s}}}g_0 L\right), \tag{7.4}$$

where $g_0 = -2n_{\mathrm{i}}\omega/c$ is the bare material gain, and where Γ is a generalized confinement factor, defined in Eq. (E.3b). Finally, the coupled equations must be supplemented by BCs at passive-active interfaces that read as follows [189]

$$\psi_+(0) = r_1\psi_-(0) + \psi_0, \tag{7.5a}$$

$$\psi_-(L)\exp(-\mathrm{i}k_z L) = r_2\psi_+(L)\exp(\mathrm{i}k_z L), \tag{7.5b}$$

where ψ_0 is the amplitude of the incident field at $z = 0$ (left passive-active interface in Fig. 7.1(a)), while r_1 (r_2) is the passive-active reflection coefficient for the left (right) passive-active interface. In the investigations in the following sections, we set $r_1 = r_2 = 0$.

The coupled equations in Eqs. (7.3) are similar to those originally developed by Kogelnik and Shank for DFB lasers [190] (that have also been employed for PhC waveguide structures [191]). But in that case the expansion basis was *plane* waves, while we here

present a coupled mode model in a basis of *Bloch* waves, i.e., the exact solutions in the passive PhC waveguide. Our approach is similar to that in [57], where Bloch mode scattering due to structural disorder in the PhC waveguide is analyzed, and combining that with the coupled Bloch mode amplifier analysis presented here would be a natural extension for accurate analysis of practical slow light PhC waveguide amplifiers [186].

7.2 Photonic crystal waveguide amplifiers

For the specific examples, we consider a 2D PhC with a triangular lattice of air holes in a semiconductor background (PhC 3 in Table 2.1). We introduce a W1 waveguide by removing one row of holes along z, and the passive waveguide supports a guided mode with dispersion and group index as shown in panels (a) and (b) in Fig. 7.3. Intuitively, the gain/loss of the amplifier may be thought to be determined by the product $g_0 L$, and we investigate two situations: A relatively long (short) amplifier with a relatively small (large) gain/loss in Section 7.2.1 (Section 7.2.2).

7.2.1 Long amplifier, low material gain/loss

In this section, we consider a relatively long amplifier, $L/a = 100$, and relatively low material gain/loss ($|n_\mathrm{i}| < 0.02$). We focus on a single frequency, $\omega a/(2\pi \mathrm{c}) = 0.2064$, at which the passive guided Bloch mode has a group index of $n_\mathrm{G} = 25$, and in the following investigate the reflection and transmission as function of the material gain or loss, which is controlled via n_i. Long structures are challenging to handle computationally with spatial discretization techniques like FDTD and FEM, while as discussed in Chapter 3 the FMM-Bloch mode expansion techniques is convenient as we only need to analyze a single supercell of length a in the passive and active parts of the structure. Thus, in this case we compare results from the semi-analytical coupled Bloch mode model with numerically exact FMM-Bloch mode computations.

In Fig. 7.2, the reflection (dash-dotted blue) and transmission (solid red) as function of $-n_\mathrm{i}$ are shown, where $-n_\mathrm{i} < 0$ ($-n_\mathrm{i} > 0$) corresponds to material loss (gain). In the figure, curves are data from the coupled Bloch mode model, while markers are the numerically exact FMM-Bloch mode computation data. The ideal transmission without DFB [Eq. (7.4)] is included as the dashed black curve. We note that the simple model agrees well with the numerically exact data and picks up all features in both the transmission and reflection. Also, the ideal slow light gain predicts the correct behavior up to values of approximately 25 dB, i.e., until this level of amplification is reached, the DFB due to the gain perturbation is essentially negligible. In the gain regime ($-n_\mathrm{i} > 0$), both the reflection and transmission increase until $-n_\mathrm{i} \simeq 0.005$, after which they both start to decrease, however with the transmission decreasing most substantially and eventually converting the structure from an amplifier to a damper ($T_\mathrm{dB} < 0$).

The agreement between the coupled Bloch mode and the numerically exact FMM-Bloch mode results suggests that either approach is correct for understanding and analyzing the slow light PhC waveguide amplifier. In the former approach, the Bloch modes of the passive PhC waveguide are used as an expansion basis, and as these are not individually solutions of Maxwell's equations when $n_\mathrm{i} \neq 0$, they couple to each other upon propagation through the active waveguide with a local feedback strength of $\kappa(z)$. Eventually this DFB starts to dominate, which gives rise to the large reflection and low transmission. In the latter approach, the Bloch modes of the active PhC waveguide are used as an expansion basis, and since these are solutions of the perturbed structure, they propagate through

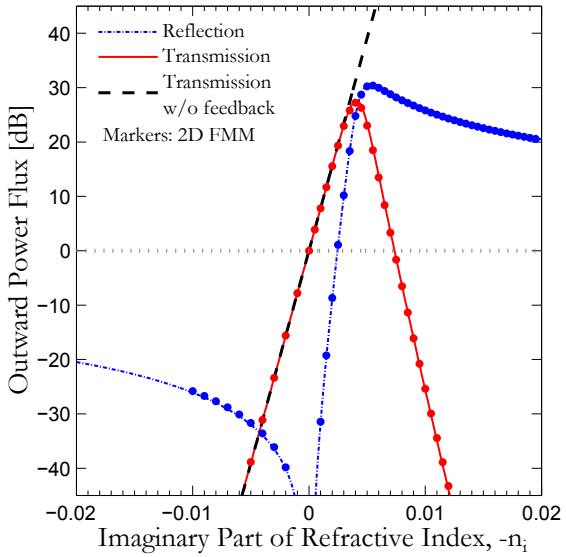

Figure 7.2 Power reflection (dash-dotted blue) and transmission (solid red) for the PhC structure in Fig. 7.1(a) as function of the imaginary part of the refractive index in the active section, $-n_{\mathrm{i}}$, with active length $L/a = 100$. The frequency is $\omega a/(2\pi \mathrm{c}) = 0.2064$ with an associated passive waveguide group index of $n_{\mathrm{G}} = 25$ (see panels (a) and (b) in Fig. 7.3). Curves are data from the coupled Bloch mode model, Eqs. (7.3), while markers stem from numerically exact FMM-Bloch mode simulations. Reprinted with permission from [188]. Copyright (2015) American Physical Society.

the active waveguide section without any back-coupling. In turn, at the active-passive interfaces a finite reflection occurs due to the mismatch between the active and passive Bloch mode field profiles, which gives a FP-like behavior of the amplifier in this picture. The equivalence between the two approaches was pointed out by Yariv and Gover [192] in a simpler system, and in their words "the problem of coupling and where it takes place is semantic. It depends on which set of (complete orthonormal) functions one chooses to expand the *total* field".

Using the coupled Bloch mode approach, we in panels (c) and (d) in Fig. 7.3 show contour maps of the transmission and reflection as function of $-n_{\mathrm{i}} > 0$ (material gain) and frequency. At all frequencies, both transmission and reflection increase with material gain, reach a maximum and then start to decrease, and the larger the group index, the smaller the material gain has to be before the amplifier turns into a damper. Additionally, at certain discrete frequencies the transmission and reflection diverge (red circular regions), which corresponds to lasing in the active PhC waveguide. This occurs at frequencies that satisfy the following phase condition

$$\left[\frac{\pi}{a} - \mathrm{Re}\,(k_z)\right] 2L = 2\pi m, \qquad m = \text{integer}, \tag{7.6}$$

and at values of $-n_{\mathrm{i}}$ where the gain exactly compensates the mirror losses. These observations are similar to those of Kogelnik and Shank for DFB lasers [190].

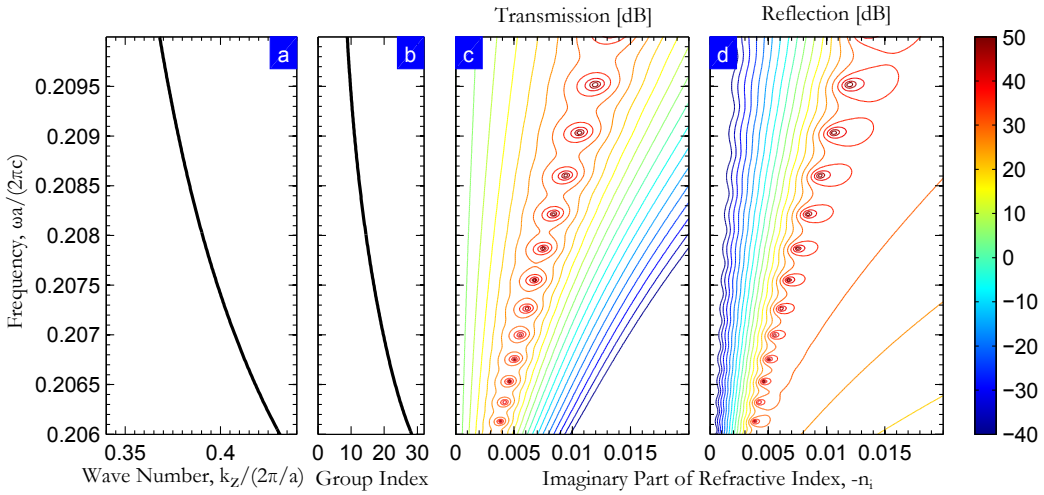

Figure 7.3 *Panels (a) and (b):* Dispersion and group index of guided Bloch mode in passive (2D) PhC W1 waveguide. The PhC consists of a triangular lattice of air holes in a semiconductor background (PhC 3 in Table 2.1). *Panels (c) and (d):* Contour maps of the transmission and reflection for the PhC amplifier in Fig. 7.1 with $L/a = 100$, as function of $-n_\mathrm{i}$ and frequency. Reprinted with permission from [188]. Copyright (2015) American Physical Society.

7.2.2 Short amplifier, high material gain/loss

As a second example, we consider a shorter PhC waveguide amplifier with an active section of length $L/a = 20$, and focus on the frequency $\omega a/(2\pi \mathrm{c}) = 0.2075$ at which the passive waveguide group index is $n_\mathrm{G} = 18.7$. For this shorter structure, it becomes feasible to solve the problem numerically with a spatial discretization technique, and we in this case compare the approximate coupled Bloch mode model to FEM simulations [193, 194].

In Fig. 7.4, we show the reflection (dash-dotted blue) and transmission (solid red) as function of $-n_\mathrm{i}$. Again, curves are data from the coupled Bloch mode model, markers are numerically exact FEM simulation data, and the black dashed curve is the ideal transmission without DFB [Eq. (7.4)]. The left (right) panel shows the data with both material gain and loss and in dB (with material gain and in linear units).

Focusing on the left panel, we observe a similar behavior as for the longer amplifier at the smallest material gain/loss levels ($|n_\mathrm{i}| < 0.02$), and in particular also a reasonable agreement between the coupled Bloch mode model and the numerically exact data. If we select the PhC lattice constant such that $\omega a/(2\pi \mathrm{c}) = 0.2075$ corresponds to the telecom wavelength $\lambda_0 = 1550\,\mathrm{nm}$, then $-n_\mathrm{i} = 0.02$ corresponds to a material gain of $g_0 \simeq 1600$ cm^{-1}. Up to this level of material gain, the coupled Bloch mode model provides a good description of the PhC waveguide amplifier. At larger material gain or loss, the coupled Bloch mode model starts to deviate from the numerically exact data, which is caused by a modification of the underlying dispersion curve. As analyzed in [195], the group index in fact starts to decrease when material gain or loss is increased, which is captured by the fully numerical approaches, but not by the coupled Bloch mode model that employs a constant group index obtained from the passive PhC waveguide. If this group index was replaced by a material gain/loss dependent group index, the validity of the coupled Bloch mode model could possibly be extended to a larger range of material gain or loss.

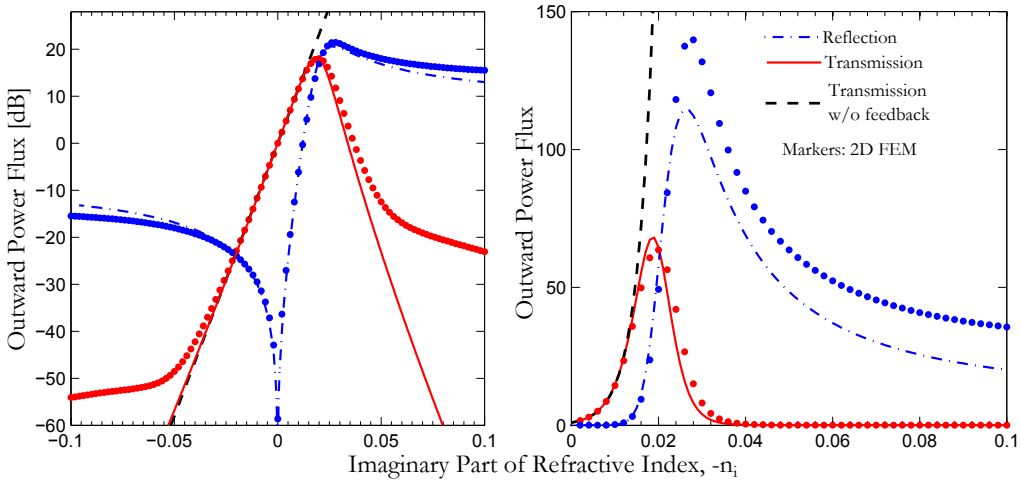

Figure 7.4 Same as in Fig. 7.2, but with $L/a = 20$, $\omega a/(2\pi c) = 0.2075$ and $n_G = 18.7$. Data markers are in this case obtained with FEM simulations. The left (right) panel shows the data in dB (linear units). Reprinted with permission from [188]. Copyright (2015) American Physical Society.

7.3 Summary

We have analyzed the properties of slow light active photonic crystal waveguides, with a finite-length active section embedded in an otherwise passive photonic crystal waveguide. We have presented an original coupled Bloch mode model, in which the guided Bloch modes of the passive waveguide are used as an expansion basis in the active waveguide, and where the slowly varying amplitudes satisfy a set of coupled differential equations. These equations, in particular, include a coupling between the counter propagating Bloch modes that is typically neglected in the analysis of slow light photonic crystal waveguide amplifiers. As a first example, we have considered a relatively long active section and relatively low material gain/loss, and in this case amplification increases up to approximately 25 dB, before a strong back reflection kicks in, which at sufficiently large material gain transforms the structure from an amplifier to a damper. We have compared the approximate coupled Bloch mode model with full Fourier modal method simulations and good agreement is found. As a second example, we have considered a relatively short active section with relatively large material gain/loss, and in this case the coupled Bloch mode model is compared with finite element method simulations, with agreement up to moderate material gain/loss levels. At larger values of the material gain, a discrepancy is observed, which we attribute to the dependence of the group index on material gain/loss; this is captured by the fully numerical approaches, but not by the coupled Bloch mode model. Finally, we have emphasized that in the coupled Bloch mode model the back scattered signal is the result of distributed feedback in the active section, while in the fully numerical approaches no distributed feedback occurs, but in turn reflections at the active-passive interfaces give rise to Fabry-Pérot-like back scattering. These pictures are equivalent and both lead to the correct behavior, as previously pointed out in the literature in simpler systems.

Chapter 8

Single-photon emission in photonic crystal waveguides

> *The photons which constitute a ray of light behave like intelligent human beings: out of all possible curves they always select the one which will take them most quickly to their goal.*
>
> Max Planck

The generation and manipulation of single quanta of light, single photons, are fundamentally interesting for exploring the quantum mechanics of light, but also for applications, such as quantum cryptography [196] and quantum information technology [9]. Single photons are generated via SE from quantum emitters, like atoms, molecules, nitrogen vacancy centers, or QDs, and for use in practical technologies, the SE emission rate and direction must be controlled. This can be achieved by embedding the quantum emitter into a suitably designed environment, and different structures, including micropillar cavities, nanowire waveguides, planar dielectric antennas, and PhC cavities and waveguides, have been proposed [10]. Cavities generally exhibit larger Purcell factors, i.e., yield faster SE, than waveguides, but also require spectral matching of the narrow quantum emitter and the narrow photonic structure. In contrast, waveguides are inherently broadband, which relaxes this requirement, but in turn offer slower SE. Furthermore, for integration on quantum optical chips, PhC membranes may constitute a practical platform [12], in which single photons can be generated and routed around, e.g. for quantum information communication [11].

In this chapter, therefore, we focus on single-photon emission from position-controlled QDs embedded in PhC membrane waveguide structures. In Section 8.1, we first present

the general theory of light emission in waveguides and discuss how this is conceptually equivalent to light emission in cavities. In Section 8.2, we present the structure to be analyzed here, introduce the position-controlled QDs and discuss design constraints. In Section 8.3, we design PhC waveguides for efficient QD emission into its guided modes, and in Section 8.4 we analyze coupling to radiation modes and the SE β factor, both spectrally and spatially, that demonstrate the importance of position control of the QDs. Finally, in Section 8.5, we show preliminary experimental results indicating that the position-controlled QDs emit into the guided modes of the PhC waveguides.

8.1 Spontaneous emission in waveguides

The possibility for large SE rates in waveguides was predicted in 1981 by Kleppner [197], who showed that close to a waveguide mode cut-off, the SE rate into this mode can be enhanced resonantly as in a cavity. Below, we derive, inspired by [27, 67] and building on the Bloch mode framework from Chapter 3, the partial LDOS into a guided mode and show that it is proportional to the group index of the guided mode. The resulting expressions are valid for general passive waveguides, i.e. not restricted to PhC waveguides, and extension to active waveguides is possible [198].

If we consider an infinitely extended waveguide (axis along z), the dipole excitation of Bloch modes is described in Section 3.4.1, and the associated Bloch mode amplitudes, a_γ and b_γ, are the solutions of Eq. (3.16a). Under the Bloch mode orthogonality discussed in that section, Eq. (3.16a) reduces to a closed-form expression for each amplitude, and in particular for the guided waveguide mode, with Bloch mode index $\gamma = \mathrm{G}$, we have

$$a_\mathrm{G} = \frac{\mathbf{j}_\mathrm{D} \cdot \mathbf{E}_\mathrm{G}^-(\mathbf{r}_\mathrm{D})}{\int_S \left[\mathbf{E}_\mathrm{G}^- \times \mathbf{H}_\mathrm{G}^+ - \mathbf{E}_\mathrm{G}^+ \times \mathbf{H}_\mathrm{G}^-\right] \cdot \mathbf{z}\,\mathrm{d}S} \tag{8.1}$$

where, for brevity, we suppress the periodic section index $\tilde{w}$ on all quantities. The denominator in Eq. (8.1) can be expressed via the guided mode power flux along the waveguide axis (P_z defined in Eq. (2.17)) [28]

$$a_\mathrm{G} = \frac{\mathbf{j}_\mathrm{D} \cdot \mathbf{E}_\mathrm{G}^-(\mathbf{r}_\mathrm{D})}{4P_z}. \tag{8.2}$$

As described in Appendix B.8, evaluation of the power emitted into the guided mode now amounts to multiplying this amplitude with the electric field of this mode dotted with the dipole current and evaluated at the dipole position

$$P_\mathrm{G} \equiv a_\mathrm{G}\left(\mathbf{j}_\mathrm{D} \cdot \mathbf{E}_\mathrm{G}^+(\mathbf{r}_\mathrm{D})\right) = \frac{|\mathbf{j}_\mathrm{D} \cdot \mathbf{E}_\mathrm{G}^+(\mathbf{r}_\mathrm{D})|^2}{4P_z} \tag{8.3}$$

where we exploited that $\mathbf{E}_\mathrm{G}^- = \left(\mathbf{E}_\mathrm{G}^+\right)^*$ [28].[1] By using that the component of the group velocity of the guided mode along the waveguide axis can be expressed as [69][2]

$$v_\mathrm{G} \equiv \frac{\mathrm{c}}{n_\mathrm{G}} = \frac{2aP_z}{\int_\mathrm{uc} \epsilon_0 \epsilon |\mathbf{E}_\mathrm{G}^+|^2\,\mathrm{d}V}, \tag{8.4}$$

[1] In computations, the counter propagating guided Bloch modes, $[\mathbf{E}_\mathrm{G}^+, \mathbf{H}_\mathrm{G}^+]$ and $[\mathbf{E}_\mathrm{G}^-, \mathbf{H}_\mathrm{G}^-]$, might have a different phase relation, yielding a phase factor that, however, appears in both numerator and denominator and hence is of no importance.

[2] This relation holds for non-dispersive materials, i.e., when ϵ does not depend on frequency. The relation can be generalized to account for material dispersion, as expressed for translationally invariant waveguides in Eq. (31-30) in [199].

where the volume integral is taken over one unit cell of the PhC waveguide with lattice constant a, we may express P_{G} as follows

$$P_{\mathrm{G}} = \frac{a n_{\mathrm{G}}}{2\mathrm{c}} \frac{|\mathbf{j}_{\mathrm{D}} \cdot \mathbf{E}_{\mathrm{G}}^{+}(\mathbf{r}_{\mathrm{D}})|^2}{\int_{\mathrm{uc}} \epsilon_0 \epsilon |\mathbf{E}_{\mathrm{G}}^{+}|^2 \, \mathrm{d}V}. \tag{8.5}$$

Normalizing finally to the power emitted by a dipole in bulk (in 3D, see Appendix A.1), we find the partial LDOS enhancement into the guided waveguide mode to be

$$\frac{\rho_{\mathrm{G}}(\mathbf{r}_{\mathrm{D}};\omega)}{\rho_{\mathrm{Bulk}}(\omega)} = \frac{3}{4\pi^2} \left(\frac{\lambda_0}{n(\mathbf{r}_{\mathrm{D}})} \right)^3 \frac{Q}{V_{\mathrm{eff}}} \eta, \tag{8.6a}$$

$$\eta = \frac{\epsilon(\mathbf{r}_{\mathrm{D}}) |\mathbf{n}_{\mathrm{D}} \cdot \mathbf{E}_{\mathrm{G}}^{+}(\mathbf{r}_{\mathrm{D}})|^2}{\max\left[\epsilon(\mathbf{r}) |\mathbf{n}_{\mathrm{D}} \cdot \mathbf{E}_{\mathrm{G}}^{+}(\mathbf{r})|^2\right]}, \tag{8.6b}$$

$$Q = \frac{\omega a}{2\mathrm{c}} n_{\mathrm{G}}, \tag{8.6c}$$

$$V_{\mathrm{eff}} = \frac{\int_{\mathrm{uc}} \epsilon |\mathbf{E}_{\mathrm{G}}^{+}|^2 \, \mathrm{d}V}{\max\left[\epsilon(\mathbf{r}) |\mathbf{n}_{\mathrm{D}} \cdot \mathbf{E}_{\mathrm{G}}^{+}(\mathbf{r})|^2\right]}, \tag{8.6d}$$

where $\mathbf{n}_{\mathrm{D}}$ is a unit normal vector along $\mathbf{j}_{\mathrm{D}}$, and where η satisfies $0 \leq \eta \leq 1$ and accounts for any spatial or oriental detuning between the guided mode and the emitter. The definitions of the waveguide mode quality factor, Q, and effective mode volume, V_{eff}, were proposed by Manga Rao and Hughes [67], and Eq. (8.6a) puts the waveguide mode LDOS enhancement in the form originally proposed by Purcell for atoms in cavities [32]. Eqs. (8.6) show that enhanced coupling into the waveguide mode can be achieved by maximizing its group index (increasing Q) and/or by minimizing its spatial extent (decreasing V_{eff}), which is conceptually equivalent to maximizing the Q/V_{eff} ratio of a *localized* mode in a closed cavity.[3] However, we here consider a *propagating* mode in an open cavity, and practically these situations are quite different.[4]

Since the achievable group indices in PhC waveguides are substantially larger than in conventional ridge or planar waveguides, this relation also motivates the use of PhC structures for enhanced light-matter interactions. In theory, the group index diverges at the band edge of the PhC waveguide, which would yield an infinite LDOS enhancement at this frequency. In practice, however, the finite size of the structure as well as disorder in fabricated structures smear out this theoretical divergence and give a finite value [67]. As a reference, high-β single-photon emission from QDs in GaAs PhC waveguides was reported in [68, 94] with experimentally measured group indices of $n_{\mathrm{G}} \simeq 30 - 50$.

The aim in later sections is to design PhC waveguides that maximize the guided mode LDOS enhancement at the frequency where the QD emits light; this will funnel a large part of this light into the waveguide mode, provided that decay into other channels is not simultaneously enhanced. Before delving into the detailed designs, we first in the following section outline the structure and properties of the QDs to be used.

8.2 Design and position-controlled quantum dots

The top panel in Fig. 8.1 shows a schematic top view of the structure we will design and analyze; brown (white) color indicates GaAs material (air), while red triangles indicate the

[3] The conceptual equivalence between emission in a cavity and in a waveguide is not surprising because, according to Kleppner [197], a waveguide "can be viewed as a cavity with ends removed to infinity".

[4] Some authors [11, 17] refer to the ratio in Eq. (8.6a) and the similar ratio for the partial radiation mode LDOS as the waveguide mode and radiation mode Purcell factors. Here, following the discussion in Section 2.2, we refer to these as partial LDOS enhancements.

Ref.	Material (Index)	h_{Mem} [nm]	a [nm]	$r\,[a]$
[68]	GaAs ($n = 3.45$)	160	235	0.31
[202]	GaAs ($n = 3.5$)	180	270	0.26
[203]	GaAs ($n = 3.5$)	180	270	0.34
[201]	GaAs (?)	320	306	0.29
[204]	GaAs (?)	200	314	0.345
[205]	GaAs ($n = 3.53$)	200	230, 255	?
[206]	GaAs (?)	150	248, 256	0.292, 0.286
[67, 200, 207]	($n = 3.4641$)	210	420	0.275
[27]	($n = 3.55$)	180	240	0.29

Table 8.1 Literature overview of QD single-photon emission in PhC membrane waveguides, with membrane material, membrane thickness, PhC lattice constant, and PhC hole radius indicated for each reference.

positions of QDs. As indicated below this sketch, the structure consists of an optimized end mirror, a slow light waveguide, a section for slow-to-fast-light transmission, a fast light waveguide and an optimized out-coupler for collection of light out of the plane. This layout is inspired by previous experimental and theoretical work on QD single-photon emission in PhC waveguides, and in Table 8.1 we collect an overview of a number of these references and the structural PhC waveguide parameters used therein. As we demonstrate in Section 8.3.2, the hole radius, r, can be used to tune the PhC waveguide for LDOS enhancement at the QD emission frequency; similarly, as used in some of the references, the PhC lattice constant, a, can be used for this tuning. In all cases, the PhC membrane material is GaAs, and with one exception membrane thicknesses $h_{\mathrm{Mem}} \leq 210\,\mathrm{nm}$, which we analyze further in Section 8.3.3. Finally, we note that in some cases the waveguides are terminated, either to air or the bulk PhC membrane lattice, for unidirectional emission and/or for FP-like enhancement of the emission [27, 68, 165, 200, 201].

Except for the adiabatic transition from the slow to the fast light waveguide, the elements in the design in the top panel in Fig. 8.1 were all included in the structures in [68], where experimental β factors up to 98% were reported. At an overall level, the *photonic* part of the system is thus very similar to what has been investigated previously. In turn, the *electronic* part, namely the QDs, are different in an important aspect; their position is controlled in the present work and not random as obtained with self-assembly growth techniques (that are commonly used, for example in [68]).

Position control of the QDs relies here on a pre-patterning of the bulk semiconductor with an array of pyramidal holes, at the bottom of which the QDs eventually form [208, 209]. A microscopy image with a top view of such a lattice of pyramidal holes is shown in the inset in the bottom panel in Fig. 8.1, and due to different growth rates on different crystal surfaces, the QDs predominantly form at the bottom of the pyramidal holes [209]. Thus, by controlling where these holes are introduced, the QD positions are implicitly controlled to a very high precision ($< 10\,\mathrm{nm}$ in previous work [210], $\simeq 20 - 30\,\mathrm{nm}$ for the present work). In addition, the emission wavelength of the QDs can, to some extent, be controlled via the size of the pyramidal hole and its specific position in the array of QDs [210]. As an example, the bottom panel in Fig. 8.1 shows micro photoluminescence spectra from such position controlled QDs (in bulk), with spectra taken at different positions on the sample being shifted vertically for clarity. The QD emission occurs around $\lambda_0 \sim 950\,\mathrm{nm}$, with small variations between the different positions on the sample and with the width of the emission peaks being due to inhomogeneous broadening; each position controlled

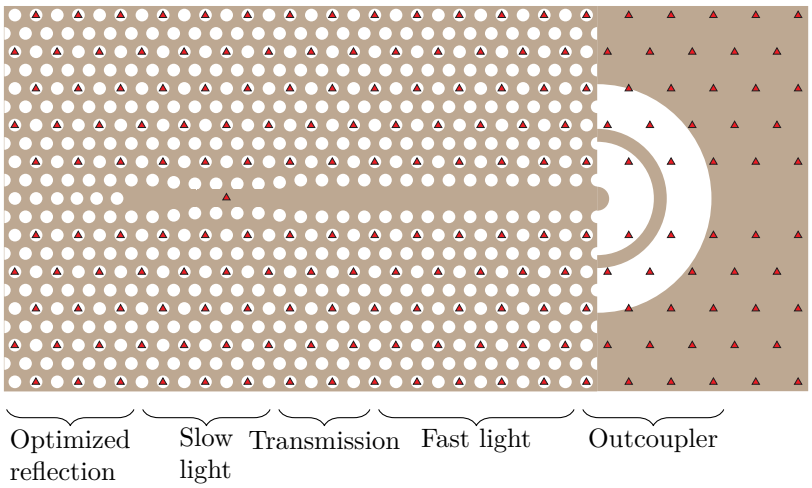

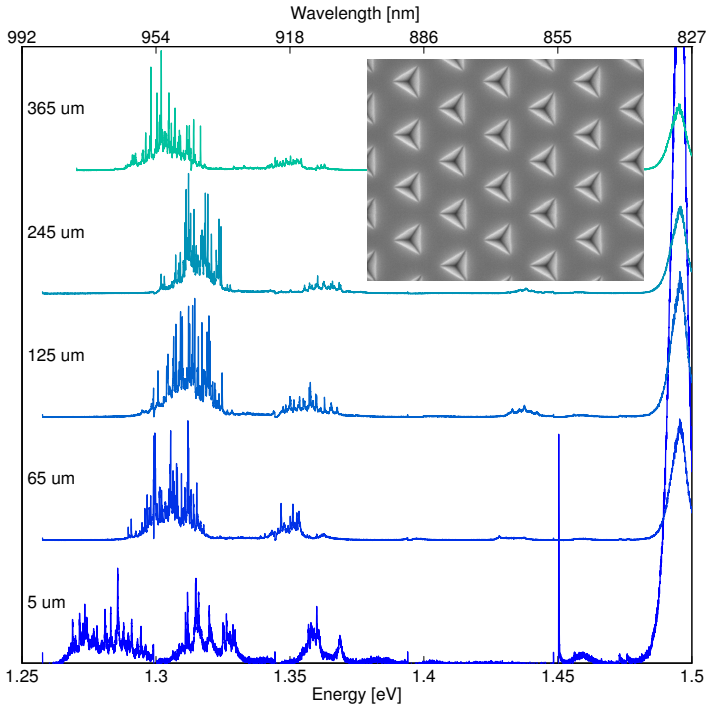

Figure 8.1 *Top panel:* Sketch of PhC waveguide structure for single-photon emission from an embedded position-controlled QD. Brown (white) color indicates GaAs material (air), while the red triangles indicate the position of QDs. QDs inside PhC holes are removed once the PhC structure is fabricated. *Bottom panel:* Micro photoluminescence spectra from position-controlled QDs (in bulk), with spectra taken at different positions on the sample being shifted vertically for clarity. The inset shows a microscopy image of the array of pyramidal holes, in which the QDs form. Illustrations and experimental data are by courtesy of Bruno Rigal, Laboratory of Physics of Nanostructures, EPFL, Switzerland.

QD emits at slightly different wavelengths. Based on these measurements, we target to optimize the PhC waveguide structure for emission at $\lambda_0^{\mathrm{QD}} = 945\,\mathrm{nm}$, and we will design the slow and fast light PhC waveguide sections with this wavelength in mind.

In addition to this, the practical fabrication process and stability of the fabricated structures impose certain design constraints. The QDs are initially fabricated at all pyramidal positions, but in the combined PhC waveguide-QD structure (top panel in Fig. 8.1), we are only interested in emission from a single QD (or a few QDs) sitting in the PhC waveguide. So when the PhC structure is subsequently fabricated, the PhC holes should appear on top of the unwanted QDs to remove these; this is illustrated in the top panel in Fig. 8.1, where all QDs inside the bulk of the PhC lattice appear at PhC hole positions, which in effect removes them. With the pyramidal lattice being fixed, this imposes constraints on how PhC holes can be positioned, but only on every second row of holes due to different pyramid and PhC lattice periods. This means, for example, that we are free to shift the hole positions in the row of holes closest to the waveguide, while the second-closest row cannot be shifted. Also, it is desirable to fabricate the PhC structure with the same hole radius, r, for all holes, as this helps to make the side walls of the holes as vertical as possible. Finally, for mechanical stability of the fabricated structure, the hole radii should not exceed $r/a = 0.3$ substantially.

8.3 Guided mode: Dispersion engineering

With the emission wavelength of the QDs fixed, we in the following design the different PhC waveguide sections for optimizing single-photon emission from the full system shown in the top panel in Fig. 8.1. We will demonstrate and explain how the size and position of the PhC holes as well as the membrane thickness influence the properties of the guided modes, which, in turn, influences the QD emission properties. This type of PhC waveguide design is called dispersion engineering, and we refer to [211] and references therein for previous theoretical and experimental work on this topic. In the next section, we outline the parameters that determine the dispersion of the PhC waveguides to be designed here, before studying the specific and quantitative designs in the subsequent sections.

8.3.1 2D confinement: Quantum well-like behavior

In Fig. 8.2, we show the intensity of the electric field x component ($|E_x|^2$) of the guided (E_x even-even) mode in a PhC membrane W1 waveguide, with structural parameters as in Fig. 4.6. The top panel shows this intensity in the xz-plane and at $y = 0$, while the bottom panel shows it in the xy-plane at $z = 0$. It is apparent that the guided mode is roughly confined in a length L_x (width of waveguide) and L_y (height of PhC membrane) along x and y, respectively, as indicated in blue in Fig. 8.2, while its propagation along z is quasi-free (Bloch form). This is similar to quantum mechanical confinement in a 2D quantum well, where, if the potential barrier is taken to be infinite, the discrete energies are of the form

$$E_{\mathrm{2D,QW}}(L_x, L_y) = c_x L_x^{-2} + c_y L_y^{-2} + c_z, \tag{8.7}$$

where the constant c_z stems from the free propagation along z. A characteristic energy of the waveguide mode is its band edge energy, and it is instructive to think of this quantity as being controlled by L_x and L_y exactly as the quantum mechanical states in the 2D quantum well. The latter parameter is directly given by the thickness of the membrane, h_{Mem}, while the former, with the constraints on the PhC lattice discussed in Section 8.2,

is controlled by the PhC lattice constant, the hole radius, and the shift of the inner row of holes[5]

$$L_x = \sqrt{3}a - 2r + 2s_{\text{inner}}. \tag{8.8}$$

In all of the following $a = 225\,\text{nm}$ is fixed, which thus leaves r and s_{inner} as practical parameters for controlling the waveguide width, L_x.

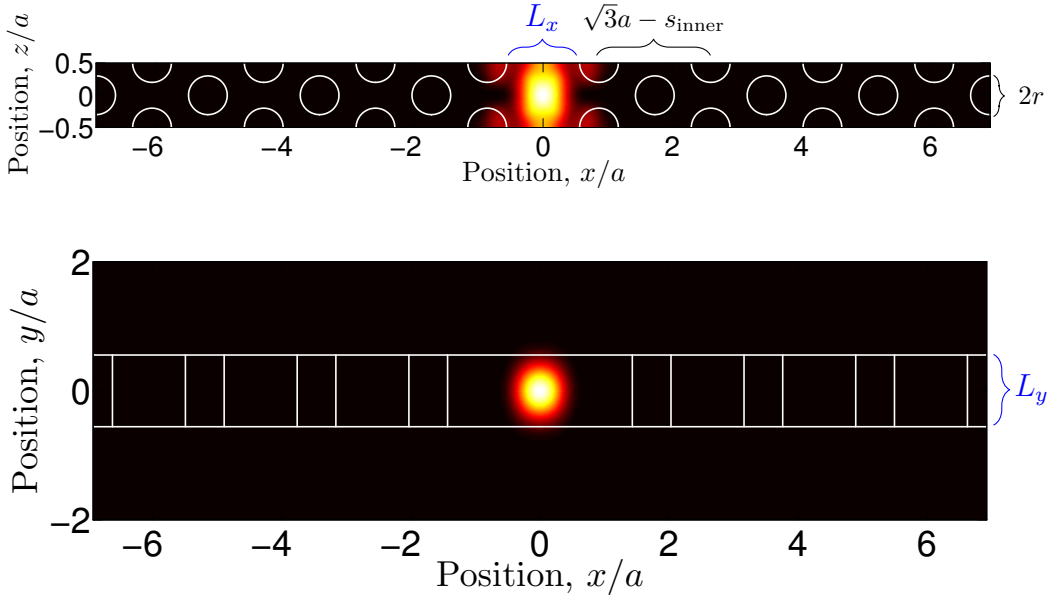

Figure 8.2 Intensity of electric field x component ($|E_x|^2$) of guided (E_x even-even) mode in PhC membrane W1 waveguide (structural parameters as in Fig. 4.6 and fast light frequency, $\omega a/(2\pi c) = 0.247$, with group index $n_G = 5.2$). *Top panel:* Field intensity in xz-plane and at $y = 0$. The width of the waveguide, $L_x = \sqrt{3}a - 2r + 2s_{\text{inner}}$, with s_{inner} being the shift along x of *only* the innermost holes, is indicated. *Bottom panel:* Field intensity in xy-plane and at $z = 0$. The height of the waveguide, $L_y = h_{\text{Mem}}$, is indicated.

To make the qualitative similarity between the present problem and the 2D infinite quantum well quantitative, we in Fig. 8.3 plot the band edge frequency for different values of L_x (left panel) and L_y (right panel). In the left panel, the membrane thickness and hole shift are fixed (see inset), and the waveguide width is varied via the hole radius; in the right panel, the hole radius and shift are fixed (see inset), while the membrane thickness is varied. In both cases, markers are data extracted from computed dispersion curves (that we present and discuss in more detail in the following sections), while the solid lines are fits inspired by Eq. (8.7) of the form $c_1 + c_2 L_\alpha^{-2}$. In the left panel, the fit is generated from three data points (red crosses), while all other markers (blue circles) are independent data. In both cases, the data points and fits match fairly well, and we employ the underlying intuition for designing the PhC waveguides for single-photon emission in the following sections.

[5]Cf. the top panel in Fig. 8.1, the first, third, fifth etc. rows of holes surrounding the waveguide can be shifted to optimize the design. Here, we focus on a shift along x of the inner holes, s_{inner}.

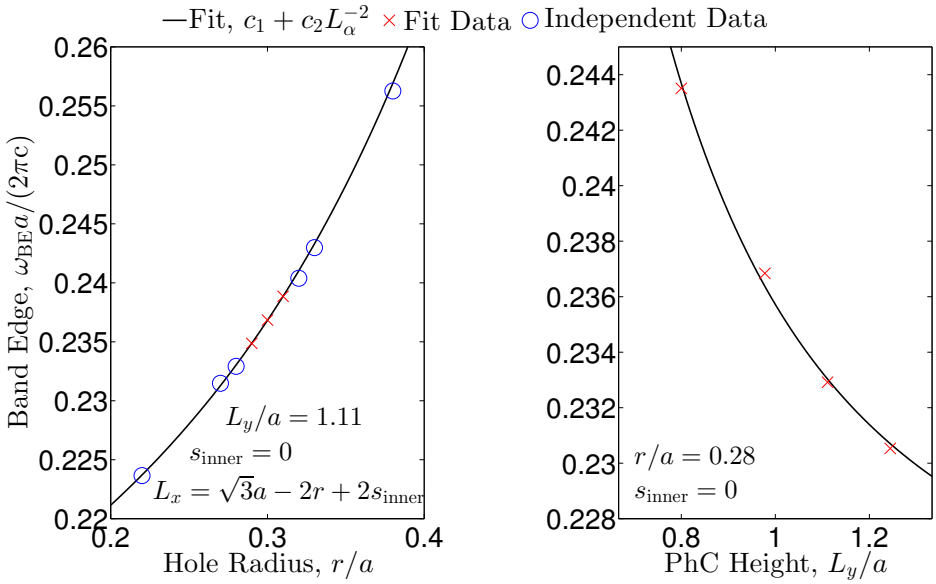

Figure 8.3 Band edge frequency, $\omega_{\rm BE} a/(2\pi c)$, for the guided ($E_x$ even-even) mode in a GaAs PhC membrane waveguide as function of structural parameters indicated in Fig. 8.2. Markers are computed data, while the solid curves are fits inspired by Eq. (8.7). *Left panel:* As function of hole radius, r/a, with inner hole shift ($s_{\rm inner} = 0$) and membrane thickness ($L_y/a = 1.11$) fixed. *Right panel:* As function of membrane thickness, L_y/a, with inner hole shift ($s_{\rm inner} = 0$) and hole radius ($r/a = 0.28$) fixed.

For better agreement with experiments, we account for the slight material dispersion of GaAs by a frequency dependent refractive index [53], both for the data in Fig. 8.3 and for the data to be presented in the Sections 8.3.2 and 8.3.3.

8.3.2 Hole radius or shift variation

In this section, we investigate the dispersion of the (E_x even-even) waveguide mode for a fixed membrane thickness ($L_y = 250\,\text{nm}$) and for varying waveguide width, L_x. This width is controlled by variations of the hole radius, r, and the shift of the inner row of holes, $s_{\rm inner}$. In Fig. 8.4, we present dispersion curves; in panel (a) without hole shifts ($s_{\rm inner} = 0$) and the hole radius as a parameter, and in panel (b) at a fixed hole radius ($r/a = 0.28$) and the hole shift as parameter.[6] In both figures, we include the targeted QD emission frequency ($\lambda_0^{\rm QD} = 945\,\text{nm}$, $\omega^{\rm QD} a/(2\pi c) = 0.238$) as the dashed green line, and we thus generally observe that we can tune the waveguide mode to match the QD emission by variations of r and $s_{\rm inner}$.

As already reported in the left panel of Fig. 8.3, increasing the radius in panel (a) shifts the band edge (and the entire dispersion curve) upwards in frequency, because the guided mode gets confined in a smaller region. Eventually, the band edge is shifted above the QD emission frequency ($r/a \geq 0.31$), and the QD in this case emits into the bandgap

[6] Computational parameters are chosen according to convergence tests (see Appendix F.1), and we estimate the accuracy on the prediction of the band edge to be $\sim 2\,\text{nm}$. Note also that we compute the Bloch modes at discrete frequencies and subsequently interpolate these data to get the dispersion curves. Depending on how the discrete frequencies fall with respect to the band edge, this procedure may make the bands look non-flat close to the band edge, which is thus caused by the computational procedure.

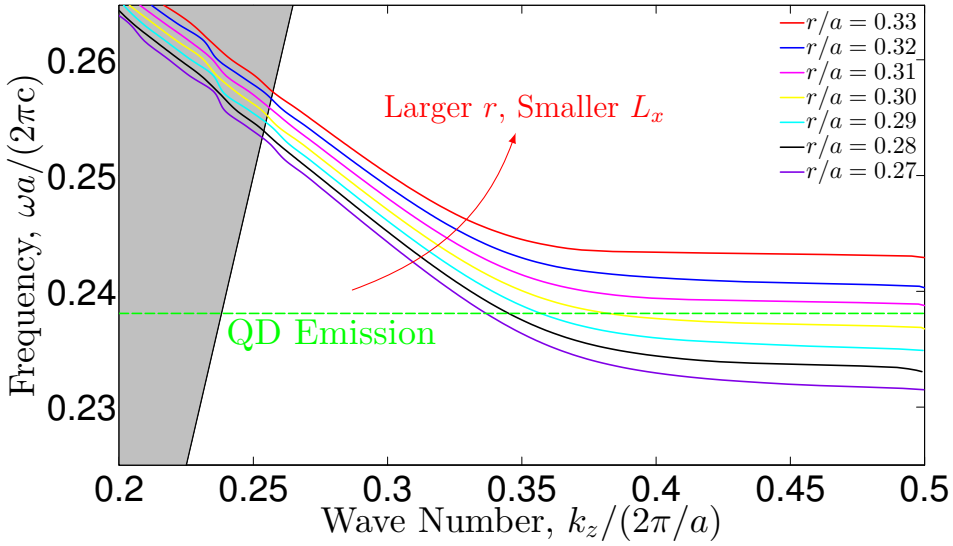

(a) No hole shift ($s_{\text{inner}} = 0$) and hole radius, r, as a parameter.

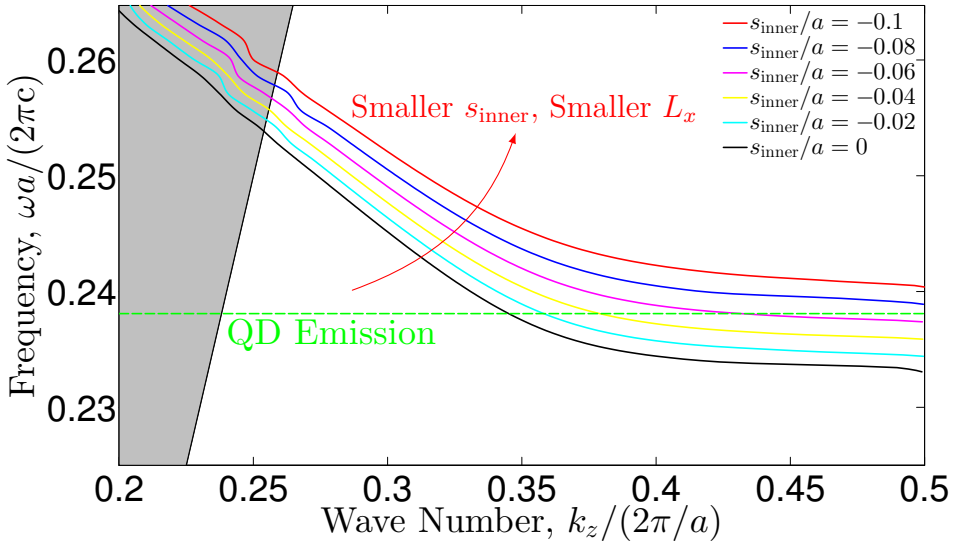

(b) Fixed hole radius ($r/a = 0.28$) and inner hole row shift, s_{inner}, as a parameter.

Figure 8.4 Dispersion curves for guided (E_x even-even) mode in a GaAs PhC membrane waveguide with lattice constant $a = 225\,\text{nm}$ and membrane thickness $L_y = h_{\text{Mem}} = 250\,\text{nm}$. The hole radius, r, or inner hole row shift, s_{inner}, are parameters.

of the PhC structure. This is not immediately desirable, but can be useful for reference measurements, e.g. for comparison to the situations with emission into the guided mode. At the smaller radii, the dispersion is tuned from the fast to the slow light region from $r/a = 0.27$ to $r/a = 0.3$.

In panel (b), shifting the inner holes around the W1 waveguide inwards ($s_{\text{inner}} < 0$)

has essentially the same effect as increasing the hole size; the waveguide width decreases, and the dispersion curves blueshift. Also here the bands eventually shift above the QD emission line ($s_{\text{inner}}/a \leq -0.08$), and as we shift the holes from $s_{\text{inner}}/a = 0$ (no shift) to $s_{\text{inner}}/a = -0.06$ the QD emission is shifted from the fast to the slow light region of the waveguide mode.

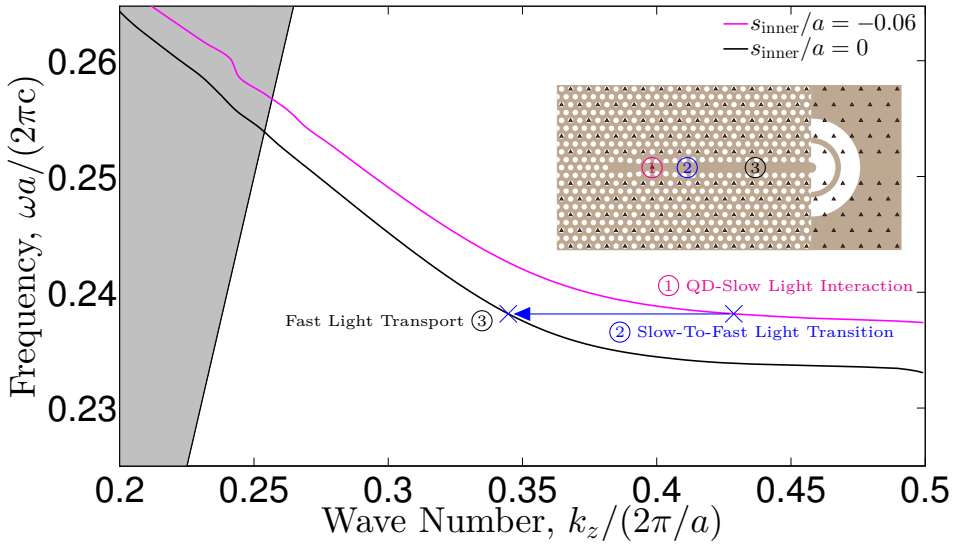

Figure 8.5 Selected dispersion curves (with $r/a = 0.28$) from Fig. 8.4 that provide an optimized design of the slow ($s_{\text{inner}}/a = -0.06$, magenta) and fast ($s_{\text{inner}}/a = 0$, black) light sections, as shown in the inset, at the QD emission frequency (blue crosses).

In Fig. 8.5, we collect dispersion curves (both with $r/a = 0.28$) for an optimized design of parts of the full structure, as shown in the inset. Blue crosses indicate the QD emission frequency, at which the fast (black) [slow (magenta)] light mode has a group index of $n_{\text{G}} = 7.2$ [$n_{\text{G}} = 53$]. The QD interacts with this slow light mode, which via Eqs. (8.6) gives an enhanced emission rate, and the slow light waveguide is then, for example, adiabatically converted into the fast light waveguide, which is used for low-loss transportation of the singly emitted photons. In the view of the results in Fig. 8.4(b), this adiabatic transition could be realized by gradually shifting the holes from $s_{\text{inner}}/a = -0.06$ (slow light) to $s_{\text{inner}}/a = 0$ (fast light) over a couple of unit cells.

In Fig. 8.6, we show the characteristics of these two waveguides, with panels (a), (b) and (c) giving the dispersion, the Q factor [Eq. (8.6c)] and the mode volume [Eq. (8.6d)], respectively, and panel (d) giving the LDOS enhancement [Eq. (8.6a)] at four positions in the waveguide with $s_{\text{inner}}/a = -0.06$ and for an x-oriented dipole. Towards the band edge, the group index, and thus the Q factor, increases dramatically (solid magenta curve, panel (b)), and at the same time the mode volume increases because the guided mode starts to penetrate more into the bulk PhC lattice. The former increase, however, occurs on a logarithmic scale, which causes the LDOS enhancement to increase similarly when the emitter is spatially optimally matched to the guided mode (solid blue curve, panel (d)). This curve is a specific example of the schematic waveguide LDOS we presented in Fig. 2.4. As the emitter is detuned spatially, this enhancement decreases, and for example at a 100 nm detuning along x (cyan dash-dotted curve, panel (d)), the LDOS is

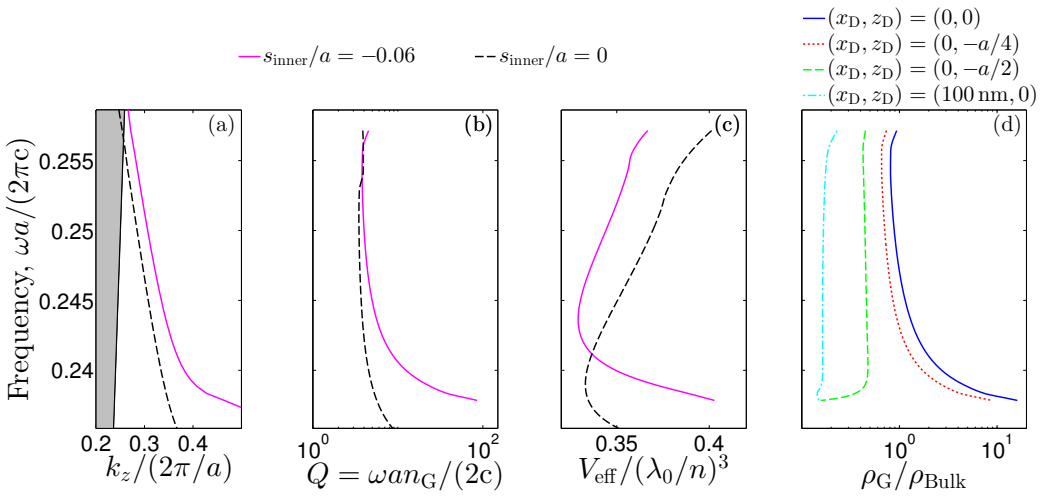

Figure 8.6 *Panels (a)-(c):* Waveguide dispersion, Q factor, and mode volume for the guided (E_x even-even) mode in the PhC membrane waveguides from Fig. 8.5. *Panel (d):* LDOS enhancement for (E_x even-even) guided mode in waveguide with $s_{\text{inner}}/a = -0.06$, at four different positions in the center of the membrane ($y_D = 0$) and for an x-oriented dipole. The data has been computed with a fixed GaAs refractive index, $n_{\text{GaAs}} = 3.4638$.

in fact decreased in the entire spectrum. This accentuates the importance of being able to control the emitter position, as the LDOS enhancement, in this case, varies by two orders of magnitude due to a 100 nm spatial detuning.

8.3.3 Membrane thickness variation

As we saw in the right panel of Fig. 8.3, the thickness of the PhC membrane impacts the band edge of the guided E_x even-even mode of the waveguide, and this thickness can thus, in principle, be used on an equal footing as the hole radius and shift for engineering the dispersion of this mode. In addition, the structure supports another type of guided mode, as we saw in Fig. 2.3, whose existence depends sensitively on the membrane thickness.

In Fig. 8.7, we display the dispersion of the PhC W1 waveguide, with fixed radius ($r/a = 0.28$), no hole shifts ($s_{\text{inner}} = 0$), and the membrane thickness, L_y, as a parameter. In addition to the dispersion for the E_x even-even guided mode, that we have focused on in the previous sections, we also here include the dispersion for the E_x odd-even guided mode(s); at sufficiently low frequencies (large wavelengths), these modes exist inside the light cone and are not bound to the membrane.[7] Starting at the thickest membrane, $L_y = 280$ nm (red crosses), the odd-even guided mode exists under the light line at all frequencies of interest, which is highly undesirable; this mode is another radiative channel that light can be coupled into.[8] Decreasing the membrane thickness to $L_y = 250$ nm (blue plus signs) pushes the E_x odd-even mode towards the light line, but it still exists

[7] Dispersion data have only been obtained for part of the spectral range for each membrane thickness; this is the cause of the incomplete dispersion curves in Fig. 8.7.

[8] E_x odd-even corresponds to E_z even-even, so for positions on the axis, $(x_D, y_D) = (0, 0)$, these modes are excited by z-oriented dipoles, while the E_x even-even modes are excited by on-axis x-oriented dipoles.

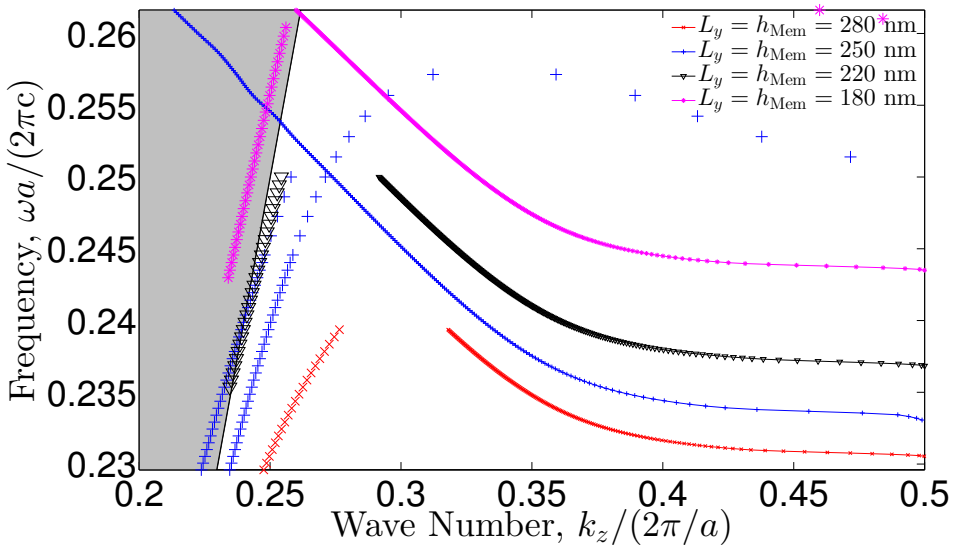

Figure 8.7 Dispersion curves as in Fig. 8.4, but here with $r/a = 0.28$ and $s_{\mathrm{inner}} = 0$ fixed and the membrane thickness, $L_y = h_{\mathrm{Mem}}$, as a parameter. In addition to the guided E_x even-even mode, the dispersion for the guided E_x odd-even modes is included. See footnote 7, p. 95, concerning the incomplete dispersion data.

under the light line in the entire spectral range of interest. Decreasing the membrane thickness even further to $L_y = 220\,\mathrm{nm}$ (black triangles) and $L_y = 180\,\mathrm{nm}$ (magenta stars) pushes the E_x odd-even further towards the light cone, and in the latter case it is entirely inside the light cone; the waveguide is single-moded. Currently, the fabrication of position-controlled QDs is limited to membranes with a thickness of $L_y = 250\,\mathrm{nm}$, but the above investigations suggest that it would be desirable to fabricate structures with thinner membranes, ideally $L_y \simeq 180\,\mathrm{nm}$.

8.4 Radiation mode coupling and β factor

The important figure of merit is the β factor, and the other important component that gives this quantity, on top of the guided mode coupling that we have optimized and analyzed in the previous sections, is the radiation mode coupling. Due to time constraints of the project and the relatively large uncertainty in obtaining this quantity with the computational method used here (see details in Section 4.3) we have, however, not optimized the PhC waveguides systematically for minimizing this quantity. Instead, we in the following sections present a few examples that illustrate general properties of both the guided mode and radiation mode couplings as well as the β factor in PhC waveguides. In these example computations, we focus on x-oriented dipoles, but for a more systematic study and comparison with experiments, other components of the dipole moment of the emitter should be included as well [27, 67, 94].

8.4.1 Spectra

In Fig. 8.8, we show spectra for the partial LDOS enhancement into the guided, $\rho_{\mathrm{G}}/\rho_{\mathrm{Bulk}}$, and into the radiation, $\rho_{\mathrm{Rad}}/\rho_{\mathrm{Bulk}}$, modes as well as of the β factor for a standard PhC

W1 waveguide (same structure as in Fig. 4.6; radius $r/a = 0.3$ and no shift of holes). These quantities have been computed for four positions of the dipole in the center of the PhC membrane ($y_\mathrm{D} = 0$).

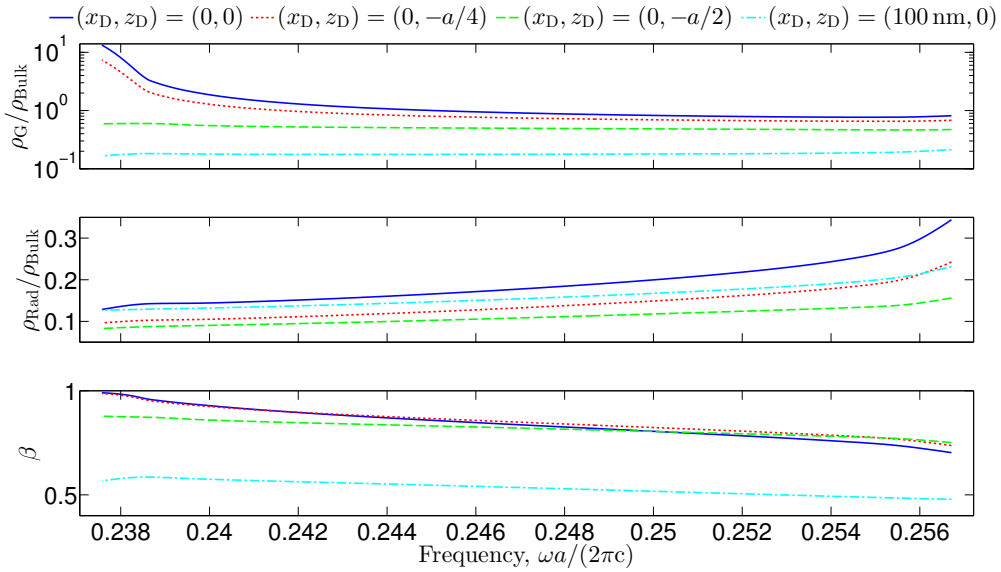

Figure 8.8 Dipole emission spectra for PhC W1 waveguide (structural parameters as in Fig. 4.6) for x-oriented dipole positioned in the center of the membrane ($y_\mathrm{D} = 0$) and with the (x, z)-position as a parameter. The top (middle) [bottom] panel shows the partial LDOS enhancement into the guided mode (partial LDOS enhancement into the radiation modes) [β factor]. Computational parameters (see Section 4.3): PhC width $d_x = 8\sqrt{3}a$, air sub- and superstrate heights $h_\mathrm{SS}/h_\mathrm{Mem} = 3$, number of staircase layers per supercell $N_\mathrm{l} = 33$, x Fourier truncation $j_\mathrm{max} = 40$, y Fourier truncation $n_\mathrm{max} = 10$, PML transformation $f_\mathrm{PML} = 1 + \mathrm{i}$ and PML thickness $h_\mathrm{PML}/h_\mathrm{Mem} = 1/3$.

The coupling to the guided mode (top panel) essentially behaves as we saw in panel (d) in Fig. 8.6; for positions close to the guided mode field maximum (solid blue and dotted red), the coupling increases dramatically towards the band edge ($\omega_\mathrm{BE} a/(2\pi \mathrm{c}) \simeq 0.237$), while for the other positions (dashed green and dash-dotted cyan) the guided mode coupling remains smaller than the bulk value in the entire spectral range. In the middle panel, the coupling to the radiation modes is smaller than the guided mode coupling, decreases by approximately a factor of two over the spectral range, and becomes smaller towards the band edge. Similar observations were reported in [17, 27], and as we typically wish to interface the emitter with the PhC waveguide towards the band edge, this works to our advantage; the radiation mode coupling, that represents radiative losses, is smallest here. It is also interesting to note that the radiation mode coupling is not constant, neither with position, nor with frequency, which is sometimes assumed when estimating β in experiments [94]. Finally, the bottom panel shows that the β factor remains larger than 50% in almost all situations, even when the emitter is spatially detuned from the guided mode field maximum (dash-dotted cyan). On the symmetry axis ($x_\mathrm{D} = 0$), the β factor is $\geq 88\%$ close to the band edge, and at the optimum position (solid blue) the β factor is $\geq 95\%$ ($\geq 90\%$) in a 5 nm (15 nm) bandwidth off from the band edge. These results demonstrate that even without any optimization a large fraction $\beta \gtrsim 90\%$ of the emitted light can be funneled into the guided mode, provided we can operate the system

sufficiently close to the band edge.

8.4.2 Spatial maps

As a second illustration, we focus again on a standard PhC W1 waveguide (same structure as in Fig. 8.6; hole radius $r/a = 0.28$ and $s_{\text{inner}} = 0$) and map the guided and radiation mode couplings as well as the β factor for a dipole at different positions in the center of the PhC membrane $(x_{\text{D}}, 0, z_{\text{D}})$. Contour plots of these quantities are shown in panel (a) [(b)] of Fig. 8.9 at a fast [slow] light frequency. Following Eqs. (8.6), evaluation of the guided mode coupling essentially amounts to computing the guided mode field at different positions, and such spatial maps have been reported in [67], while in [212] spatial maps of total (guided plus radiation modes) emission enhancements were presented. Splitting the emission into the contributions to guided and radiation mode channels is intricate [17, 213], and to the best of our knowledge spatial maps as those in Fig. 8.9 have only been reported once previously [11].

Focusing first on the guided mode coupling (top panels), this quantity exhibits its maximum in the center of the supercell, $(x_{\text{D}}, z_{\text{D}}) = (0, 0)$. As the emitter is moved away from this maximum, the guided mode coupling falls off, but at different rates in different directions; the decrease of $\rho_{\text{G}}/\rho_{\text{Bulk}}$ away from the maximum with x is more pronounced than with z, as we also observed in the top panel in Fig. 8.8. Thus, spatial detuning of the emitter along the length of the waveguide is preferable over detuning in the perpendicular directions. As the guided mode starts to penetrate more into the bulk of the PhC lattice closer to the band edge, the guided mode coupling acquires non-negligible values around $(x_{\text{D}}, z_{\text{D}}) = (\pm 1, 0)a$ at the slow light frequency, while the coupling essentially vanishes here at the fast light frequency.

The radiation mode coupling (middle panel) is more homogeneous in the entire spatial region than the guided mode coupling, and is generally one (two) order(s) of magnitude(s) smaller than the guided mode coupling at the fast (slow) light frequency. As a consequence, the β factor remains $\gtrsim 90\%$ in a relatively large spatial region centrally in the waveguide, a region that becomes slightly larger as we approach the band edge.

8.5 Experiments with position-controlled quantum dots

The fabrication of position-controlled QDs in PhC membrane waveguide structures as well as experimental measurements of these are currently in progress, and no final results have been obtained at this point. However, Fig. 2.1 shows an example of a fabricated structure, and some initial measurements have been performed; these are collected in Fig. 8.10.

In the top panel, the structure with five position-controlled QDs in a PhC waveguide is sketched. In different structures, the light intensity has been measured at the QD positions (I_{QD}) and at the out-coupler (I_{outc}). By varying the hole radius, both PhC waveguides operating in the fast light region and in the bandgap have been investigated; in panel (a) [(b)], the ratio $I_{\text{outc}}/I_{\text{QD}}$ as function of distance for a fast light [bandgap] PhC waveguide is shown. The intensity ratio is large for the guiding waveguide (panel (a)) and decreases with distance for the bandgap structure (panel (b)), which is a signature that the QDs couple into the guided mode, and that guiding of light to the out-coupler takes place. These results are thus a first indication that the QD emission is coupled into the guided mode.

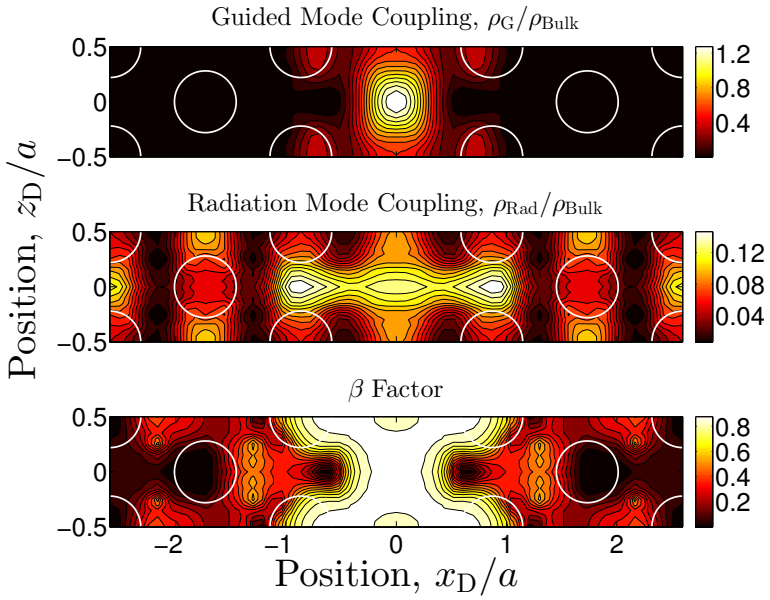

(a) Fast light, frequency $\omega a/(2\pi c) = 0.238$, group index $n_G = 7.8$.

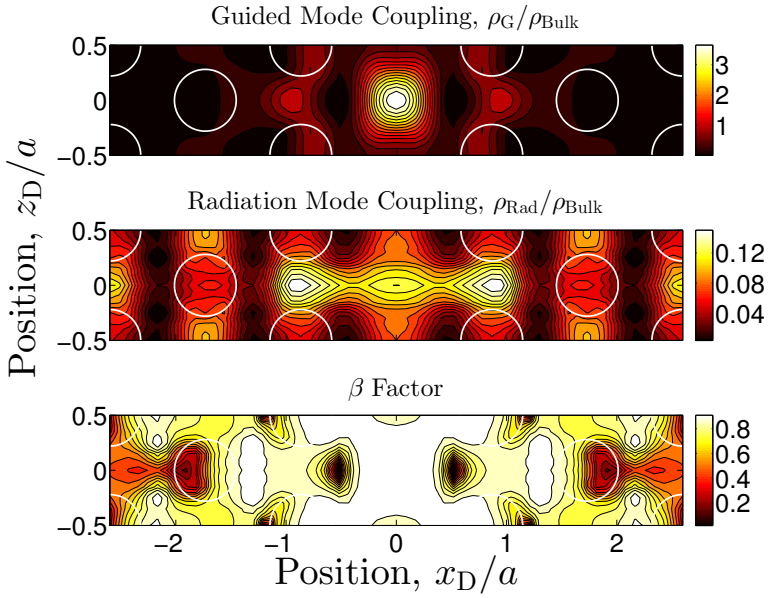

(b) Slow light, frequency $\omega a/(2\pi c) = 0.235$, group index $n_G = 27$

Figure 8.9 Spatial dipole emission maps for the PhC W1 waveguide from Fig. 8.6 ($r/a = 0.28$ and $s_{inner} = 0$) in the center of the membrane, $y_D = 0$, and at two frequencies. Computational parameters (see Section 4.3): PhC width $d_x = 8\sqrt{3}a$, air sub- and superstrate heights $h_{SS}/h_{Mem} = 4.2$, number of staircase layers per supercell $N_l = 33$, x Fourier truncation $j_{max} = 30$, y Fourier truncation $n_{max} = 14$, PML transformation $f_{PML} = 1 + i$ and PML thickness $h_{PML}/h_{Mem} = 3/2$.

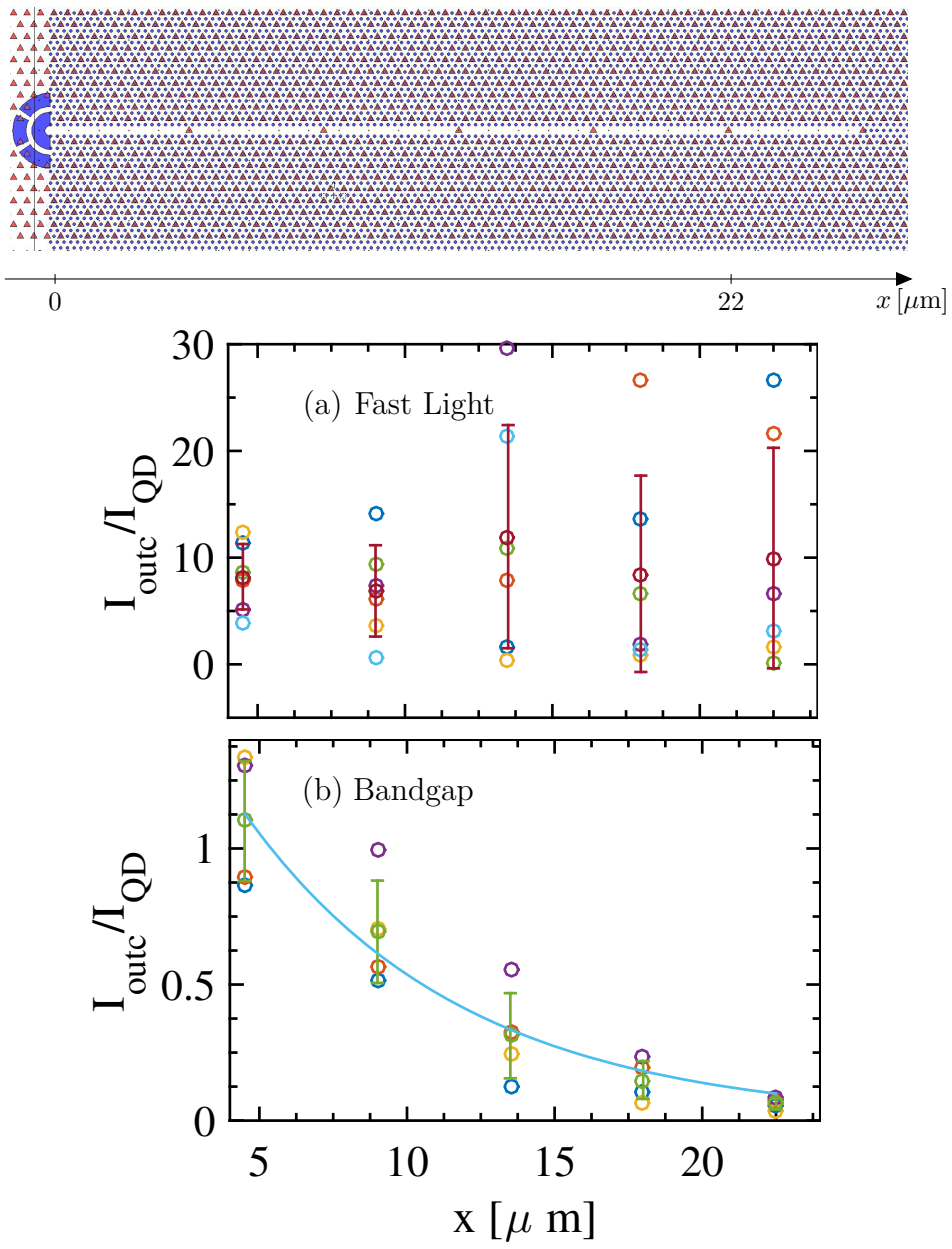

Figure 8.10 Preliminary experimental results with emission of position-controlled QDs in a PhC waveguide. *Top panel:* Sketch of structure with five position-controlled QDs in a PhC waveguide. *Panel (a):* Guiding waveguide, i.e., waveguide mode band edge is below QD emission frequency. Ratio of intensity collected at out-coupler to intensity collected at QD positions along length of waveguide. *Panel (b):* As panel (a), but for a non-guiding waveguide, i.e., waveguide mode band edge is above QD emission frequency. Illustrations and experimental data are by courtesy of Bruno Rigal, Laboratory of Physics of Nanostructures, EPFL, Switzerland.

8.6 Summary

We have in detail analyzed single-photon emission from position-controlled quantum dots embedded in photonic crystal membrane waveguides. First, we showed that the partial local density of states into the guided mode of a photonic crystal waveguide can be expressed in closed form and is proportional to the group index of the guided mode. This motivates to match the quantum dot emission spectrum with the slow light region of the guided mode for enhanced light emission into this well-controlled mode. Then, we introduced the specific photonic crystal structure that contains both slow and fast light waveguide sections, briefly described how position-controlled quantum dots can be fabricated, and showed an example of the emission spectrum from such quantum dots. We focused on the dispersion engineering of the guided modes and introduced a qualitative and semi-quantitative analogy of these modes with the bound electronic states in a 2D quantum well. Building on this analogy, we analyzed the dispersion of the guided mode of interest as function of structural parameters of the photonic crystal lattice, with which we can tune the slow and fast light regions to match with the quantum dot emission spectrum. We also briefly pointed out the impact of the membrane thickness on the existence of a second guided mode in the spectral range of interest. Next, we showed example calculations of the spectral and spatial dependence of both guided and radiation mode couplings as well as the β factor. These quantities are found to be highly position dependent, and the coupling to radiation modes, which for the applications here represent losses, is in all cases small relative to the guided mode coupling. Thus, even far-off the band edge and at a non-optimum position the β factor remains above 50% and quickly approaches unity at the optimum positions and towards the band edge. This is caused by the large index contrast between GaAs and the surrounding air that suppresses the coupling to the freely propagating radiation modes. Finally, we have presented preliminary experimental results, indicating that light can be coupled from individual position-controlled quantum dots into the guided mode and guided over relatively long distances.

Chapter 9

Plasmonic dimer antennas

> *The sciences do not try to explain, they hardly even try to interpret, they mainly make models. By a model is meant a mathematical construct which, with the addition of certain verbal interpretations, describes observed phenomena. The justification of such a mathematical construct is solely and precisely that it is expected to work – that is, correctly to describe phenomena from a reasonably wide area.*
>
> John von Neumann

Plasmons are collective oscillations of free charge carriers, and since metals contain many free electrons (compared to insulators and undoped semiconductors), most materials in plasmonic systems are metals, with noble metals like gold and silver as typical examples [214]. Prominent types include plasmons existing in bulk metals (volume plasmons) and plasmons propagating at metal-insulator interfaces (surface plasmon polaritons), but we shall in this chapter concentrate on the plasmons localized at metal-insulator interfaces, *localized surface plasmons* (LSPs). In Section 9.1, we outline a modeling technique for aggregates of spheres, and in the rest of the chapter we focus on the plasmonic dimer consisting of a pair of sub-wavelength sized noble metal spheres that we introduce in more detail in Section 9.2.

The LSPs of the dimer may exhibit extremely large field enhancements close to the particle surfaces and in the gap between the particles, referred to as "hot spots" [134], and these large fields may lead to enhanced light-matter interactions, as we explore computationally in Section 9.3.1. Also, LSP modes of plasmonic nanostructures may give rise to both enhanced absorption and scattering into the far field when interacting with light [215], and we explore this computationally for the plasmonic dimer in Section 9.3.2.

In Section 9.3.3, we revisit the concept of QNMs for describing the LSP modes of the dimer. By considering a single spherical particle of sub-wavelength dimensions embedded in a bulk background, it is possible to derive an approximate condition for the existence of the fundamental LSP mode, known as the Fröhlich condition [215]

$$\mathrm{Re}\left(\epsilon_{\mathrm{Ma}}(\omega)\right) = -2\epsilon_{\mathrm{B}}, \tag{9.1}$$

where ϵ_{Ma} and ϵ_{B} are the permittivity of the particle and of the background, respectively. Throughout the chapter, this background is taken to be dielectric, i.e., with ϵ_{B} being positive and real, and $\mathrm{Re}\left(\epsilon_{\mathrm{Ma}}(\omega)\right)$ thus needs to be negative for the LSP to exist, which is satisfied, for example, by gold and silver in the visible part of the spectrum [216]. For more complicated plasmonic nanostructures, we cannot write the LSP dispersion in closed form, but in Section 9.4 we employ both experiments, numerical computations, and a semi-analytical nanocircuit model to quantify the LSP dispersion in gold and silver dimers.

Many features of metal optics are captured by the Drude model for the metal permittivity. This model is based on a free-electron description of the metal and leads to $\epsilon_{\mathrm{Ma}}(\omega) = 1 - \omega_{\mathrm{p}}^2/\left(\omega^2 + \mathrm{i}\gamma\omega\right)$, where ω_{p} and γ are material dependent plasma and electron collision frequencies. For the plasmonic silver dimer that we investigate computationally in Section 9.3, we use this model and the parameters $\hbar\left(\omega_{\mathrm{p}}, \gamma\right) = (7.9, 0.06)$ eV [217]. For comparison with experiments in Section 9.4, we use a more elaborate model, the Lorentz-Drude model, that in addition to a free-electron Drude term (*intra*band transitions in the metal) also includes a number of bound-electron Lorentz-oscillator terms (*inter*band transitions in the metal) [218]. As a final note, we mention that in recent years much attention has been paid to plasmonic nanostructures with tiny features, like dimers with extremely small gaps, and that both theories of nonlocal response [219–221] and experimental observations of quantum mechanical charge tunneling [222] have been reported. In this chapter, however, we stay in regimes with dimer gaps $d/R \geq 0.1$ (R being the sphere radius) where these effects are negligible, and where classical electrodynamics thus suffices [220, 223].

9.1 Modeling of aggregates of spherical scatterers

For gaining insight into the optical response of aggregates of spherical scatterers, we have developed a modeling technique based on a volume integral equation and the dyadic Green's function. All details are presented elsewhere [162, 224], and we here just briefly review the formalism. We also refer to [225] for a review of this class of methods for modeling of plasmonic nanostructures.

A source field $\mathbf{E}_{\mathrm{B}}$ impinges on a collection of spherical scatterers, each with permittivity $\epsilon_j(\omega)$, embedded in a homogeneous background with permittivity ϵ_{B}, as shown schematically in Fig. 9.1. The total electric field $\mathbf{E}$ is the solution of the following *implicit* volume integral equation, the so-called Lippmann-Schwinger equation [226]

$$\mathbf{E}(\mathbf{r}) = \mathbf{E}_{\mathrm{B}}(\mathbf{r}) + k_0^2 \int_{V_{\mathrm{scat}}} \mathbf{G}_{\mathrm{B}}(\mathbf{r}, \mathbf{r}')\Delta\epsilon(\mathbf{r}')\mathbf{E}(\mathbf{r}')\,\mathrm{d}\mathbf{r}', \tag{9.2}$$

where V_{scat} is the volume of the spherical scatterers, $\Delta\epsilon(\mathbf{r}') \equiv \epsilon(\mathbf{r}') - \epsilon_{\mathrm{B}}$ is the dielectric contrast, and $\mathbf{G}_{\mathrm{B}}(\mathbf{r}, \mathbf{r}')$ is the dyadic Green's function of the background medium. A popular approach for solving Eq. (9.2) is to discretize the scatterer volumes into a finite number of polarizable dipoles, which converts the equation into a linear system of algebraic

equations. This technique, known as the discrete dipole approximation (DDA) [227], is simple to implement and versatile with respect to the specific shape of the scatterers. In turn, the number of discrete dipoles needed for modeling closely spaced metallic particles to obtain accurate results is large, and fictitious currents are induced for large index contrasts, leading to inaccurate results [225, 228].

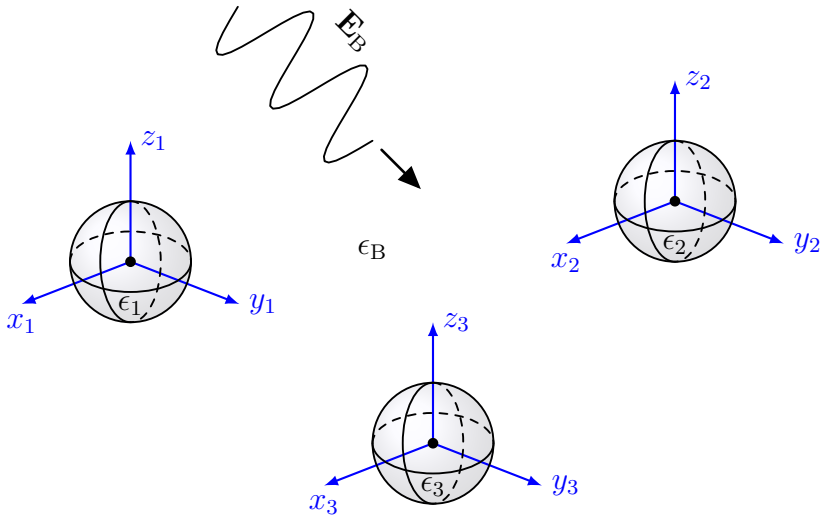

Figure 9.1 Example of scattering geometry where an incoming field, $\mathbf{E}_\mathrm{B}$, impinges on $N = 3$ spherical scatterers embedded in a homogeneous background of permittivity ϵ_B. The scatterers have permittivities ϵ_j, and the local coordinate systems are indicated. Reprinted with permission from [162]. Copyright (2013) Optical Society of America.

For more accurate results, therefore, we propose an alternative expansion basis of scalar spherical waves; these functions obey the spherical symmetry of the scatterers, and we thus expect that a smaller number of basis functions will suffice to obtain high accuracy. The price to pay is the higher spatial complexity of these functions as compared to the DDA approach with piecewise constant basis functions. Specifically, the electric field inside scatterer j is expanded around the center of the scatterer

$$\mathbf{E}(\mathbf{r}_j) = \sum_{\alpha,l,m} a_{j\alpha lm} \psi^j_{l,m}(\mathbf{r}_j)\mathbf{e}_\alpha, \tag{9.3a}$$

$$\psi^j_{l,m}(\mathbf{r}_j) \equiv S_j(\mathbf{r}) j_l(k_j r_j) Y^m_l(\theta_j, \phi_j), \tag{9.3b}$$

where $\mathbf{e}_\alpha$ is a unit vector of the Cartesian direction α, $j_l(k_j r_j)$ and $Y^m_l(\theta_j, \phi_j)$ are spherical Bessel functions and spherical harmonics, respectively, represented in the local coordinate system, and $k_j \equiv \sqrt{\epsilon_j} k_0$. Finally, $S_j(\mathbf{r})$ is unity for $\mathbf{r}$ inside scatterer j and zero everywhere else, ensuring that basis functions of different scatterers are orthogonal. Inserting the expansion in Eq. (9.3a) into Eq. (9.2), projecting onto $\psi^{j'}_{l',m'}(\mathbf{r}_{j'})\mathbf{e}_{\alpha'}$ and summing over all free indices produces the matrix equation

$$\mathbf{a} = \mathbf{M}_\mathrm{B}\mathbf{a}_\mathrm{B} + k_0^2 \mathbf{G}\boldsymbol{\Delta\epsilon}\,\mathbf{a}, \tag{9.4}$$

where the vector $\mathbf{a}_\mathrm{B}$ contains the expansion coefficients of the source field, $\mathbf{E}_\mathrm{B}$, in the same basis as in Eq. (9.3b), but with k_j replaced by $k_\mathrm{B} \equiv \sqrt{\epsilon_\mathrm{B}} k_0$. The excitation can be

any field that we can express in this basis, and in the following sections we investigate both near-field (dipole emitter) and far-field (plane wave) sources. $\mathbf{M}_\mathrm{B}$ is a diagonal matrix with spatial overlaps of $j_l(k_j r_j)$ and $j_l(k_\mathrm{B} r_j)$, and $\mathbf{G}$ is a non-diagonal matrix with elements of the form

$$\left[\mathbf{G}_{j,j'}^{\alpha\alpha'}\right]_{l,l'}^{m,m'} \equiv \int_{V_j}\int_{V_{j'}} \left\{\psi_{l,m}^{j}(\mathbf{r}_j)\right\}^* \mathbf{G}_\mathrm{B}^{\alpha\alpha'}(\mathbf{r},\mathbf{r}')\psi_{l',m'}^{j'}(\mathbf{r}'_{j'})\,\mathrm{d}\mathbf{r}'_{j'}\,\mathrm{d}\mathbf{r}_j. \tag{9.5}$$

The matrix elements in Eq. (9.5) can be expressed in closed form, as detailed in [162, 224]. Once these have been computed, Eq. (9.4) can be inverted to yield $\mathbf{a}$, for a given excitation field as specified in $\mathbf{a}_\mathrm{B}$, and the field inside the scatterers is then known. Subsequently, the governing Eq. (9.2) is an *explicit* equation for positions outside the scatterers, allowing for straightforward evaluation of important characteristics such as the extinction cross section and the LDOS; see again [162, 224] for details. In numerical calculations, the l-sum in Eq. (9.3a) is truncated at l_max, and unless otherwise stated $l_\mathrm{max} = 8$ is used. The formalism presented here can, in principle, handle an arbitrary number N of non-overlapping spherical scatterers and has been successfully applied for chains of up to $N = 20$ plasmonic particles [224, 229]. In the following, we focus on the simplest non-trivial case, $N = 2$, and the plasmonic dimer to be introduced in Section 9.2.

For sub-wavelength sized scatterers, an approximate approach is to take the field inside each scatterer as a constant; this is essentially a quasi-static approximation where all parts of the scatterer are assumed to respond simultaneously to the excitation field. Then, in Eq. (9.2), the electric field can be taken outside of the integral, and this equation becomes an algebraic equation for the $3N$ field values inside the scatterers [224]. This procedure is a limiting case of the DDA, where each scatterer is represented as a single polarizable dipole, and in the following we refer to this approximate and physically appealing picture as the dipole approximation (DA).[1] For the plasmonic dimer, this gives rise to dipole-dipole LSP modes that are shown schematically in the top panel in Fig. 9.5, as we return to in Section 9.3.3.

9.2 Plasmonic dimer

As a specific structure, we consider a plasmonic dimer that is made up of a pair of metallic and spherical particles each with dimension much smaller than the wavelength of light. The dimer is shown schematically in Fig. 9.2 and is described by four parameters: The radius of each particle, R, the surface-to-surface distance between the particles, d, and the material of the particles and of the dielectric background, giving implicitly their permittivities, $\epsilon_\mathrm{Ma}(\omega)$ and ϵ_B.

The dimer is the simplest extension of the single-sphere case, described by Mie theory [130, 230], and as we shall see, the inclusion of a second sphere, and thus of the length scale d, dramatically increases the complexity and richness of the system. At the same time, the dimer is a prototypical plasmonic nanostructure, for which many results have already been reported, and in the following sections, we shall make reference to some of these previous studies.

[1] This is a *different* dipole approximation than the one encountered in the theory of light-matter interactions, that we discussed in Section 2.2.

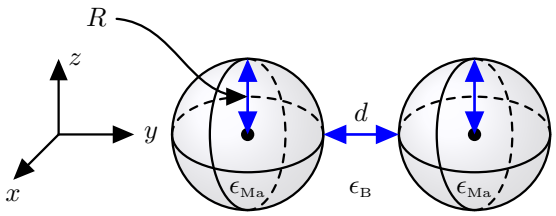

Figure 9.2 Schematic of plasmonic dimer consisting of two metallic and spherical particles, each with radius R and surface-to-surface distance d. The permittivity of the dielectric background and of each sphere are ϵ_{B} and $\epsilon_{\mathrm{Ma}}(\omega)$, respectively, with Ma indicating the particle material, being for example Au or Ag. Reprinted with permission from [162]. Copyright (2013) Optical Society of America.

9.3 Computational investigations

9.3.1 Near-field excitation: Antenna-enhanced spontaneous emission

By positioning the plasmonic dimer in the vicinity of a quantum emitter, it is possible to alter the LDOS at the position of the emitter and thus its SE decay rate. The LDOS is proportional to the imaginary part of the dyadic Green's function [Eq. (2.13)] that we can compute using the technique from Section 9.1, with the dyadic Green's function of the background medium as the source field. We focus on the LDOS enhancement for quantum emitters positioned near a plasmonic dimer with $R = 25\,\mathrm{nm}$ and $d/R = 0.4$, which is the same structure as investigated in [217].

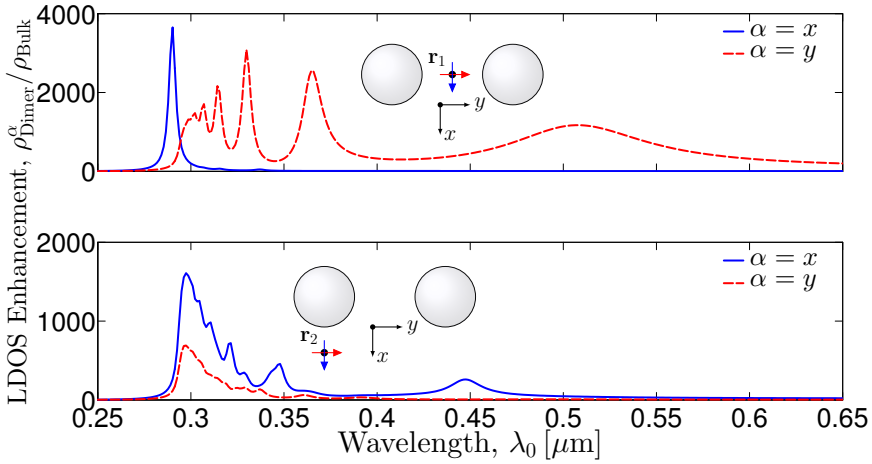

Figure 9.3 LDOS enhancement, $\rho^{\alpha}_{\mathrm{Dimer}}/\rho_{\mathrm{Bulk}}$, spectra for dipole emitter at two positions, $\mathbf{r}_1 = (0,0,0)$ (top panel) and $\mathbf{r}_2 = (R + d/2)(1,-1,0)$ (bottom panel), in the vicinity of an Ag dimer, embedded in SiO_2 ($\epsilon_{\mathrm{B}} = 2.25$), and with $R = 25\,\mathrm{nm}$ and $d/R = 0.4$. Two orientations of the dipole moment of the emitter, $\alpha \in \{x, y\}$, have been employed. Reprinted (adapted) with permission from [162]. Copyright (2013) Optical Society of America.

In Fig. 9.3, we show the LDOS enhancement spectra for $\alpha = x$ [$\alpha = y$] oriented dipoles in blue [red] at the symmetric (asymmetric) position indicated in the inset in the top

(bottom) panel. The broad peak of the y oriented dipole in the middle of the dimer gap (dashed red curve in top panel) around $\lambda_0 = 505\,\text{nm}$ corresponds to the fundamental LSP mode with quality factor $Q \simeq 5.7$ and has a peak value of $\rho^y_{\text{Dimer}}/\rho_{\text{Bulk}} = 1172$, which is in quantitative agreement with the value of ~ 1200 reported in [217]. In addition, the y oriented dipole exhibits strong LDOS enhancement in most of the considered spectral range, $\rho^y_{\text{Dimer}}/\rho_{\text{Bulk}} \gg 1$, with several peaks occurring at shorter wavelengths than the fundamental LSP mode and each corresponding to a higher-order LSP mode. In turn, the LDOS of the x oriented dipole is only moderately enhanced, $\rho^x_{\text{Dimer}}/\rho_{\text{Bulk}} \sim 5 - 10$, at most wavelengths, but exhibits one strong enhancement peak at $\lambda_0 \simeq 290\,\text{nm}$, with an enhancement that is larger than at any wavelength for the y oriented dipole. We note that the LDOS enhancement in this case includes both radiative and non-radiative decay, and that the latter is non-negligible due to Ohmic losses in the metal. As noted by Koenderink [217], Purcell factors and mode volumes are ill-defined for plasmonic nanostructures, but by using a rigorous QNM theory, Sauvan *et al.* [150] developed a generalized Purcell factor formula that takes both material dispersion and the QNM field divergence (see Section 5.5) into account.

Due to the x and y mirror symmetries of the structure, the LSP modes will obey the same symmetries; their electric field components E_x and E_y are even or odd functions of x and y, and for a given mode these two field components have opposite parities [90]. As an example, the fundamental LSP mode at $\lambda_0 = 505\,\text{nm}$ is E_y even-even and E_x odd-odd giving rise to the strong LDOS enhancement for the y oriented dipole at the symmetric position at this wavelength, while for the x oriented dipole the LDOS enhancement due to *this* LSP mode vanishes identically. Weak coupling to *other* LSP modes of the dimer, however, causes the LDOS enhancement to take a finite value at this wavelength ($\rho^x_{\text{Dimer}}/\rho_{\text{Bulk}} \simeq 6.4$). Finally, we note that all peaks occur at distinct wavelengths for the two dipole orientations, which is a consequence of the high-symmetry position.

One way to alter the LDOS enhancement of the quantum emitters, thus, is to place them at a position with less symmetry, which is examined in the bottom panel of Fig. 9.3 at the position $\mathbf{r}_2$. Based on the symmetry considerations from the previous paragraph, we expect the emitters to be influenced by more LSP modes, since fewer of these exhibit electric field nodes at this position. This is observed as strong LDOS enhancement for both orientations in the $290\,\text{nm} \lesssim \lambda_0 \lesssim 360\,\text{nm}$ range, where contributions from several LSP modes give asymmetric peaks [150].[2] At the same time, the x oriented dipole exhibits an LDOS enhancement of $\rho^x_{\text{Dimer}}/\rho_{\text{Bulk}} \simeq 260$ around $\lambda_0 = 448\,\text{nm}$ with an almost-Lorentzian shape, which is caused by a spectrally and spatially almost-isolated LSP mode.

9.3.2 Far-field excitation: Extinction efficiency

Plasmonic nanostructures, like the dimer considered here, are strong absorbers and scatterers of light when the wavelength is close to that of an LSP mode of the structure [215, 231]. The relative strength of absorption and scattering due to the LSP modes depends both on particle sizes and distances [224], and under excitation with polarized light from the far field (plane waves), an important characteristic is the sum of the absorption and scattering cross sections, called the extinction cross section, C_{ext}. This is an equivalent area over which the structure interacts with the excitation field, and it is customary to

[2] A similar behavior was observed for the two PhC cavity structure in Fig. 5.9, where the influence from several QNMs gave an asymmetric feature in the LDOS enhancement spectrum.

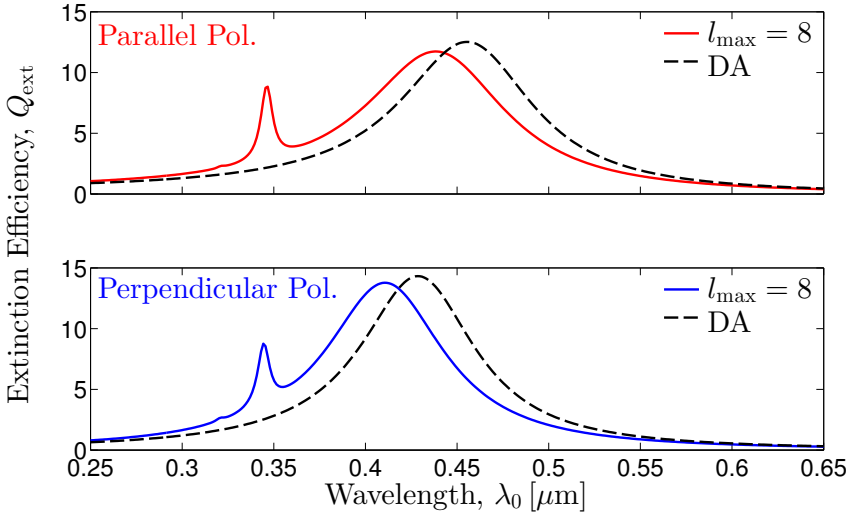

Figure 9.4 Extinction efficiency, Q_{ext}, versus excitation wavelength, λ_0, for scattering of a plane wave on two Ag spheres of radius $R = 25\,\text{nm}$, spaced by $d/R = 2$ and embedded in SiO_2 ($\epsilon_B = 2.25$). The incoming field is polarized parallel (**y**, top panel) or perpendicularly (**x**, bottom panel) to the dimer axis. The spectra have been obtained using the formalism from Section 9.1 with $l_{\max} = 8$ and the DA. Reprinted with permission from [162]. Copyright (2013) Optical Society of America.

normalize this quantity to the geometric cross-sectional area of the structure, giving the extinction efficiency, $Q_{\text{ext}} \equiv C_{\text{ext}}/(2\pi R^2)$.

In Fig. 9.4, the extinction efficiency as function of wavelength is shown for a dimer with particle radii $R = 25\,\text{nm}$ and spacing $d/R = 2$. The top (bottom) panel shows results for light polarized parallel (perpendicularly) to the dimer axis, and in both cases the spectra have been computed with the full numerical formalism (solid curves) and with the approximate DA (dashed curves). For both polarizations, the numerically exact and the approximate scheme both predict a broad resonance around $\lambda_0 \sim 440\,\text{nm}$ ($\sim 410\,\text{nm}$) for parallel (perpendicular) polarizations, while the narrower feature around $\lambda_0 \sim 350\,\text{nm}$ is only captured by the full numerical approach and not by the DA. This peak corresponds to a higher-order LSP mode of the dimer that cannot be described by the simple picture of two coupled dipoles, not even qualitatively. Finally, we note that the wavelengths of the lowest-order LSP modes (appearing in the $\lambda_0 \simeq 400 - 450\,\text{nm}$ range in Fig. 9.4) are predicted with an accuracy of $\sim 4\%$ by the DA compared to the numerically exact results. Thus, the DA is fairly accurate to predict the lowest-order modes of the dimer with the particle spacing considered here ($d/R = 2$), in agreement with previous findings [232]. In contrast, as the particles are brought closer, the DA and the dipole-dipole picture of the dimer become less accurate, which we examine further Section 9.4.

9.3.3 Quasi-normal modes revisited

As mentioned in Section 9.3.1, the LSP modes of plasmonic nanostructures can be described as QNMs [111, 150–152, 157, 160, 162, 163], that we in Chapter 5 used for a description of PhC resonators. Specifically, in Eq. (9.4) we may remove the excitation

field ($\mathbf{a}_\mathrm{B} = \mathbf{0}$) and solve the resulting equation,

$$\mathbf{G}(\lambda_0)\mathbf{\Delta\epsilon}(\lambda_0)\mathbf{a} = \left(\frac{\lambda_0}{2\pi}\right)^2 \mathbf{a} \tag{9.6}$$

as a self-consistent eigenvalue equation for the LSP QNM wavelengths and field distributions. In Eq. (9.6), we stress the wavelength dependence of the matrices on the LHS, and in practice we solve the equation iteratively by computing the eigenvalues of the matrix on the LHS and define the error $\xi = \Pi - (\lambda_0/2\pi)^2$ where Π is the eigenvalue closest to $(\lambda_0/2\pi)^2$. When this error tends to zero, or when $1/|\xi|$ diverges, the LSP QNM is located spectrally.

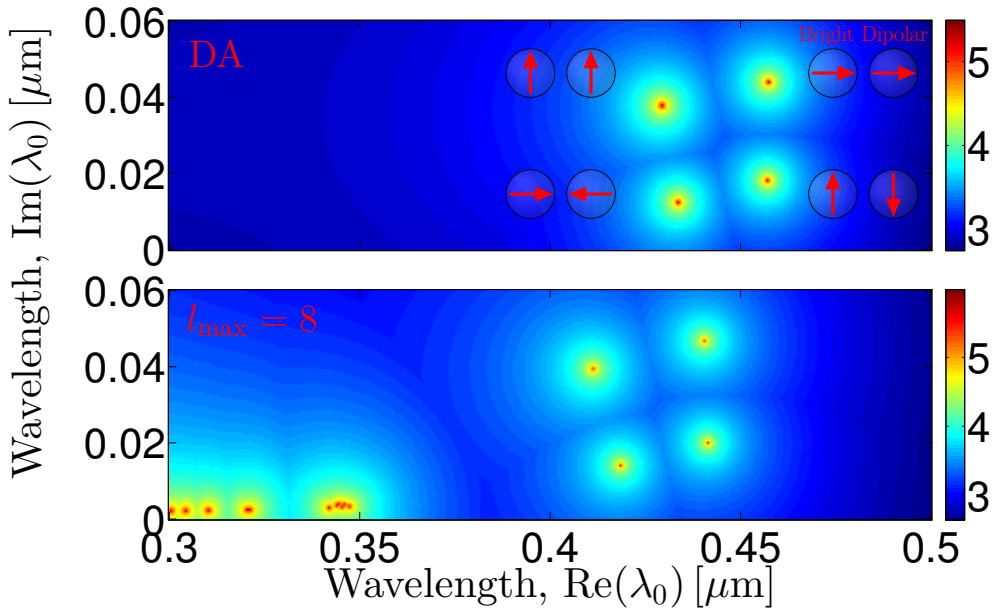

Figure 9.5 QNM LSP Error map, $\log_{10}(1/|\xi|)$, for the plasmonic dimer in Fig. 9.4 as function of $\mathrm{Re}(\lambda_0)$ and $\mathrm{Im}(\lambda_0)$. Red spots, where $|\xi|$ diverges, indicate spectral positions of QNM LSP modes. Data in the top (bottom) panel have been obtained with the DA approach (with $l_{\mathrm{max}} = 8$). In the DA, the orientation of the dipoles are schematically indicated.

For the dimer considered in Section 9.3.2, with extinction efficiency spectra as shown in Fig. 9.4, we show $\log_{10}(1/|\xi|)$ as function of $\mathrm{Re}(\lambda_0)$ and $\mathrm{Im}(\lambda_0)$ in Fig. 9.5. The top (bottom) panel shows data in the DA (with $l_{\mathrm{max}} = 8$), and red spots, where $|\xi|$ tends to zero, indicate the spectral positions of the LSP QNMs.[3] In the DA, where each sphere is treated as a polarizable dipole, the associated eigenvectors give the dipole orientations, and in the top panel, inspired by [233, 234], we schematically show these for the four LSPs that are found with this approach. The two LSPs with parallel dipoles have the largest values of $\mathrm{Im}(\lambda_0)$ (smallest Q factors) and are the bright modes; these couple to the far field and appear as the peaks in the spectra in Fig. 9.4. In contrast, the

[3]We note the similarity between this QNM map and the PhC slow light amplifier transmission and reflection contour maps in Fig. 7.3. In that case, real frequencies are considered and gain is added to yield lasing at discrete values of both frequency and gain. In the present situation, QNMs are similar self-sustained solutions that exist at discrete values of $\mathrm{Re}(\lambda_0)$ and $\mathrm{Im}(\lambda_0)$.

LSPs with anti-parallel dipoles have smaller values of $\mathrm{Im}(\lambda_0)$ (largest Q factors) and are the dark modes that are not visible in the far-field spectra. The dark modes are thus an example of modes that scattering excitation may be "blind" to, as discussed in Section 5.2.1. For a more elaborate study using the DA of the dipole-dipole modes of single particles, dimers, and trimers, see [234]. Comparing the top and bottom panels in Fig. 9.5, the four dipole-dipole-like LSPs are preserved when we include more basis functions ($l_{\mathrm{max}} = 8$), but shift spectrally as we also observed Fig. 9.4. In addition, a large number of higher-order LSPs appear in the range $300\,\mathrm{nm} \leq \mathrm{Re}(\lambda_0) \leq 350\,\mathrm{nm}$, that the DA does not capture. We also note that the spectral position of the bright dipolar-like LSP is the same in the bottom panel in Fig. 9.5 as in the top panel in Fig. 9.4. In the following section, we focus on this LSP and its dependence on the dimer spacing.

9.4 Scaling of bright dipolar plasmon energy with particle spacing

The spectral response of individual plasmonic nanoparticles depends sensitively on their shape, size, specific metal, and dielectric environment [215]. In addition to these dependencies, the response of collections of plasmonic nanoparticles depends on their relative positioning, and for the plasmonic dimer the spectral position of the LSP modes depends strongly on the particle spacing, d [229, 235, 236]. This makes the plasmonic dimer a viable system for accurate sensing at the nanoscale, and dimer assisted DNA sensing has already been demonstrated [237]. A prerequisite for accurate sensing, however, is a precise description of the LSP mode energy as function of distance, which is the topic of this section.

We focus on the bright dipolar mode of the dimer that gave rise to the extinction efficiency peak around $\lambda_0 = 440\,\mathrm{nm}$ in the top panel of Fig. 9.4 (spacing $d/R = 2$) and the LDOS enhancement around $\lambda_0 = 505\,\mathrm{nm}$ in the top panel in Fig. 9.3 (spacing $d/R = 0.4$). From these investigations, it is apparent that this LSP mode redshifts with decreasing distance, which, if we keep the dipole-dipole picture from Fig. 9.5 in mind, stems from the attractive alignment of the two dipole moments, which lowers the energy of the system as the dipoles are brought closer. Here, we are interested in an accurate description of this redshift with spacing, since this is what is needed for quantitative sensing at the nanoscale. As reviewed in a recent publication [238], many experimental and computational investigations of the functional form of this dependence have been carried out, and based on the suggestion by Jain *et al.* of an exponential dependence in the so-called "universal plasmon ruler equation" [235], much attention has been paid to estimating the amplitude and characteristic decay length entering in this function.

In the work presented here, we focus on the $d/R \leq 1$ range, where the dipole-dipole picture of the dimer, that the "universal plasmon ruler equation" is based on, is particularly questionable [232]. We employ electron energy-loss spectroscopy (EELS) and scanning transmission electron microscopy (STEM) for investigating gold and silver dimers, where it is possible to address individual dimers with high spatial ($\sim 0.4\,\mathrm{nm}$) and spectral (~ 0.15 eV) resolutions, prompting accurate estimations of both particle sizes, dimer gaps, and plasmon energies. The experimental data are compared with full 3D simulations, with the method from Section 9.1 that goes beyond the simple dipole-dipole description, as well as a semi-analytical equivalent nanocircuit model [239].

9.4.1 Experiment: Electron energy-loss spectroscopy

In the experiments, gold and silver dimers are positioned on substrates, and STEM images of structures with different gap sizes can be seen in Figs. 9.6(a) and (c). As is apparent, the particles are quasi-spherical and approximately of the same size, but deviations from perfectly spherical shapes and size variations might explain small discrepancies between experiments and computations.

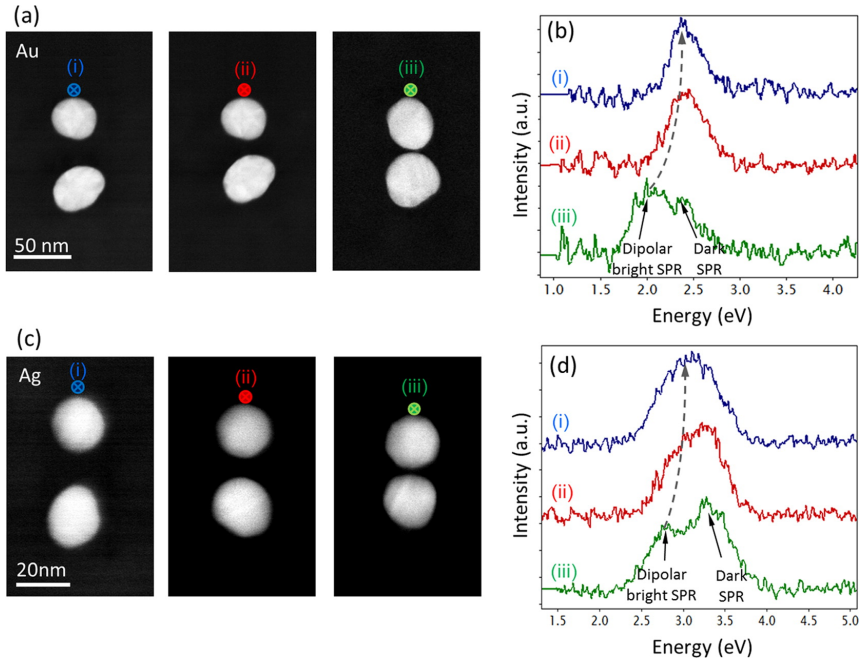

Figure 9.6 *Panels (a) and (c):* STEM images of (a) gold and (c) silver dimers with different separation distances. The dots in the images denote the position of the electron beam. *Panels (b) and (d):* Corresponding EEL spectra of the dimers in (a) and (c). Reprinted with permission from [239]. Copyright (2014) American Chemical Society.

The dimers are excited by an electron beam at the periphery of one of the particles, as indicated with the colored markers in Figs. 9.6(a) and (c), and EEL spectra as those in Figs. 9.6(b) and (d) are recorded for each dimer. The redshift of the bright dipolar LSP mode for smaller distances (blue to red to green) is clearly visible, and for each structure, dimensions and bright mode energy are collected, the latter using Gaussian fits to the peaks in the EEL spectra.

9.4.2 Simulations: Far-field excitation with polarized light

We excite the dimer from the far field with polarized light (polarization parallel to the dimer axis) and compute the extinction efficiency, as in Sec. 9.3.2, at different particle spacings. The peak appearing at the longest wavelength corresponds to the bright dipolar mode, and in the following we collect these wavelengths as function of the particle size and dimer spacing. In the experiments, dimers are positioned on substrates, and while the extension of the formalism developed in Section 9.1 to layered backgrounds is, in principle, possible [21], only homogeneous backgrounds can currently be handled. Thus,

to emulate the substrate in the experiments, we calibrate the background permittivity, ϵ_{B}, for single gold and silver particles, such that the experimental and simulated wavelength of the lowest-order LSP mode matches. These values, $\epsilon_{\mathrm{B}}^{\mathrm{Au}} = 1.35$ and $\epsilon_{\mathrm{B}}^{\mathrm{Ag}} = 1.25$, are then used to simulate the dimers.

Finally, we note that the computational formalism used here could be extended to simulate directly the EELS response of dimers (and other aggregates of spheres) [240], and that both transformation optics [241], FDTD [242], and QNM [243] approaches for this have been developed. However, far-field excitation suffices for analyzing accurately the bright dipolar mode, as we saw when comparing Figs. 9.4 and 9.5, and this is therefore what we do here.

9.4.3 Results and fitting

In Fig. 9.7, experimental and computational results for the bright dipolar plasmon mode energies as function of the particle distance, $x = d/D$ with $D = 2R$ being the particle diameter, are collected for (a) gold and (b) silver. Experimental and computational data agree well and both predict a distinct redshift of the mode energy as the particles are brought closer. An often used figure of merit is the fractional wavelength shift $y \equiv \Delta\lambda/\lambda_0$, where $\Delta\lambda \equiv \lambda_{\mathrm{p}} - \lambda_0$ and λ_0 is the LSP wavelength of the single particle (and not, here, the free-space wavelength), as a measure for the shifting strength of the mode; the larger y and $\partial y/\partial d$ at a given spacing, the more sensitive the dimer is. This quantity is shown in Figs. 9.7(c) and (d) for the gold and silver dimers, and we observe that the silver dimers are more sensitive with larger fractional wavelength shifts, thus making them better candidates for nanoscale sensing.

The fractional wavelength shift has been investigated in many previous studies [238], especially with an emphasis on the functional form of its dependence on the particle spacing. It has been suggested to scale exponentially as $y \propto \exp(-x/\tau)$, with $\tau \simeq 0.2$ being a decay length that is independent of the specific metal and surrounding medium, the size of the particles as well as their shape [235]. According to [235], this exponential form is an approximation to a $\sim (d+2R)^{-3}$ dependence that a dipole-dipole description of the dimer yields, and which has been shown to be fairly accurate down to approximately $d/R \simeq 1$ [232, 244]. To test this, part of the data from Figs. 9.7(c) and (d) are shown in Figs. 9.8(a) and (c), but this time in *semi-log* plots. The dashed lines are exponential fits to the EELS data, with fitting parameters and R^2 values indicated in the insets in the figures. The experimental data thus reproduce the universal scaling, $\tau \simeq 0.2$, but the fits are not perfect; predicting x (the gap size) at a given value of y (fractional wavelength shift) using the fits is up to 50% wrong at either end of the considered range ($0.05 < x < 0.5$).

As an alternative, therefore, the same data are shown in Figs. 9.8(b) and (d), but in *log-log* plots. Polynomial fits and associated R^2 values are again included as insets, suggesting a $\sim (1/d)^{0.9}$ dependence of the fractional wavelength shift in the $0.1 < d/R < 1$ range. This finding is in good agreement with the $\sim (1/d)^{0.89}$ dependence found computationally in [236], where the almost inverse d dependence of the fractional wavelength shift is found, more generally, for chains of spherical metal particles and explained on the basis of the van der Waals potential between spheres that scales as $1/d$. Using these fits, errors in estimating x from y are up to 14%, which is considerably smaller than with the exponential fits, as discussed in the previous paragraph.

Overall, an approximately inverse dependence of the fractional wavelength shift on the dimer gap, $\Delta\lambda/\lambda_0 \sim (1/d)$, in the $0.1 < d/R < 1$ range thus appears to be a more accurate description than the inverse cubic or exponential dependence that a coupled

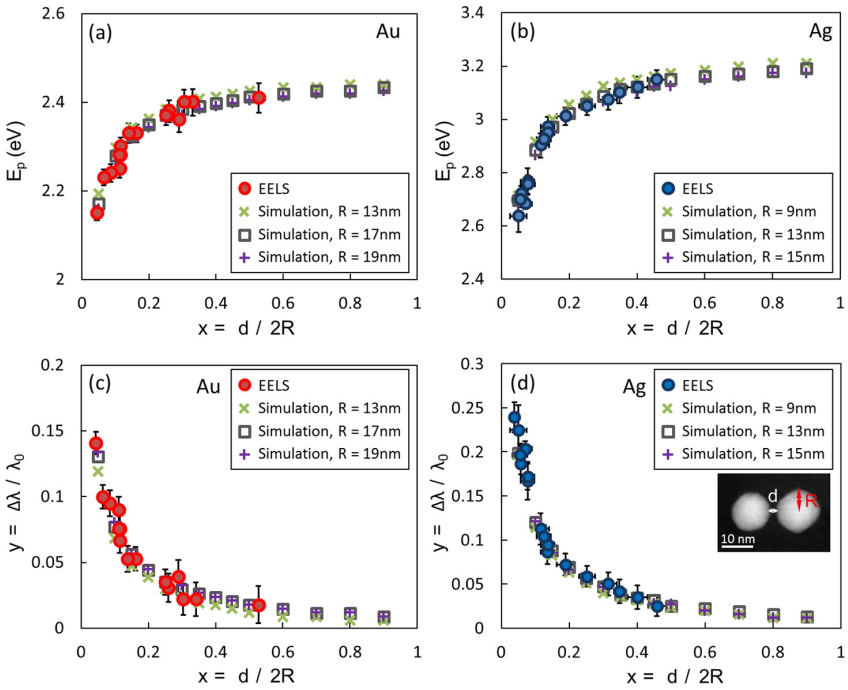

Figure 9.7 *Panels (a) and (b):* LSP energies, E_{p}, measured with EELS and simulated for (a) gold and (b) silver dimers as functions of the gap size, $x = d/(2R)$. *Panels (c) and (d):* The corresponding fractional wavelength shifts, $y = \Delta\lambda/\lambda_0$, where $\Delta\lambda \equiv \lambda_{\mathrm{p}} - \lambda_0$ and λ_0 is the LSP wavelength of the isolated particles, as functions of the gap size, $x = d/(2R)$ in (c) gold and (d) silver dimers. Reprinted with permission from [239]. Copyright (2014) American Chemical Society.

dipole-dipole approximation gives rise to. In the plasmon hybridization picture [245], this is caused by the increasing importance of higher-order multipoles for decreasing distance: The dipole mode of the individual particle does not only interact with the dipole mode of the other particle, but also with the quadrupolar and higher-order modes. Altogether, this changes the bright dipolar mode dispersion that cannot accurately be described in the dipole-dipole approximation.

9.4.4 Equivalent model: Two capacitance coupled LC circuits

As a means for gaining more intuitive insights into the optical response of plasmonic nanostructures, nanocircuit models in which a given nanostructure is replaced by lumped circuit elements, well-known from electrical engineering, have been proposed [246]. As shown in the left panel in Fig. 9.9, the plasmonic dimer can be represented as two gap capacitance coupled LC circuits.

Using detailed expressions for the individual inductances and capacitances in this circuit, the following expression for the fractional wavelength shift of the dimer circuit can be derived (see details in [239])

$$\frac{\Delta\lambda}{\lambda_0} = \frac{2q\left(\dfrac{C_{\mathrm{g}}}{\pi R}\right)}{p + 2q\epsilon_{\mathrm{B}}}, \tag{9.7}$$

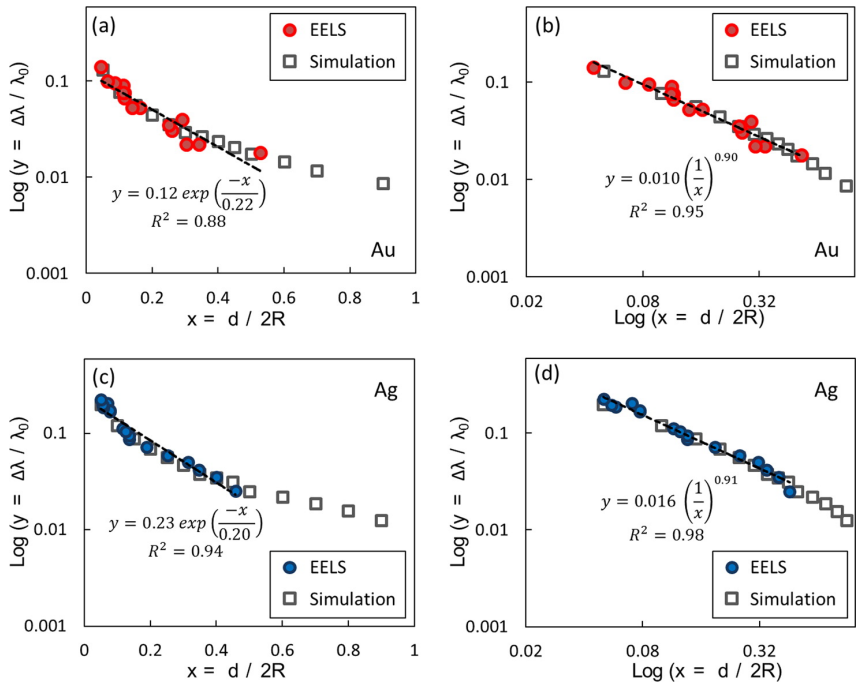

Figure 9.8 The same data as in Figs. 9.7(c) and (d) [Fractional wavelength shifts vs. gap size. For gold and silver only computed data for $R = 17$ nm and $R = 13$ nm, respectively, are included]. *Panels (a) and (c):* Data in *semi-log* plots for (a) gold and (c) silver. *Panels (b) and (d):* Data in *log-log* plots for (b) gold and (d) silver. Reprinted with permission from [239]. Copyright (2014) American Chemical Society.

where p and q are linear fitting parameters between the free-space wavelength, λ, and $\mathrm{Re}\,(\epsilon_{\mathrm{Ma}})$, approximately valid in the visible part of the spectrum for both gold and silver. The gap capacitance, C_{g}, is estimated as the capacitance of two metal plates of the same surface area as the cross-sectional area of the metal particles [247]

$$C_{\mathrm{g}} = \frac{\pi R^2 \epsilon_{\mathrm{B}}}{d}, \tag{9.8}$$

where it is assumed that the accumulated charges are spread uniformly over the entire cross-sectional area of the particles.

In the right panel of Fig. 9.9, the EELS measured fractional wavelength shifts versus gap size are shown as the colored circles, while data from the nanocircuit model, Eq. (9.7), with the gap capacitance given by Eq. (9.8), are included as black crosses. The tendency in the latter data agrees with the EELS measurements, but quantitatively the nanocircuit model overestimates the fractional wavelength shift. One possible explanation for this is that in the dimer, charges are not distributed uniformly over the entire cross-sectional area, but instead concentrated on a smaller area. If we assume this effective area to be only one fourth of the cross-sectional area, the gap capacitance is reduced by a factor of four, $C_{\mathrm{g}}^{\mathrm{Dimer}} = C_{\mathrm{g}}/4$, and the dimer nanocircuit model leads to the black plus signs in the right panel of Fig. 9.9. With this correction, the nanocircuit model is observed to agree well with the experimental data, thus demonstrating the applicability of lumped circuit models for analyzing and designing plasmonic nanostructures.

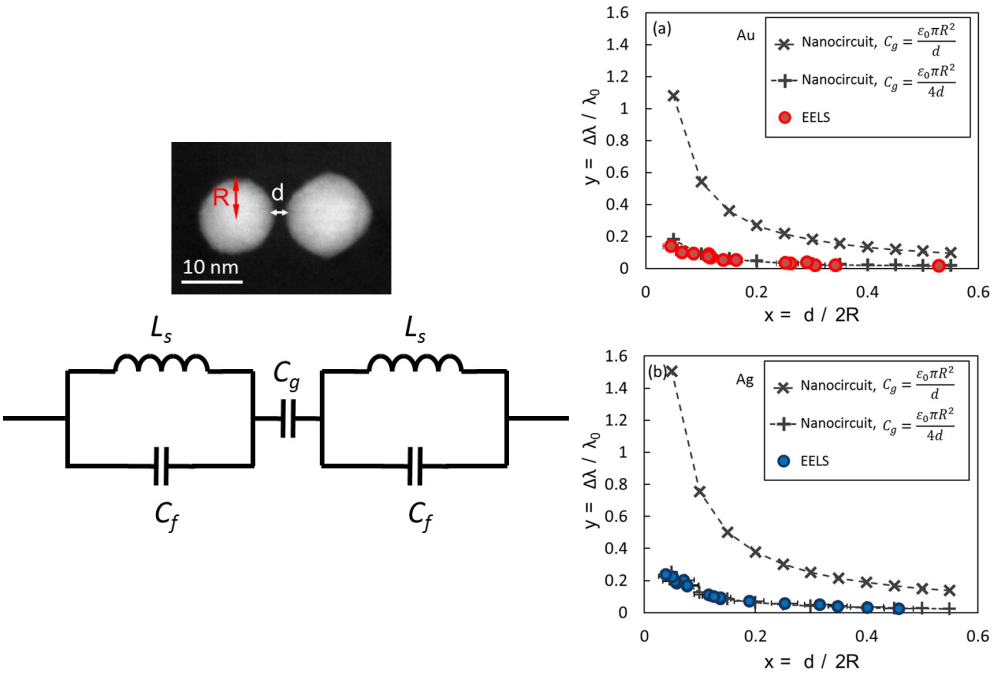

Figure 9.9 *Left panel:* Two capacitance-coupled LC circuits as an equivalent representation of two closely spaced metal spheres. *Right panel:* Fractional wavelength shifts, $y = \Delta\lambda/\lambda_0$, where $\Delta\lambda \equiv \lambda_p - \lambda_0$ and λ_0 is the LSP wavelength of the isolated particles, as functions of the gap size, $x = d/(2R)$, for (a) gold and (b) silver. Both EELS (colored circles) and nanocircuit (black crosses and plus signs) data are included. Reprinted with permission from [239]. Copyright (2014) American Chemical Society.

9.5 Summary

We have analyzed, both theoretically and experimentally, the localized surface plasmon modes of a plasmonic dimer, consisting of a pair of noble metal spheres of $\sim 20\,\text{nm}$ dimensions. We have presented a computational approach based on an implicit volume integral equation for the electric field that we solve in a basis of spherical waves. This basis adopts the spherical symmetry of the spherical scatterers and thus prompts highly accurate computations. Then, we analyzed computationally the local density of states enhancement spectra for different dipole orientations and at different positions close to the dimer, and multiple peaks are observed that we attribute to localized surface plasmon modes of the structure. We also investigated the extinction efficiency of the dimer, both using the full numerical approach and an approximate dipole approximation where each sub-wavelength sized scatterer is treated as a polarizable dipole. Both approaches predict the existence of dipole-dipole-like localized surface plasmon modes, while higher-order modes are not captured in the approximate approach. This is illustrated further by computing the localized surface plasmon modes as quasi-normal modes, where also the dark modes, that far-field excitation is "blind" to, are found. Finally, we focus on one of these localized surface plasmon modes, the bright dipolar mode, and investigate the scaling of the plasmon energy of this mode with particle spacing. Electron energy-loss spectroscopy and scanning transmission electron microscopy are used for mapping out plasmon energies as function of distance for gold and silver dimers. These data are compared to extinction

efficiency computations, and agreement is found. Staying in the sub-radius distance regime, both approaches predict a polynomial dependence on the relative shift of the plasmon wavelengths, which thus disagrees with the celebrated exponential dependence in the "plasmon ruler equation". Finally, the polynomial dependence is explained on the basis of an equivalent circuit model of the dimer, where a quantitative agreement between measurements and the circuit model is found when correcting for the accumulation of charges on the nanoparticles.

CHAPTER 10

Highlights and outlook

> *The whole strenuous intellectual work of an industrious research worker would appear, after all, in vain and hopeless, if he were not occasionally through some striking facts to find that he had, at the end of all his criss-cross journeys, at last accomplished at least one step which was conclusively nearer the truth.*
>
> Max Planck

We have focused on photonic crystal membrane structures, where point and line defects form cavities and waveguides that can be used for localizing and guiding light. The natural solutions of Maxwell's equations in such periodic structures are Bloch modes, and we have presented a computational framework for analyzing light emission and propagation in the basis of Bloch modes. The framework has been implemented in a software package, and the overall scope of the project has been twofold: (1) To assess the quality and feasibility of the framework for modeling and analysis of full 3D photonic crystal membrane structures, and (2) to use the framework for gaining new insights into photonic crystal structures, with an emphasis on waveguides, slow light effects, and coupled cavity-waveguide structures.

Highlights

Quality and feasability of computational framework The computational Bloch mode framework has been presented in detail with expansions in a basis of plane waves or Fourier series. Furthermore, the coupling of several photonic crystal sections is treated with a Bloch mode scattering matrix algorithm, leading to easy extraction of coupling

at the level of the individual Bloch modes. Finally, the excitation of Bloch modes by dipole sources has been described, which allows for a numerical calculation of the dyadic Green's function and thus of the local density of states in photonic crystal structures.

We have in detail analyzed the impact from perfectly matched layer boundary conditions and the size of the computational domain for the problem of dipole emission in a photonic crystal membrane waveguide. We have used existing formulations of perfectly matched layers and systematically varied the parameters of these as well as the domain size to estimate the associated computational errors on the dipole emission. The error on the coupling to the guided mode is relatively small, $\sim 5\%$, when the size of the domain is varied, while the error in computing the coupling to the radiation modes is more substantial, $\sim 20\%$. The important figure of merit, the β factor, however is dominated by the guided mode coupling due to dielectric screening in the photonic crystal membrane, and this quantity generally exhibits the smallest computational error, $\sim 1\%$, with the domain size. *In addition*, errors from spatial and Fourier discretization should be estimated and included. In other situations where the radiation mode coupling is the important contribution, the relatively large uncertainty on this quantity will manifest itself more clearly. As an example of a problem that is dominated by this radiation mode contribution, preliminary calculations of the Q factor of a photonic crystal membrane cavity (not reported in the thesis) have shown an extreme sensitivity to both perfectly matched layer parameters, domain size, and Fourier resolution, with errors in some cases exceeding 100%. This illustrates the complexity in *accurate* modeling of full 3D photonic crystal membrane structures.

Convergence and error investigations as those reported here are found very sparsely in the literature, probably because they are tedious to carry out. It is our impression that in many cases computational errors from the finite domain size are not estimated and thus could dominate over physical effects. *It is the hope of the author that the results in this thesis will increase the awareness of the problem of convergence, domain size, and error estimates, and that more serious and systematic estimates of computational uncertainties will be included in the photonics literature in the future.*

Photonic crystal waveguides, slow light effects, and coupled cavity-waveguide structures We have focused on photonic crystal waveguide structures, to which additional features have been added; (a) one or two side-coupled cavities, (b) a side-coupled cavity and a scattering site in the waveguide, (c) material gain in part of the photonic crystal, and (d) a dipole source. These structures have been investigated computationally and theoretically, and in (d) external collaborators have additionally provided preliminary experimental results. In (a), we have introduced quasi-normal modes as a natural framework for describing leaky cavities. We have developed original techniques for computing and normalizing quasi-normal modes in extended systems, and we have demonstrated that a single (one cavity) or two (two cavities) quasi-normal modes constitute an accurate basis for describing the local density of states semi-analytically in these structures. This contribution thus extends the use of quasi-normal modes from isolated resonators, previously reported in the literature, to extended systems, which might find applications in analysis of integrated optical circuits. In (b), we have demonstrated that the shape of the transmission spectrum can be controlled by varying the cavity-scattering site distance, which might be a stepping stone towards the development of energy-efficient photonic crystal optical switches. In (c), we have presented an original coupled Bloch mode model for analyzing active photonic crystal waveguides in the slow light regime, with material gain treated as a perturbation and including back-coupling that is typically

neglected. The model predicts a maximum amplification of $\sim 20 - 25$ dB, and that at larger material gain, the amplification starts to decrease due to strong back-coupling, which puts fundamental limitations on the maximum achievable amplification. Finally, in (d), we have analyzed photonic crystal membranes in the scope of single-photon emission into waveguides. This work has been part of a collaboration with external partners, that fabricate position-controlled quantum dots inside photonic crystals, and the theoretical work has focused on design of waveguides for spectral matching of guided modes with quantum dot emission. The effect of structural photonic crystal parameters on the waveguide dispersion has been analyzed in detail, demonstrating that we can tune the quantum dot emission lines from the fast light region to the slow light region and further into the bandgap. We have also presented the trends of both spectra and spatial maps of guided and radiation mode coupling as well as of the β factor, and these demonstrate that β approaches unity towards the band edge and stays in excess of 50% even when detuned spectrally and spatially from the optimum situation.

Finally, disjoint from the investigations of photonic crystals, we have investigated the localized surface plasmon modes of plasmonic dimers consisting of pairs of nanosize gold and silver spheres. These have been investigated computationally and experimentally, and we have systematically mapped out the dependence of the plasmon wavelength with particle distance in the sub-radius distance range. This has shown an almost-inverse scaling of the relative shift with distance, which is a scaling not found when treating the sub-wavelength sized particles as polarizable dipoles. These insights could find application in the development of nanoparticle-based biological sensors.

Outlook

The applications of the computational Bloch mode framework demonstrate its feasibility for analysis and design of photonic crystal waveguide structures, where the access to individual Bloch modes and associated scattering matrix coefficients represent significant advantages compared to the finite-difference time-domain and finite element methods. At the same time, the framework has some limitations, which might restrict its usefulness for systematic design of full 3D photonic crystal membrane structures. Most importantly, the local plane wave, or Fourier series, expansion of the Bloch modes is inefficient for representing material and field component discontinuities, as large numbers of plane waves need to be included for convergence. In 2D structures, convergence with respect to the plane wave resolution can be obtained, but when extending to 3D structures, practical limits are reached before satisfactory convergence is obtained. The problem of fine resolution in 3D structures is not specific to the method used here; similar fine spatial resolutions are required with the finite-difference time-domain and finite element methods. However, with those methods and in particular commercial software implementing these, efficient parallelization allows to handle these on multi-core computing clusters, where > 100 cores can be exploited *efficiently*. At present, as we crank up the Fourier resolution in 3D computations, the matrices that define the Bloch mode eigenvalue problem and scattering matrices grow accordingly and cannot efficiently exploit $\gg 10$ cores. *A means for splitting these large matrix problems into smaller and parallelizable parts appears indispensable to make the method competitive for 3D problems.*

With any computational method, design based on numerical simulations of full 3D structures is extremely demanding, and the development of simplified, yet accurate, models is thus of great practical interest. The semi-analytical quasi-normal mode theory for the local density of states in photonic crystal cavities reported in this thesis is one

such example. We have validated this model in 2D systems, but the extension to 3D systems is, at the formal level, straightforward. This extension is demanding in the once-and-for-all computation and normalization of the quasi-normal modes, but once this is done, it allows for transparent (and fast compared to full numerical simulations) analysis of dipole emission in photonic crystal membrane cavities, for example coupled to a waveguide. *An important question here is how the partial coupling to guided and to radiation modes can be handled within the quasi-normal mode theory.* As the quasi-normal modes can be represented in the Bloch mode basis, the guided mode contribution to the semi-analytical local density of states expansion can likely be retrieved straightforwardly. Another example of a simple and effective model is the coupled Bloch mode model for analyzing slow light photonic crystal waveguide amplifiers, and *it appears natural to combine this model with a similar model for disorder in photonic crystals [57] for a rigorous and efficient analysis of both slow light amplifiers and lasers [62, 186].*

Finally, we mention recent proposals and demonstrations of directional emission of single-photons from quantum dots in photonic crystal waveguides, where spin degrees of freedom in the quantum dots are exploited [37, 38, 248]. *It would be appealing to pursue similar problems with position-controlled quantum dots, as also here efficient spatial matching of the emitter with the optical mode plays a key role.*

APPENDIX A

Photonics engineering in nanostructures

A.1 Dipole power emission and local density of states spectra in bulk

In this appendix, we state the powers emitted by point sources (dipoles) in bulk in both 2D and 3D. By inserting the dipole current density from Eq. (3.14) into the RHS of Poynting's theorem, Eq. (2.6a), we get an expression for the dipole power emission in a general structure

$$P_{\mathrm{D}} = -\frac{1}{2}\mathrm{Re}\left[\mathbf{j}_{\mathrm{D}}^{*} \cdot \mathbf{E}_{\mathrm{D}}(\mathbf{r}_{\mathrm{D}})\right], \tag{A.1}$$

where $\mathbf{E}_{\mathrm{D}}(\mathbf{r}_{\mathrm{D}})$ is the electric field produced by the dipole at the position of the dipole. This field can be expressed in terms of the dyadic Green's function, cf. Eq. (2.11), from which the dipole power emission becomes

$$P_{\mathrm{D}} = \frac{\omega\mu_0}{2}\mathrm{Im}\left[\mathbf{G}^{\alpha\alpha}(\mathbf{r}_{\mathrm{D}}, \mathbf{r}_{\mathrm{D}}; \omega)\right] |\mathbf{j}_{\mathrm{D}}|^2, \tag{A.2}$$

Case	$P_{\mathrm{Bulk}}(\omega)$	$\rho_{\mathrm{Bulk}}(\omega)$
3D	$\frac{\sqrt{\epsilon}}{12\pi\epsilon_0}\frac{\omega^2}{\mathrm{c}^3}\lvert\mathbf{j}_{\mathrm{D}}\rvert^2$	$\frac{\sqrt{\epsilon}}{3\pi^2}\frac{\omega^2}{\mathrm{c}^3}$
2D TE	$\frac{\omega\mu_0}{8}\lvert\mathbf{j}_{\mathrm{D}}\rvert^2$	$\frac{\omega}{2\pi\mathrm{c}^2}$
2D TM	$\frac{\omega\mu_0}{16}\lvert\mathbf{j}_{\mathrm{D}}\rvert^2$	$\frac{\omega}{4\pi\mathrm{c}^2}$

Table A.1 Dipole power emission and LDOS spectra in 2D and 3D bulk.

where the dipole is oriented along the direction α. This is a general expression for the power radiated by a dipole in an arbitrary system. In 2D and 3D bulk, the dyadic Green's function can be expressed in closed form [249], and using these expressions we state the bulk dipole power and LDOS [cf. Eq. (2.13)] in Table A.1.

APPENDIX B

Bloch mode expansion technique for periodic photonic structures

B.1 Layer eigenmode eigenvalue problem

In this appendix, we derive the layer eigenmode eigenvalue equation in Eq. (3.4), following essentially the procedures from [76, 77, 80]. The starting point is the two Maxwell curl equations, Eqs. (2.5a) and (2.5b), that in Cartesian coordinates and without sources read as follows

$$\partial_y E_z - \partial_z E_y = \mathrm{i}\omega\mu_0 H_x, \tag{B.1a}$$
$$\partial_z E_x - \partial_x E_z = \mathrm{i}\omega\mu_0 H_y, \tag{B.1b}$$
$$\partial_x E_y - \partial_y E_x = \mathrm{i}\omega\mu_0 H_z, \tag{B.1c}$$
$$\partial_y H_z - \partial_z H_y = -\mathrm{i}\omega\epsilon_0\epsilon E_x, \tag{B.1d}$$
$$\partial_z H_x - \partial_x H_z = -\mathrm{i}\omega\epsilon_0\epsilon E_y, \tag{B.1e}$$
$$\partial_x H_y - \partial_y H_x = -\mathrm{i}\omega\epsilon_0\epsilon E_z. \tag{B.1f}$$

We express H_z and E_z from Eqs. (B.1c) and (B.1f), respectively,

$$H_z = -\frac{\mathrm{i}}{\omega\mu_0}\left(\partial_x E_y - \partial_y E_x\right), \tag{B.2a}$$
$$E_z = \frac{\mathrm{i}}{\omega\epsilon_0}\frac{1}{\epsilon}\left(\partial_x H_y - \partial_y H_x\right), \tag{B.2b}$$

which we insert into Eqs. (B.1a), (B.1b), (B.1d) and (B.1e) to obtain four coupled equations for the lateral components of $\mathbf{E}$ and $\mathbf{H}$

$$\frac{\mathrm{i}}{\omega\epsilon_0}\partial_y\left[\frac{1}{\epsilon}\left(\partial_x H_y - \partial_y H_x\right)\right] - \partial_z E_y = \mathrm{i}\omega\mu_0 H_x, \tag{B.3a}$$

$$\partial_z E_x - \frac{\mathrm{i}}{\omega\epsilon_0}\partial_x\left[\frac{1}{\epsilon}\left(\partial_x H_y - \partial_y H_x\right)\right] = \mathrm{i}\omega\mu_0 H_y, \tag{B.3b}$$

$$-\frac{\mathrm{i}}{\omega\mu_0}\partial_y\left[\partial_x E_y - \partial_y E_x\right] - \partial_z H_y = -\mathrm{i}\omega\epsilon_0\epsilon E_x, \tag{B.3c}$$

$$\partial_z H_x + \frac{\mathrm{i}}{\omega\mu_0}\partial_x\left[\partial_x E_y - \partial_y E_x\right] = -\mathrm{i}\omega\epsilon_0\epsilon E_y. \tag{B.3d}$$

In matrix form, these equations read as follows

$$\begin{bmatrix} -\partial_x\frac{1}{\epsilon}\partial_y & \partial_x\frac{1}{\epsilon}\partial_x + k_0^2 \\ -k_0^2 - \partial_y\frac{1}{\epsilon}\partial_y & \partial_y\frac{1}{\epsilon}\partial_x \end{bmatrix}\begin{bmatrix} H_x \\ H_y \end{bmatrix} = -\mathrm{i}\omega\epsilon_0\partial_z\begin{bmatrix} E_x \\ E_y \end{bmatrix}, \tag{B.4a}$$

$$\begin{bmatrix} \partial_x\partial_y & -\partial_x^2 - k_0^2\epsilon \\ k_0^2\epsilon + \partial_y^2 & -\partial_y\partial_x \end{bmatrix}\begin{bmatrix} E_x \\ E_y \end{bmatrix} = -\mathrm{i}\omega\mu_0\partial_z\begin{bmatrix} H_x \\ H_y \end{bmatrix}. \tag{B.4b}$$

The differential operators on the LHSs and RHSs in Eqs. (B.4) depend only on $\mathbf{r}_\perp$ and z, respectively, and all field components hence acquire the z-dependence $\sim \exp\left(\pm\mathrm{i}\beta z\right)$, yielding

$$\begin{bmatrix} -\partial_x\frac{1}{\epsilon}\partial_y & \partial_x\frac{1}{\epsilon}\partial_x + k_0^2 \\ -k_0^2 - \partial_y\frac{1}{\epsilon}\partial_y & \partial_y\frac{1}{\epsilon}\partial_x \end{bmatrix}\begin{bmatrix} H_x \\ H_y \end{bmatrix} = \pm\beta\omega\epsilon_0\begin{bmatrix} E_x \\ E_y \end{bmatrix}, \tag{B.5a}$$

$$\begin{bmatrix} \partial_x\partial_y & -\partial_x^2 - k_0^2\epsilon \\ k_0^2\epsilon + \partial_y^2 & -\partial_y\partial_x \end{bmatrix}\begin{bmatrix} E_x \\ E_y \end{bmatrix} = \pm\beta\omega\mu_0\begin{bmatrix} H_x \\ H_y \end{bmatrix}, \tag{B.5b}$$

where it is implied that $E_x \equiv E_x(\mathbf{r}_\perp)$ and similarly for all other field components. To solve Eqs. (B.5), we expand the relative permittivity and the lateral field components in plane waves, or Fourier series, in the lateral coordinates as given in Eqs. (3.3). In a given layer q with $\epsilon(\mathbf{r}_\perp) = \epsilon^q(\mathbf{r}_\perp)$ specified, the corresponding Fourier coefficients, $\hat{\epsilon}_{j;n}$, are obtained by straightforward inversion of Eq. (3.3a)

$$\hat{\epsilon}_{j;n} = \frac{1}{d_x d_y}\int_{d_x}\int_{d_y}\epsilon(x,y)\exp\left[-\mathrm{i}\left(k_j^x x + k_n^y y\right)\right]\,\mathrm{d}y\,\mathrm{d}x. \tag{B.6}$$

We insert the expansions in Eqs. (3.3) into Eqs. (B.5), which, following [80], produces the coupled Fourier space equations

$$\mathbf{F}\begin{bmatrix} \mathbf{h}^x \\ \mathbf{h}^y \end{bmatrix} \equiv \begin{bmatrix} \mathbf{k}^x\boldsymbol{\epsilon}^{-1}\mathbf{k}^y & -\mathbf{k}^x\boldsymbol{\epsilon}^{-1}\mathbf{k}^x + k_0^2\mathbf{I} \\ -k_0^2\mathbf{I} + \mathbf{k}^y\boldsymbol{\epsilon}^{-1}\mathbf{k}^y & -\mathbf{k}^y\boldsymbol{\epsilon}^{-1}\mathbf{k}^x \end{bmatrix}\begin{bmatrix} \mathbf{h}^x \\ \mathbf{h}^y \end{bmatrix} = \pm\beta\omega\epsilon_0\begin{bmatrix} \mathbf{e}^x \\ \mathbf{e}^y \end{bmatrix}, \tag{B.7a}$$

$$\mathbf{G}\begin{bmatrix} \mathbf{e}^x \\ \mathbf{e}^y \end{bmatrix} \equiv \begin{bmatrix} -\mathbf{k}^x\mathbf{k}^y & \left(\mathbf{k}^x\right)^2 - k_0^2\boldsymbol{\epsilon}^y \\ k_0^2\boldsymbol{\epsilon}^x - \left(\mathbf{k}^y\right)^2 & \mathbf{k}^y\mathbf{k}^x \end{bmatrix}\begin{bmatrix} \mathbf{e}^x \\ \mathbf{e}^y \end{bmatrix} = \pm\beta\omega\mu_0\begin{bmatrix} \mathbf{h}^x \\ \mathbf{h}^y \end{bmatrix}. \tag{B.7b}$$

where $\mathbf{k}^\alpha$ is a diagonal matrix with diagonal elements k_j^α, and where $\boldsymbol{\epsilon}$ is a generalized Toeplitz matrix with elements $\hat{\epsilon}_{j-j';n-n'}$. The matrices $\boldsymbol{\epsilon}^x$ and $\boldsymbol{\epsilon}^y$ are special Toeplitz matrices that use the correct Fourier factorization rules, due to Li [80], and that are constructed numerically as discussed in [81]. Solving Eq. (B.7b) for the transverse magnetic field Fourier coefficients, $[\mathbf{h}^x\ \mathbf{h}^y]^{\mathrm{T}}$, and inserting this into Eq. (B.7a) produces the eigenvalue equation in Eq. (3.4).

B.2 Eigenmode R- and T-matrices

In this appendix, we derive the explicit expressions for the eigenmode single-interface R- and T-matrices in Eqs. (3.7). We assume to illuminate the interface with the $\hat{\zeta}$th eigenmode, $u_\zeta^q = \delta_{\zeta,\hat{\zeta}}$ and $d_\zeta^{q+1} = 0$, and match the lateral field components [see Eqs. (3.5)] on either side of the interface at $z = z_{q,q+1}$

$$\sum_\zeta \mathbf{E}^q_{\perp,\zeta}(\mathbf{r}_\perp)\left[\delta_{\zeta,\hat{\zeta}}\exp\left(\mathrm{i}\beta_\zeta^q(z_{q,q+1}-z_{q-1,q})\right)+d_\zeta^q\right] = \sum_\zeta \mathbf{E}^{q+1}_{\perp,\zeta}(\mathbf{r}_\perp)u_\zeta^{q+1}, \tag{B.8a}$$

$$\sum_\zeta \mathbf{H}^q_{\perp,\zeta}(\mathbf{r}_\perp)\left[\delta_{\zeta,\hat{\zeta}}\exp\left(\mathrm{i}\beta_\zeta^q(z_{q,q+1}-z_{q-1,q})\right)-d_\zeta^q\right] = \sum_\zeta \mathbf{H}^{q+1}_{\perp,\zeta}(\mathbf{r}_\perp)u_\zeta^{q+1}. \tag{B.8b}$$

We then replace the unknown eigenmode amplitudes using Eqs. (3.6)

$$\sum_\zeta \mathbf{E}^q_{\perp,\zeta}(\mathbf{r}_\perp)\left[\delta_{\zeta,\hat{\zeta}}+R^{q,q+1}_{\zeta,\hat{\zeta}}\right] = \sum_\zeta \mathbf{E}^{q+1}_{\perp,\zeta}(\mathbf{r}_\perp)T^{q,q+1}_{\zeta,\hat{\zeta}}, \tag{B.9a}$$

$$\sum_\zeta \mathbf{H}^q_{\perp,\zeta}(\mathbf{r}_\perp)\left[\delta_{\zeta,\hat{\zeta}}-R^{q,q+1}_{\zeta,\hat{\zeta}}\right] = \sum_\zeta \mathbf{H}^{q+1}_{\perp,\zeta}(\mathbf{r}_\perp)T^{q,q+1}_{\zeta,\hat{\zeta}}. \tag{B.9b}$$

The eigenmodes are expanded on the *same* plane waves in each layer [cf. Eqs. (3.3)] that we can readily match (see Appendix B.3) by replacing the lateral field components with their Fourier coefficient matrices

$$\sum_\zeta \mathbf{e}_\zeta^q\left[\delta_{\zeta,\hat{\zeta}}+R^{q,q+1}_{\zeta,\hat{\zeta}}\right] = \sum_\zeta \mathbf{e}_\zeta^{q+1}T^{q,q+1}_{\zeta,\hat{\zeta}}, \tag{B.10a}$$

$$\sum_\zeta \mathbf{h}_\zeta^q\left[\delta_{\zeta,\hat{\zeta}}-R^{q,q+1}_{\zeta,\hat{\zeta}}\right] = \sum_\zeta \mathbf{h}_\zeta^{q+1}T^{q,q+1}_{\zeta,\hat{\zeta}}, \tag{B.10b}$$

where $\mathbf{e}_\zeta^q$ are the eigenvectors from Eq. (3.4). In matrix form these equations read

$$\mathbf{e}^q\left(\mathbf{I}+\mathbf{R}^{q,q+1}\right) = \mathbf{e}^{q+1}\mathbf{T}^{q,q+1}, \tag{B.11a}$$

$$\mathbf{h}^q\left(\mathbf{I}-\mathbf{R}^{q,q+1}\right) = \mathbf{h}^{q+1}\mathbf{T}^{q,q+1}, \tag{B.11b}$$

and the reflection and transmission matrices are hence determined as in Eqs. (3.7).

B.3 Plane wave matching at layer interface

The aim of this appendix is to show that Eqs. (B.10) is an equivalent way of expressing Eqs. (B.9). We show this for the electric field equations, with the magnetic field equations following from the same arguments. The starting point is to express the eigenmode electric field profile as follows

$$\mathbf{E}^q_{\perp,\zeta}(\mathbf{r}_\perp) = \mathbf{P}^{\mathrm{T}}\cdot\mathbf{e}_\zeta^q, \tag{B.12}$$

where $\mathbf{P}$ is the vector containing twice the plane waves included in the expansions in Eqs. (3.3); once for the x- and once for the y-components of the electric field. The vector $\mathbf{e}_\zeta^q$ is an eigenvector from Eq. (3.4). We insert this into both sides of Eq. (B.9a) and find

$$\sum_\zeta \mathbf{P}^{\mathrm{T}}\cdot\mathbf{e}_\zeta^q\left[\delta_{\zeta,\hat{\zeta}}+R^{q,q+1}_{\zeta,\hat{\zeta}}\right] = \sum_\zeta \mathbf{P}^{\mathrm{T}}\cdot\mathbf{e}_\zeta^{q+1}T^{q,q+1}_{\zeta,\hat{\zeta}}, \tag{B.13}$$

where importantly the plane wave vector, $\mathbf{P}$, does *not* depend on the layer index, neither on the eigenmode index ζ. Hence, we can factor it out of the equation

$$\mathbf{P}^{\mathrm{T}} \cdot \Big\{ \sum_{\zeta} \mathbf{e}_{\zeta}^{q} \left[\delta_{\zeta,\hat{\zeta}} + R_{\zeta,\hat{\zeta}}^{q,q+1} \right] = \sum_{\zeta} \mathbf{e}_{\zeta}^{q+1} T_{\zeta,\hat{\zeta}}^{q,q+1} \Big\}, \tag{B.14}$$

and the expression inside the curled brackets is exactly Eq. (B.10a).

B.4 S-matrix iteration scheme

In this appendix, we state the multi-layer S-matrix iteration scheme, as derived and expressed in [23]. The "forward" iteration scheme is

$$\mathbf{SR}^{1,q+1} = \mathbf{SR}^{1,q} + \mathbf{ST}^{q,1}\mathbf{P}^{q,-}\mathbf{R}^{q,q+1}\mathbf{P}^{q,+} \left[\mathbf{I} - \mathbf{M}_{\mathrm{for}}^{q}\right]^{-1} \mathbf{ST}^{1,q}, \tag{B.15aa}$$

$$\mathbf{ST}^{1,q+1} = \mathbf{T}^{q,q+1}\mathbf{P}^{q,+} \left[\mathbf{I} - \mathbf{M}_{\mathrm{for}}^{q}\right]^{-1} \mathbf{ST}^{1,q}, \tag{B.15ab}$$

$$\mathbf{SR}^{q+1,1} = \mathbf{R}^{q+1,q} + \mathbf{T}^{q,q+1}\mathbf{P}^{q,+} \left[\mathbf{I} - \mathbf{M}_{\mathrm{for}}^{q}\right]^{-1} \mathbf{SR}^{q,1}\mathbf{P}^{q,-}\mathbf{T}^{q+1,q}, \tag{B.15ac}$$

$$\begin{aligned}\mathbf{ST}^{q+1,1} = {} & \mathbf{ST}^{q,1}\mathbf{P}^{q,-}\mathbf{T}^{q+1,q} \\ & + \mathbf{ST}^{q,1}\mathbf{P}^{q,-}\mathbf{R}^{q,q+1}\mathbf{P}^{q,+} \left[\mathbf{I} - \mathbf{M}_{\mathrm{for}}^{q}\right]^{-1} \mathbf{SR}^{q,1}\mathbf{P}^{q,-}\mathbf{T}^{q+1,q},\end{aligned} \tag{B.15ad}$$

$$\mathbf{M}_{\mathrm{for}}^{q} \equiv \mathbf{SR}^{q,1}\mathbf{P}^{q,-}\mathbf{R}^{q,q+1}\mathbf{P}^{q,+}, \tag{B.15ae}$$

and the "backward" iteration scheme is

$$\mathbf{SR}^{q-1,Q} = \mathbf{R}^{q-1,q} + \mathbf{T}^{q,q-1}\mathbf{P}^{q,-}\mathbf{SR}^{q,Q}\mathbf{P}^{q,+} \left[\mathbf{I} - \mathbf{M}_{\mathrm{back}}^{q}\right]^{-1} \mathbf{T}^{q-1,q}, \tag{B.15ba}$$

$$\mathbf{ST}^{q-1,Q} = \mathbf{ST}^{q,Q}\mathbf{P}^{q,+} \left[\mathbf{I} - \mathbf{M}_{\mathrm{back}}^{q}\right]^{-1} \mathbf{T}^{q-1,q}, \tag{B.15bb}$$

$$\mathbf{SR}^{Q,q-1} = \mathbf{SR}^{Q,q} + \mathbf{ST}^{q,Q}\mathbf{P}^{q,+} \left[\mathbf{I} - \mathbf{M}_{\mathrm{back}}^{q}\right]^{-1} \mathbf{R}^{q,q-1}\mathbf{P}^{q,-}\mathbf{ST}^{Q,q}, \tag{B.15bc}$$

$$\begin{aligned}\mathbf{ST}^{Q,q-1} = {} & \mathbf{T}^{q,q-1}\mathbf{P}^{q,-}\mathbf{ST}^{Q,q} \\ & + \mathbf{T}^{q,q-1}\mathbf{P}^{q,-}\mathbf{SR}^{q,Q}\mathbf{P}^{q,+} \left[\mathbf{I} - \mathbf{M}_{\mathrm{back}}^{q}\right]^{-1} \mathbf{R}^{q,q-1}\mathbf{P}^{q,-}\mathbf{ST}^{Q,q},\end{aligned} \tag{B.15bd}$$

$$\mathbf{M}_{\mathrm{back}}^{q} \equiv \mathbf{R}^{q,q-1}\mathbf{P}^{q,-}\mathbf{SR}^{q,Q}\mathbf{P}^{q,+}, \tag{B.15be}$$

with

$$\mathbf{P}_{\zeta,\zeta'}^{q,\pm} \equiv \delta_{\zeta\zeta'} \exp\left(\mathrm{i}\beta_{\zeta}^{q}(z_{q,q+1} - z_{q-1,q})\right). \tag{B.15c}$$

In these equations, S-matrices with neighboring superscripts are single-interface R- or T-matrices; $\mathbf{SR}^{1,2}$, for example, denotes the single-interface R-matrix, $\mathbf{SR}^{1,2} \equiv \mathbf{R}^{1,2}$. For computational efficiency and speed, it is beneficial to reuse matrices in each iteration, e.g. by only computing the matrix $\mathbf{P}^{q,+}\left[\mathbf{I} - \mathbf{M}_{\mathrm{for}}^{q}\right]^{-1}$ $\left[\mathbf{P}^{q,+}\left[\mathbf{I} - \mathbf{M}_{\mathrm{back}}^{q}\right]^{-1}\right]$ once per iteration in Eqs. (B.15a) [Eqs. (B.15b)].

B.5 Supercell S-matrices

In this appendix, we express explicitly the supercell S-matrices, $\mathbf{S}^w_{ij}$, that are introduced in Eq. (3.11). By inspection of Eqs. (3.8), (3.9), and (3.11), these S-matrices are

$$\mathbf{S}^w_{11} = \mathbf{S}\mathbf{T}^{q,q+N_1^w}\mathbf{P}^{q,+}, \tag{B.16a}$$

$$\mathbf{S}^w_{12} = \mathbf{S}\mathbf{R}^{q+N_1^w,q}, \tag{B.16b}$$

$$\mathbf{S}^w_{21} = \mathbf{P}^{q,-}\mathbf{S}\mathbf{R}^{q,q+N_1^w}\mathbf{P}^{q,+}, \tag{B.16c}$$

$$\mathbf{S}^w_{22} = \mathbf{P}^{q,-}\mathbf{S}\mathbf{T}^{q+N_1^w,q}. \tag{B.16d}$$

All involved matrices are defined in Appendix B.4.

B.6 Bloch mode R-, T- and S-matrices

In this appendix, we establish the Bloch mode R-, T- and S-matrix formalism. The starting point is an expansion of the lateral components of the electric and magnetic fields in periodic section w on Bloch modes [see Eqs. (3.17)] that, in turn, are expanded on eigenmodes [see Eqs. (3.9)]

$$\begin{aligned}\mathbf{E}^w_\perp(\mathbf{r}_\perp, z) = \sum_\zeta \mathbf{E}^q_{\perp,\zeta}(\mathbf{r}_\perp) \sum_\gamma \Big\{ & a^w_\gamma \left[u^{q,+}_{\zeta,\gamma} \exp\left(\mathrm{i}\beta^q_\zeta (z - z_{q-1,q})\right) + d^{q,+}_{\zeta,\gamma} \exp\left(-\mathrm{i}\beta^q_\zeta (z - z_{q-1,q})\right)\right] \\ & + b^w_\gamma \left[u^{q,-}_{\zeta,\gamma} \exp\left(\mathrm{i}\beta^q_\zeta (z - z_{q-1,q})\right) + d^{q,-}_{\zeta,\gamma} \exp\left(-\mathrm{i}\beta^q_\zeta (z - z_{q-1,q})\right)\right] \Big\},\end{aligned} \tag{B.17a}$$

$$\begin{aligned}\mathbf{H}^w_\perp(\mathbf{r}_\perp, z) = \sum_\zeta \mathbf{H}^q_{\perp,\zeta}(\mathbf{r}_\perp) \sum_\gamma \Big\{ & a^w_\gamma \left[u^{q,+}_{\zeta,\gamma} \exp\left(\mathrm{i}\beta^q_\zeta (z - z_{q-1,q})\right) - d^{q,+}_{\zeta,\gamma} \exp\left(-\mathrm{i}\beta^q_\zeta (z - z_{q-1,q})\right)\right] \\ & + b^w_\gamma \left[u^{q,-}_{\zeta,\gamma} \exp\left(\mathrm{i}\beta^q_\zeta (z - z_{q-1,q})\right) - d^{q,-}_{\zeta,\gamma} \exp\left(-\mathrm{i}\beta^q_\zeta (z - z_{q-1,q})\right)\right] \Big\},\end{aligned} \tag{B.17b}$$

where all sub- and superscripts and their meaning are summarized in Table 3.1. We also recall that the eigenmode profiles, $\mathbf{E}^q_{\perp,\zeta}$ and $\mathbf{H}^q_{\perp,\zeta}$, are expanded on plane waves, cf. Eqs. (3.3).

Single interface: Reflection and transmission matrices

For the single-section interface between sections w and $w+1$, illuminated from section w, we define the Bloch mode R- and T-matrices in analogy with the corresponding eigenmode R- and T-matrices in Eqs. (3.6)

$$b^w_\gamma = \sum_{\gamma'} R^{w,w+1}_{\gamma,\gamma'} \tilde{a}^w_{\gamma'}, \tag{B.18a}$$

$$a^{w+1}_\gamma = \sum_{\gamma'} T^{w,w+1}_{\gamma,\gamma'} \tilde{a}^w_{\gamma'}. \tag{B.18b}$$

where $\tilde{a}^w_\gamma = \mathbf{P}^{w,+}_{\gamma,\gamma} a^w_\gamma$, with $\mathbf{P}^{w,+}_{\gamma,\gamma}$ defined in Eq. (B.22). Using then the field expansions in Eqs. (B.17) and the above definition of the R- and T-matrices, we express the lateral

field continuity in the section interface as in Eqs. (B.10)

$$\sum_{\zeta} \mathbf{e}_{\zeta}^{q(w)} \sum_{\gamma} \left\{ \left[u_{\zeta,\gamma}^{q(w),+} + d_{\zeta,\gamma}^{q(w),+} \right] \delta_{\gamma,\hat{\gamma}} + \left[u_{\zeta,\gamma}^{q(w),-} + d_{\zeta,\gamma}^{q(w),-} \right] R_{\gamma,\hat{\gamma}}^{w,w+1} \right\}$$
$$= \sum_{\zeta} \mathbf{e}_{\zeta}^{q(w+1)} \sum_{\gamma} \left\{ \left[u_{\zeta,\gamma}^{q(w+1),+} + d_{\zeta,\gamma}^{q(w+1),+} \right] T_{\gamma,\hat{\gamma}}^{w,w+1} \right\}, \tag{B.19a}$$

$$\sum_{\zeta} \mathbf{h}_{\zeta}^{q(w)} \sum_{\gamma} \left\{ \left[u_{\zeta,\gamma}^{q(w),+} - d_{\zeta,\gamma}^{q(w),+} \right] \delta_{\gamma,\hat{\gamma}} + \left[u_{\zeta,\gamma}^{q(w),-} - d_{\zeta,\gamma}^{q(w),-} \right] R_{\gamma,\hat{\gamma}}^{w,w+1} \right\}$$
$$= \sum_{\zeta} \mathbf{h}_{\zeta}^{q(w+1)} \sum_{\gamma} \left\{ \left[u_{\zeta,\gamma}^{q(w+1),+} - d_{\zeta,\gamma}^{q(w+1),+} \right] T_{\gamma,\hat{\gamma}}^{w,w+1} \right\}, \tag{B.19b}$$

that in matrix form read as follows

$$\underbrace{\mathbf{e}^{q(w)} \left[\mathbf{u}^{q(w),+} + \mathbf{d}^{q(w),+} \right]}_{\equiv \mathbf{N}_1^{q(w),+}} + \underbrace{\mathbf{e}^{q(w)} \left[\mathbf{u}^{q(w),-} + \mathbf{d}^{q(w),-} \right]}_{\equiv \mathbf{N}_2^{q(w),-}} \mathbf{R}^{w,w+1}$$
$$= \underbrace{\mathbf{e}^{q(w+1)} \left[\mathbf{u}^{q(w+1),+} + \mathbf{d}^{q(w+1),+} \right]}_{\equiv \mathbf{N}_3^{q(w+1),+}} \mathbf{T}^{w,w+1}, \tag{B.20a}$$

$$\underbrace{\mathbf{h}^{q(w)} \left[\mathbf{u}^{q(w),+} - \mathbf{d}^{q(w),+} \right]}_{\equiv \mathbf{N}_4^{q(w),+}} + \underbrace{\mathbf{h}^{q(w)} \left[\mathbf{u}^{q(w),-} - \mathbf{d}^{q(w),-} \right]}_{\equiv \mathbf{N}_5^{q(w),-}} \mathbf{R}^{w,w+1}$$
$$= \underbrace{\mathbf{h}^{q(w+1)} \left[\mathbf{u}^{q(w+1),+} - \mathbf{d}^{q(w+1),+} \right]}_{\equiv \mathbf{N}_6^{q(w+1),+}} \mathbf{T}^{w,w+1}. \tag{B.20b}$$

The solutions of these equations can be expressed as follows

$$\mathbf{T}^{w,w+1} = \left[\left(\mathbf{N}_2^{q(w),-} \right)^{-1} \mathbf{N}_3^{q(w+1),+} - \left(\mathbf{N}_5^{q(w),-} \right)^{-1} \mathbf{N}_6^{q(w+1),+} \right]^{-1}$$
$$\times \left[\left(\mathbf{N}_2^{q(w),-} \right)^{-1} \mathbf{N}_1^{q(w),+} - \left(\mathbf{N}_5^{q(w),-} \right)^{-1} \mathbf{N}_4^{q(w),+} \right], \tag{B.21a}$$

$$\mathbf{R}^{w,w+1} = \left(\mathbf{N}_2^{q(w),-} \right)^{-1} \left[\mathbf{N}_3^{q(w+1),+} \mathbf{T}^{w,w+1} - \mathbf{N}_1^{q(w),+} \right]. \tag{B.21b}$$

These equations can be compared to Eqs. (6.167)-(6.168) in [23]; therein, the eigenmodes enter via an inner product, while here they simply enter as Fourier coefficient matrices. The R- and T-matrices for illumination from section $w+1$ onto section w, $\mathbf{R}^{w+1,w}$ and $\mathbf{T}^{w+1,w}$, are obtained as in Eqs. (B.21) by swapping w with $w+1$ and $+$ with $-$. We also note that in the special case of layers constituting the periodic sections, such that Bloch modes equal eigenmodes, the matrices $\mathbf{u}^{q(w),+}$ and $\mathbf{d}^{q(w),-}$ ($\mathbf{u}^{q(w),-}$ and $\mathbf{d}^{q(w),+}$) can be taken as identity (zero) matrices, and Eqs. (B.21) reduce to Eqs. (3.7), as expected.

Multiple interfaces: Scattering matrices

The Bloch mode expansion in periodic structures is conceptually equivalent to the eigenmode expansion in layers, and we can thus reuse the eigenmode S-matrix theory

for the Bloch modes. Specifically, we use Eqs. (B.15) and replace the layer indices q with section indices w and the eigenmode propagation matrices with the Bloch mode propagation matrices

$$\mathbf{P}^{w,\pm}_{\gamma,\gamma'} \equiv \delta_{\gamma\gamma'} \left[\exp\left(\mathrm{i}k^{w,\pm}_{z,\gamma} a\right)\right]^{\pm N^w_\mathrm{s}}, \tag{B.22}$$

where N^w_s is the number of repetitions of the supercell in periodic section w.

B.7 Dipole Bloch mode amplitudes: Single periodic section

In this appendix, we derive Eqs. (3.16) for the dipole excited Bloch mode amplitudes in a single periodic section, $w = \tilde{w}$, following [23, 28]. The starting point is the Lorentz reciprocity theorem in Eq. (2.7), and as we are interested in the fields generated by a dipole, we set $\mathbf{j}_1$ equal to the dipole current in Eq. (3.14) and $\mathbf{j}_2 = \mathbf{0}$, which simplifies Eq. (2.7) into

$$\int_S [\mathbf{E} \times \mathbf{H}_2 - \mathbf{E}_2 \times \mathbf{H}] \cdot \mathbf{n}\, \mathrm{d}S = \mathbf{j}_\mathrm{D} \cdot \mathbf{E}_2(\mathbf{r}_\mathrm{D}), \tag{B.23}$$

where $[\mathbf{E}, \mathbf{H}]$ are the dipole fields we are looking to determine. At our convenience, we take S to be a rectangular box, whose z-constant surfaces are brought arbitrarily close to the dipole source from below (at $z = z^-_\mathrm{D}$, surface S_1) and above (at $z = z^+_\mathrm{D}$, surface S_2); the extent of the x- and y-constant surfaces are then infinitesimal,[1] and only the integrations on the z-constant surfaces remain

$$\begin{aligned} &-\int_{S_1} \left[\mathbf{E}(z^-_\mathrm{D}) \times \mathbf{H}_2(z^-_\mathrm{D}) - \mathbf{E}_2(z^-_\mathrm{D}) \times \mathbf{H}(z^-_\mathrm{D})\right] \cdot \mathbf{z}\, \mathrm{d}S \\ &\qquad + \int_{S_2} \left[\mathbf{E}(z^+_\mathrm{D}) \times \mathbf{H}_2(z^+_\mathrm{D}) - \mathbf{E}_2(z^+_\mathrm{D}) \times \mathbf{H}(z^+_\mathrm{D})\right] \cdot \mathbf{z}\, \mathrm{d}S = \mathbf{j}_\mathrm{D} \cdot \mathbf{E}_2(\mathbf{r}_\mathrm{D}). \end{aligned} \tag{B.24}$$

Finally, we insert the Bloch mode expansions of the dipole excited fields $\mathbf{E}$ and $\mathbf{H}$ [Eqs. (3.15)] and let the fields $[\mathbf{E}_2, \mathbf{H}_2]$ be an arbitrary up- or downward Bloch mode, with index γ', which produces the following two equations

$$\begin{aligned} &-\sum_\gamma b^{\tilde{w}}_\gamma \int_{S_1} \left[\mathbf{E}^{\tilde{w},-}_\gamma(z^-_\mathrm{D}) \times \mathbf{H}^{\tilde{w},+}_{\gamma'}(z^-_\mathrm{D}) - \mathbf{E}^{\tilde{w},+}_{\gamma'}(z^-_\mathrm{D}) \times \mathbf{H}^{\tilde{w},-}_\gamma(z^-_\mathrm{D})\right] \cdot \mathbf{z}\, \mathrm{d}S \\ &\qquad + \sum_\gamma a^{\tilde{w}}_\gamma \int_{S_2} \left[\mathbf{E}^{\tilde{w},+}_\gamma(z^+_\mathrm{D}) \times \mathbf{H}^{\tilde{w},+}_{\gamma'}(z^+_\mathrm{D}) - \mathbf{E}^{\tilde{w},+}_{\gamma'}(z^+_\mathrm{D}) \times \mathbf{H}^{\tilde{w},+}_\gamma(z^+_\mathrm{D})\right] \cdot \mathbf{z}\, \mathrm{d}S \\ &\qquad\qquad = \mathbf{j}_\mathrm{D} \cdot \mathbf{E}^{\tilde{w},+}_{\gamma'}(\mathbf{r}_\mathrm{D}), \end{aligned} \tag{B.25a}$$

$$\begin{aligned} &-\sum_\gamma b^{\tilde{w}}_\gamma \int_{S_1} \left[\mathbf{E}^{\tilde{w},-}_\gamma(z^-_\mathrm{D}) \times \mathbf{H}^{\tilde{w},-}_{\gamma'}(z^-_\mathrm{D}) - \mathbf{E}^{\tilde{w},-}_{\gamma'}(z^-_\mathrm{D}) \times \mathbf{H}^{\tilde{w},-}_\gamma(z^-_\mathrm{D})\right] \cdot \mathbf{z}\, \mathrm{d}S \\ &\qquad + \sum_\gamma a^{\tilde{w}}_\gamma \int_{S_2} \left[\mathbf{E}^{\tilde{w},+}_\gamma(z^+_\mathrm{D}) \times \mathbf{H}^{\tilde{w},-}_{\gamma'}(z^+_\mathrm{D}) - \mathbf{E}^{\tilde{w},-}_{\gamma'}(z^+_\mathrm{D}) \times \mathbf{H}^{\tilde{w},+}_\gamma(z^+_\mathrm{D})\right] \cdot \mathbf{z}\, \mathrm{d}S \\ &\qquad\qquad = \mathbf{j}_\mathrm{D} \cdot \mathbf{E}^{\tilde{w},-}_{\gamma'}(\mathbf{r}_\mathrm{D}), \end{aligned} \tag{B.25b}$$

These equations can be expressed as in Eqs. (3.16).

[1] In [23, 250], the z-constant surfaces are taken at arbitrary z-coordinates, i.e., not necessarily infinitesimally close to the source, and periodic or Dirichlet BCs are used as an argument for the cancellation of the contributions from x- and y-constant surfaces. In [28], this cancellation is explained by a PML suppression of the fields on the x- and y-constant surfaces.

B.8 Practical evaluation of dipole power emission

When we have determined the fields from a dipole in Eq. (3.17), with Bloch mode amplitudes as in Eqs. (3.18), Eq. (2.14) allows us to obtain the modification of the SE rate or the LDOS by evaluation of the power modification. We obtain the power by evaluating either side in Poynting's theorem, Eq. (2.6a), and afterwards normalize to well-known values of the dipole emission in bulk (that are given in Appendix A.1). By inserting the dipole current density from Eq. (3.14) into the RHS of Poynting's theorem, we find that this power reduces to an electric field evaluation at the dipole position, which from Eq. (3.17) simply becomes a summation over Bloch modes evaluated at this position

$$P_{\mathrm{D}} = -\frac{1}{2}\sum_{\gamma} \mathrm{Re}\left\{\mathbf{j}_{\mathrm{D}}^{*} \cdot \left[a_{\gamma}^{\tilde{w},\mathrm{ab}}\mathbf{E}_{\gamma}^{\tilde{w},+}(\mathbf{r}_{\perp,\mathrm{D}}, z_{\mathrm{D}}) + b_{\gamma}^{\tilde{w},\mathrm{ab}}\mathbf{E}_{\gamma}^{\tilde{w},-}(\mathbf{r}_{\perp,\mathrm{D}}, z_{\mathrm{D}})\right]\right\}. \tag{B.26}$$

This expression is used when evaluating the LDOS in 2D PhCs in Chapter 5. In Chapters 4 and 8, where we consider dipole emission in 3D PhC waveguides and need to include PML BCs, we have observed that evaluation of the total emitted power using Eq. (B.26) in some cases yields unphysical results (negative powers and discontinuous spectra). Instead, we obtain the total emission power, P_{Tot}, by evaluation of the LHS of Poynting's theorem, Eq. (2.6a), where we integrate the power flux out through a box that is entirely contained within the PMLs [28]. Then, we obtain the power emitted into the guided mode, P_{G}, by evaluation as in Eq. (B.26), but with the sum only containing this guided mode. Finally, the emission into the radiation modes is obtained as $P_{\mathrm{Rad}} = P_{\mathrm{Tot}} - P_{\mathrm{G}}$. On energy conservation grounds, the size of the integration box should not matter, but we have observed some sensitivity, which in a few cases has led to negative values of P_{Rad} or computed β factors outside the range from zero to unity. This kind of sensitivity to the size of the power integration box was also observed in [17].

B.9 2D limit of Fourier modal method: TE and TM

In this appendix, we express explicitly the layer eigenmode eigenvalue problem in the 2D limit with structures that are uniform along the y axis. As explained in Section 3.5.2, only the y k-vector that equals zero, $k_{n=0}^{y}$, contributes in the plane waves expansions in Eqs. (3.3) in this case, and in the Fourier representation of the matrices $\mathbf{F}$ and $\mathbf{G}$ [Eqs. (B.7)] we can thus let $\mathbf{k}^{y} = \mathbf{0}$. Doing so, we readily obtain two independent problems, the TE and TM problems

$$\left[k_0^2\boldsymbol{\epsilon}^{y} - (\mathbf{k}^{x})^2\right]\mathbf{e}^{y} = \beta^2\mathbf{e}^{y}, \qquad \text{(TE)} \tag{B.27a}$$

$$\boldsymbol{\epsilon}^{x}\left[-\mathbf{k}^{x}\boldsymbol{\epsilon}^{-1}\mathbf{k}^{x} + k_0^2\right]\mathbf{h}^{y} = \beta^2\mathbf{h}^{y}, \qquad \text{(TM)} \tag{B.27b}$$

where the special Toeplitz matrices, $\boldsymbol{\epsilon}^{x}$ and $\boldsymbol{\epsilon}^{y}$ due to Li [80], reduce to the inverse of the Toeplitz matrix with the Fourier coefficients of $1/\epsilon(x)$ and the Toeplitz matrix with the Fourier coefficients of $\epsilon(x)$, respectively. These 2D equations thus take the well-known forms, including the correct Fourier factorization [23, 79]. The Fourier coefficients of the other field components, especially $\mathbf{h}^{x}$ in the TE and $\mathbf{e}^{x}$ in the TM case, are obtained from explicit evaluation of Eqs. (B.7) with $\mathbf{k}^{y} = \mathbf{0}$.

APPENDIX C

Boundary conditions for open photonic structures

C.1 Perfectly matched layer transformed layer eigenmode eigenvalue problem

In this appendix, we derive the versions of the matrices **F** and **G**, that enter into the layer eigenmode eigenvalue problem [Eq. (3.4)] when PMLs are included as described in Section 4.2.1. With the PML coordinate transform of the partial derivative given in Eq. (4.2), we can formulate the coupled differential equations in Eqs. (B.5) in the PML transformed space

$$\begin{bmatrix} -X\partial_{x'}\frac{1}{\epsilon}Y\partial_{y'} & X\partial_{x'}\frac{1}{\epsilon}X\partial_{x'}+k_0^2 \\ -k_0^2-Y\partial_{y'}\frac{1}{\epsilon}Y\partial_{y'} & Y\partial_{y'}\frac{1}{\epsilon}X\partial_{x'} \end{bmatrix}\begin{bmatrix} H_{x'} \\ H_{y'} \end{bmatrix} = \pm\beta\omega\epsilon_0\begin{bmatrix} E_{x'} \\ E_{y'} \end{bmatrix}, \tag{C.1a}$$

$$\begin{bmatrix} X\partial_{x'}Y\partial_{y'} & -X\partial_{x'}X\partial_{x'}-k_0^2\epsilon \\ k_0^2\epsilon+Y\partial_{y'}Y\partial_{y'} & -Y\partial_{y'}X\partial_{x'} \end{bmatrix}\begin{bmatrix} E_{x'} \\ E_{y'} \end{bmatrix} = \pm\beta\omega\mu_0\begin{bmatrix} H_{x'} \\ H_{y'} \end{bmatrix}, \tag{C.1b}$$

where X and Y are the functions defined in Eq. (4.3). Expanding these functions in Fourier series, as in Eqs. (3.3), Eqs. (C.1) become the following matrix equations in the

PML transformed Fourier space

$$\mathbf{F}\begin{bmatrix}\mathbf{h}^{x'}\\ \mathbf{h}^{y'}\end{bmatrix} \equiv \begin{bmatrix}\tilde{\mathbf{k}}^{x'}\boldsymbol{\epsilon}^{-1}\tilde{\mathbf{k}}^{y'} & -\tilde{\mathbf{k}}^{x'}\boldsymbol{\epsilon}^{-1}\tilde{\mathbf{k}}^{x'}+k_0^2\mathbf{I}\\ -k_0^2\mathbf{I}+\tilde{\mathbf{k}}^{y'}\boldsymbol{\epsilon}^{-1}\tilde{\mathbf{k}}^{y'} & -\tilde{\mathbf{k}}^{y'}\boldsymbol{\epsilon}^{-1}\tilde{\mathbf{k}}^{x'}\end{bmatrix}\begin{bmatrix}\mathbf{h}^{x'}\\ \mathbf{h}^{y'}\end{bmatrix} = \pm\beta\omega\epsilon_0\begin{bmatrix}\mathbf{e}^{x'}\\ \mathbf{e}^{y'}\end{bmatrix}, \tag{C.2a}$$

$$\mathbf{G}\begin{bmatrix}\mathbf{e}^{x'}\\ \mathbf{e}^{y'}\end{bmatrix} \equiv \begin{bmatrix}-\tilde{\mathbf{k}}^{x'}\tilde{\mathbf{k}}^{y'} & \tilde{\mathbf{k}}^{x'}\tilde{\mathbf{k}}^{x'}-k_0^2\boldsymbol{\epsilon}^{y'}\\ k_0^2\boldsymbol{\epsilon}^{x'}-\tilde{\mathbf{k}}^{y'}\tilde{\mathbf{k}}^{y'} & \tilde{\mathbf{k}}^{y'}\tilde{\mathbf{k}}^{x'}\end{bmatrix}\begin{bmatrix}\mathbf{e}^{x'}\\ \mathbf{e}^{y'}\end{bmatrix} = \pm\beta\omega\mu_0\begin{bmatrix}\mathbf{h}^{x'}\\ \mathbf{h}^{y'}\end{bmatrix}, \tag{C.2b}$$

$$\tilde{\mathbf{k}}^{x'} \equiv \mathbf{X}\mathbf{k}^{x'}, \tag{C.2c}$$

$$\tilde{\mathbf{k}}^{y'} \equiv \mathbf{Y}\mathbf{k}^{y'}, \tag{C.2d}$$

where $\mathbf{k}^{\alpha}$ is the diagonal matrix defined right after Eqs. (B.7), while $\mathbf{X}$ ($\mathbf{Y}$) is the generalized Toeplitz matrix with the Fourier coefficients of X (Y). Including the PMLs thus amounts to computing the Fourier coefficients of X and Y and redefining the Fourier representations of the differential operators, cf. Eqs. (C.2c)-(C.2d). In the trivial case of no PMLs, the matrices $\mathbf{X}$ and $\mathbf{Y}$ become unity matrices, and Eqs. (C.2), as expected, reduce to the formulation in Eqs. (B.7).

APPENDIX D

Coupled photonic crystal cavity-waveguide structures: A quasi-normal mode approach

D.1 Nonlocal boundary condition method: Convergence of quasi-normal mode frequency

For the side-coupled PhC cavity-waveguide structure introduced in Section 5.2, with $d_{\text{cav}} = 2a$, we check the validity of the single guided mode QNM BC in Eq. (5.6) by varying the size of the simulation domain along the length of the PhC waveguide. In Fig. D.1, where $L_y = 18a$ is a fixed height of the 2D domain, L_x is the variable length of the domain along the waveguide axis (the coordinate convention here, and only here, is different than in the rest of thesis). At each value of L_x, the QNM is determined, and the curves show the error of the QNM frequency, $\tilde{\omega}$, both with respect to a chosen reference, $L_{\text{max}} = 18a$ (red solid), and for successive increases of L_x (blue dashed). As is clear, the error decreases exponentially, i.e., the single guided mode approximation to the QNM becomes exponentially better as the computational domain is enlarged, consistent with the exponential decay of all other Bloch modes. In the results presented in Chapter 5, a fixed value of $L_x = 18a$ is thus used.

D.2 Heuristic explanation of quasi-normal mode field divergence

As we saw in Fig. 5.4, the QNM field amplitudes diverge in the far field in the coupled PhC cavity-waveguide systems, and this is a general property of QNMs [157]. At first

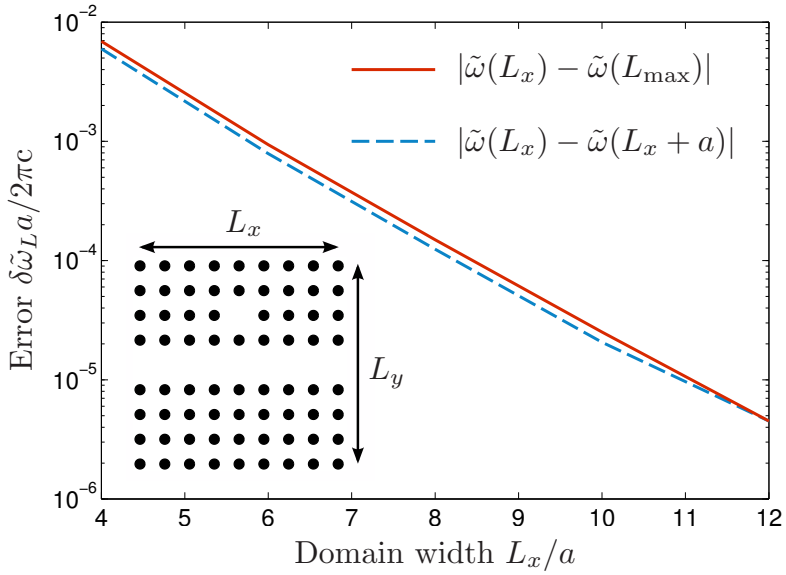

Figure D.1 FEM and nonlocal BC method: Change in QNM frequency, $\tilde{\omega}$, with increasing calculation domain length L_x as defined in the inset. The red solid curve shows the difference to a reference calculation with fixed domain size $L_{\max} = 18a$, and the blue dashed curve shows the difference between results using successively larger domain sizes. $L_y = 18a$ is a fixed domain height. Reprinted with permission from [169]. Copyright (2014) Optical Society of America

sight, this may seem unphysical, but as explained in the following it accurately reflects the properties of any resonator with a finite Q factor.

For the sake of mathematical simplicity we consider a 1D resonator of finite extent, located around $z = 0$, that is coupled to air on either side. This structure supports QNMs, and the spatial form of the QNMs far to the right of the resonator ($z \gg 0$) is $\sim \exp\left(\mathrm{i}\tilde{k}z\right)$, with $\tilde{k} = \tilde{\omega}/\mathrm{c}$; this is the Silver-Müller radiation condition in 1D. With $\mathrm{Im}\left(\tilde{\omega}\right) < 0$, this wave diverges as $z \to \infty$, but we need to include the time-dependence to fully understand the behavior of the QNM

$$E(z,t) \propto \begin{cases} \exp\left[\mathrm{i}\left(\tilde{k}z - \tilde{\omega}t\right)\right] = \exp\left[\dfrac{1}{\mathrm{c}}\left(\mathrm{iRe}\left(\tilde{\omega}\right) + \mathrm{Im}\left(\tilde{\omega}\right)\right)\left(z - \mathrm{c}t\right)\right] & 0 \ll z \leq \mathrm{c}t \\ 0 & z > \mathrm{c}t \gg 0 \end{cases}. \quad \text{(D.1)}$$

This form shows that the QNM is "the propagating front of the decaying state" [164] that at any finite time t vanishes for $z > ct \gg 0$; this is a manifestation of causality. In Fig. D.2, we plot the real part of the field in Eq. (D.1) as function of z and at three times, $t_1 < t_2 < t_3$. The outward propagating wave front is clearly observed, which, in turn, depletes the energy in the resonator, consistent with the finite Q factor of the QNM.

The illustration in Fig. D.2 describes what happens when QNMs are computed with time-domain methods like FDTD: A temporal pulse, with a given power and of finite temporal extent and thus containing a finite amount of energy, is released inside the resonator, and the fields are allowed to decay. Far from the resonator, but at finite times, the associated QNM fields look as illustrated in Fig. D.2.

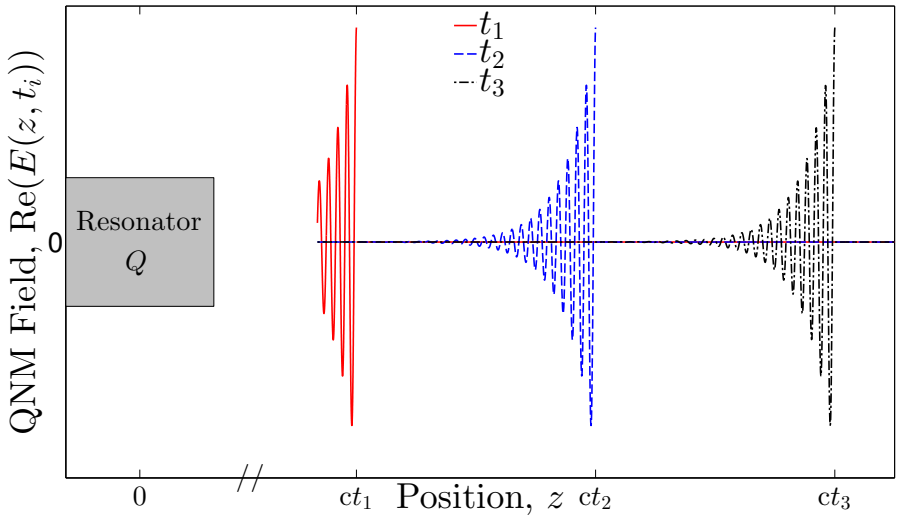

Figure D.2 Real part of the 1D QNM field in Eq. (D.1) at three times $t_1 < t_2 < t_3$, such that $0 \ll ct_i$. The arbitrary resonator, with quality factor Q, is shown schematically at $z = 0$.

D.3 Roundtrip matrix method: Convergence of quasi-normal mode frequency

For the side-coupled PhC cavity-waveguide structure introduced in Section 5.2, we here demonstrate convergence of the QNM frequency, $\mathrm{Re}\,(\tilde{\omega})$, and quality factor, Q, with the Fourier truncation, $j_{\max}$, and the number of staircase layers used to discretize each rod in the PhC lattice, $N_{\mathrm{Staircase}}$.

For a cavity-waveguide distance $d_{\mathrm{cav}} = 2a$, the top [bottom] panel in Fig. D.3 shows $\mathrm{Re}\,(\tilde{\omega})$ [Q] as function of $N_{\mathrm{Staircase}}$ and with $j_{\max}$ as a parameter. Both quantities become flat as $N_{\mathrm{Staircase}}$ increases and the curves also lie closer for increasing values of $j_{\max}$, demonstrating convergence with both parameters. For both quantities, we obtain three correct digits ($\mathrm{Re}\,(\tilde{\omega}) = 0.397$, $Q = 146$) with $j_{\max} \geq 50$ and $N_{\mathrm{Staircase}} \geq 128$, and these are therefore the values we use throughout Chapter 5.

D.4 Photonic crystal cavity in-line-coupled to waveguide: Quasi-normal mode computations with different cavity sections

In Section 5.4.1, we introduced the roundtrip matrix method for computing QNMs that relies on the definition of an internal cavity section w, see Fig. 5.3. In Section 5.2, we considered a structure with a single internal section, $w = 2$, and for which this section was naturally *and* necessarily chosen as the roundtrip cavity section. In this appendix, we look at a different structure that contains more potential cavity sections and demonstrate that choosing either leads to the same QNM.

We consider the same 2D rectangular PhC lattice with a W1 waveguide as introduced in Section 5.2.1. We remove the side-coupled cavity and instead implement an in-line cavity by surrounding a single row of the W1 waveguide by mirrors constituted of blocking elements, as shown in Fig. D.4. Sections 1 and 9 are the waveguide sections in which

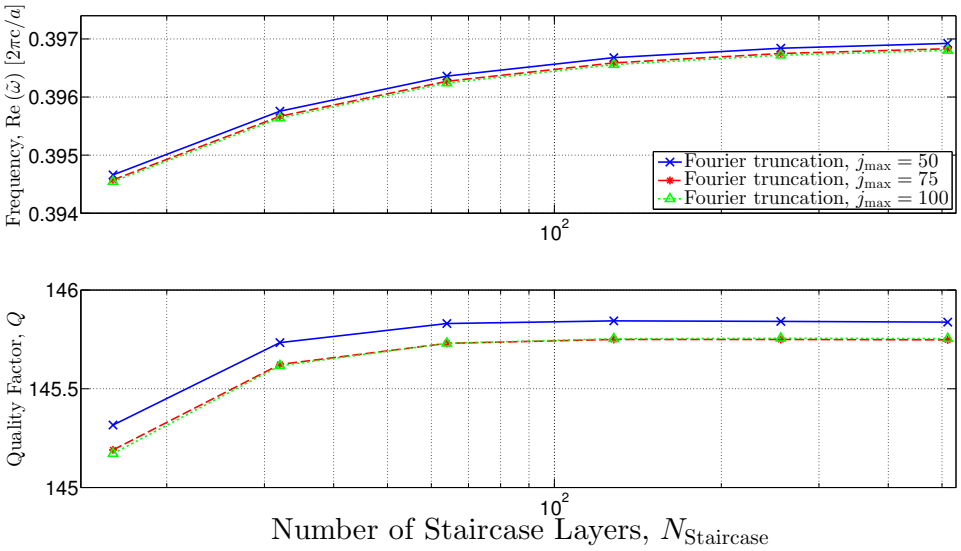

Figure D.3 Convergence for cavity side-coupled to a W1 waveguide in a 2D rectangular PhC lattice, with cavity-waveguide distance $d_{\text{cav}} = 2a$ (see Fig. 5.1). QNM frequency $\text{Re}\,(\tilde{\omega})$ (top panel) and quality factor Q (bottom panel) as function of number of staircase layers, $N_{\text{Staircase}}$, and with Fourier truncation, $j_{\max}$, as a parameter.

Cavity w	$\lvert\tilde{\omega}_5 - \tilde{\omega}_w\rvert/\lvert\tilde{\omega}_5\rvert$	$\int \lvert E_y^5 - E_y^w\rvert\,\mathrm{d}\mathbf{r} / \int \lvert E_y^5\rvert\,\mathrm{d}\mathbf{r}$
5	0	0
4	$7.8 \cdot 10^{-14}$	$1.6 \cdot 10^{-10}$
3	$3.8 \cdot 10^{-14}$	$1.3 \cdot 10^{-10}$
2	$2.4 \cdot 10^{-14}$	$3.6 \cdot 10^{-10}$

Table D.1 Relative deviations of the QNM frequencies and near-field distributions for different choices of the cavity section w for the in-line-coupled PhC cavity in Fig. D.4. The QNM frequency is $\tilde{\omega}a/(2\pi c) = 0.375 - 0.0012i$.

the QNM is outgoing and diverging, and sections 2, 3, and 4 (6, 7, and 8) constitute the bottom (top) mirror surrounding the central cavity section 5. Additionally, we vary the refractive indices of the blocking elements in the waveguide in sections 2, 3, 4, 6, 7 and 8 linearly as

$$n_w = n_{\text{Back}} + \Delta_w \left(n_{\text{Rods}} - n_{\text{Back}}\right), \tag{D.2a}$$

$$\Delta_2 = \Delta_8 = 0.9, \quad \Delta_3 = \Delta_7 = 0.6, \quad \Delta_4 = \Delta_6 = 0.3. \tag{D.2b}$$

with $n_{\text{Rods}} = \sqrt{\epsilon_{\text{Rods}}}$ and $n_{\text{Back}} = \sqrt{\epsilon_{\text{Back}}}$.

A QNM, with complex frequency $\tilde{\omega}a/(2\pi c) = 0.375 - 0.0012i$, may be readily calculated using Section 5 as the cavity section. However, as is apparent from the field distribution shown in Fig. D.4, the mode leaks into the surrounding mirrors, and we may use other sections as the cavity in the roundtrip matrix method for determining the QNM. We use sections 2, 3, and 4 as the cavity and determine the QNM of the structure in Fig. D.4. In Table D.1, we give the corresponding relative deviations of the QNM frequencies and the near-field distributions compared to the values obtained when using section 5 as the cavity.

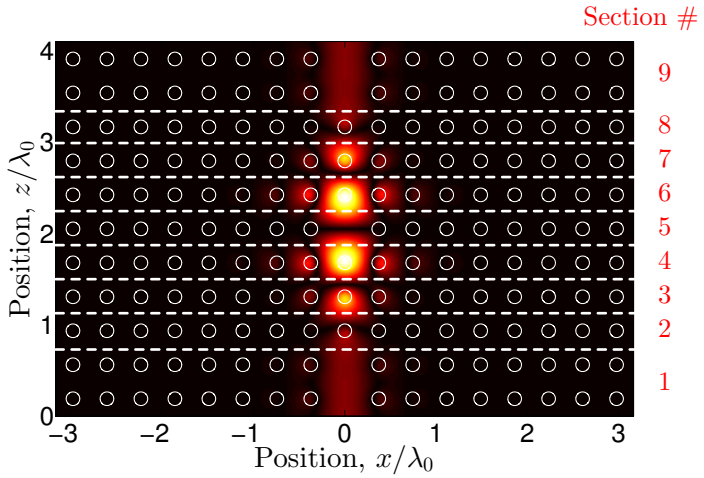

Figure D.4 QNM field distribution ($|E_y|$) in a cavity in-line-coupled to a W1 waveguide in a 2D rectangular PhC lattice. The cavity is formed by surrounding one row (section 5) by blocking elements in the waveguide, constituted by sections 2, 3, and 4 (bottom mirror) and sections 6, 7, and 8 (top mirror). The refractive index of the blocking elements is varied linearly as specified in Eqs. (D.2). The QNM is independent of the choice of cavity section, cf. Table D.1. Reprinted with permission from [87]. Copyright (2014) Optical Society of America

Both quantities are orders of magnitude smaller than unity, illustrating that different choices of the cavity section lead to the same QNM. This demonstrates the insensitivity to the choice of cavity in the roundtrip matrix method, which is an important property for structures that do not contain a well-defined cavity, e.g. the adiabatic micropillar cavity structure of [138].

APPENDIX E

Optical amplification in slow light photonic crystal waveguides

E.1 Ideal slow light gain

In the appendix, we derive the ideal slow light gain in Eq. (7.4). The starting point is the coupled Bloch mode equations, Eqs. (7.3), in the limit of no feedback, $\kappa(z) = 0$. In this case, the coupled equations uncouple, and we can write the solution for $\psi_+(L)/\psi_+(0)$ as

$$\frac{\psi_+(L)}{\psi_+(0)} = \exp\left[\frac{\mathrm{i}\omega}{\mathrm{c}} n_\mathrm{G} \chi_\mathrm{pert} \int_0^L \delta(z)\,\mathrm{d}z\right]. \tag{E.1}$$

To first order in the index perturbation, we have $\chi_\mathrm{pert} \simeq 2\mathrm{i}n_\mathrm{s}n_\mathrm{i} = -\mathrm{i}g_0 n_\mathrm{s}\mathrm{c}/\omega$, from which the above relation becomes

$$\frac{\psi_+(L)}{\psi_+(0)} = \exp\left(g_0 n_\mathrm{G} n_\mathrm{s} \tilde{\delta} L\right). \tag{E.2}$$

where we also exploited the slow variation of $\delta(z)$ over the extent of a supercell [251] to replace it by a supercell average, $\tilde{\delta} \equiv 1/a \int_0^a \delta(z)\,\mathrm{d}z$. Finally, by inserting the expression for $\delta(z)$ we find the ideal slow light gain

$$T_\mathrm{Ideal} \equiv \left|\frac{\psi_+(L)}{\psi_+(0)}\right|^2 = \exp\left(\Gamma \frac{n_\mathrm{G}}{n_\mathrm{s}} g_0 L\right), \tag{E.3a}$$

$$\Gamma \equiv \frac{2n_\mathrm{s}^2 \int_\mathrm{uc} \epsilon_0 F(\mathbf{r})|\mathbf{e}|^2\,\mathrm{d}V}{\int_\mathrm{uc} \left[\epsilon_0 \epsilon_\mathrm{B}(\mathbf{r})|\mathbf{e}|^2 + \mu_0|\mathbf{h}|^2\right]\,\mathrm{d}V}, \tag{E.3b}$$

where Γ is a generalized confinement factor that accounts for the mode overlap with the active material [187].

APPENDIX F

Single-photon emission in photonic crystal waveguides

F.1 Dispersion curves: Computational parameters

In Fig. F.1, we display data for the dispersion of the guided E_x even-even modes of the PhC membrane that we investigate more systematically in Section 8.3 (radius $r/a = 0.28$, no shift of holes $s_{\text{inner}} = 0$ and membrane thickness $L_y = 250\,\text{nm}$). Based on the investigations in Chapter 4, we fix the air height to $h_{\text{SS}}/h_{\text{Mem}} = 3$, the PhC width to $d_x = 8\sqrt{3}a$, the number of staircase layers per supercell $N_{\text{l}} = 33$, but in the view of Fig. 4.6 vary the Fourier truncations, $j_{\max}$ (x) and $n_{\max}$ (y). Different marker types correspond to different values of $j_{\max}$; different colors to different values of $n_{\max}$.

The general picture is that different Fourier truncations give data that lie closer far from the band edge ($k_z/(2\pi/a) \simeq 0.4$), but that spread as the band edge ($k_z/(2\pi/a) = 0.5$) is approached. Data in the figure are computed with steps in wavelength of 1 nm, and we thus estimate that we can predict the band edge with an accuracy of 2 nm if we let $j_{\max} = 40$ and $n_{\max} = 14$; these, and the values quoted above, are the computational parameters we use in Chapter 8, unless otherwise stated.

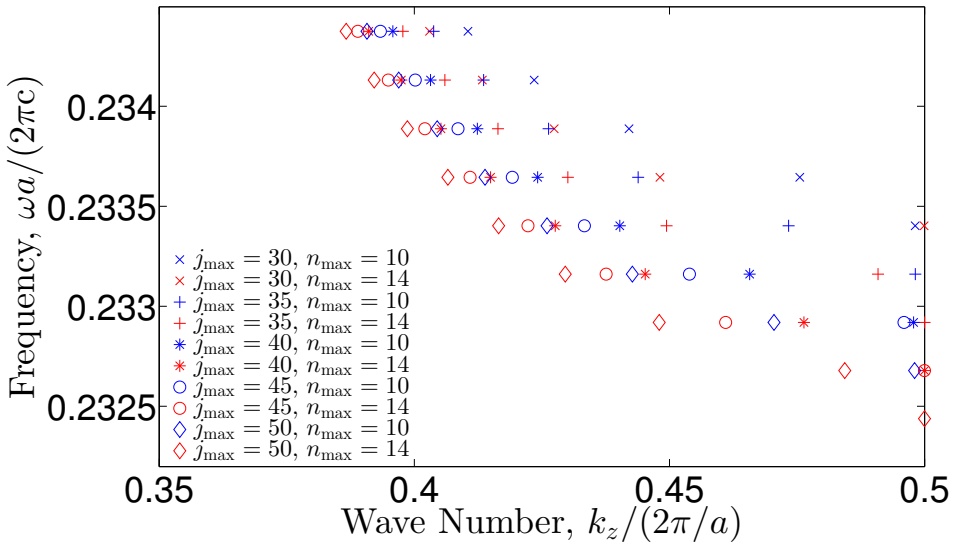

Figure F.1 Dispersion data for guided (E_x even-even) waveguide mode in GaAs PhC membrane waveguide with structural parameters as in Fig. 8.4 (radius $r/a = 0.28$, no shift of holes $s_{\text{inner}} = 0$ and membrane thickness $L_y = 250\,\text{nm}$). The x and y Fourier truncations, $j_{\max}$ and $n_{\max}$ are parameters.

Bibliography

[1] D. Miller, "Device requirements for optical interconnects to silicon chips," Proc. IEEE **97**, 1166–1185 (2009).

[2] Intel Labs, "The 50G Silicon Photonics Link," White Paper (2010).

[3] P. Coteus, J. Knickerbocker, C. Lam, and Y. Vlasov, "Technologies for exascale systems," IBM J. Res. Dev. **55**, 14:1–14:12 (2011).

[4] J. Joannopoulos, S. Johnson, J. Winn, and R. Meade, *Photonic Crystals: Molding the Flow of Light* (Princeton University Press, 2011), 2nd ed.

[5] T. F. Krauss, "Planar photonic crystal waveguide devices for integrated optics," Phys. Status Solidi A **197**, 688–702 (2003).

[6] M. Notomi, A. Shinya, K. Nozaki, T. Tanabe, S. Matsuo, E. Kuramochi, T. Sato, H. Taniyama, and H. Sumikura, "Low-power nanophotonic devices based on photonic crystals towards dense photonic network on chip," IET Circuits Devices Syst. **5**, 84–93 (2011).

[7] T. F. Krauss, "Slow light in photonic crystal waveguides," J. Phys. D: Appl. Phys. **40**, 2666 (2007).

[8] T. Baba, "Slow light in photonic crystals," Nat. Photonics **2**, 465–473 (2008).

[9] H. J. Kimble, "The quantum internet," Nature **453**, 1023–1030 (2008).

[10] N. Gregersen, P. Kaer, and J. Mørk, "Modeling and design of high-efficiency single-photon sources," IEEE J. Sel. Top. Quantum Electron. **19**, 9000516–9000516 (2013).

[11] P. Lodahl, S. Mahmoodian, and S. Stobbe, "Interfacing single photons and single quantum dots with photonic nanostructures," Rev. Mod. Phys. **87**, 347–400 (2015).

[12] P. Yao, V. S. C. Manga Rao, and S. Hughes, "On-chip single photon sources using planar photonic crystals and single quantum dots," Laser Photonics Rev. **4**, 499–516 (2010).

[13] A. V. Lavrinenko, J. Lægsgaard, N. Gregersen, F. Schmidt, and T. Søndergaard, *Numerical Methods in Photonics* (CRC Press, 2014).

[14] A. Taflove, *Computational Electrodynamics: The Finite-difference Time-domain Method* (Artech House, 1995).

[15] K. Yee, "Numerical solution of initial boundary value problems involving Maxwell's equations in isotropic media," IEEE Trans. Antennas Propag. **14**, 302–307 (1966).

[16] J. Reddy, *An Introduction to the Finite Element Method* (McGraw-Hill Education, 2005), 3rd ed.

[17] A. Javadi, "Quantum electrodynamics with 1D artificial atoms: from Purcell enhancement to single-photon nonlinearities," Ph.D. thesis, Niels Bohr Institute, University of Copenhagen (2015).

[18] A. Peterson, S. Ray, and R. Mittra, *Computational Methods for Electromagnetics* (Wiley, 1998), chap. 1, pp. 1–36.

[19] A. V. Lavrinenko, J. Lægsgaard, N. Gregersen, F. Schmidt, and T. Søndergaard, *Numerical Methods in Photonics* (CRC Press, 2014), chap. 7, pp. 197–249.

[20] R. F. Harrington, *Field Computation by Moment Methods* (Wiley-IEEE Press, 1993).

[21] M. Paulus, P. Gay-Balmaz, and O. J. F. Martin, "Accurate and efficient computation of the Green's tensor for stratified media," Phys. Rev. E **62**, 5797–5807 (2000).

[22] P. Bienstman, "Rigorous and efficient modelling of wavelength scale photonic components," Ph.D. thesis, Department of Information Technology, Ghent University (2001).

[23] A. V. Lavrinenko, J. Lægsgaard, N. Gregersen, F. Schmidt, and T. Søndergaard, *Numerical Methods in Photonics* (CRC Press, 2014), chap. 6, pp. 139–195.

[24] N. Gregersen, "Optical methods for characterization of surface structures on a nanometer scale," Ph.D. thesis, Department of Communications, Optics & Materials, Technical University of Denmark (2006).

[25] P. Lalanne, "Electromagnetic analysis of photonic crystal waveguides operating above the light cone," IEEE J. Quantum Electron. **38**, 800–804 (2002).

[26] C. Sauvan, P. Lalanne, and J.-P. Hugonin, "Slow-wave effect and mode-profile matching in photonic crystal microcavities," Phys. Rev. B **71**, 165118 (2005).

[27] G. Lecamp, P. Lalanne, and J.-P. Hugonin, "Very large spontaneous-emission β factors in photonic-crystal waveguides," Phys. Rev. Lett. **99**, 023902 (2007).

[28] G. Lecamp, J.-P. Hugonin, and P. Lalanne, "Theoretical and computational concepts for periodic optical waveguides," Opt. Express **15**, 11042–11060 (2007).

[29] B. Maes, J. Petráček, S. Burger, P. Kwiecien, J. Luksch, and I. Richter, "Simulations of high-Q optical nanocavities with a gradual 1D bandgap," Opt. Express **21**, 6794–6806 (2013).

[30] P. Gutsche, "Convergence study of the Fourier modal method for nano-optical scattering problems in comparison with the finite element method," M.Sc. thesis, Zuse Institute Berlin (2014).

[31] L. Novotny and B. Hecht, *Principles of Nano-Optics* (Cambridge University Press, 2012), chap. 2, pp. 12–44.

[32] E. Purcell, "Spontaneous emission probabilities at radio frequencies," Phys. Rev. **69**, 681 (1946).

[33] K. Drexhage, "Influence of a dielectric interface on fluorescence decay time," J. Lumin. **1-2**, 693–701 (1970).

[34] P. Goy, J. M. Raimond, M. Gross, and S. Haroche, "Observation of cavity-enhanced single-atom spontaneous emission," Phys. Rev. Lett. **50**, 1903–1906 (1983).

[35] L. Novotny and B. Hecht, *Principles of Nano-Optics* (Cambridge University Press, 2012), chap. 8, pp. 224–281.

[36] M. L. Andersen, S. Stobbe, A. S. Sørensen, and P. Lodahl, "Strongly modified plasmon-matter interaction with mesoscopic quantum emitters," Nat. Phys. **7**, 215–218 (2011).

[37] B. le Feber, N. Rotenberg, and L. Kuipers, "Nanophotonic control of circular dipole emission," Nat. Commun. **6**, 6695 (2015).

[38] A. B. Young, A. C. T. Thijssen, D. M. Beggs, P. Androvitsaneas, L. Kuipers, J. G. Rarity, S. Hughes, and R. Oulton, "Polarization engineering in photonic crystal waveguides for spin-photon entanglers," Phys. Rev. Lett. **115**, 153901 (2015).

[39] J. Bleuse, J. Claudon, M. Creasey, N. S. Malik, J.-M. Gérard, I. Maksymov, J.-P. Hugonin, and P. Lalanne, "Inhibition, enhancement, and control of spontaneous emission in photonic nanowires," Phys. Rev. Lett. **106**, 103601 (2011).

[40] J. Mørk, P. T. Kristensen, P. Kaer, M. Heuck, Y. Yu, and N. Gregersen, "Cavity photonics," in "Photonics Volume 2: Nanophotonic Structures and Materials," (Wiley, 2015), chap. 2, pp. 21–51.

[41] J. Joannopoulos, S. Johnson, J. Winn, and R. Meade, *Photonic Crystals: Molding the Flow of Light* (Princeton University Press, 2011), chap. 4, pp. 44–65.

[42] V. P. Bykov, "Spontaneous emission from a medium with a band spectrum," Sov. J. Quantum Electron. **4**, 861 (1975).

[43] Y. Yamamoto, S. Machida, and G. Björk, "Microcavity semiconductor laser with enhanced spontaneous emission," Phys. Rev. A **44**, 657–668 (1991).

[44] J.-M. Gérard and B. Gayral, "Strong Purcell effect for InAs quantum boxes in three-dimensional solid-state microcavities," J. Lightwave Technol. **17**, 2089–2095 (1999).

[45] G. Lecamp, P. Lalanne, J.-P. Hugonin, and J.-M. Gérard, "Energy transfer through laterally confined Bragg mirrors and its impact on pillar microcavities," IEEE J. Quantum Electron. **41**, 1323–1329 (2005).

[46] E. Yablonovitch, "Inhibited spontaneous emission in solid-state physics and electronics," Phys. Rev. Lett. **58**, 2059–2062 (1987).

[47] S. John, "Strong localization of photons in certain disordered dielectric superlattices," Phys. Rev. Lett. **58**, 2486–2489 (1987).

[48] P. Lodahl, A. Floris van Driel, I. S. Nikolaev, A. Irman, K. Overgaag, D. Vanmaekelbergh, and W. L. Vos, "Controlling the dynamics of spontaneous emission from quantum dots by photonic crystals," Nature **430**, 654–657 (2004).

[49] J. Joannopoulos, S. Johnson, J. Winn, and R. Meade, *Photonic Crystals: Molding the Flow of Light* (Princeton University Press, 2011), chap. 6, pp. 95–121.

[50] K. Busch, G. von Freymann, S. Linden, S. Mingaleev, L. Tkeshelashvili, and M. Wegener, "Periodic nanostructures for photonics," Phys. Rep. **444**, 101–202 (2007).

[51] J. Joannopoulos, S. Johnson, J. Winn, and R. Meade, *Photonic Crystals: Molding the Flow of Light* (Princeton University Press, 2011), chap. 8, pp. 135–155.

[52] J. Jensen and O. Sigmund, "Topology optimization for nano-photonics," Laser Photonics Rev. **5**, 308–321 (2011).

[53] S. Gehrsitz, F. K. Reinhart, C. Gourgon, N. Herres, A. Vonlanthen, and H. Sigg, "The refractive index of $Al_xGa_{1-x}As$ below the band gap: Accurate determination and empirical modeling," J. Appl. Phys. **87**, 7825–7837 (2000).

[54] F. Bloch, "Über die quantenmechanik der elektronen in kristallgittern," Z. Phys. **52**, 555–600 (1929).

[55] J. Joannopoulos, S. Johnson, J. Winn, and R. Meade, *Photonic Crystals: Molding the Flow of Light* (Princeton University Press, 2011), chap. 5, pp. 66–93.

[56] S. Hughes, L. Ramunno, J. Young, and J. Sipe, "Extrinsic optical scattering loss in photonic crystal waveguides: Role of fabrication disorder and photon group velocity," Phys. Rev. Lett. **94**, 033903 (2005).

[57] M. Patterson, S. Hughes, S. Combrié, N.-V.-Q. Tran, A. De Rossi, R. Gabet, and Y. Jaouën, "Disorder-induced coherent scattering in slow-light photonic crystal waveguides," Phys. Rev. Lett. **102**, 253903 (2009).

[58] S. Mazoyer, J.-P. Hugonin, and P. Lalanne, "Disorder-induced multiple scattering in photonic-crystal waveguides," Phys. Rev. Lett. **103**, 063903 (2009).

[59] V. Savona, "Electromagnetic modes of a disordered photonic crystal," Phys. Rev. B **83**, 085301 (2011).

[60] N. Mann, S. Combrié, P. Colman, M. Patterson, A. D. Rossi, and S. Hughes, "Reducing disorder-induced losses for slow light photonic crystal waveguides through Bloch mode engineering," Opt. Lett. **38**, 4244–4247 (2013).

[61] D. Melati, A. Melloni, and F. Morichetti, "Real photonic waveguides: guiding light through imperfections," Adv. Opt. Photon. **6**, 156–224 (2014).

[62] W. Xue, Y. Yu, L. Ottaviano, Y. Chen, E. Semenova, K. Yvind, and J. Mork, "Threshold characteristics of slow-light photonic crystal lasers," (2015). Preprint, arXiv:1508.05349v1 [physics.optics].

[63] P. Lalanne, C. Sauvan, and J.-P. Hugonin, "Photon confinement in photonic crystal nanocavities," Laser Photonics Rev. **2**, 514–526 (2008).

[64] L. Novotny and B. Hecht, *Principles of Nano-Optics* (Cambridge University Press, 2012), chap. 13, pp. 414–447.

[65] L. Coldren and S. Corzine, *Diode lasers and photonic integrated circuits* (Wiley, 1995), chap. 4, pp. 111–184, 1st ed.

[66] G. Lecamp, P. Lalanne, and J.-P. Hugonin, "The electromagnetic properties of light emission into semiconductor waveguides," in "Nanophotonics," (SPIE, 2006), pp. 61950E–61950E–7.

[67] V. S. C. Manga Rao and S. Hughes, "Single quantum-dot Purcell factor and β factor in a photonic crystal waveguide," Phys. Rev. B **75**, 205437 (2007).

[68] M. Arcari, I. Söllner, A. Javadi, S. Lindskov Hansen, S. Mahmoodian, J. Liu, H. Thyrrestrup, E. H. Lee, J. D. Song, S. Stobbe, and P. Lodahl, "Near-unity coupling efficiency of a quantum emitter to a photonic crystal waveguide," Phys. Rev. Lett. **113**, 093603 (2014).

[69] J. Joannopoulos, S. Johnson, J. Winn, and R. Meade, *Photonic Crystals: Molding the Flow of Light* (Princeton University Press, 2011), chap. 3, pp. 25–43.

[70] M. Palamaru and P. Lalanne, "Photonic crystal waveguides: Out-of-plane losses and adiabatic modal conversion," Appl. Phys. Lett. **78**, 1466–1468 (2001).

[71] Q. Cao, P. Lalanne, and J.-P. Hugonin, "Stable and efficient Bloch-mode computational method for one-dimensional grating waveguides," J. Opt. Soc. Am. A **19**, 335–338 (2002).

[72] P. Yeh, A. Yariv, and C.-S. Hong, "Electromagnetic propagation in periodic stratified media. I. General theory," J. Opt. Soc. Am. **67**, 423–438 (1977).

[73] E. Popov, M. Nevière, B. Gralak, and G. Tayeb, "Staircase approximation validity for arbitrary-shaped gratings," J. Opt. Soc. Am. A **19**, 33–42 (2002).

[74] D. F. G. Gallagher and T. P. Felici, "Eigenmode expansion methods for simulation of optical propagation in photonics – Pros and cons," in "Integrated Optics: Devices, Materials, and Technologies VII, 69," (2003), pp. 69–82.

[75] H. Kim and B. Lee, "Pseudo-Fourier modal analysis of two-dimensional arbitrarily shaped grating structures," J. Opt. Soc. Am. A **25**, 40–54 (2008).

[76] E. Noponen and J. Turunen, "Eigenmode method for electromagnetic synthesis of diffractive elements with three-dimensional profiles," J. Opt. Soc. Am. A **11**, 2494–2502 (1994).

[77] M. G. Moharam, E. B. Grann, D. A. Pommet, and T. K. Gaylord, "Formulation for stable and efficient implementation of the rigorous coupled-wave analysis of binary gratings," J. Opt. Soc. Am. A **12**, 1068–1076 (1995).

[78] L. Li, "Formulation and comparison of two recursive matrix algorithms for modeling layered diffraction gratings," J. Opt. Soc. Am. A **13**, 1024–1035 (1996).

[79] L. Li, "Use of Fourier series in the analysis of discontinuous periodic structures," J. Opt. Soc. Am. A **13**, 1870–1876 (1996).

[80] L. Li, "New formulation of the Fourier modal method for crossed surface-relief gratings," J. Opt. Soc. Am. A **14**, 2758–2767 (1997).

[81] P. Lalanne, "Effective properties and band structures of lamellar subwavelength crystals: Plane-wave method revisited," Phys. Rev. B **58**, 9801–9807 (1998).

[82] A. Sudbo, "Why are accurate computations of mode fields in rectangular dielectric waveguides difficult?" J. Lightwave Technol. **10**, 418–419 (1992).

[83] T. Tamir and H. C. Wang, "Scattering of electromagnetic waves by a sinusoidally stratified half-space. I. Formal solution and analytic approximations," Can. J. Phys. **44**, 2073–2094 (1966).

[84] T. Tamir, "Scattering of electromagnetic waves by a sinusoidally stratified half-space. II. Diffraction aspects at the Rayleigh and Bragg wavelengths," Can. J. Phys. **44**, 2461–2494 (1966).

[85] J. J. Hench and Z. Strakoš, "The RCWA method - A case study with open questions and perspectives of algebraic computations," Electron. Trans. Numer. Anal. **31**, 331–357 (2008).

[86] L. C. Botten, N. A. Nicorovici, R. C. McPhedran, C. M. d. Sterke, and A. A. Asatryan, "Photonic band structure calculations using scattering matrices," Phys. Rev. E **64**, 046603 (2001).

[87] J. R. de Lasson, P. T. Kristensen, J. Mørk, and N. Gregersen, "Roundtrip matrix method for calculating the leaky resonant modes of open nanophotonic structures," J. Opt. Soc. Am. A **31**, 2142–2151 (2014).

[88] J. Ctyroky, "3-D bidirectional propagation algorithm based on Fourier series," J. Lightwave Technol. **30**, 3699–3708 (2012).

[89] Private communication with author of [88].

[90] Z.-Y. Li and K.-M. Ho, "Application of structural symmetries in the plane-wave-based transfer-matrix method for three-dimensional photonic crystal waveguides," Phys. Rev. B **68**, 245117 (2003).

[91] C. Zhou and L. Li, "Formulation of the Fourier modal method for symmetric crossed gratings in symmetric mountings," J. Opt. A: Pure Appl. Opt. **6**, 43 (2004).

[92] J. Bischoff, "Formulation of the normal vector RCWA for symmetric crossed gratings in symmetric mountings," J. Opt. Soc. Am. A **27**, 1024–1031 (2010).

[93] D. Pissoort, B. Denecker, P. Bienstman, F. Olyslager, and D. D. Zutter, "Comparative study of three methods for the simulation of two-dimensional photonic crystals," J. Opt. Soc. Am. A **21**, 2186–2195 (2004).

[94] M. Arcari, I. Söllner, A. Javadi, S. Lindskov Hansen, S. Mahmoodian, J. Liu, H. Thyrrestrup, E. H. Lee, J. D. Song, S. Stobbe, and P. Lodahl, "Near-unity coupling efficiency of a quantum emitter to a photonic crystal waveguide," Supplementary Material of Phys. Rev. Lett. **113**, 093603 (2014) (2014).

[95] M. Minkov, U. P. Dharanipathy, R. Houdré, and V. Savona, "Statistics of the disorder-induced losses of high-Q photonic crystal cavities," Opt. Express **21**, 28233–28245 (2013).

[96] R. Faggiani, A. Baron, X. Zang, L. Lalouat, S. A. Schulz, K. Vynck, B. O'Regan, B. Cluzel, F. de Fornel, T. F. Krauss, and P. Lalanne, "Ultimate limits of light confinement in randomly-perturbed periodic structures," (2015). Preprint, arXiv:1505.03472v1 [physics.optics].

[97] G. Arfken and H. Weber, *Mathematical Methods For Physicists* (Elsevier Science, 2005), chap. 14, pp. 881–930, 6th ed.

[98] H. S. Sözüer, J. W. Haus, and R. Inguva, "Photonic bands: Convergence problems with the plane-wave method," Phys. Rev. B **45**, 13962–13972 (1992).

[99] T. Weiss, G. Granet, N. A. Gippius, S. G. Tikhodeev, and H. Giessen, "Matched coordinates and adaptive spatial resolution in the Fourier modal method," Opt. Express **17**, 8051–8061 (2009).

[100] S. Essig and K. Busch, "Generation of adaptive coordinates and their use in the Fourier Modal Method," Opt. Express **18**, 23258–23274 (2010).

[101] J. Küchenmeister, "Three-dimensional adaptive coordinate transformations for the Fourier modal method," Opt. Express **22**, 1342–1349 (2014).

[102] J. Ctyroky, "Efficient boundary conditions for bidirectional propagation algorithm based on Fourier series," J. Lightwave Technol. **27**, 2575–2582 (2009).

[103] C. D. Taylor, D.-H. Lam, and T. Shumpert, "Electromagnetic pulse scattering in time-varying inhomogeneous media," IEEE Trans. Antennas Propag. **17**, 585–589 (1969).

[104] D. E. Merewether, "Transient currents induced on a metallic body of revolution by an electromagnetic pulse," IEEE Trans. Electromagn. Compat. **EMC-13**, 41–44 (1971).

[105] K. S. Kunz and K.-M. Lee, "A three-dimensional finite-difference solution of the external response of an aircraft to a complex transient em environment: Part I-the method and its implementation," IEEE Trans. Electromagn. Compat. **EMC-20**, 328–333 (1978).

[106] A. Taflove and M. Brodwin, "Numerical solution of steady-state electromagnetic scattering problems using the time-dependent Maxwell's equations," IEEE Trans. Microwave Theory Tech. **23**, 623–630 (1975).

[107] A. Taflove, "Application of the finite-difference time-domain method to sinusoidal steady-state electromagnetic-penetration problems," IEEE Trans. Electromagn. Compat. **EMC-22**, 191–202 (1980).

[108] G. Mur, "Absorbing boundary conditions for the finite-difference approximation of the time-domain electromagnetic-field equations," IEEE Trans. Electromagn. Compat. **EMC-23**, 377–382 (1981).

[109] J.-P. Bérenger, "A perfectly matched layer for the absorption of electromagnetic waves," J. Comput. Phys. **114**, 185–200 (1994).

[110] M. G. Moharam and T. K. Gaylord, "Rigorous coupled-wave analysis of planar-grating diffraction," J. Opt. Soc. Am. **71**, 811–818 (1981).

[111] T. Weiss, N. A. Gippius, S. G. Tikhodeev, G. Granet, and H. Giessen, "Derivation of plasmonic resonances in the Fourier modal method with adaptive spatial resolution and matched coordinates," J. Opt. Soc. Am. A **28**, 238–244 (2011).

[112] P. Lalanne and E. Silberstein, "Fourier-modal methods applied to waveguide computational problems," Opt. Lett. **25**, 1092–1094 (2000).

[113] E. Silberstein, P. Lalanne, J.-P. Hugonin, and Q. Cao, "Use of grating theories in integrated optics," J. Opt. Soc. Am. A **18**, 2865–2875 (2001).

[114] J.-P. Hugonin and P. Lalanne, "Perfectly matched layers as nonlinear coordinate transforms: a generalized formalization," J. Opt. Soc. Am. A **22**, 1844–1849 (2005).

[115] D. De Zutter and F. Olyslager, "Analysis of waveguide discontinuities using perfectly matched layers," Electron. Lett. **34**, 2138–2140 (1998).

[116] P. Bienstman and R. Baets, "Optical modelling of photonic crystals and VCSELs using eigenmode expansion and perfectly matched layers," Opt. Quantum Electron. **33**, 327–341 (2001).

[117] P. Bienstman, H. Derudder, R. Baets, F. Olyslager, and D. De Zutter, "Analysis of cylindrical waveguide discontinuities using vectorial eigenmodes and perfectly matched layers," IEEE Trans. Microwave Theory Tech. **49**, 349–354 (2001).

[118] N. Gregersen and J. Mørk, "An improved perfectly matched layer for the eigenmode expansion technique," Opt. Quantum Electron. **40**, 957–966 (2008).

[119] W. C. Chew and W. H. Weedon, "A 3D perfectly matched medium from modified Maxwell's equations with stretched coordinates," Microwave Opt. Technol. Lett. **7**, 599–604 (1994).

[120] S. Hewlett and F. Ladouceur, "Fourier decomposition method applied to mapped infinite domains: scalar analysis of dielectric waveguides down to modal cutoff," J. Lightwave Technol. **13**, 375–383 (1995).

[121] A. Armaroli, A. Morand, P. Benech, G. Bellanca, and S. Trillo, "Three-dimensional analysis of cylindrical microresonators based on the aperiodic Fourier modal method," J. Opt. Soc. Am. A **25**, 667–675 (2008).

[122] J. Ctyroky, P. Kwiecien, and I. Richter, "Fourier series-based bidirectional propagation algorithm with adaptive spatial resolution," J. Lightwave Technol. **28**, 2969–2976 (2010).

[123] M. Pisarenco and I. Setija, "Alternative discretization in the aperiodic Fourier modal method leading to reduction in computational costs," in "Modeling Aspects in Optical Metrology IV," (SPIE, 2013), p. 87890K.

[124] F. Bordas, M. J. Steel, C. Seassal, and A. Rahmani, "Confinement of band-edge modes in a photonic crystal slab," Opt. Express **15**, 10890–10902 (2007).

[125] P. T. Kristensen, C. V. Vlack, and S. Hughes, "Generalized effective mode volume for leaky optical cavities," Opt. Lett. **37**, 1649–1651 (2012).

[126] M. Pisarenco, J. Maubach, I. Setija, and R. Mattheij, "Aperiodic Fourier modal method in contrast-field formulation for simulation of scattering from finite structures," J. Opt. Soc. Am. A **27**, 2423–2431 (2010).

[127] B. Guizal, D. Barchiesi, and D. Felbacq, "Electromagnetic beam diffraction by a finite lamellar structure: an aperiodic coupled-wave method," J. Opt. Soc. Am. A **20**, 2274–2280 (2003).

[128] N. Bonod, E. Popov, and M. Nevière, "Differential theory of diffraction by finite cylindrical objects," J. Opt. Soc. Am. A **22**, 481–490 (2005).

[129] J. R. de Lasson, T. Christensen, J. Mørk, and N. Gregersen, "Modeling of cavities using the analytic modal method and an open geometry formalism," J. Opt. Soc. Am. A **29**, 1237–1246 (2012).

[130] G. Mie, "Articles on the optical characteristics of turbid tubes, especially colloidal metal solutions," Ann. Phys. **25**, 377–445 (1908).

[131] H. M. Lai, P. T. Leung, K. Young, P. W. Barber, and S. C. Hill, "Time-independent perturbation for leaking electromagnetic modes in open systems with application to resonances in microdroplets," Phys. Rev. A **41**, 5187–5198 (1990).

[132] H. A. Atwater and A. Polman, "Plasmonics for improved photovoltaic devices," Nat. Mater. **9**, 205–213 (2010).

[133] L. Yang, H. Wang, B. Yan, and B. M. Reinhard, "Calibration of silver plasmon rulers in the 1-25 nm separation range: Experimental indications of distinct plasmon coupling regimes," J. Phys. Chem. C **114**, 4901–4908 (2010).

[134] N. Mirsaleh-Kohan, V. Iberi, P. D. Simmons, N. W. Bigelow, A. Vaschillo, M. M. Rowland, M. D. Best, S. J. Pennycook, D. J. Masiello, B. S. Guiton, and J. P. Camden, "Single-molecule surface-enhanced Raman scattering: Can STEM/EELS image electromagnetic hot spots?" J. Phys. Chem. Lett. **3**, 2303–2309 (2012).

[135] K. Nozaki, T. Tanabe, A. Shinya, S. Matsuo, T. Sato, H. Taniyama, and M. Notomi, "Sub-femtojoule all-optical switching using a photonic-crystal nanocavity," Nat. Photonics **4**, 477–483 (2010).

[136] A. Dousse, J. Suffczynski, A. Beveratos, O. Krebs, A. Lemaitre, I. Sagnes, J. Bloch, P. Voisin, and P. Senellart, "Ultrabright source of entangled photon pairs," Nature **466**, 217–220 (2010).

[137] S. Strauf and F. Jahnke, "Single quantum dot nanolaser," Laser Photonics Rev. **5**, 607–633 (2011).

[138] M. Lermer, N. Gregersen, F. Dunzer, S. Reitzenstein, S. Höfling, J. Mørk, L. Worschech, M. Kamp, and A. Forchel, "Bloch-wave engineering of quantum dot micropillars for cavity quantum electrodynamics experiments," Phys. Rev. Lett. **108**, 057402 (2012).

[139] A. Schwagmann, S. Kalliakos, D. J. P. Ellis, I. Farrer, J. P. Griffiths, G. A. C. Jones, D. A. Ritchie, and A. J. Shields, "In-plane single-photon emission from a L3 cavity coupled to a photonic crystal waveguide," Opt. Express **20**, 28614–28624 (2012).

[140] J. D. Jackson, *Classical Electrodynamics* (Wiley, 1998), chap. 8, pp. 352–406.

[141] R. Lang, M. O. Scully, and W. E. Lamb, "Why is the laser line so narrow? A theory of single-quasimode laser operation," Phys. Rev. A **7**, 1788–1797 (1973).

[142] E. S. C. Ching, P. T. Leung, and K. Young, "Optical processes in microcavities – the role of quasinormal modes," in "Optical Processes in Microcavities," (World Scientific, 1996), pp. 1–75.

[143] D. A. Powell, "Resonant dynamics of arbitrarily shaped meta-atoms," Phys. Rev. B **90**, 075108 (2014).

[144] S. M. Dutra and G. Nienhuis, "What is a quantized mode of a leaky cavity?" in "Modern Challenges in Quantum Optics," (Springer, 2001), chap. 21, pp. 338–354.

[145] L. Vaĭnshteĭn, "Open resonators for lasers," Soviet Physics-JETP **17**, 709–719 (1963).

[146] K. Ujihara, "Quantum theory of a one-dimensional optical cavity with output coupling. Field quantization," Phys. Rev. A **12**, 148–158 (1975).

[147] E. S. C. Ching, P. T. Leung, A. Maassen van den Brink, W. M. Suen, S. S. Tong, and K. Young, "Quasinormal-mode expansion for waves in open systems," Rev. Mod. Phys. **70**, 1545–1554 (1998).

[148] K. M. Lee, P. T. Leung, and K. M. Pang, "Dyadic formulation of morphology-dependent resonances. I. Completeness relation," J. Opt. Soc. Am. B **16**, 1409–1417 (1999).

[149] A. Settimi, S. Severini, N. Mattiucci, C. Sibilia, M. Centini, G. D'Aguanno, M. Bertolotti, M. Scalora, M. Bloemer, and C. M. Bowden, "Quasinormal-mode description of waves in one-dimensional photonic crystals," Phys. Rev. E **68**, 026614 (2003).

[150] C. Sauvan, J.-P. Hugonin, I. S. Maksymov, and P. Lalanne, "Theory of the spontaneous optical emission of nanosize photonic and plasmon resonators," Phys. Rev. Lett. **110**, 237401 (2013).

[151] Q. Bai, M. Perrin, C. Sauvan, J.-P. Hugonin, and P. Lalanne, "Efficient and intuitive method for the analysis of light scattering by a resonant nanostructure," Opt. Express **21**, 27371–27382 (2013).

[152] R.-C. Ge, P. T. Kristensen, J. F. Young, and S. Hughes, "Quasinormal mode approach to modelling light-emission and propagation in nanoplasmonics," New J. Phys. **16**, 113048 (2014).

[153] S. Dutra, *Cavity Quantum Electrodynamics: The Strange Theory of Light in a Box*, Wiley Series in Lasers and Applications (Wiley, 2005).

[154] A. Isaacson, C. McCurdy, and W. Miller, "On the possibility of calculating Siegert eigenvalues for autoionizing electronic states," Chem. Phys. **34**, 311–317 (1978).

[155] A. Landau, I. Haritan, P. R. Kapralova-Zdanska, and N. Moiseyev, "Atomic and molecular complex resonances from real eigenvalues using standard (hermitian) electronic structure calculations," (2015). Preprint, arXiv:1508.00439v1 [quant-ph].

[156] A. G. Fox and T. Li, "Computation of optical resonator modes by the method of resonance excitation," IEEE J. Quantum Electron. **4**, 460–465 (1968).

[157] P. T. Kristensen and S. Hughes, "Modes and mode volumes of leaky optical cavities and plasmonic nanoresonators," ACS Photonics **1**, 2–10 (2014).

[158] L. Novotny and B. Hecht, *Principles of Nano-Optics* (Cambridge University Press, 2012), chap. 11, pp. 338–368.

[159] P. Martin, *Multiple Scattering. Interaction of Time-Harmonic Waves with N Obstacles* (Cambridge University Press, 2006), chap. 1, pp. 1–28.

[160] R.-C. Ge and S. Hughes, "Design of an efficient single photon source from a metallic nanorod dimer: a quasi-normal mode finite-difference time-domain approach," Opt. Lett. **39**, 4235–4238 (2014).

[161] S. Burger, F. Schmidt, and L. Zschiedrich, "Numerical investigation of photonic crystal microcavities in silicon-on-insulator waveguides," in "Photonic and Phononic Crystal Materials and Devices X," (SPIE, 2010), pp. 76091Q–76091Q–7.

[162] J. R. de Lasson, J. Mørk, and P. T. Kristensen, "Three-dimensional integral equation approach to light scattering, extinction cross sections, local density of states, and quasi-normal modes," J. Opt. Soc. Am. B **30**, 1996–2007 (2013).

[163] J. Mäkitalo, M. Kauranen, and S. Suuriniemi, "Modes and resonances of plasmonic scatterers," Phys. Rev. B **89**, 165429 (2014).

[164] S. G. Tikhodeev, A. L. Yablonskii, E. A. Muljarov, N. A. Gippius, and T. Ishihara, "Quasiguided modes and optical properties of photonic crystal slabs," Phys. Rev. B **66**, 045102 (2002).

[165] A. Akimov, N. Gippius, and S. Tikhodeev, "Optical Fano resonances in photonic crystal slabs near diffraction threshold anomalies," JETP Lett. **93**, 427–430 (2011).

[166] D. A. Bykov and L. L. Doskolovich, "Numerical methods for calculating poles of the scattering matrix with applications in grating theory," J. Lightwave Technol. **31**, 793–801 (2013).

[167] N. Gregersen, S. Reitzenstein, C. Kistner, M. Strauss, C. Schneider, S. Höfling, L. Worschech, A. Forchel, T. Nielsen, J. Mørk, and J.-M. Gérard, "Numerical and experimental study of the Q factor of high-Q micropillar cavities," IEEE J. Quant. Electron. **46**, 1470–1483 (2010).

[168] Z. Hu and Y. Y. Lu, "Simple boundary condition for terminating photonic crystal waveguides," J. Opt. Soc. Am. B **29**, 1356–1360 (2012).

[169] P. T. Kristensen, J. R. de Lasson, and N. Gregersen, "Calculation, normalization, and perturbation of quasinormal modes in coupled cavity-waveguide systems," Opt. Lett. **39**, 6359–6362 (2014).

[170] P. T. Leung, S. Y. Liu, and K. Young, "Completeness and time-independent perturbation of the quasinormal modes of an absorptive and leaky cavity," Phys. Rev. A **49**, 3982–3989 (1994).

[171] P. T. Kristensen, R.-C. Ge, and S. Hughes, "Normalization of quasinormal modes in leaky optical cavities and plasmonic resonators," Phys. Rev. A **92**, 053810 (2015).

[172] E. A. Muljarov, M. B. Doost, and W. Langbein, "Exact mode volume and Purcell factor of open optical systems," (2014). Preprint, arXiv:1409.6877v2 [cond-mat.mes-hall].

[173] G. Hardy, *Divergent Series* (Oxford at the Clarendon Press, 1949), chap. 4, pp. 64–93.

[174] J. R. de Lasson, P. T. Kristensen, J. Mørk, and N. Gregersen, "Semianalytical quasi-normal mode theory for the local density of states in coupled photonic crystal cavity-waveguide structures," Opt. Lett. **40**, 5790–5793 (2015).

[175] P. R. Villeneuve, D. S. Abrams, S. Fan, and J. D. Joannopoulos, "Single-mode waveguide microcavity for fast optical switching," Opt. Lett. **21**, 2017–2019 (1996).

[176] S. Fan, "Sharp asymmetric line shapes in side-coupled waveguide-cavity systems," Appl. Phys. Lett. **80**, 908–910 (2002).

[177] M. Heuck, P. T. Kristensen, Y. Elesin, and J. Mørk, "Improved switching using Fano resonances in photonic crystal structures," Opt. Lett. **38**, 2466–2468 (2013).

[178] U. Fano, "Effects of configuration interaction on intensities and phase shifts," Phys. Rev. **124**, 1866–1878 (1961).

[179] Y. Yu, M. Heuck, H. Hu, W. Xue, C. Peucheret, Y. Chen, L. K. Oxenløwe, K. Yvind, and J. Mørk, "Fano resonance control in a photonic crystal structure and its application to ultrafast switching," Appl. Phys. Lett. **105**, 061117 (2014).

[180] Y. Yu, H. Hu, L. K. Oxenløwe, K. Yvind, and J. Mork, "Ultrafast all-optical modulation using a photonic-crystal Fano structure with broken symmetry," Opt. Lett. **40**, 2357–2360 (2015).

[181] A. D. Osterkryger, J. R. de Lasson, M. Heuck, Y. Yu, J. Mørk, and N. Gregersen, "Spectral symmetry of Fano resonances in a waveguide coupled to a microcavity," (2015). Preprint, arXiv:1512.05869v1 [physics.optics].

[182] J. Mork, Y. Chen, and M. Heuck, "Photonic crystal Fano laser: Terahertz modulation and ultrashort pulse generation," Phys. Rev. Lett. **113**, 163901 (2014).

[183] J. R. de Lasson, P. T. Kristensen, J. Mørk, and N. Gregersen, "A Bloch modal approach for engineering waveguide and cavity modes in two-dimensional photonic crystals," in "Photonic Crystal Materials and Devices XI," (SPIE, 2014), p. 91270F.

[184] M. Born and E. Wolf, *Principles of Optics: Electromagnetic Theory of Propagation, Interference and Diffraction of Light* (Elsevier Science Limited, 1980), chap. 7, pp. 256–369.

[185] J. P. Dowling, M. Scalora, M. J. Bloemer, and C. M. Bowden, "The photonic band edge laser: A new approach to gain enhancement," J. Appl. Phys. **75**, 1896–1899 (1994).

[186] S. Ek, P. Lunnemann, Y. Chen, E. Semenova, K. Yvind, and J. Mørk, "Slow-light-enhanced gain in active photonic crystal waveguides," Nat. Commun. **5**, 5039 (2014).

[187] S. Ek, P. Lunnemann, Y. Chen, E. Semenova, K. Yvind, and J. Mørk, "Slow-light-enhanced gain in active photonic crystal waveguides," Supplementary Material of Nat. Commun. **5**, 5039 (2014) (2014).

[188] Y. Chen, J. R. de Lasson, N. Gregersen, and J. Mørk, "Impact of slow-light enhancement on optical propagation in active semiconductor photonic-crystal waveguides," Phys. Rev. A **92**, 053839 (2015).

[189] B. Tromborg, H. Lassen, and H. Olesen, "Traveling wave analysis of semiconductor lasers: modulation responses, mode stability and quantum mechanical treatment of noise spectra," IEEE J. Quantum Electron. **30**, 939–956 (1994).

[190] H. Kogelnik and C. V. Shank, "Coupled-wave theory of distributed feedback lasers," J. Appl. Phys. **43**, 2327–2335 (1972).

[191] S. Olivier, H. Benisty, C. Weisbuch, C. Smith, T. Krauss, and R. Houdré, "Coupled-mode theory and propagation losses in photonic crystal waveguides," Opt. Express **11**, 1490–1496 (2003).

[192] A. Yariv and A. Gover, "Equivalence of the coupled-mode and Floquet-Bloch formalisms in periodic optical waveguides," Appl. Phys. Lett. **26**, 537–539 (1975).

[193] G. Bao, "Finite element approximation of time harmonic waves in periodic structures," SIAM J. Numer. Anal. **32**, 1155–1169 (1995).

[194] C. Fietz, "Absorbing boundary condition for Bloch-Floquet eigenmodes," J. Opt. Soc. Am. B **30**, 2615–2620 (2013).

[195] J. Grgić, J. R. Ott, F. Wang, O. Sigmund, A.-P. Jauho, J. Mørk, and N. A. Mortensen, "Fundamental limitations to gain enhancement in periodic media and waveguides," Phys. Rev. Lett. **108**, 183903 (2012).

[196] A. Beveratos, R. Brouri, T. Gacoin, A. Villing, J.-P. Poizat, and P. Grangier, "Single photon quantum cryptography," Phys. Rev. Lett. **89**, 187901 (2002).

[197] D. Kleppner, "Inhibited spontaneous emission," Phys. Rev. Lett. **47**, 233–236 (1981).

[198] T. Søndergaard and B. Tromborg, "General theory for spontaneous emission in active dielectric microstructures: Example of a fiber amplifier," Phys. Rev. A **64**, 033812 (2001).

[199] A. Snyder and J. Love, *Optical Waveguide Theory* (Springer, 1983).

[200] V. S. C. Manga Rao and S. Hughes, "Single quantum dot spontaneous emission in a finite-size photonic crystal waveguide: Proposal for an efficient "on chip" single photon gun," Phys. Rev. Lett. **99**, 193901 (2007).

[201] T. Ba Hoang, J. Beetz, L. Midolo, M. Skacel, M. Lermer, M. Kamp, S. Höfling, L. Balet, N. Chauvin, and A. Fiore, "Enhanced spontaneous emission from quantum dots in short photonic crystal waveguides," Appl. Phys. Lett. **100**, 061122 (2012).

[202] A. Laucht, S. Pütz, T. Günthner, N. Hauke, R. Saive, S. Frédérick, M. Bichler, M.-C. Amann, A. W. Holleitner, M. Kaniber, and J. J. Finley, "A waveguide-coupled on-chip single-photon source," Phys. Rev. X **2**, 011014 (2012).

[203] A. Laucht, T. Günthner, S. Pütz, R. Saive, S. Frédérick, N. Hauke, M. Bichler, M.-C. Amann, A. W. Holleitner, M. Kaniber, and J. J. Finley, "Broadband Purcell enhanced emission dynamics of quantum dots in linear photonic crystal waveguides," J. Appl. Phys. **112**, 093520 (2012).

[204] A. Schwagmann, S. Kalliakos, I. Farrer, J. P. Griffiths, G. A. C. Jones, D. A. Ritchie, and A. J. Shields, "On-chip single photon emission from an integrated semiconductor quantum dot into a photonic crystal waveguide," Appl. Phys. Lett. **99**, 261108 (2011).

[205] S. J. Dewhurst, D. Granados, D. J. P. Ellis, A. J. Bennett, R. B. Patel, I. Farrer, D. Anderson, G. A. C. Jones, D. A. Ritchie, and A. J. Shields, "Slow-light-enhanced single quantum dot emission in a unidirectional photonic crystal waveguide," Appl. Phys. Lett. **96**, 031109 (2010).

[206] T. Lund-Hansen, S. Stobbe, B. Julsgaard, H. Thyrrestrup, T. Sünner, M. Kamp, A. Forchel, and P. Lodahl, "Experimental realization of highly efficient broadband coupling of single quantum dots to a photonic crystal waveguide," Phys. Rev. Lett. **101**, 113903 (2008).

[207] S. Hughes, "Enhanced single-photon emission from quantum dots in photonic crystal waveguides and nanocavities," Opt. Lett. **29**, 2659–2661 (2004).

[208] A. Hartmann, L. Loubies, F. Reinhardt, and E. Kapon, "Self-limiting growth of quantum dot heterostructures on nonplanar {111}B substrates," Appl. Phys. Lett. **71**, 1314–1316 (1997).

[209] G. Biasiol and E. Kapon, "Mechanisms of self-ordering of quantum nanostructures grown on nonplanar surfaces," Phys. Rev. Lett. **81**, 2962–2965 (1998).

[210] M. Felici, P. Gallo, A. Mohan, B. Dwir, A. Rudra, and E. Kapon, "Site-controlled InGaAs quantum dots with tunable emission energy," Small **5**, 938–943 (2009).

[211] L. H. Frandsen, A. V. Lavrinenko, J. Fage-Pedersen, and P. I. Borel, "Photonic crystal waveguides with semi-slow light and tailored dispersion properties," Opt. Express **14**, 9444–9450 (2006).

[212] V. S. C. Manga Rao and S. Hughes, "Numerical study of exact Purcell factors in finite-size planar photonic crystal waveguides," Opt. Lett. **33**, 1587–1589 (2008).

[213] P. Yao and S. Hughes, "Controlled cavity QED and single-photon emission using a photonic-crystal waveguide cavity system," Phys. Rev. B **80**, 165128 (2009).

[214] S. Maier, *Plasmonics: Fundamentals and Applications* (Springer, 2007).

[215] S. Maier, *Plasmonics: Fundamentals and Applications* (Springer, 2007), chap. 5, pp. 65–88.

[216] S. Maier, *Plasmonics: Fundamentals and Applications* (Springer, 2007), chap. 1, pp. 5–19.

[217] A. F. Koenderink, "On the use of Purcell factors for plasmon antennas," Opt. Lett. **35**, 4208–4210 (2010).

[218] A. D. Rakić, A. B. Djurišić, J. M. Elazar, and M. L. Majewski, "Optical properties of metallic films for vertical-cavity optoelectronic devices," Appl. Opt. **37**, 5271–5283 (1998).

[219] S. Raza, G. Toscano, A.-P. Jauho, M. Wubs, and N. A. Mortensen, "Unusual resonances in nanoplasmonic structures due to nonlocal response," Phys. Rev. B **84**, 121412 (2011).

[220] G. Toscano, S. Raza, A.-P. Jauho, N. A. Mortensen, and M. Wubs, "Modified field enhancement and extinction by plasmonic nanowire dimers due to nonlocal response," Opt. Express **20**, 4176–4188 (2012).

[221] N. A. Mortensen, S. Raza, M. Wubs, T. Søndergaard, and S. I. Bozhevolnyi, "A generalized non-local optical response theory for plasmonic nanostructures," Nat. Commun. **5**, 5:3809 (2014).

[222] J. A. Scholl, A. García-Etxarri, A. L. Koh, and J. A. Dionne, "Observation of quantum tunneling between two plasmonic nanoparticles," Nano Lett. **13**, 564–569 (2013).

[223] S. Kadkhodazadeh, J. B. Wagner, H. Kneipp, and K. Kneipp, "Coexistence of classical and quantum plasmonics in large plasmonic structures with subnanometer gaps," Appl. Phys. Lett. **103**, 083103 (2013).

[224] J. R. de Lasson, "Electromagnetic scattering in micro- and nanostructured materials," M.Sc. thesis, DTU Fotonik, Technical University of Denmark (2012).

[225] T. Søndergaard, "Modeling of plasmonic nanostructures: Green's function integral equation methods," Phys. Status Solidi B **244**, 3448–3462 (2007).

[226] L. Novotny and B. Hecht, *Principles of Nano-Optics* (Cambridge University Press, 2012), chap. 16, pp. 500–522.

[227] B. T. Draine and P. J. Flatau, "Discrete-dipole approximation for scattering calculations," J. Opt. Soc. Am. A **11**, 1491–1499 (1994).

[228] A. Peterson, S. Ray, and R. Mittra, *Computational Methods for Electromagnetics* (Wiley, 1998), chap. 2, pp. 37–93.

[229] J. R. de Lasson, P. T. Kristensen, and J. Mørk, "Multiple-scattering formalism beyond the quasistatic approximation: Analyzing resonances in plasmonic chains," AIP Conf. Proc. **1475**, 158–160 (2012).

[230] M. Born and E. Wolf, *Principles of Optics: Electromagnetic Theory of Propagation, Interference and Diffraction of Light* (Elsevier Science Limited, 1980), chap. 13, pp. 611–664.

[231] A. Novitsky, A. V. Uskov, C. Gritti, I. E. Protsenko, B. E. Kardynał, and A. V. Lavrinenko, "Photon absorption and photocurrent in solar cells below semiconductor bandgap due to electron photoemission from plasmonic nanoantennas," Prog. Photovoltaics Res. Appl. **22**, 422–426 (2014).

[232] S. Y. Park and D. Stroud, "Surface-plasmon dispersion relations in chains of metallic nanoparticles: An exact quasistatic calculation," Phys. Rev. B **69**, 125418 (2004).

[233] J. Butet, S. Dutta-Gupta, and O. J. F. Martin, "Surface second-harmonic generation from coupled spherical plasmonic nanoparticles: Eigenmode analysis and symmetry properties," Phys. Rev. B **89**, 245449 (2014).

[234] S. Dutta-Gupta and O. J. F. Martin, "Insight into the eigenmodes of plasmonic nanoclusters based on the Green's tensor method," J. Opt. Soc. Am. B **32**, 194–200 (2015).

[235] P. K. Jain, W. Huang, and M. A. El-Sayed, "On the universal scaling behavior of the distance decay of plasmon coupling in metal nanoparticle pairs: A plasmon ruler equation," Nano Lett. **7**, 2080–2088 (2007).

[236] N. Harris, M. D. Arnold, M. G. Blaber, and M. J. Ford, "Plasmonic resonances of closely coupled gold nanosphere chains," J. Phys. Chem. C **113**, 2784–2791 (2009).

[237] J. I. L. Chen, Y. Chen, and D. S. Ginger, "Plasmonic nanoparticle dimers for optical sensing of DNA in complex media," J. Am. Chem. Soc. **132**, 9600–9601 (2010).

[238] A. I. Dolinnyi, "Nanometric rulers based on plasmon coupling in pairs of gold nanoparticles," J. Phys. Chem. C **119**, 4990–5001 (2015).

[239] S. Kadkhodazadeh, J. R. de Lasson, M. Beleggia, H. Kneipp, J. B. Wagner, and K. Kneipp, "Scaling of the surface plasmon resonance in gold and silver dimers probed by EELS," J. Phys. Chem. C **118**, 5478–5485 (2014).

[240] F. J. García de Abajo, "Relativistic energy loss and induced photon emission in the interaction of a dielectric sphere with an external electron beam," Phys. Rev. B **59**, 3095–3107 (1999).

[241] M. Kraft, Y. Luo, and J. B. Pendry, "Transformation optics and EELS in plasmonics," in "Progress In Electromagnetics Research Symposium (PIERS)," (2015).

[242] Y. Cao, A. Manjavacas, N. Large, and P. Nordlander, "Electron energy-loss spectroscopy calculation in finite-difference time-domain package," ACS Photonics **2**, 369–375 (2015).

[243] R.-C. Ge and S. Hughes, "Quasinormal mode theory and modelling of electron energy loss spectroscopy," (2015). Preprint, arXiv:1510.01170v1 [cond-mat.mes-hall].

[244] S. A. Maier, M. L. Brongersma, P. G. Kik, and H. A. Atwater, "Observation of near-field coupling in metal nanoparticle chains using far-field polarization spectroscopy," Phys. Rev. B **65**, 193408 (2002).

[245] P. Nordlander, C. Oubre, E. Prodan, K. Li, and M. I. Stockman, "Plasmon hybridization in nanoparticle dimers," Nano Lett. **4**, 899–903 (2004).

[246] N. Engheta, A. Salandrino, and A. Alù, "Circuit elements at optical frequencies: Nanoinductors, nanocapacitors, and nanoresistors," Phys. Rev. Lett. **95**, 095504 (2005).

[247] D. Griffiths, *Introduction to Electrodynamics* (Prentice Hall, 1999), chap. 2, pp. 58–109, 3rd ed.

[248] I. Söllner, S. Mahmoodian, S. L. Hansen, L. Midolo, A. Javadi, G. Kiršanske, T. Pregnolato, H. El-Ella, E. H. Lee, J. D. Song, S. Stobbe, and P. Lodahl, "Deterministic photon-emitter coupling in chiral photonic circuits," Nat. Nanotechnol. **10**, 775–778 (2015).

[249] O. J. F. Martin and N. B. Piller, "Electromagnetic scattering in polarizable backgrounds," Phys. Rev. E **58**, 3909–3915 (1998).

[250] A. V. Lavrinenko, J. Lægsgaard, N. Gregersen, F. Schmidt, and T. Søndergaard, *Numerical Methods in Photonics* (CRC Press, 2014), chap. 2, pp. 5–23.

[251] Y. Chen and J. Mørk, "Distributed feedback effects in active semiconductor photonic crystal waveguides," in "Advanced Photonics Congress," (Optical Society of America, 2012), p. ITu2C.4.